Parson, L., Hawkins, J., Allan, J., et al., 1992
Proceedings of the Ocean Drilling Program, Initial Reports, Vol. 135

4. SITE 834[1]

Shipboard Scientific Party[2]

HOLE 834A

Date occupied: 20 December 1990

Date departed: 23 December 1990

Time on hole: 2 days, 15 min

Position: 18°34.058′S, 177°51.735′W

Bottom felt (rig floor; m, drill-pipe measurement): 2702.9

Distance between rig floor and sea level (m): 10.65

Water depth (drill-pipe measurement from sea level, m): 2692.3

Total depth (rig floor; m): 2852.40

Penetration (m): 149.50

Number of cores (including cores with no recovery): 20

Total length of cored section (m): 149.5

Total core recovered (m): 113.17

Core recovery (%): 75.7

Oldest sediment cored:
Depth (mbsf): 133.00
Nature: claystone/tuff
Earliest age: early Pliocene

Hard rock:
Depth (mbsf): 112.50
Nature: basalt
Measured velocity (km/s): 3.10–4.62 (average = 4.15)

HOLE 834B

Date occupied: 23 December 1990

Date departed: 30 December 1990

Time on hole: 7 days, 12 hr, 1 min

Position: 18°34.052′S, 177°51.737′W

Bottom felt (rig floor; m, drill-pipe measurement): 2699.1

Distance between rig floor and sea level (m): 68

Water depth (drill-pipe measurement from sea level, m): 2688.4

Total depth (rig floor; m): 3134.4

Penetration (m): 435.30

Number of cores (including cores with no recovery): 59

Total length of cored section (m): 375.50

Total core recovered (m): 105.5

Core recovery (%): 28.1

Oldest sediment cored:
Depth (mbsf): 310.6
Nature: calcarenite
Earliest age: late Miocene
Measured velocity (km/s): 1.5

Hard rock:
Depth (mbsf): 106.2
Nature: basalt
Measured velocity (km/s): 4.2

Basement:
Depth (mbsf): 163.4
Nature: basalt
Measured velocity (km/s): 4.2

Principal results: Site 834 is located in the western Lau Basin about 100 km east of the Lau Ridge. The Lau Ridge is the remnant arc of the trench-arc-backarc system related to the convergent plate margin of the Tonga Trench. The site is in a small, north-trending basin of about 200 to 400 m relief. Single-channel seismic reflection data indicated that the basin fill is about 0.17 s two-way traveltime (TWT); drilling encountered basalt at a depth of 112.5 m.

The main scientific objectives for Site 834 were (1) to sample igneous rocks formed in the first 0.5 m.y. of crustal extension of the Lau Basin; (2) to determine the age of the beginning of the basin opening; (3) to collect a sedimentary, paleontologic, and paleomagnetic record from the basin fill; and (4) to determine physical and chemical properties of the cores. The site was selected on the assumption that the small basin formed early in the history of crustal extension and that the drill cores would preserve a record of the early magmatic and sedimentary processes. Magnetic data are ambiguous in that various ages had been assigned to the anomaly at this site. The combination of accurate dates for the basal sediments with a detailed magnetic stratigraphy in the cores was expected to resolve this question. The chemistry and petrology of the igneous basement were required to understand magma evolution from the arc-like to MORB-like rocks that have been collected in the basin by dredging.

A continuous sedimentary sequence was recovered at Hole 834A down to 112.5 mbsf (Fig. 1). Below this, sediments are intercalated with basaltic layers of varied thickness. These are flows or sills and it is possible that both forms are represented. The interlayered sediment and basalt continues down to 164 mbsf. The sedimentary assemblage consists of clayey nannofossil oozes, turbiditic foraminiferal sands and oozes, clayey nannofossil mixed sediments, and claystones. Many of these units are interbedded with epiclastic vitric ash or, more rarely, pyroclastic air-fall tuff layers. The sequence can be divided into four lithologic units, primarily on differences in sediment composition, particularly on the occurrence of vitric ashes and the increasing clay content of the sediment downhole.

Unit I is 42 m thick and is composed predominantly of brown clayey nannofossil oozes with occasional interbeds of turbiditic calcareous sands and oozes. Although three vitric ash layers are present in the upper 12 m, volcaniclastic material is generally rare in the rest of the unit. Based on paleomagnetic and biostratigraphic data, the age span of Unit I is late Pleistocene to 2.3 Ma.

Unit II extends from 42 to 78 mbsf and is composed of clayey nannofossil mixed sediment interbedded with vitric ash layers. Volcaniclastic sediments, either primary pyroclastic air-fall ashes or, much more commonly, epiclastic clastic turbidites, make up 20% of the total bulk of Unit II. Individual ash layers range from 0.02 to 1.20 m in thickness. Paleomagnetic and biostratigraphic data suggest that the age span of Unit II is 2.3 to 3.8 Ma. Unit III extends from 78 to 112.5 mbsf and is distinguished from Unit II by its increased vitric ash content. Thick vitric ashes are the dominant lithology. These are interbedded with iron-oxyhydroxide-stained nannofossil clayey mixed sediments and nannofossil clays. The base of Unit III is, as yet, poorly

[1] Parson, L., Hawkins, J., Allan, J., et al., 1992. *Proc. ODP, Init. Repts.,* 135: Ocean Drilling Program (College Station, TX).

[2] Shipboard Scientific Party is as given in the list of participants preceding the contents.

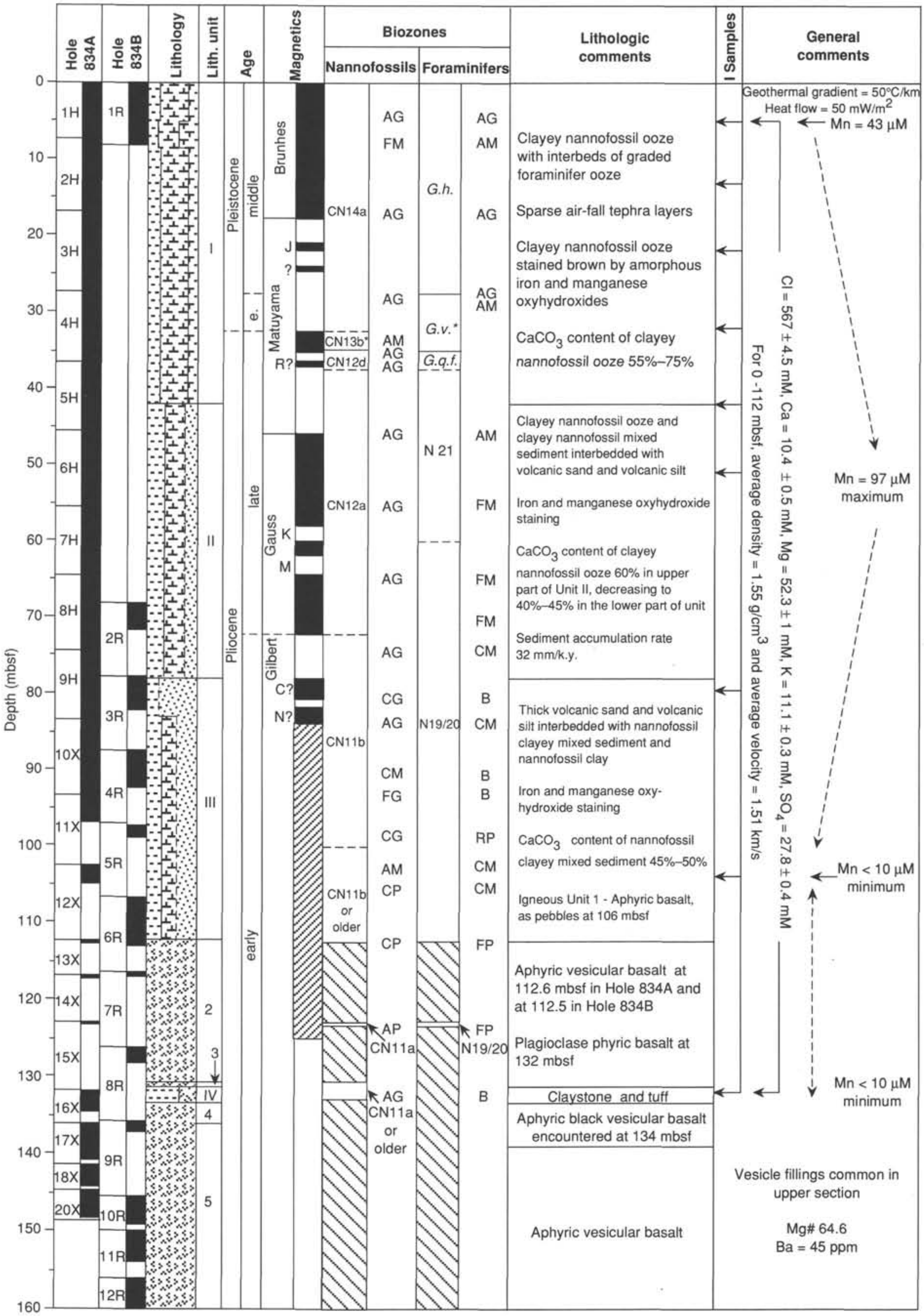

Figure 1. Site summary, Site 834. Abbreviations for abundance are as follows: A = abundant, C = common, F = few, R = rare, and B = barren. Those for preservation are as follows: G = good, M = moderate, and P = poor. Planktonic foraminifer zones are abbreviated as follows: *G. h.* = *Globorotalia hessi*, *G. v.* = *Globorotalia viola*, and *G. q. f.* = *Globigerinoides quadrilobatus fistulosus*.

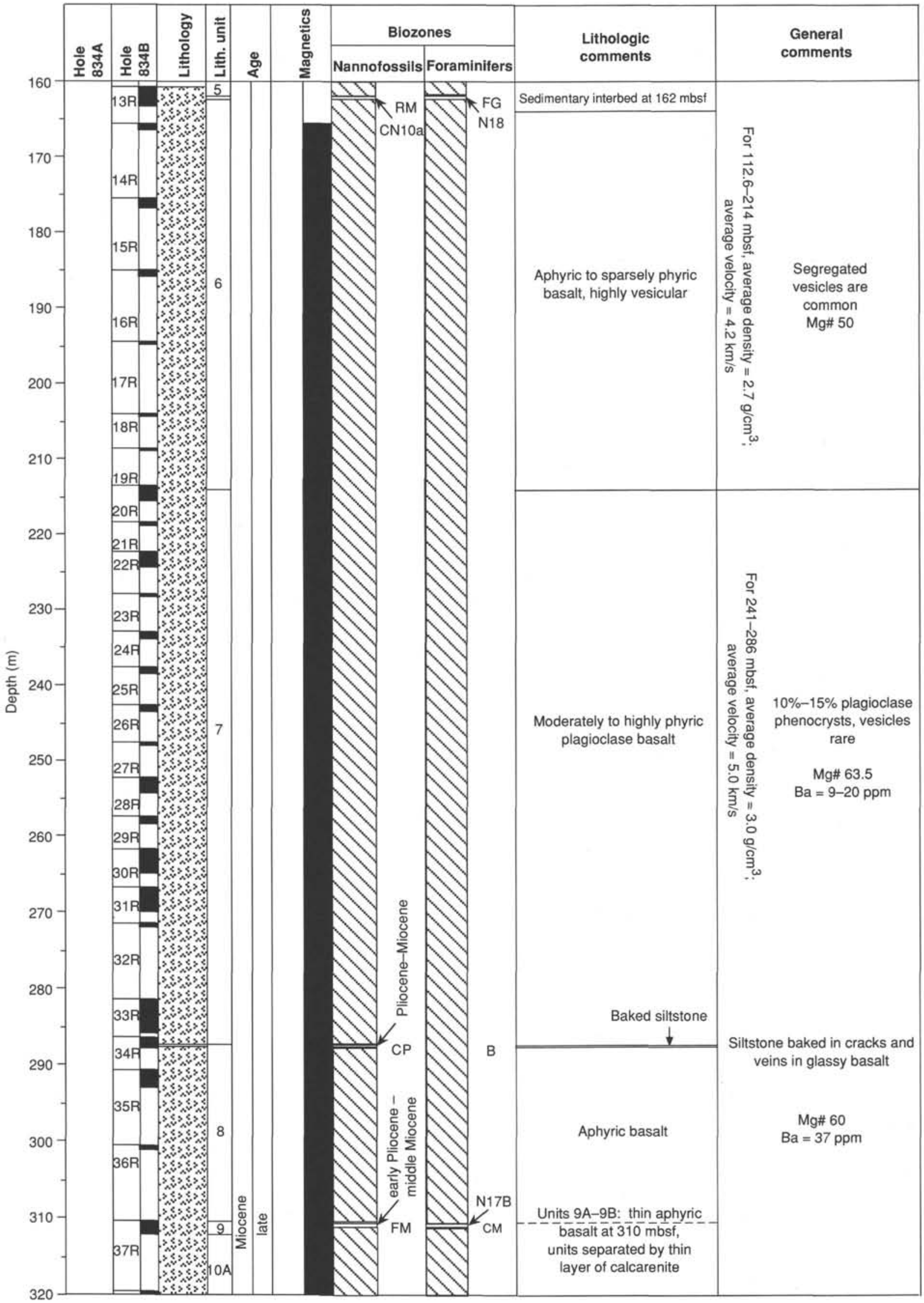

Figure 1 (continued).

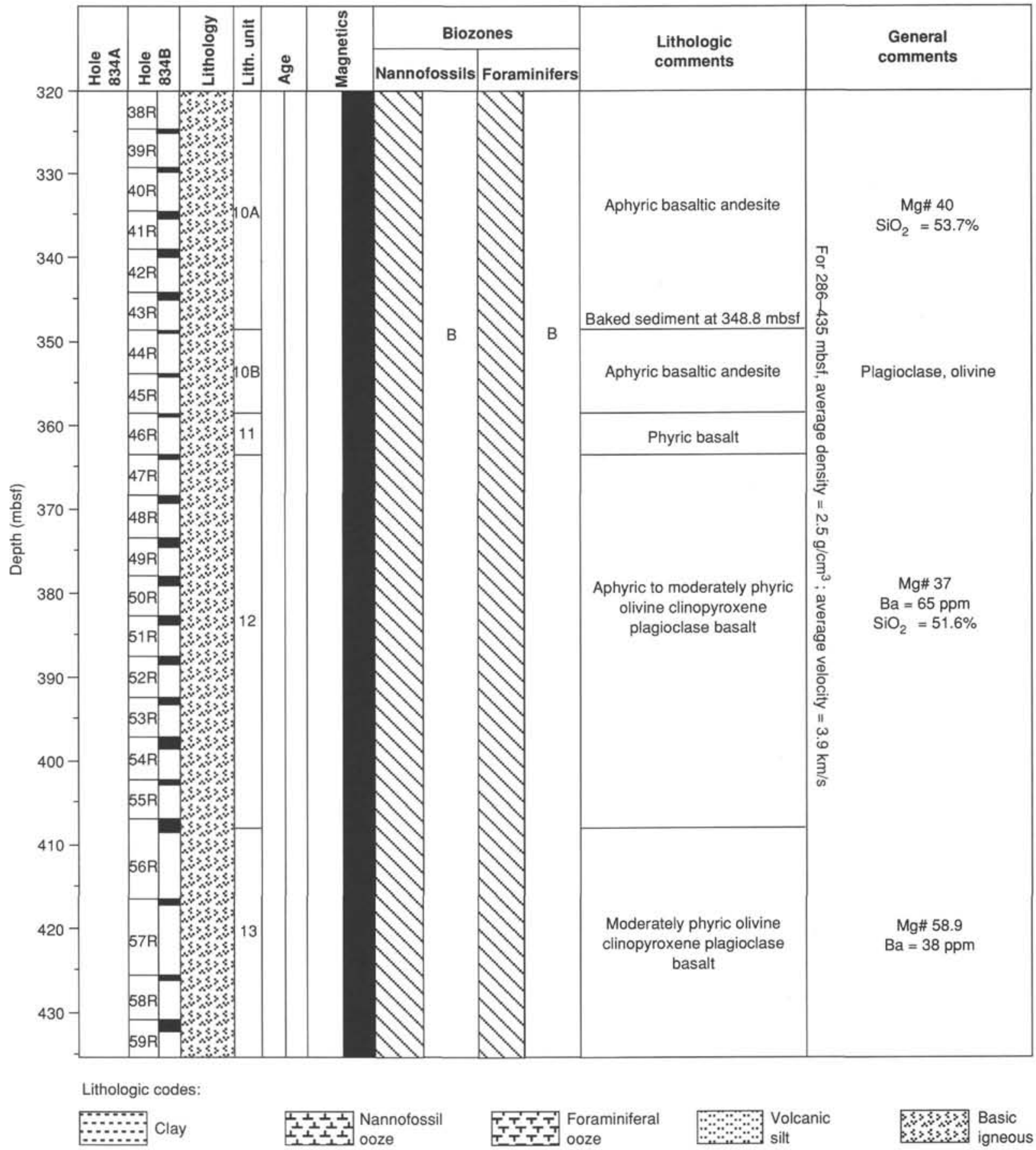

Figure 1 (continued).

constrained by paleomagnetic or biostratigraphic data, but is interpreted as lower Pliocene in age. Unit IV is composed primarily of firm or indurated claystones, vitric tuffs, and calcarenites, which are found as thin bands of intercalated sediments within lava flows. These are generally shallow-water to neritic sediments probably deposited close to the time at which the basin first began to open.

Biostratigraphic studies of sediment cores show that sediment Unit I contains abundant well-preserved planktonic foraminifers and calcareous nannofossils ranging in age from middle Pleistocene (N22, *Globorotalia crassiformis hessi* Subzone; CN14a) to late Pliocene (top of N21; CN12a). Unit II is almost completely restricted to the late Pliocene (Zone N21 to N19/20; CN12a to CN11b), with only the top part of Core 135-834A-9H ranging into the early Pliocene; planktonic foraminiferal assemblages are less diverse and not as well preserved as Unit I. In Unit III preservation continues to deteriorate and assemblages are of low diversity. The age of Unit III is entirely early Pliocene (CN11b to CN11a), being based mainly on calcareous nannofossils because of the poor and patchy distribution of foraminifers. Two horizons contained good planktonic foraminiferal faunas indicating Zone N19/20. Within the basalt units were ash beds containing N19/20 planktonic foraminifers and CN11a calcareous nannofossils.

Sedimentation rates show fairly low accumulation rates for the sequence above the basalts, averaging 20 m/k.y. The basalts were accumulated over at least a 2-m.y. interval, with accumulation rates of around 110 m/k.y.

Interstitial pore waters from the sediments showed little variation in composition throughout the sampled section and suggested that the interstitial fluids behaved as an open system. Hydrocarbon analyses of the fluids showed only background levels.

A well-behaved, detailed magnetic polarity record was obtained from the sediments of Hole 834A down to 75 mbsf, revealing all polarity chrons and major subchrons back to about 4.0 Ma. The approximately 320 m of volcanic rocks in Hole 834B, which extend the polarity record farther back in time, show a major normal polarity between 165 and 435 mbsf. This is interpreted as the upper normal polarity part of Chron 5 (marine magnetic anomaly 3A), implying a magnetic age of about 5.5 Ma for the bottom of the hole. Cyclical variations in the modified Q-ratio (the ratio of AF-cleaned remanent magnetization to susceptibility) with a period of about 41 k.y. in the sediment magnetic record suggests that climatic Milankovitch cycles are present in the sediments.

One of the major objectives for Site 834 was to recover samples of the igneous basement to compare its petrology with rocks from the Lau Ridge (arc) and the basaltic rocks exposed on the active ridge axes of the backarc basin. The igneous rocks drilled at Site 834 are from flows (or possibly sills) intercalated with sediments and a thick section that probably constitutes the igneous "basement." Petrographic information from visual core descriptions and thin section studies were used to define 13 units at the site. Interpretation of major element data collected by X-ray fluorescence demonstrates similarity to Lau Basin backarc crust rather than to Lau Ridge arc samples. The first igneous rocks were recovered at about 112 mbsf. The samples (Unit 1) are sparsely phyric plagioclase olivine basalt. Aphyric basalt (Unit 2) was recovered at Hole 834B at about 112.5 mbsf. A series of thin flows (Units 3 and 4) was cored in Hole 834A but not at Hole 834B; these are underlain by a distinctive poikilitic textured diabase (Unit 5) also found in both holes and extending from 136 mbsf down to about 162 mbsf in Hole 834B. A sedimentary interbed, found at 162 mbsf in Core 135-834B-13R, separates Units 5 and 6. Unit 5 is highly altered in its upper part and appears to be a single thick cooling unit best interpreted as a flow. Units 6 through 13 include aphyric, olivine-phyric, plagioclase-phyric, plagioclase-olivine phyric, and olivine clinopyroxene plagioclase basalts and basaltic andesites. A common and relatively distinctive feature of many of these basalt units is their tendency to have a pervasive microvesicular texture that gives them a noticeable porosity. In many, several size ranges of vesicles are noted. The abundance of vesicles seems to be consistent with the recognition of shallow-water to neritic faunal assemblages in the sedimentary interbeds. Highly vesicular basalts are common in other parts of the Lau Basin, even on the axial ridges at depths of 2500 m, as well as in other backarc basins. This may be attributed to the high volatile content, mainly water but also CO_2, that has been measured on these rocks. However, with a few exceptions, there is little evidence for extensive postmagmatic hydrothermal alteration or mineralization in these or in most backarc basin basalts. Sulfides appear to be primary and are limited to globules of copper-iron sulfides, some with pyrrhotite intergrowths, in the groundmass. Some vesicles also have copper-iron sulfide encrustations. Rock alteration appears to be either deuteric or normal low-temperature, seafloor alteration and leads to oxidation of the sulfides and palagonitization of the glass.

The age of Units 1–9 is well constrained by paleontologic dating of thin sedimentary interbeds. The youngest basalt layers are lower Pliocene; the oldest ones for which we have paleontologic dating are upper Miocene.

Physical properties of the sediments sampled in Hole 834A generally show little change with depth, with the bulk density averaging 1.53 g/cm^3 and the sonic velocity averaging 1.51 km/s. However, thin turbidite flows show marked increases in both velocity and density, and a slight decrease in bulk density accompanies increased vitric ash content below about 78 mbsf. The basalts sampled in Holes 834A and 834B show marked changes in the bulk density and velocity. Basalts between 112 and 215 mbsf have an average bulk density of 2.7 g/cm^3 and an average velocity of 4.23 km/s. Below 286 mbsf, these values decrease to 2.5 g/cm^3 and 3.92 km/s. The changes in bulk density and velocity are apparently related to the degree of vesicularity and, hence, the effective porosity within the basalts.

BACKGROUND AND OBJECTIVES

Background

Location and Bathymetry

Site 834 is located in the northwestern part of the Lau Basin about 100 km east of the Lau Ridge (Fig. 2). The Lau Ridge is the remnant arc in the tectonic/morphologic system that includes the Tonga Trench, Tonga (volcanic) Arc, and Lau (backarc) Basin. The drill site is in one of several narrow, discontinuous, sedimented grabens or half-grabens that trend in a northerly direction nearly parallel to the Lau Ridge, the geologic feature that forms the western boundary of the Lau Basin. The fault-bounded basins are separated by subparallel, narrow, partially buried basement ridges that rise a few hundred meters above the floors of the basins. The basins reach water depths ranging from 2500 to more than 2900 m; Site 834 is located in a water depth of 2705 m. In this discussion we use the informal name Basin 834 to refer to the basin in which the drill site is located. Scarps bounding Basin 834 rise steeply to 2440-m water depth on the east and to 2520 m on the west (Fig. 3). Although the regional bathymetric fabric trends north-south, Basin 834 is not bounded by parallel sides. Our detailed bathymetric and seismic reflection profiler data are located by the grid of the ship tracks shown in Figures 4A–4B, which was used to define the size, shape, and sediment thickness of the basin. A structural/morphological interpretation of the data is presented in Figure 5. Basin 834 is about 2.7 km wide at its northern end, widens to about 8.2 km at the latitude of Site 834, and narrows again to about 1.6 km at its southern end. A broad, steep-sided ridge that extends 5.5 km to the north and 26.5 km to the south of the drill site separates Basin 834 from another broader basin to the west.

In the vicinity of the site the total sedimentary section is 0.17 s TWT thick. A thin regional seismostratigraphic unit (about 0.1 s TWT in thickness), which we refer to as "Seismic Unit A" ("Introduction and Principal Results" chapter, this volume) forms a uniform cover to the basement and sedimented basin topography alike. The sediment section is underlain by a zone of low-frequency, discontinuous reflectors marking the acoustic basement, although the roughness of the basement may prevent the precise identification of the basin floor. In the absence of refraction data or other appropriate seismic velocity control, we used a mean seismic velocity of 2.0 km/s to correct the sedimentary time section to a depth section, and thus we estimated approximately 170 m of sediment thickness at the drill site.

Site 834 is flanked both to the east and the south by a succession of several ridges and basins of several scales, each having a morphology similar to the basin-ridge topography at the site. Site 835 is located in one of these basins 62 km to the east. A broad, north-south bathymetric high, located 50 km to the east of Site 834 and centered on 18°35′S, 177°25′W shoals to about 1650 m at its summit. The rocks forming the bathymetric high are of unknown composition, but they may mark the location of an extinct spreading ridge abandoned after migration, or a jump, of the backarc spreading axis to the east. Alternatively, they may be remnants of older crust derived from the Lau Ridge or its forearc. Sidescan sonar images of pervasive, north-south linear features along the crest are interpreted as evidence for recent tectonism, and a number of scattered, brightly backscattering areas of the seafloor could be recent lava flows, although they have been described elsewhere as sediment slumps (von Stackelberg and von Rad, 1990). Together these observations support interpretations that there was a period of off-axis magmatism, reflecting either waning magmatic activity on a spreading center or rejuvenation of magmatism and spreading.

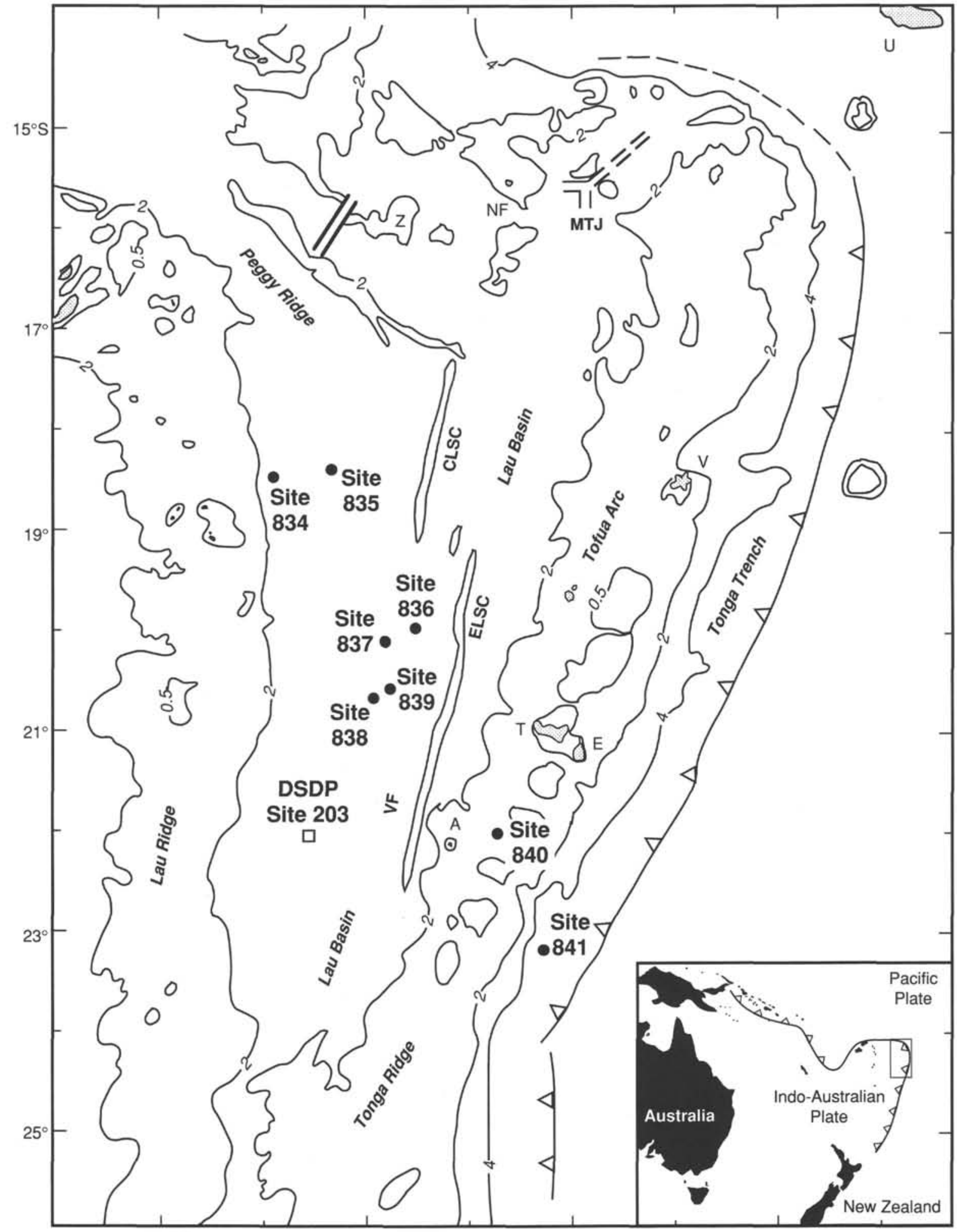

Figure 2. Regional bathymetry and location of Site 834. Figure also illustrates the locations of other drill sites in the Lau Basin and the major geologic features of the Tonga Trench and Lau Basin system. Z = Zephyr Shoal; islands include T = Tongatapu, E = 'Eua, V = Vavau, NF = Niua Fo'ou, A = Ata, and U = Upolu. The locations of the Central Lau (CLSC) and Eastern Lau (ELSC) spreading centers, Valu Fa (VF) Ridge, and Mangatolu Triple Junction (MTJ) are from von Stackelberg (1990), Parson et al. (1989), Hawkins et al. (1989), and Nilsson et al. (1989). The location of DSDP Site 203 is shown as an open square. Contour interval in thousands of meters.

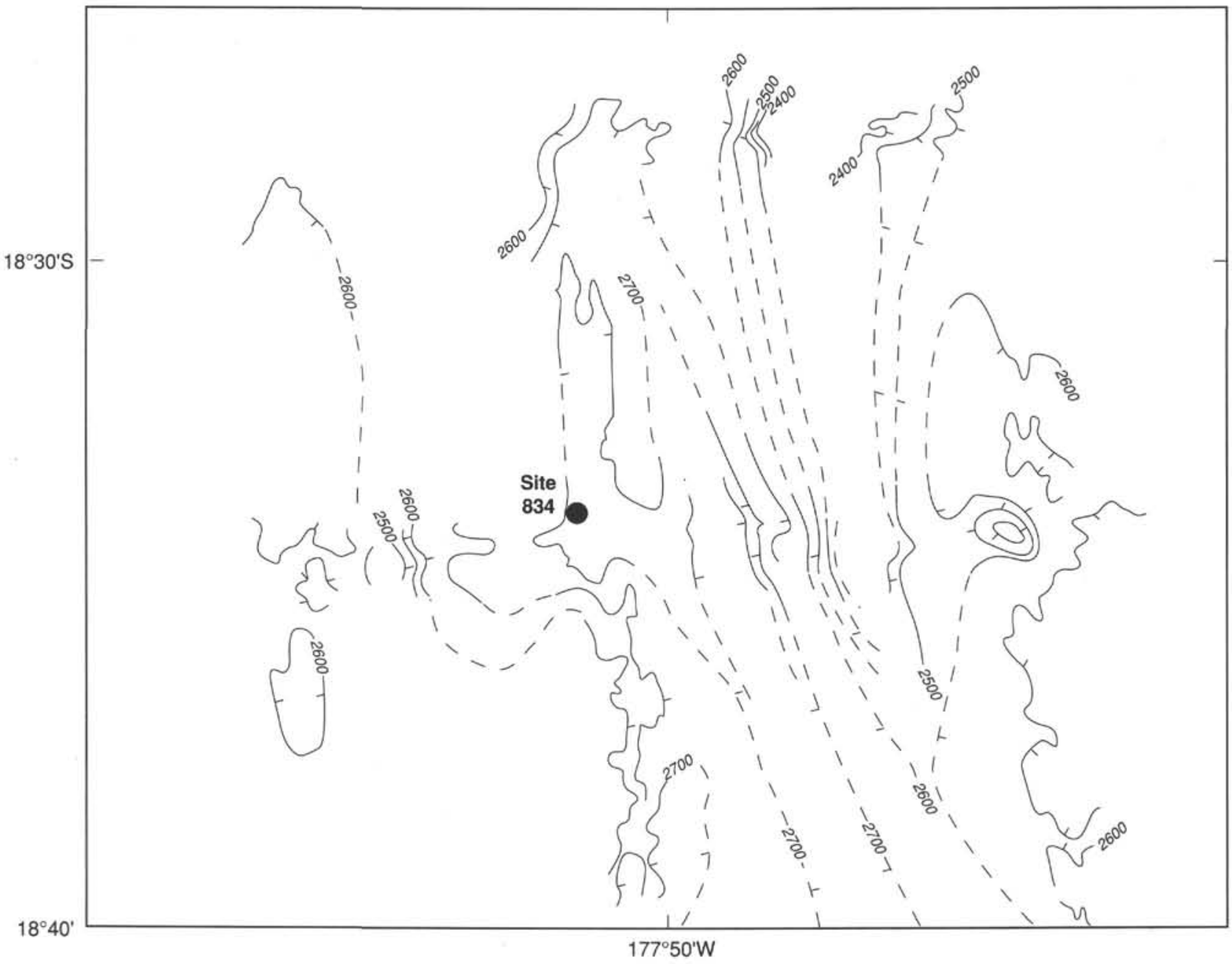

Figure 3. Detailed bathymetry of Basin 834 based on SeaBeam and conventional bathymetric profiles. Contour intervals in meters.

There is a major change in the geology of the basin near 176°30′W, some 150 km east of Site 834, as evidenced by the rocks collected by dredging, seafloor acoustic character, and fabric as seen in GLORIA records, magnetic anomalies, and seafloor bathymetry. These striking changes mark the location of the Central Lau Spreading Center (CLSC), which is one of the major morphologic-tectonic-petrologic features of the Lau Basin (Hawkins, 1988, 1989; Hawkins et al., 1989; Parson et al., 1990; von Stackelberg and von Rad, 1990). The CLSC is presently the main site of backarc spreading forming new crust of the Lau Basin. Its bathymetric and magnetic patterns, together with interpretations of the regional tectonic patterns, indicate that it is propagating southward into older Lau Basin crust; the propagating rift tip is at about 19°16′S. The age of the CLSC is equivocal because the magnetic anomaly pattern is unclear, but the propagator appears to have initiated from the southeastern termination of the Peggy Ridge and advanced southward for at least 1–2 m.y. The propagator tip is located some 120 km from Basin 834, at around 19°16′S, 176°32′W, and thus it is unlikely to have exerted any influence on either magmatic activity at Site 834 or the volcaniclastic sediments of the upper parts of the section. Rocks from the CLSC include depleted N-MORB type tholeiitic basalts and fractionated basalts, oceanic andesites and dacites, and Fe-Ti-rich basalts (Hawkins, 1974, 1976, 1977, 1988, 1989; Hawkins and Melchior, 1985). A more complete discussion of the CLSC is given in the "Introduction and Principal Results" chapter (this volume).

Nearly 200 km to the northeast of Site 834, the northwest-striking Peggy Ridge (Chase, 1971) truncates the western sector of the central Lau Basin. Rising to <1000 m, the ridge extends over 300 km northwest from the northern limit of the CLSC axis. It presently marks a line of right-lateral motion coupled with a component of east-west extension associated with the spreading on the CLSC and the backarc extension, respectively. A more complete discussion of the Peggy Ridge is given in the "Introduction and Principal Results" chapter (this volume).

Geological Setting

The western side of the Lau Basin is characterized by a number of small partly sedimented basins (Parson et al., this volume) and is bounded on the west by the islands and atoll reefs of the Lau Ridge. Site 834 is in one of these small basins about 100 km east of the axis of the Lau Ridge. The nature of the crust that underlies the western Lau Basin, and Site 834, is not known but several interpretations are possible. For example, the crust may be (1) remnants of the forearc that originally lay to the east of the Lau Ridge, (2) either allochthonous or autochthonous blocks of Lau Ridge volcanic material, (3) remnants of both arc and forearc crust, or (4) newly formed crust of backarc basin basalt. Whatever the origin of the western Lau Basin basement, the clastic sedimen-

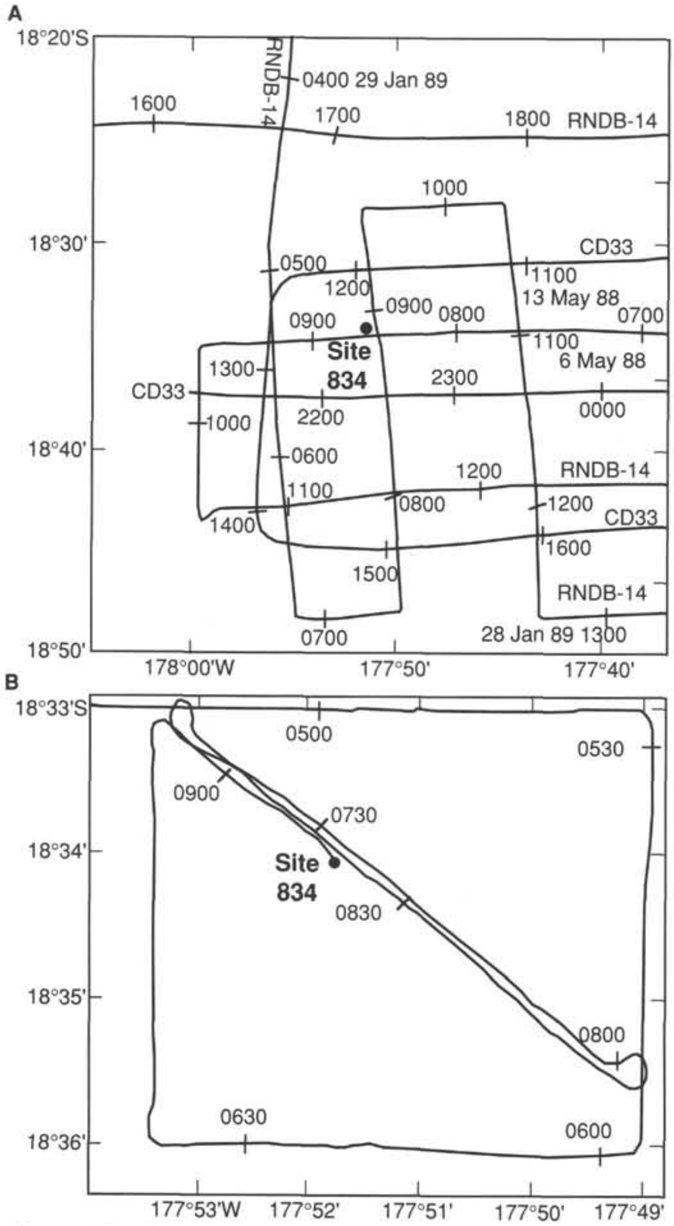

Figure 4. Track charts showing the locations of the seismic lines used to select Site 834, comprising (**A**) the *Charles Darwin* (CD33; Parson et al., 1989) and the *Thomas Washington* (RNDB-14, Hawkins, 1989), and (**B**) the *JOIDES Resolution*.

tary fill of the lesser basins must have been derived largely from the Lau Ridge. The timing, geometry, and tectonic style of crustal extension on the Lau Ridge may be indicative of geological processes that resulted in crustal extension in the western Lau Basin. Thus, an understanding of the geology of the Lau Ridge may be helpful in understanding the evolution of the western Lau Basin. Our initial results show that the beginning of opening of the Lau Basin, and the earliest volcanic activity in the basin, overlapped in time with extension and volcanism on the Lau Ridge.

The Lau Ridge comprises emergent and coral-capped parts of a remnant volcanic arc, active until the late Miocene or early Pliocene (5–3.5 Ma), according to Gill (1976), Cole et al. (1985), and Woodhall (1985). The Lau Ridge is presumed to have been part of the former "Melanesian island arc" that included what are now the Fiji Platform, New Hebrides–Vanuatu Ridge, and the

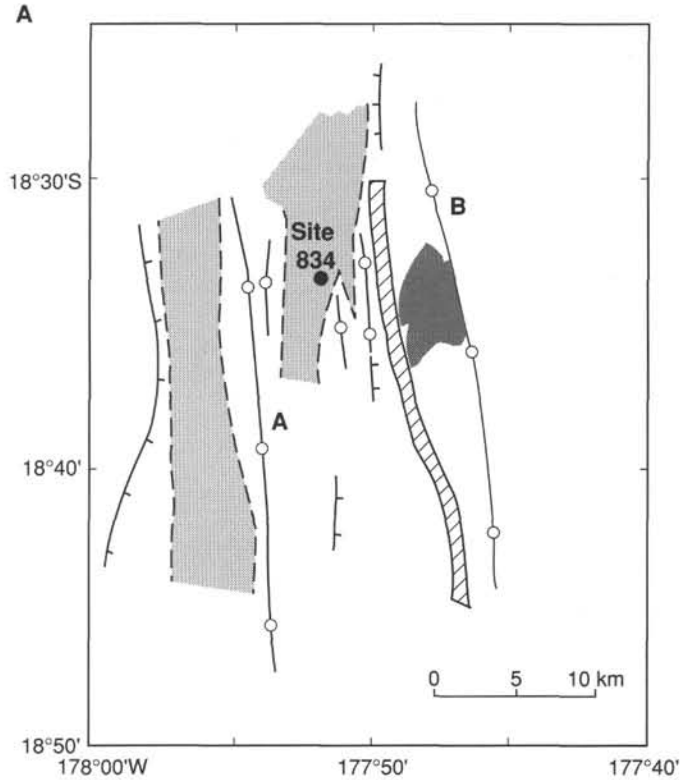

Figure 5. **A.** Morphotectonic setting of Site 834 based on seismic reflection profiler data and GLORIA data located in Figure 4. **B.** Seismostratigraphic interpretation of *JOIDES Resolution* profile across Site 834, illustrating the correlation of sedimentary Unit I with planar-laminated seismic Unit A and sedimentary Units II and III with seismic Unit B. SB = seismic bottom reflector and TD = total depth.

Tonga Ridge (Woodhall, 1985; Cole et al., 1985). The Lau Ridge and Tonga Ridge were separated during the extensional development of the Lau Basin (e.g., Karig, 1970; Woodhall, 1985; Cunningham and Anscombe, 1985). The oldest known rocks exposed on the Lau Ridge are pre-middle Miocene lava flows, and pyroclastic and volcaniclastic rocks of the Lau Group. These display a broad range in composition from basalt to rhyolite; basaltic andesite and andesite are the major rock types of the Lau Group. Both tholeiitic and calc-alkaline low- to high-K magma series are represented. Intrusive rocks, found on several islands, represent the same magma types as the volcanic rocks (Woodhall, 1985). The chemistry and petrology of the Lau Group volcanic rocks indicate that the Lau Ridge displays the early and mature stages of volcanic arc evolution (Cole et al., 1985). There is no direct evidence for pre-middle Miocene volcanism on the Lau Ridge, but Oligocene and early Miocene volcanism and sedimentation has been postulated on the basis of the occurrence of rocks with these ages elsewhere in the region. Cole (1960) and Colley et al. (1986) report late Eocene and early Oligocene volcanic rocks on Viti Levu, Fiji; early and middle Miocene volcanic rocks have been reported from the Tonga Ridge (Cunningham and Anscombe, 1985). Middle and late Miocene volcanism on the Lau Ridge has been confirmed by radiometric age dates that range from 14 to 6 Ma (Cole et al., 1985). Volcanic activity continued into Pliocene time, as indicated by 4.5–2.5 Ma rocks of the Korobasaga Volcanic Group and <2.5 Ma rocks of the Mago Volcanic Group (Cole et al., 1985).

The spectrum of radiometric ages indicates that the volcanic activity was more or less continuous from Miocene through Pliocene time. Crustal extension on the Lau Ridge was contempora-

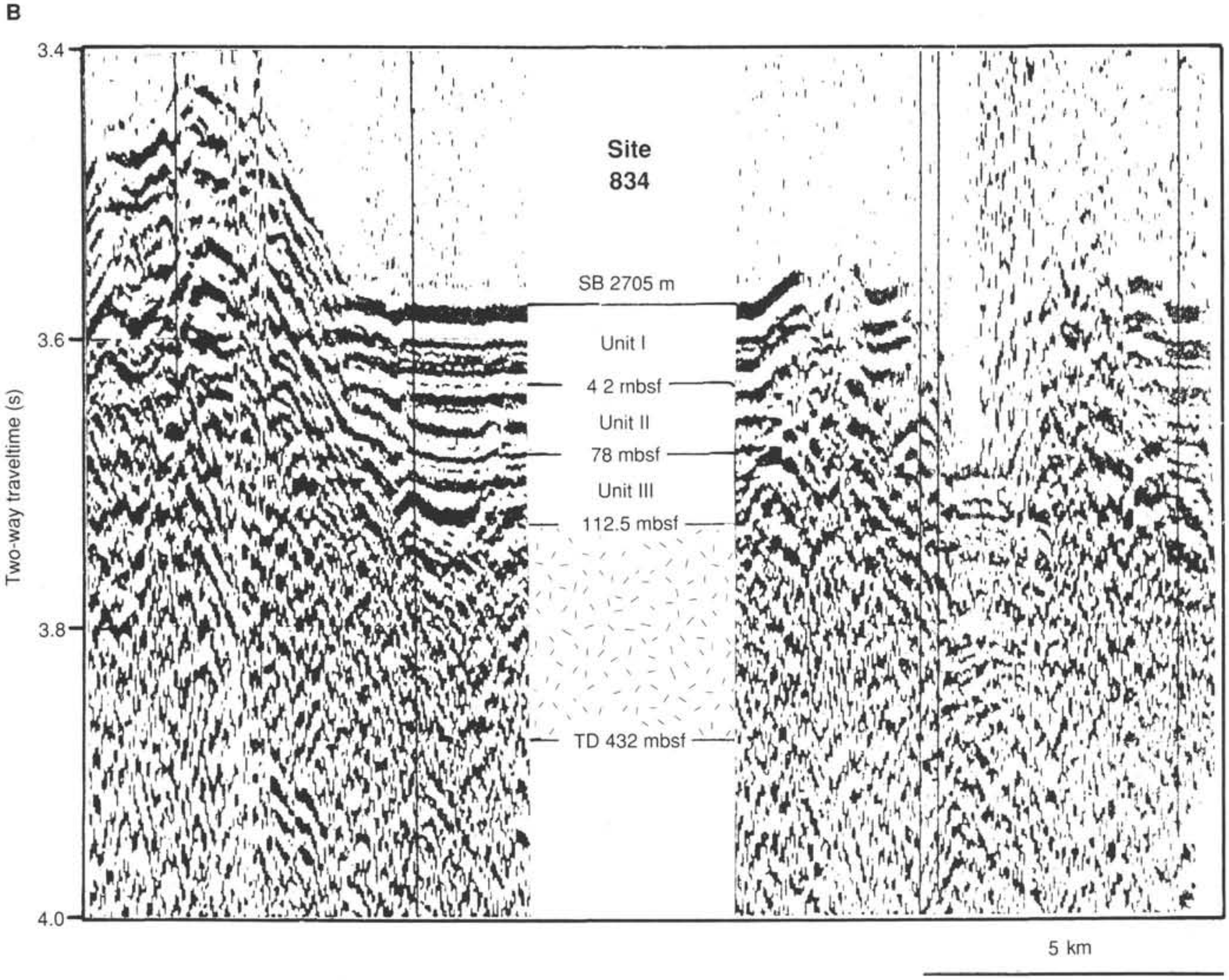

Figure 5 (continued).

neous with this volcanism (e.g., 4.5–2.5 Ma basalts of the Korobasaga Group) during the time that Whelan et al. (1985) relate to the "early rifting stage" in the evolution of the Lau Ridge. The timing of this rifting and the associated volcanism on the Lau Ridge, which was dominated by tholeiitic basalt, broadly overlaps in time with the beginning of extension of the crust of the western Lau Basin.

Regional Structural Synthesis

The structural interpretation of the area of Site 834 has been based on the integration of seismic reflection data with those from long-range sidescan sonar (GLORIA) records. The area essentially comprises a series of north-trending basement blocks, ranging from 50 km to <10 km in length and <5 km in width, that separate the linear, sediment-filled basins (Parson et al., this volume). Some of the basement blocks have a morphologic asymmetry in profile, suggesting some small amount of rotation. The sense of asymmetry is neither clear nor consistent; thus, interpretations of the style of rifting or the geometry of fault planes in the western basin are speculative. Basin 834 tapers to the south and is flanked on both the east and west sides by 50-m-high ridges (Fig. 5). Between Site 834 and Ridge B to the east, a well-defined, openly sinuous channel has been traced for more than 25 km from north to south. The channel floor is approximately 1.0 km wide, lies between 100 and 135 m deeper than the basin floor, and displays a constant depth of around 2812 m. This feature cannot be resolved on GLORIA sidescan records, and the uniform backscattering pattern of the floor of the channel could be interpreted as indicative that it is inactive and partly buried. Farther to the east of the channel, a diffuse area of strongly backscattering seafloor, approximately 3–4 km across as seen on GLORIA records, is tentatively interpreted as mass-wasted material shed from the adjacent ridge (B; Fig. 5). At the southern end of Basin 834, another series of minor ridges interrupt Unit A and probably extend farther south to link with an east-facing scarp complex south of 18°42′S.

Seismic Stratigraphy at Site 834

Published and unpublished single-channel and multichannel seismic reflection data have been used to assess the local tectonic setting of Site 834 and place it in the context of the geological evolution of the Lau Basin region. Our suggested schematic section illustrating the structure of the Lau Basin and Tonga arc and forearc is presented in Figure 17 of the "Introduction and Principal Results" chapter (this volume). This interpretation represents a composite east-west profile, orthogonal to the regional basin fabric, approximately along latitudes 18°40′S, 20°20′S, and between 22° and 23°S. A detailed interpretation of seismic reflection profile data collected during site surveying with the *JOIDES Resolution* is included in this section.

Single-channel seismic reflection data acquired during the *JOIDES Resolution* survey is shown in Figure 6 together with an interpretive stratigraphic column summarizing the lithologic units (Fig. 7). The vertical exaggeration is about 15:1. The uppermost part of the section is clearly overprinted by the decaying water-gun bubble pulse, but below about 0.06 s in the section the seismic stratigraphy is essentially unmodified. Three seismic units (A, B, and C) are recognized in these records at Site 834 (Figs. 6 and 7), and they correspond to similar seismic units identified elsewhere in the Lau Basin (see "Introduction and Principal Results" chapter). These are Seismic Unit A, the youngest unit, planar, weakly laminated, uniformly distributed throughout the basin, and found both on elevated topography and in the deepest basins (this seismic unit here approximately correlates to sedimentary Unit I); Seismic Unit B, defined by a series of regular and well-stratified laminations occupying the lower sections of the deepest sedimentary basins (this seismic unit here approximately correlates to sedimentary Units II and III, collectively); and Seismic Unit C, a complex pattern of low-frequency, discontinuous reflectors that defines the lower surface of Units A and B throughout the basin. We refer to Seismic Unit C as the acoustic basement. The boundaries between lithostratigraphic Units I, II, and III (see "Lithostratigraphy" section, this chapter) are not resolved in the seismic profile. Despite the interference from the decaying water-gun signal, a series of closely spaced seismic strata are discernible within the section. The underlying lithologic differences, such as the interbedded flow (sills?) and sediment sequences, cannot be resolved with the seismic data. Subvertical zones of disturbed

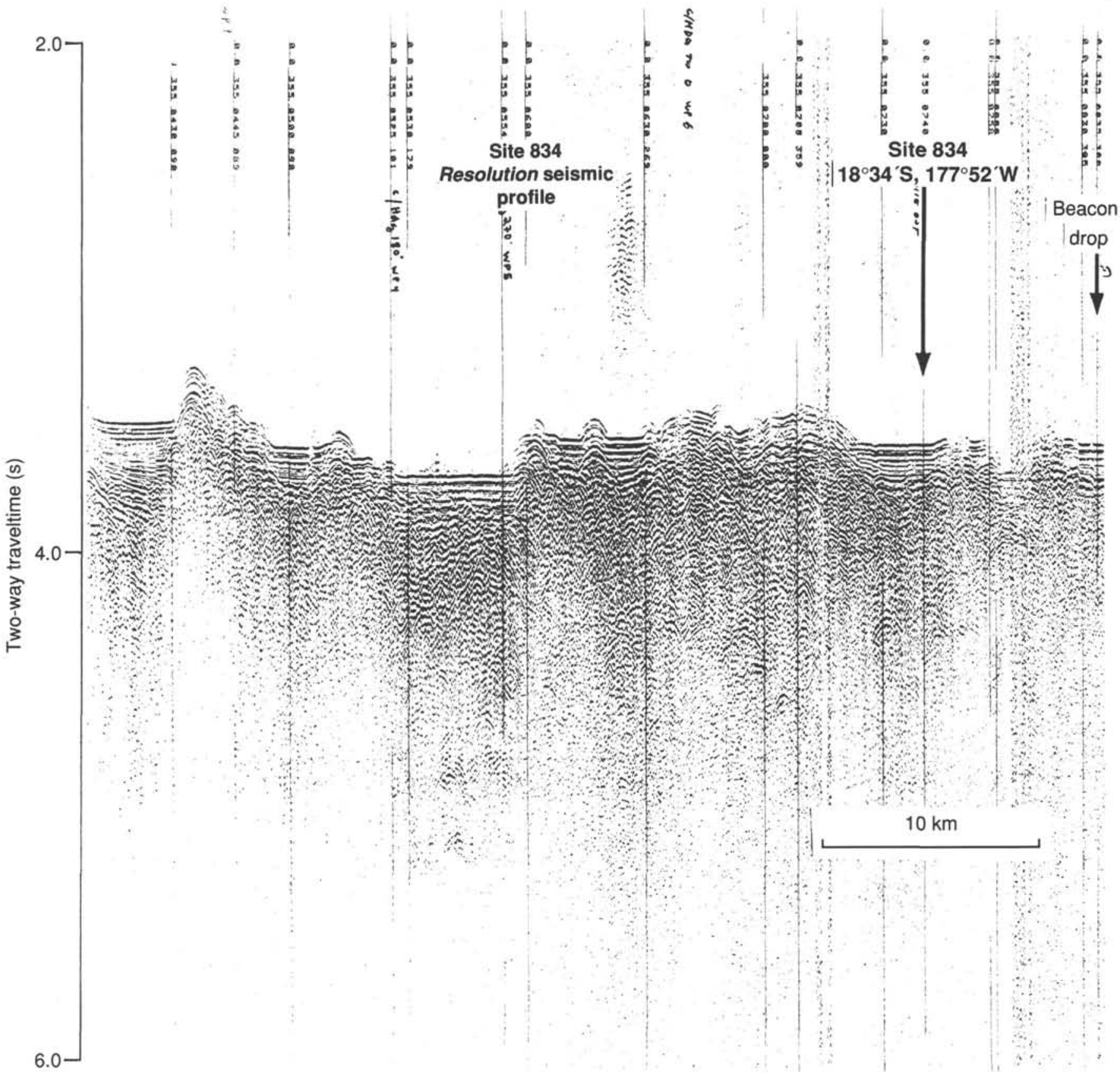

Figure 6. Single-channel seismic reflection profile across Site 834 acquired by the *JOIDES Resolution* during the site survey. Track located in Figure 4B.

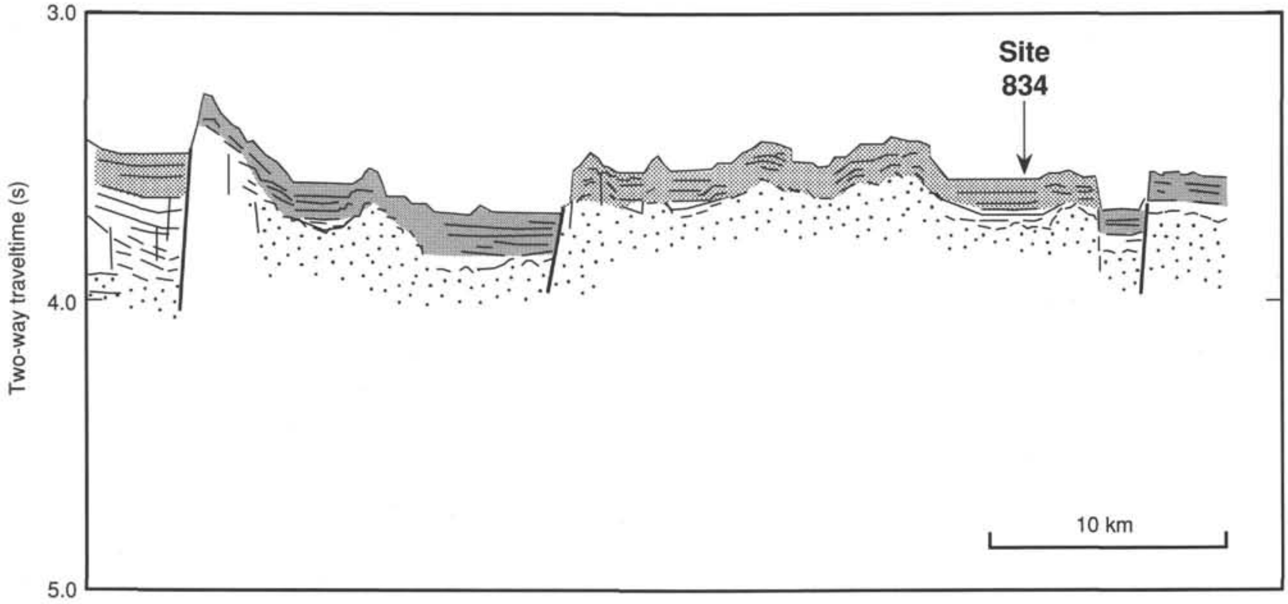

Figure 7. Line drawing interpretation of the single-channel seismic profiles adjacent to Site 834, acquired by *JOIDES Resolution* and illustrated in Figure 6. Dark stipple in uppermost section corresponds to seismic Unit A. Unit B is unornamented. Unit C (acoustic basement) is light stippled.

section, up to about 0.5 km thick, occur on either flank of Basin 834. These zones extend from the basement to the seafloor, where minor inflections of the seafloor can be identified. A weak deflection of the seismic strata across each of these zones indicates that they are likely to be near-vertical faults, but the lack of discernible offset precludes significant amounts of throw. Lateral motion on these structures, however, cannot be ruled out.

Magnetic Data

Lau Basin

As discussed in the "Introduction and Principal Results" section (this chapter), the magnetic anomaly data for the Lau Basin have proved difficult to interpret, and attempts to model the crustal structural fabric and ages of magnetic lineations in terms of plate tectonic theory have met with only limited success. Models have been developed by several workers that have presented widely varying interpretations for the age of the earliest backarc crust in the Lau Basin. These uncertainties range from an original estimate of 5–10 Ma (Sclater et al., 1972) to 2.5 Ma (Malahoff et al., 1982). One of the primary reasons for drilling at backarc Site 834 was to attempt to resolve uncertainties about the age of the igneous basement and, thus, by inference, the age of the beginning of opening of the basin.

Lawver et al. (1976) presented the first interpretation of the crustal accretion pattern in the Lau Basin based on magnetic anomaly data and demonstrated the discontinuous and nonparallel nature of the anomalies. Expanding on these data, Weissel (1977) proposed that there were north-striking anomalies as old as 2′ (3 Ma) in the western Lau Basin between 17° and 18°45′S. Further, he suggested that the seafloor occupying the intervening basin between these anomalies and the eastern flank of the Lau Ridge was an earlier zone of magmatic accretion generated at some time between 3 and 5–6 Ma. These ages are equivalent to the age of some of the volcanic rocks of the Lau Ridge (Gill, 1976). An extensive set of aeromagnetic data were used by Malahoff et al. (1982) to make a comprehensive interpretation of the Lau Basin and surrounding areas. They proposed that the oldest anomaly at the extreme western part of the basin (along 177°W) was 2′. A more recent revision of the aeromagnetic data (Malahoff et al., in press) has extended the range of spreading anomalies to anomaly 3′ in the far western part of the basin along the eastern foot of the slope of the Lau Ridge. Site 834 lies on the older (i.e., western side) of this anomaly on crust postulated to be between 3 and 6 m.y. old according to these various interpretations of crustal age. A new compilation of all available magnetic data, including aeromagnetic and marine data derived from over 50 survey programs, is discussed in the "Introduction and Principal Results" chapter (this volume). If we assume that all of the Lau Basin crust, between a projected trace of the Eastern Lau Spreading Center and Site 834, was formed by seafloor spreading, we can estimate a half spreading rate of 32 mm/yr.

Site 834

A new compilation of marine and aeromagnetic anomaly data is presented in Figure 8, combined with a provisional interpretation revised from Murthy (1990). North-south linear correlations of profile anomalies are possible over only a maximum of 35 km, and anomaly amplitude is highly variable throughout. Local along-strike variations between 300 and –250 nT over periods of 50 km are common.

Heat Flow Data

Few published heat flow data are available for the Lau Basin (see Fig. 6 of the "Introduction and Principal Results" chapter, this volume), and only one station has been taken close to Site 834; a value of 1.70 μcal/cm^2 was determined near 18°30′S, 177°40′W (Sclater et al., 1972). This is significantly lower than values between 2.82 and 2.39 μcal/cm^2 for crust generated at mid-oceanic ridges of various spreading rates over the past 10 m.y. (Sclater et al., 1971) and is lower than several of the other measurements for the Lau Basin that are as high as 6.75 μcal/cm^2 (Sclater et al., 1972). Heat flow values in the northwestern Lau Basin show a scatter from 0.36 μcal/cm^2 to 1.70 μcal/cm^2; these are low relative to theoretical values for 5-m.y.-old oceanic crust (Sclater et al., 1971) and are lower than expected from the general

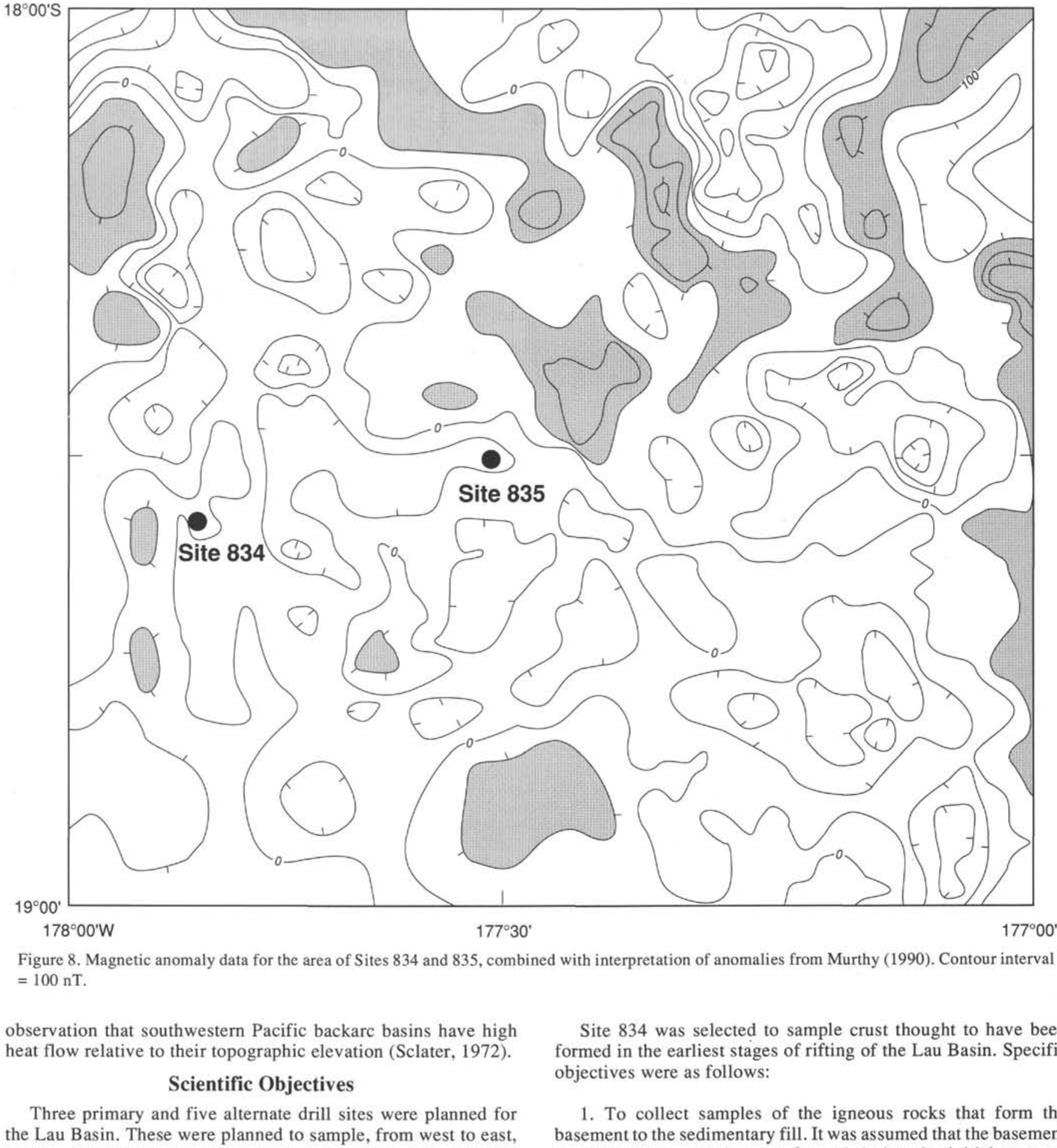

Figure 8. Magnetic anomaly data for the area of Sites 834 and 835, combined with interpretation of anomalies from Murthy (1990). Contour interval = 100 nT.

observation that southwestern Pacific backarc basins have high heat flow relative to their topographic elevation (Sclater, 1972).

Scientific Objectives

Three primary and five alternate drill sites were planned for the Lau Basin. These were planned to sample, from west to east, progressively younger crust along a transect from a site near the Lau Ridge remnant arc to a site located on relatively young crust near the active axial ridge, the Central Lau Spreading Center (CLSC). The scientific objectives for Site 834, as for the other backarc sites planned for Leg 135, were to sample the sedimentary column and the igneous "basement," and to collect paleontologic and geophysical data in order to understand the geologic evolution of the Lau Basin. The data would be important not only for deciphering the regional geologic history, but also for comparing the history of the Lau Basin with that of other western Pacific backarc basins to improve our understanding of how backarc basins form and evolve.

Site 834 was selected to sample crust thought to have been formed in the earliest stages of rifting of the Lau Basin. Specific objectives were as follows:

1. To collect samples of the igneous rocks that form the basement to the sedimentary fill. It was assumed that the basement would be new oceanic crust formed during the initial stage of opening of the basin but this assumption needed to be verified. Recovery of igneous "basement" samples, and the basal sedimentary sediments, would give information about the age of the crust and the style and the timing of rifting as well as the composition of the early magmas and, by inference, the nature of their source. It was planned to drill 200 m into the igneous rocks to assess temporal variations in magma chemistry.

2. To core the sediment column to get a record of the history of basin subsidence and sedimentation. These samples would enable us to investigate the petrology, stratigraphy, and paleontology of the sedimentary column and to understand the deposi-

tional environment, the provenance of the sediments, the sediment accumulation rates, and the alteration and diagenetic history of the sediments. The contribution of hydrothermally derived material could be assessed in the sedimentary section, and its post-rift variation and distribution identified. There was active volcanism on the nearby Lau Ridge during Miocene and Pliocene time, and the presence of interbedded ash layers and fossiliferous horizons in the basin would help in recognizing episodicity and chemical variability in this volcanism. The cores would also be useful in interpreting the record of the subsidence history of the Lau Basin and the concurrent uplift and erosion history of the Lau Ridge. The cores were also expected to yield information on paleoceanographic environments and on the effects of hydrothermal activity on the sediments and their chemistry.

3. To make an integrated interpretation of lithostratigraphy, biostratigraphy, and magnetic stratigraphy, and to use these data to determine the age of the onset of crustal extension and magmatic activity in the Lau Basin. The clastic rocks and ash layers of the sedimentary fill would also provide a record of Lau Ridge volcanism.

Sites 834, 835, 836, 837, 838, and 839 were located on variably aged crust to enable us to collect data that would help in constructing a petrologic time series along a flow line of magmatic crustal accretion across the Lau Basin. The sites were selected to constrain possible models for the extension of the backarc basin. We have discussed some of these models in the "Introduction and Principal Results" chapter (this volume). Site 834 fits into these hypothetical models as one of the first basins to open and receive sediment. Our suggested models allow two possible settings for the beginning of rifting, one in the forearc (Hawkins et al., 1984) and one in the arc itself (Karig, 1970). Rifting in the forearc could have formed close to the eastern foot of the arc or well out into the forearc toward the trench. The newly formed small basin may have been rifted enough to allow direct upwelling of mantle-derived melts to form new backarc crust (i.e., an oceanic crustal section), and fill a potential void in the old crust. If there were less extension, the older crust would have been modified by the emplacement of dikes, sills, flows, and pillow complexes. In either case, the infilling of the basins would likely include sediments derived from the adjoining high standing blocks of crust and the magmatic filling would intrude or be interbedded with sedimentary layers.

OPERATIONS

Introduction

Leg 135 officially began at 1900 hr UTC on 16 December 1990, when the *JOIDES Resolution* (SEDCO/BP 471) dropped anchor in Suva Harbor, Fiji, staying at anchorage because of a lack of dock space. After the Fijian authorities cleared the vessel, the crew change was accomplished by tug by 2330 hr UTC. The ship finally docked at 0700 hr UTC December 17. The scientific portion of the leg began at 0800 hr UTC on 20 December 1990 with the departure of the *JOIDES Resolution* from the docks at Suva, Fiji, following a 4-day port call. After the pilot left the ship at 0848 hr, the *Resolution* steamed eastward past many small islands of the Fiji group, arriving in the vicinity of Site 834 at 0315 hr UTC, 21 December, after a transit of 210 nmi. Although it rained throughout most of the transit, the voyage was pleasant because of the mild seas.

Site Approach and Site Survey

Site 834 is situated at the westernmost margin of the central Lau Basin in a small steep-sided trough trending north and lying parallel to the eastern flank of the Lau Ridge. For purposes of discussion, we give it the informal name of Basin 834. This trough is one of several discontinuous features separating narrow, partially buried basement ridges emerging up to 300 m above the sedimented basin floor. The Site 834 area was selected using a number of intersecting single-channel seismic reflection profiles acquired by the *Charles Darwin* and *Thomas Washington* during 1988 and 1989, respectively (Fig. 4A). It was located well to the east of the foot of the Lau Ridge to avoid the possibility of encountering poorly consolidated and heterogeneous mass-wasted sediments shed from the Lau Ridge while attempting to sample the oldest backarc crust in the Lau Basin.

The seismic data were used to identify a suitable sedimentary section overlying acoustic basement in water depth of 2704 m (at 3.62 s TWT). Seismic profiles recorded by the *JOIDES Resolution* (Fig. 6) illustrate the sequence comprising a series of subparallel planar seismic laminae occupying the basin to a depth of 0.17 s TWT below seafloor, and overlying an irregular hummocky surface characterized by a series of stacked, low-frequency seismic reflectors. The upper surface of this unit was referred to as the acoustic basement, although on processed single-channel data recorded previously during the *Thomas Washington* surveys a poorly defined, semicontinuous event was observed at the site at around 3.88 s TWT, 0.26 s below seafloor. An average seismic velocity of 2.0 km/s was used to convert the sediment time section to a depth section, suggesting a sedimentary section of at least 170 m above the acoustic basement, and a possible target of a deeper horizon at 194 m below seafloor (mbsf). Adjacent seismic profiles data collected by the *Charles Darwin* and *Thomas Washington* (Fig. 4A) suggested that the target basin was discontinuous in form, narrowing sharply toward the north to less than 2 km wide (Fig. 5). To ascertain the accurate extent of the basin, a series of short seismic profiles were collected in a box-shaped survey around the site using the full shipboard underway geophysics system (Fig. 4B).

After slowing to deploy two 80-in.^{3} water guns, a 60-element single-channel Teledyne streamer, and a Geometrics 801 proton precession magnetometer (at 18°33′S 178°03′W, 11.2 nmi from the proposed 834 site), the ship completed the pre-site survey by 0708 hr UTC. A final northwest-southeast survey line was taken through the site, which was crossed at 0741 hr UTC. At 0805 hr UTC the ship made a Williamson turn, adopted a reciprocal course to mark the site, and a beacon was dropped at 0835 UTC. Underway geophysical gear was recovered immediately afterward, with the ship returning to the site to begin coring operations at 0910 hr UTC (Fig. 4B).

Drilling and Logging Summary

Our original plan was to drill three adjacent holes at Site 834, with the principal objective of reaching 200 m of basement penetration. Hole 834A was planned to be an APC/XCB/MDCB hole, with the goal of obtaining a complete and relatively undisturbed sediment section from Basin 834. It was originally hoped that the motor-driven core barrel (MDCB) would provide a short section of basement underlying the projected 170-m thick sedimentary section. Hole 834B was to be an rotary core barrel (RCB) hole that washed through most of the sediments, commencing coring just above the sediment-basement interface and continuing to 50-m basement penetration or bit destruction. The sedimentary section and sediment-basement interface in Hole 834B would then be logged. Hole 834C was planned to be a deep-penetration reentry hole (200 m into basement), using a reentry cone with casing installed through the sediments and sediment-basement interface. However, during the coring of Hole 834A we discovered that the sedimentary section was only 112.5 m thick. Because hole conditions also proved to be stable, we decided to attempt reaching the basement objectives in Hole 834B, using a free-fall funnel (FFF) to provide reentry for bit changes.

Hole 834A

Hole 834A was spudded in at 2020 hr UTC, 21 December 1990, at a position of 18°34.058′S, 177°51.735′W. A mud-line core established the seafloor depth as 2702.9 m below the driller's datum. Nine cores were taken with the advanced piston corer (APC), to a depth of 83.6 mbsf. A nonmagnetic drill collar was used, and the multishot tool provided orientation for Cores 135-834A-4H to -9H. A temperature measurement was made after Core 135-834A-5H using the downhole water sampler and temperature probe (WSTP). Recovery using the APC was excellent, with over 100% recovery. The sediments stiffened rapidly with depth, requiring an early change to the extended core barrel (XCB) (Table 1). Three cores of sediments were taken with the XCB, with moderate recovery (38.6%) to a depth of 112.5 mbsf. At this point, igneous rocks (basalt) were encountered, and the decision was made to stay with the hard formation, 5-tooth tungsten carbide XCB bit, as recovery of the basalt was good. Six more cores were cut of igneous rock and minor interlayered sediment (to a depth of 144.6 mbsf), with variable recovery averaging 30.6%. Two of the hard formation bits were used, as one was destroyed by overheating in the basalt and was changed after Core 135-834A-12X.

The decision was then made to try to obtain several basalt cores with the new motor-driven core barrel (MDCB) before terminating the hole and beginning rotary coring in Hole 834B. However, it failed to turn on Core 135-834A-19N during its 20-min test run. One more XCB core was cut in the basalt to ensure that the source of failure in the MDCB was not in the rock being cut. This last core yielded 3.69 m of core from a penetration of 4.9 m (a recovery of 75.3%).

Hole 834B

The ship then moved about 15 m to the northwest and spudded Hole 834B (LG-2) at 1545 hr UTC, 23 December 1990, at a position of 18°34.052′S, 177°51.737°′W. A 9⅞-in. RBI C-4 four-cone bit, rotary core barrel (RCB), bottom-hole assembly (BHA) was used, smaller in diameter than the 11¾-in. BHA used with the APC and XCB. A wash core (135-834B-1R) determined the water depth to be 2699.1 m below the driller's datum. The hole was washed from 0.0 to 68.2 mbsf, with temperature measurements taken using the WSTP tool at 30.1, 48.9, and 68.2 mbsf. Cores 135-834B-2R to -34R were taken from 68.2 to 290.8 mbsf, with 222.6 m cored and 71.67 m recovered (32.2% recovery). Basalt was encountered at 112.5 mbsf (in Core 135-834B-6R). High torque and drag from ledges of fractured basalt required reaming during each pipe connection as well as frequent mud sweeps to maintain the open hole. Small basalt cobbles and fracture wedges often jammed the hard-rock core catcher, reducing recovery. As a result, half cores (4.7–5.0 m in length) were cut through most of the section to improve recovery. As a 250-m basement penetration was desired (362 mbsf), the 39¼ hr on the bit prevented the completion of the hole with that bit at the operating coring rate of 3.0 m/hr. Coring was stopped, therefore, after Core 135-834B-34R to make a bit change.

Inasmuch as hole conditions proved to be stable, the original plan to set a reentry cone and drill a third hole to reach basement objectives was reassessed. Instead, it was decided to deploy a free-fall funnel (FFF) on the string to allow a bit change and reentry into Hole 834B. The FFF was dropped at 2335 hr UTC on 26 December. The search for the FFF required 4 hr using the Colmec TV camera. The Mesotech sonar was not run, because one of the two sonar tools had galled threads on the pressure case and some telemetry problems. Reentry was made at 0335 hr UTC 27 December 1990.

Coring with the RCB continued with another 9⅞-in. RBI C-44-cone bit, with Cores 135-834B-35R to -59R cut from 2989.9 to 3134.4 m below rig floor (290.8–435.3 mbsf); 144.5 m was cored and 24.56 m recovered (17.0% recovery). The basement penetration goal was exceeded, and coring was terminated to save time for additional sites. Overall, 59.8 m was washed, 375.5 m was cored, and 105.47 m was recovered (28.09% recovery) in Hole 834B.

After conditioning the hole for logging with a short trip of the drill string, the bit was dropped with the hydraulic bit release (HBR). The open end of the pipe was pulled to 74.6 mbsf, and logs were run as follows:

Run No. 1: "Quad Combo" induction/density/sonic/caliper/gamma ray. The log found bottom 3.5 m above the driller's total depth and required 3¼ hr to run.

Run No. 2: Geochemical/aluminum clay tool/gamma ray. The log found bottom 1.0 m above the driller's total depth and required 6½ hr to run.

Run No. 3: Formation microscanner/gamma ray. The log found bottom 0.6 m above the driller's total depth; a double run was made that took 4¼ hr.

Run No. 4: Digital borehole televiewer (BHTV). The initial attempt to run the digital BHTV was aborted because of a power supply failure and took 2¾ hr. The back-up analog BHTV was run, which found bottom 170 m off bottom. The log required 3⅚ hr to run.

Log quality was hampered by numerous ledges and cavities in the basalt. The hole was left full of seawater, and the BHA cleared the seafloor at 1625 hr UTC on 30 December 1990, reaching the rig floor at 2040 hr the same day. After securing the ship for transit, the *JOIDES Resolution* left the site at 2100 UTC on 30 December 1990, for the transit to Site 835.

LITHOSTRATIGRAPHY

Introduction

The sedimentary sequence recovered at Site 834 comprises 114.6 m of clayey nannofossil oozes, turbiditic foraminiferal sands and oozes, clayey nannofossil mixed sediments, and claystones (Fig. 9). Frequently, these units are interbedded with epiclastic and pyroclastic vitric ash layers. The age of the sedimentary sequence ranges from the middle Pleistocene to the late Miocene. Below 112.5 mbsf the sequence is interlayered with a number of thick basaltic lava flows, although thin pockets of intercalated sediments were recovered to 164 mbsf. All sediment cores were described by the team of shipboard sedimentologists and sampled for smear-slide description, carbonate analysis, vitric ash refractive index, and X-ray diffraction (XRD) studies. Our lithostratigraphic summary is derived from a composite of both holes. We have divided the sedimentary sequence at Site 834 into four lithologic units, based primarily on differences in sediment composition, especially the occurrence of vitric ashes and the increasing clay content of the sediment downhole (Fig. 10).

Unit I

Intervals: Sections 135-834A-1H-1 through -5H-3 and 135-834B-1R-1 through -1R-6
Depth: 0–42 mbsf

Unit I is 42 m thick and is composed predominantly of brown to dark yellowish brown, iron-oxyhydroxide-stained, clayey nannofossil ooze with occasional interbeds of white to light gray,

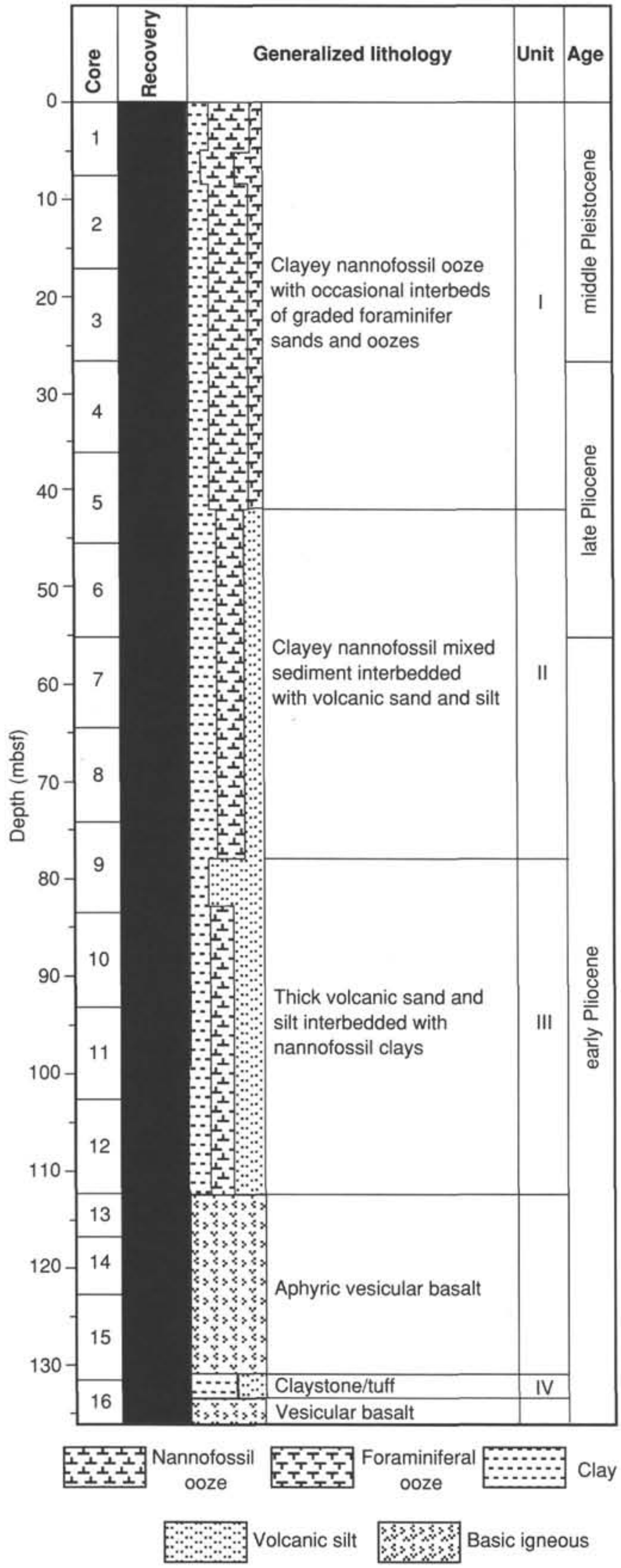

Figure 9. Lithologic summary for Hole 834A, indicating the main lithologic units identified with age as well as a generalized graphic lithology for Site 834.

graded foraminiferal sands and oozes. Three vitric ash layers (from 6 to 15 cm thick) are present in the upper 12 m of Unit I, although volcaniclastic material is rare in the rest of the unit. The age span of Unit I, based on paleomagnetic and biostratigraphic data, is from the late Pleistocene to 2.6 Ma (late Pliocene) with an average sedimentation rate of 18.2 mm/k.y. (see "Sediment Accumulation Rates" section, this chapter).

Clayey Nannofossil Ooze

The clayey nannofossil ooze contains about 30% clay-sized material, with the rest of the sediment composed primarily of calcareous nannofossils (60–70 vol%) with a much smaller percentage of planktonic foraminifers (5–10 vol%). The ratio of clay-sized particles, calcareous nannofossils, and foraminifers remain fairly constant throughout the red clayey nannofossil ooze of Unit I (Fig. 10). The clayey nannofossil ooze frequently appears homogeneous over long intervals, although mottling, mostly attributable to bioturbation, occurs throughout the sequence, which also contains rare pumice fragments (up to 4 cm across). Pumice fragments are most common in Sections 135-834A-2H-1 to -3H-7 (7.6–26.6 mbsf). Some of the pumice fragments have very pale brown haloes surrounding them. These are up to 5 mm in thickness and are probably related to *in situ* weathering of the pumice.

The clayey nannofossil ooze contains 55–75 %$CaCO_3$, with only minor variations throughout the unit. Figure 10 shows the total variation in $CaCO_3$ downcore throughout the cored sedimentary sequence at Hole 834A, as well as the downcore variation in $CaCO_3$ for the clayey nannofossil oozes only (i.e., all values relating to turbidites and air-fall tuffs have been removed to view the variation in $CaCO_3$ content in the background hemipelagic/pelagic sediments).

The clayey nannofossil ooze is stained a distinctive brown to dark yellowish brown color (Munsell color values: 10YR 3/4, 3/6). Smear slide analysis shows that this is a result of the presence of amorphous iron and manganese oxyhydroxides. These oxyhydroxides occur as both aggregates and as surface coatings on the individual sediment grains, such as foraminifers, nannofossil, and clay aggregates and, to a lesser extent, volcanic glass. Because the oxyhydroxides occur predominantly as surface coatings, estimates of their volume abundance by smear slide analysis are difficult to make, but they may occur in concentrations of up to 5%. Figure 10 also illustrates downcore color variations in the clayey nannofossil oozes of Hole 834A. Color designations follow the 10YR hue of Munsell (1975) and are grouped into Munsell color fields. The presence of amorphous iron and manganese oxyhydroxide in recent sediments throughout the central Lau Basin is well documented (Hodkinson et al., 1986) and has been shown to have a hydrothermal origin (Cronan et al., 1986; Reich et al., 1990).

Graded Foraminiferal Sands and Oozes

White to light gray interbeds of foraminiferal sands and oozes occur throughout Unit I. These characteristically display sharp basal contacts, with bases that are frequently graded. The tops of these interbeds are typically bioturbated and gradational with the overlying sediment (which is most commonly clayey nannofossil ooze). They range from 1–2 cm to 3.5 m in thickness. The thickest such interbed occurs in Sections 135-834A-1H-4 to -2H-1 (4.8–8.55 mbsf). The foraminiferal sand/ooze interbeds are much thinner elsewhere in Unit 1, and several thin units (up to 10 cm thick) occur within Core 135-834A-3H. These have an irregular depositional cyclicity of 0.4–2.9 m. The lower parts of these beds comprise benthic and pelagic foraminifer tests and debris, reworked carbonate rock fragments (intraclasts), together with redeposited neritic, molluscan, calcareous algal, and echinoid de-

Table 1. Coring summary, Site 834.

Core no.	Date (Dec. 1991)	Time (local)	Depth (mbsf)	Cored (m)	Recovered (m)	Recovery (%)	Age
135-834A-							
1H	21	2020	0.0–7.6	7.6	7.64	100.0	middle Pleistocene
2H	21	2100	7.6–17.1	9.5	9.04	95.1	middle Pleistocene
3H	21	2145	17.1–26.6	9.5	9.98	105.0	middle Pleistocene
4H	21	2245	26.6–36.1	9.5	10.07	106.0	upper Pliocene
5H	21	2350	36.1–45.6	9.5	9.88	104.0	upper Pliocene
6H	22	0150	45.6–55.1	9.5	9.82	103.0	upper Pliocene
7H	22	0230	55.1–64.6	9.5	9.90	104.0	upper Pliocene
8H	22	0320	64.6–74.1	9.5	9.83	103.0	upper Pliocene
9H	22	0420	74.1–83.6	9.5	9.86	104.0	upper Pliocene
10X	22	0530	83.6–93.2	9.6	4.66	48.5	upper Pliocene
11X	22	0610	93.2–102.9	9.7	4.21	43.4	upper Pliocene
12X	22	0650	102.9–112.5	9.6	3.27	34.0	upper Pliocene
13X	22	0750	112.5–117.0	4.5	0.28	6.2	Barren
14X	22	0925	117.0–123.0	6.0	0.42	7.0	Barren
15X	22	1230	123.0–131.9	8.9	0.73	8.2	upper Pliocene
16X	22	1455	131.9–136.3	4.4	2.28	51.8	Barren
17X	22	1735	136.3–141.6	5.3	5.02	94.7	Barren
18X	22	2000	141.6–144.6	3.0	2.59	86.3	
19N	22	2220	144.6–144.6	0.0	0.00	0.0	
20X	23	0225	144.6–149.5	4.9	3.69	75.3	
Coring totals				149.5	113.17	75.7	
135-834B-							
1R	23	1625	0.0–8.4	8.4	8.42	100.0	middle Pleistocene
2R	23	2225	68.2–77.8	9.6	3.17	33.0	upper Pliocene
3R	23	2310	77.8–87.4	9.6	4.70	48.9	upper Pliocene
4R	23	2350	87.4–97.1	9.7	5.18	53.4	upper Pliocene
5R	24	0020	97.1–106.8	9.7	1.30	13.4	upper Pliocene
6R	24	0110	106.8–116.4	9.6	5.98	62.3	upper Pliocene
7R	24	0315	116.4–126.1	9.7	0.90	9.3	Barren
8R	24	0505	126.1–135.8	9.7	2.48	25.5	Barren
9R	24	0710	135.8–145.4	9.6	1.26	13.1	Barren
10R	24	0855	145.4–150.0	4.6	4.17	90.6	Barren
11R	24	1050	150.0–156.0	6.0	3.92	65.3	lower Pliocene
12R	24	1305	156.0–161.0	5.0	5.29	106.0	Barren
13R	24	1445	161.0–165.7	4.7	2.37	50.4	lower Pliocene
14R	24	1655	165.7–175.4	9.7	0.56	5.8	
15R	24	1840	175.4–185.0	9.6	1.81	18.8	
16R	24	2020	185.0–194.3	9.3	1.29	13.9	
17R	24	2200	194.3–204.0	9.7	0.32	3.3	
18R	24	2345	204.0–208.8	4.8	0.49	10.2	
19R	25	0055	208.8–213.6	4.8	0.18	3.8	
20R	25	0340	213.6–218.4	4.8	1.86	38.7	
21R	25	0545	218.4–223.2	4.8	0.60	12.5	
22R	25	0835	223.2–228.0	4.8	2.21	46.0	
23R	25	1010	228.0–232.9	4.9	0.18	3.7	
24R	25	1135	232.9–237.9	5.0	1.02	20.4	
25R	25	1355	237.9–242.6	4.7	0.96	20.4	
26R	25	1625	242.6–247.6	5.0	0.99	19.8	
27R	25	1820	247.6–252.3	4.7	0.19	4.0	
28R	25	2215	252.3–257.3	5.0	2.57	51.4	
29R	26	0030	257.3–261.9	4.6	0.88	19.1	
30R	26	0410	261.9–266.9	5.0	4.02	80.4	
31R	26	0735	266.9–271.5	4.6	3.43	74.5	
32R	26	1415	271.5–281.2	9.7	0.54	5.6	
33R	26	1835	281.2–286.2	5.0	4.80	96.0	
34R	26	2115	286.2–290.8	4.6	2.05	44.5	
35R	26	2025	290.8–300.5	9.7	1.95	20.1	
36R	27	2350	300.5–310.2	9.7	0.70	7.2	
37R	28	0110	310.2–319.8	9.6	1.94	20.2	
38R	28	0230	319.8–324.8	5.0	0.44	8.8	
39R	28	0350	324.8–329.4	4.6	0.32	7.0	
40R	28	0510	329.4–334.4	5.0	0.58	11.6	
41R	28	0640	334.4–339.1	4.7	1.23	26.2	
42R	28	0800	339.1–344.1	5.0	0.73	14.6	
43R	28	0920	344.1–348.8	4.7	1.15	24.4	
44R	28	1025	348.8–353.8	5.0	0.17	3.4	
45R	28	1125	353.8–358.5	4.7	0.08	1.7	
46R	28	1320	358.5–363.5	5.0	0.21	4.2	
47R	28	1430	363.5–368.2	4.7	1.24	26.4	
48R	28	1550	368.2–373.2	5.0	1.23	24.6	
49R	28	1715	373.2–377.9	4.7	1.10	23.4	
50R	28	1845	377.9–382.9	5.0	0.92	18.4	
51R	28	2005	382.9–387.5	4.6	1.22	26.5	

Table 1 (continued).

Core no.	Date (Dec. 1991)	Time (local)	Depth (mbsf)	Cored (m)	Recovered (m)	Recovery (%)	Age
135-834B- (cont.)							
52R	28	2130	387.5–392.5	5.0	1.60	32.0	
53R	28	2240	392.5–397.2	4.7	0.96	20.4	
54R	28	2355	397.2–402.2	5.0	1.67	33.4	
55R	29	0100	402.2–406.9	4.7	0.75	15.9	
56R	29	0235	406.9–416.3	9.4	1.82	19.3	
57R	29	0345	416.3–426.0	9.7	0.85	8.8	
58R	29	0505	426.0–431.0	5.0	0.82	16.4	
59R	29	0630	431.0–435.3	4.3	1.67	38.8	
Coring totals				375.5	105.44	28.1	

bris. The units fine upward, grading into a nannofossil ooze with foraminifers in the upper part of the unit. Normally graded bedding is common near the base, but complete "Bouma sequences" (Bouma, 1962) are not developed. These beds are interpreted from their sedimentological characteristics as turbidite units, although they typically show only partial "Bouma sequences." This is not unusual for carbonate turbidites as they may not develop the typical sequence of sedimentary structures (e.g., distinct scour marks and convolute bedding or planar laminations) characteristic of siliciclastic turbidites (Thomson and Thomasson, 1969). These differences may be a result of the fact that calcareous muds are less thixotropic than clay muds (Flügel, 1982). Therefore, in spite of the weak development of the sedimentary structures typical of siliciclastic turbidites, the graded foraminiferal sand and associated ooze units are interpreted as allochthonous units probably deposited by turbidity currents derived from a carbonate platform.

Volcaniclastic Deposits

Vitric ashes are generally rare in Unit I. However, three megascopic ash layers occur at 11.13–11.20, 12.42–12.57, and 13.16–13.22 mbsf. Analyses of smear slide samples suggest that microscopically distinguishable ash layers occur at 2.0 and 8.0 mbsf (Fig. 10). The ash layers are composed almost exclusively of optically unaltered, colorless, felsic glass shards. Because of the significantly different Munsell Color Chart hue of the volcanic ash layers, these are not shown in the downcore color variation diagram (Fig. 10).

Unit II

Intervals: Sections 135-834A-5H-4 through -9H-3 and 135-834B-2R-1 through -3R-1
Depth: 42–78 mbsf

Unit II is composed of clayey nannofossil mixed sediment interbedded with vitric ash layers. Compositionally, Unit II is characterized by a marked increase in volcaniclastic material, especially glass. Unlike Unit I, Unit II shows a gradual increase in clay content downcore. Foraminifers also decrease in abundance downcore, becoming rare below 70 mbsf.

Clayey Nannofossil Ooze

Clayey nannofossil ooze is also the predominant sediment type in the upper part of Unit II, although its clay content steadily increases downcore so that by 68 mbsf, the sediment becomes a "mixed sediment" in the classification of Mazzullo et al. (1987). This is reflected in the decreasing $CaCO_3$ content of the clayey nannofossil ooze/mixed sediment, which averages around 60% in the upper part of Unit II but decreases to 40%–45% in the lower part of the unit (Fig. 10). The clayey nannofossil oozes are slightly to moderately mottled throughout Unit II and contain isolated pumice fragments and mud clasts. The clayey nannofossil oozes of Unit II are more intensely stained by iron oxyhydroxides than are those of Unit I. Their color is typically brown to dark brown (10YR 4/3, 3/3) and very dark grayish brown (10YR 3/1, 3/2) (Fig. 10). However, the darkest colored nannofossil oozes of Hole 834A, very dark brown to black (10YR 2/1, 2/2; Fig. 10), are only seen in this unit. Within Unit II, however, a significantly lighter section, pale brown to light yellowish brown in color (10YR 6/3, 6/4, Fig. 10), occurs at 54 mbsf and represents an allochthonous carbonate sequence. Variations in the abundance of iron and manganese oxyhydroxides, and hence color variations in the clayey nannofossil oozes throughout the sedimentary section at Site 834, are likely to depend on the balance between hydrothermal input and its dilution by other sediment components.

Volcaniclastic Sediments

Volcaniclastic sediments, either primary pyroclastic air-fall ashes or, much more commonly, epiclastic turbidites, compose 20% of the total bulk of Unit II. Individual ash layers range from 2 to 120 cm in thickness. Many of the vitric ash layers contain as little as 5%–10% $CaCO_3$. Most of the epiclastic ash units show graded silty or sometimes sandy bases that are overlain by silty planar- and cross-laminated T_c and T_d Bouma units. The upper parts of the turbidites are often structureless (T_e Bouma division) as a result of the rapid deposition of fine-grained material. The upper boundaries are usually gradational with the overlying units and the upper parts of turbidites may show extensive bioturbation. Most of the epiclastic vitric ashes are composed of colorless, optically unaltered, felsic volcanic glass, although some contain small amounts of anhedral-subhedral feldspar and pyroxene grains. An alternately dark-and light-banded silty base of a thick epiclastic turbidite is seen in the interval 135-834A-8H-4, 5–50 cm (69.6 mbsf). Individual light- and dark-colored bands within the basal section are 1–5 cm thick. Smear slide analysis shows compositional segregation in the layers, with foraminifers being concentrated in the lighter bands and mineral crystals and cleavage fragments in the darker bands (Fig. 11). Silt-sized felsic glass shards frequently occur in minor amounts within the clayey nannofossil oozes.

Paleomagnetic and biostratigraphic data suggest that the age span of Unit II is 2.6–3.5 m.y. (see "Sediment Accumulation Rates" section, this chapter).

Unit III

Intervals: Sections 135-834A-9H-3 through -12X-2 and 135-834B-3R-1 through -6R-4
Depth: 78–112.5 mbsf

Unit III is distinguished from Unit II by its greater vitric ash content. Thick vitric ashes, mainly of epiclastic turbiditic origin, are the dominant lithology. They are interbedded with iron-oxyhydroxide-stained, nannofossil clayey mixed sediments and nannofossil clays. In Unit III, volcaniclastic sediments make up 40% of the bulk sediment. The age of the base of Unit III is, as yet,

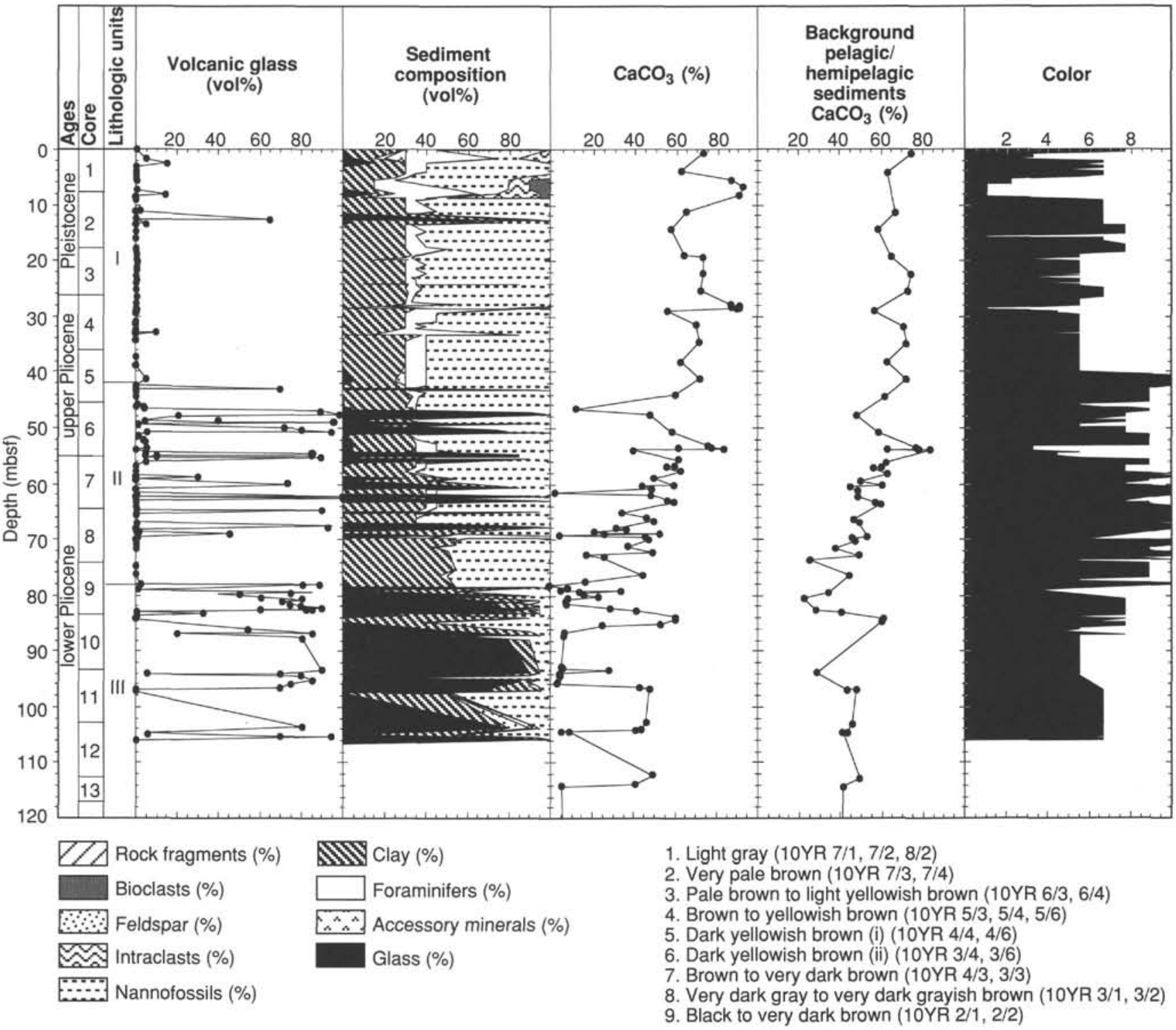

Figure 10. Downcore plots of volcanic glass occurrence (in volume percent); sediment composition (based on analysis of 165 smear slides, in volume percent); $CaCO_3$ profile; $CaCO_3$ in the clayey nannofossil oozes/mixed sediments; and color variations in the calcareous turbidites, clayey nannofossil oozes, and clayey nannofossil mixed sediments in the sedimentary sequences cored at Hole 834A. Note the abrupt increase in the volume percent of volcanic glass at the beginning of Unit II as well as in Unit III, the increase in clay downcore in Unit II, and the decrease in abundance of foraminifers. Foraminifer peaks within Unit I mark the position of calcareous turbidites. The downcore profile for the $CaCO_3$ content of the clayey nannofossil oozes/mixed sediments has had all $CaCO_3$ values related to allochthonous sediments (turbidites and vitric ash layers) removed, yielding the variation in $CaCO_3$ content in the background hemipelagic/pelagic sediments. Color designations follow the 10YR HUE of the Munsell Soil Color Chart (1975) and have been grouped into the Munsell color fields listed. Note the correlation of the darkest colored part of the sequence with Unit II (42–78 mbsf). Lighter colored intervals correlate with calcareous turbidite units. Because of the significantly different color HUE of the volcanic ash layers, these are not shown on this diagram.

poorly constrained by paleomagnetic or biostratigraphic data, but it is interpreted as lower Pliocene in age (see "Biostratigraphy" section, this chapter).

Nannofossil Clayey Mixed Sediments

The nannofossil clayey mixed sediments show minor to moderate mottling throughout and in some places show gradational contacts with underlying vitric ashes. They are generally lighter in color than the clayey nannofossil oozes of Unit II (Fig. 10). From the base of Unit II into Unit III, colors become lighter, being similar to Unit I except for the absence of allochthonous carbonate beds. The darker colors of Unit II, however, extend 8 m into Unit III. The nannofossil clayey mixed sediments contain only 45%–50% $CaCO_3$ (Fig. 10). Overturned and isoclinal slump folds within the nannofossil clayey mixed sediments occur in Section 135-834A-9H-5 at 83–89 cm (Fig. 12).

Volcaniclastic Sediments

Vitric ashes form layers up to 2.1 m thick. They frequently have graded or laminated bases and typically contain up to 90% glass shards, most of which are colorless and appear to be felsic in composition. Some of the ash layers show flame structures along their basal contacts with the underlying sediments (Fig. 13). The remainder of the sediment is composed of clay-sized material

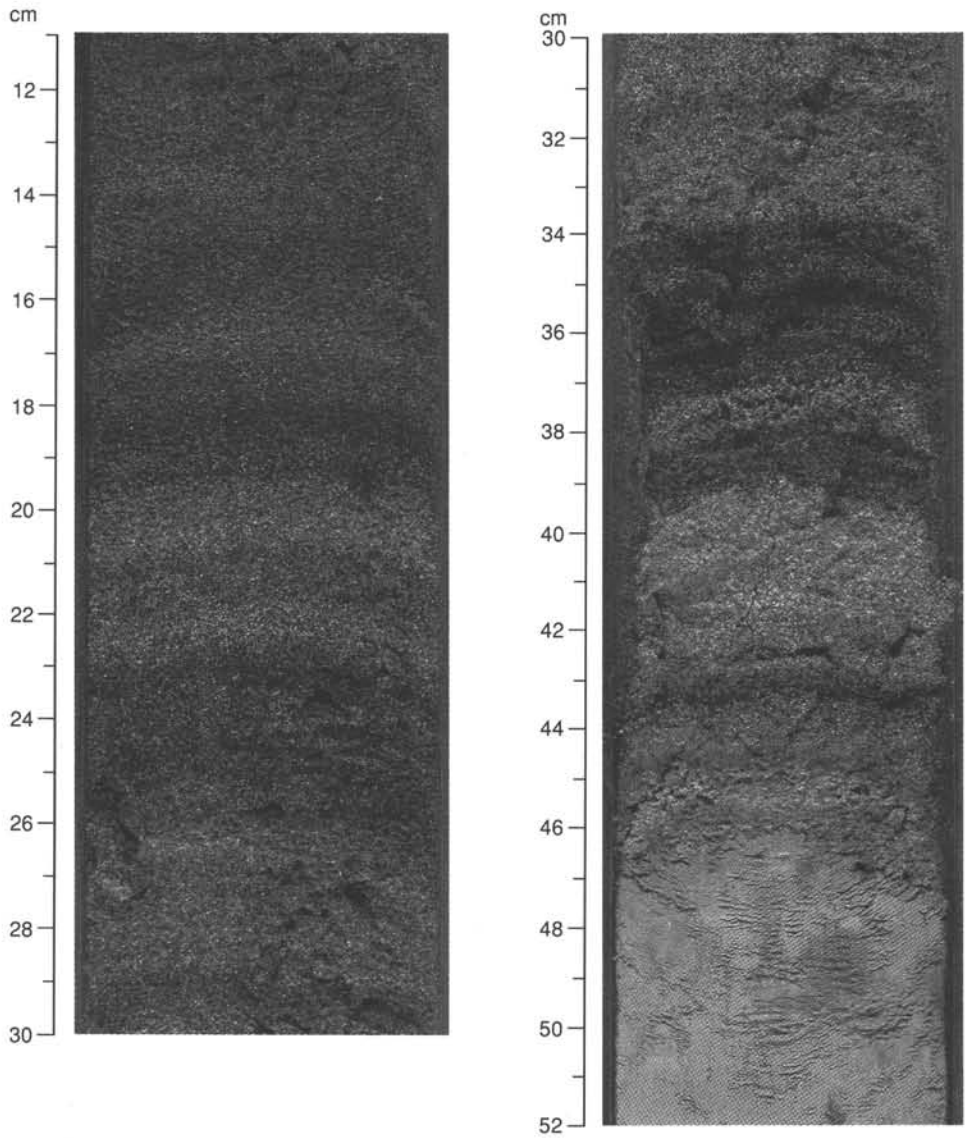

Figure 11. Dark- and light-banded silty base of a thick epiclastic turbidite is seen in the interval 135-834A-8H-4, 11–52 cm (69.6 mbsf). Individual light- and dark-colored bands are 1–4 cm thick. Smear slide analysis shows compositional segregation in the layers, with foraminifers concentrated in the lighter bands and mineral crystals and cleavage fragments in the darker bands.

and nannofossils. Foraminifers are relatively uncommon compared to higher in the section. Unit III is underlain by a vesicular basalt lava flow at 112.5 mbsf. The lowermost 30 cm of the unit contains small, vesicular basalt clasts derived from the underlying lava flow.

Unit IV

Intervals: Sections 135-834A-16X-1 through -16X-2 and 135-834B-13R-2, -37R-1, and -37R-2

Depth: 131.5–162.62 and 310.45–312.1 mbsf

Unit IV is composed primarily of firm or indurated claystones, vitric tuffs and calcarenites, which occur as thin bands of intercalated sediments between lava flows. In Core 135-834A-16X, 1.35 m of barren claystone overlies 0.65 m of cross-laminated, graded crystal-rich tuffs that directly overlie vesicular basalt (Fig. 14). The claystone has an indurated, baked margin 7 cm thick at the contact with the overlying lava flow. The claystone shows a marked color change in Section 135-834A-16X-1 at 126 cm. The line of the color change is inclined and does not disturb the sedimentary structure. The color changes from 2.5 Y 5/4 (light olive brown) to 7.5 YR 6/0 (gray) downsection. The lack of any disturbance to the sedimentary structure or change in lithology suggests that the color change is secondary in origin. Similar features have been interpreted as fronts of iron enrichment derived from hydrothermal fluids associated with volcanism (e.g., Bostrom and Peterson, 1969) and have been recognized previously at DSDP Site 203 in the Lau Basin (Burns et al., 1973). No evidence of thermal alteration of the vitric tuffs by the underlying flow is present. The tuffs below the claystone show mineral segregation in their graded base, with crystal- and glass-rich bands and a layer enriched in opaques, possibly magnetite.

In Section 135-834B-13R-2, 9 cm of laminated nannofossil clay overlies 16 cm of indurated clay that contains near-spherical brown siltstone intraclasts <1 cm in diameter. This indurated clay in turn overlies 5 cm of iron-stained nannofossil chalk. In Core

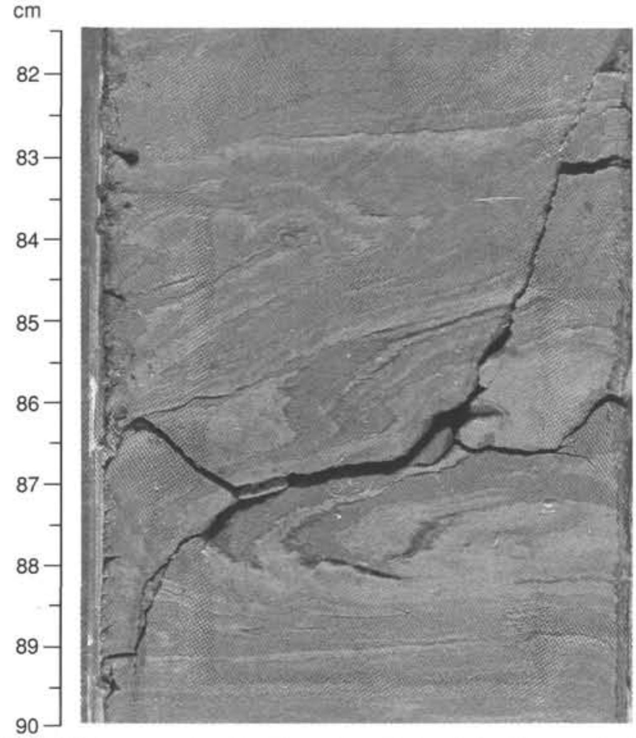

Figure 12. Overturned and isoclinal slump folds within the nannofossil clayey mixed sediments of Unit III (Section 135-834A-9H-5, 81.5–90 cm).

135-834B-37R, 116 cm of calcarenite with laminated mudstone intraclasts is intercalated between layers of basalt.

Volcanic Ash and Tephrochronology

Forty-five sediment layers containing significant amounts (>75%) of dominantly ash-sized, volcanic-derived components are distinguished in Units I–III (Table 2). These include five well-preserved layers of fallout tephra and a number of less distinct layers that are variously modified by bioturbation and/or erosion. Redeposited, epiclastic ashes (i.e., volcanic silts and sands) are overall much more abundant by volume and number than primary pyroclastic ashes.

About 30 ash samples from Holes 834A and 834B were examined in smear slides, and refractive indices of optically clear, isotropic glass shards were determined in 12 samples to evaluate their SiO_2 content. For refractive index measurements, the sediment was cleaned in an ultrasonic bath for 5 min and split into the grain-size fractions 36–64 μm (5ϕ), 64–125 μm (4ϕ), and >125 μm (3ϕ) by sieving. The 5ϕ-glass fraction was analyzed using a reference set of immersion oils with a precision of $n = \pm 0.002$. Silica contents were estimated from the refractive indices using data from Church and Johnson (1980) and Schmincke (1981).

Primary Fallout Deposits

Well-preserved primary tephra layers (T1–T5), ranging in thickness from 3 to 11 cm, were only identified in the upper half of the sedimentary sequence at 42.85 mbsf (T1), 47.48 mbsf (T2), 62.15 mbsf (T3), 62.62 mbsf (T4), and 64.66 mbsf (T5). These occur as discrete, often weakly graded beds with sharp upper and lower boundaries within clayey nannofossil ooze. Maximum grain-sizes that normally occur at the base of the layers range from ca. 100 to 600 μm.

The five tephra layers (T1–T5) are characterized as follows:

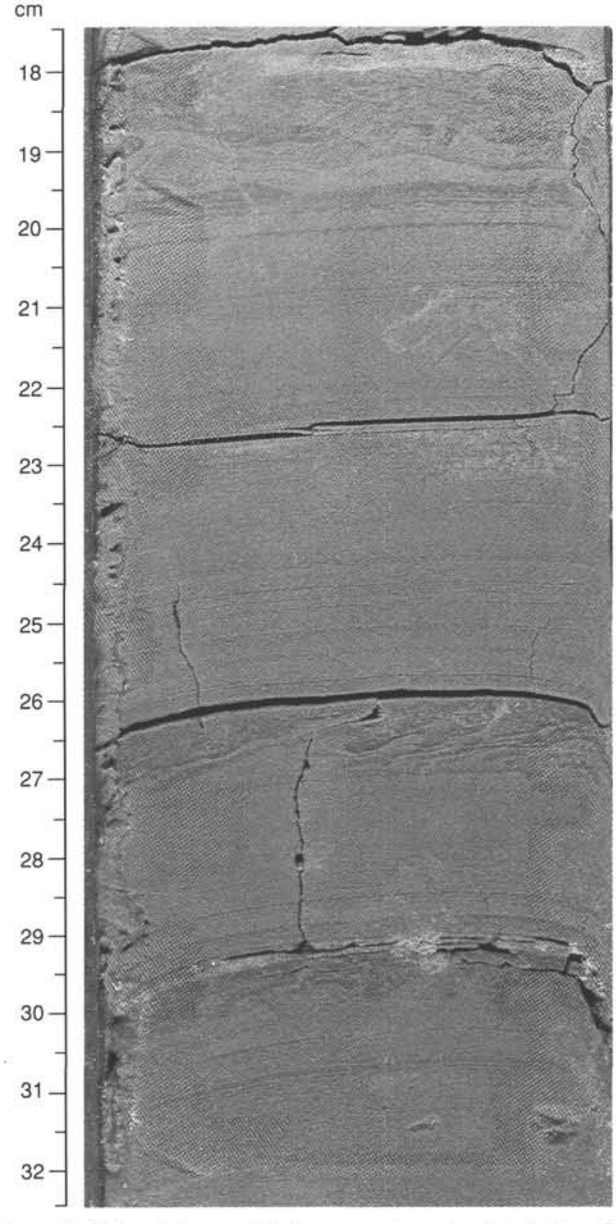

Figure 13. Thin ash layers with flame structures developed along their basal contacts with the underlying sediments in Unit III (Section 135-834A-9H-6, 17.5–32.5 cm).

1. T1 = The vitric shards, which are mostly vesicle-free, angular and colorless, are 10–20 μm diameter and form characteristic irregular clusters up to 200 μm in diameter, often centered around a phenocryst. Pumiceous shards are rare. Phenocrysts reach about 100 μm maximum dimension and comprise plagioclase, augite, hypersthene, biotite, hornblende (partly oxidized), and opaques.
2. T2 = This tephra is characterized by an abundance of large (up to 600 μm), pale brown to medium brown, elongate pumice shards with fibrous and cellular structures, in addition to bubble wall and bubble junction shards. Phenocrysts are predominantly augite, but they also include zoned plagioclase, hornblende, and opaques.
3. T3–T5 = These vitric ashes occur within an interval of only about 2.5 m and show slightly varying proportions of clear, colorless fibrous pumice, and bubble wall and platy, angular, vesicle-free shards. Pumiceous clasts are the dominant grain type,

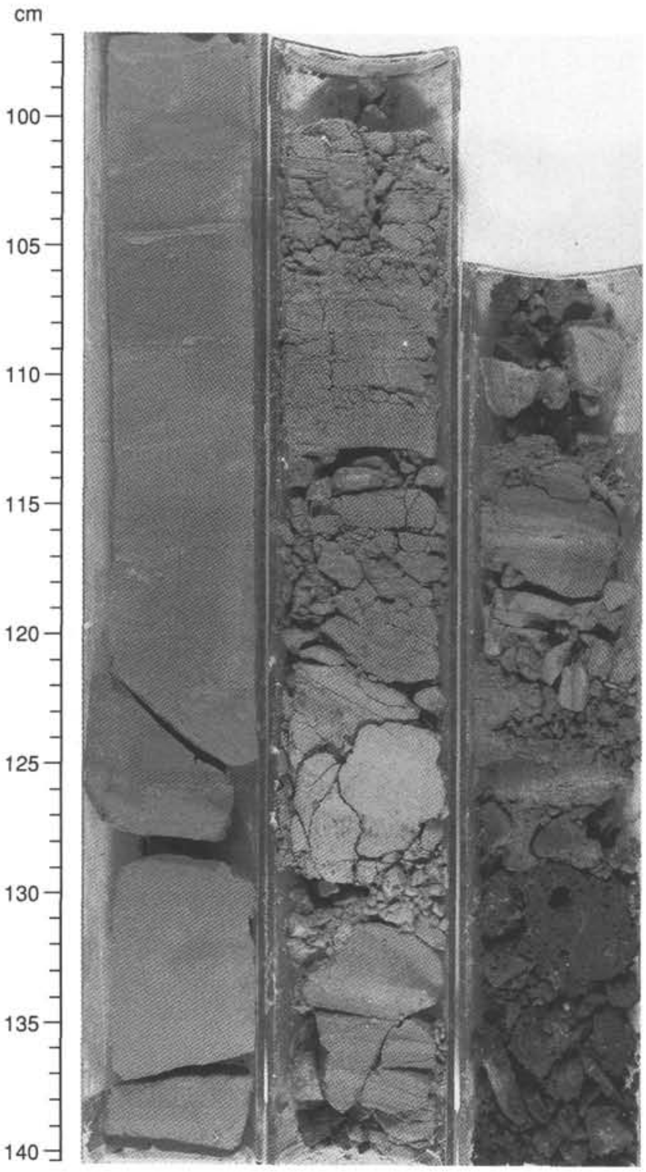

Figure 14. Barren claystone containing thin volcanic ash layers overlying cross-laminated, graded, crystal-rich tuffs that directly overlie vesicular basalt within Unit IV (top of sequence: top of left core; bottom of sequence: bottom of right core). The marked color change at 126 cm in the left core is interpreted as a secondary color change reflecting a front of iron enrichment derived from hydrothermal fluids associated with volcanism. The color changes from 2.5 Y 5/4 (light olive brown) to 7.5 YR 6/0 (gray) downsection. The tuffs below the claystone show mineral segregation in their graded base, with crystal- and glass-rich bands and a layer enriched in opaques (from left to right, Sections 135-834A-16X-1, 135-834A-16X-2, and 135-834A-16X-CC).

especially in T4, whereas bubble wall and platy shards occur more frequently in T3 and T5. Minerals of igneous origin found in all three tephras are plagioclase, augite, biotite, and opaques. Amphibole is restricted to T3, whereas hypersthene was only found in T5.

The colorless appearance of vitric, often pumiceous shards in layers T1–T5 and the common occurrence of water-bearing minerals such as amphibole and biotite grains (presumably phenocrysts) are strong indicators for an origin of these tephras from differentiated to highly differentiated dacitic to rhyolitic magmas. The high vesicularity of many pumice shards is indicative of subaerial Plinian-style eruptions, which often result in the deposition of widespread ash layers. The median diameter of fallout ashes has been related to the maximum distance from their eruptive sources by Fisher (1964) and Walker (1971). With estimated median values of about 50 μm to about 100 μm for T1 to T5, eruptive sites may have been as far away as about 1000 km for the coarser grained layers and several thousand kilometers for the finer grained tephras.

The lack of well-preserved fallout ashes below T5 (about 3.2 Ma) does not mean that their deposition never occurred. Their preservation within an environment of frequent high-energy turbidity currents is unlikely.

Reworked Volcaniclastics (Epiclastic Deposits)

General Characteristics

Reworked volcaniclastics occur in highly variable amounts in turbidite deposits, ranging in thickness from a few tens of centimeters to about 1.5 m. These turbidites, which dominate Units II and III (i.e., below 42 mbsf; Tables 2–3 and Fig. 15), consist of well-sorted beds that normally show a distinct grain-size grading within the silt-size range and mineral segregated layers. Zones of high concentrations of volcaniclastic material (80–100 vol%) are restricted to the bases of the units (here informally called volcanic enriched base [VEB]). The VEBs, which are often light yellow or gray in color, normally make up 15%–25% of the total thickness of individual units. Their upper boundary is not as sharp as the lower contact, but is generally quite pronounced where the sediment grades rapidly into brown and dark brown nannofossil ooze, with much lesser amounts of volcaniclastic material in the central and upper parts of the individual turbidites. The turbidites often have sharp, partly eroded contacts with the units below and have strong contrasts in color, grain-size, and sediment composition.

Internally, the epiclastic ash layers are often structureless, although parallel lamination does occur, especially close to the bases. In one instance, cross lamination occurs in association with parallel laminae (Section 135-834A-8H-4, 10 cm). In another thick-bedded, laminated, volcanic silt interval (Sections 135-834A-9X-6, 109 cm, and -9X-5, 75 cm) small-scale (up to 6 cm thick) isoclinal slump folds occur between evenly bedded material at a number of levels. In this, and in a few other thick-bedded sequences, the sediment is finely laminated with alternating light clayey nannofossil mixed sediment and darker volcanic glass layers.

One distinct epiclastic bed (Bed BA) has a minimum thickness of 135 cm, with a base at 69.56 mbsf (corresponding to an age of about 3.3 Ma). It shows a completely different internal structure and composition of vitric shards (see below). It is made up of alternating light to medium grey and dark grey to black layers, contains predominantly silt-sized grains and fines upward overall, but grain-size grading may also occur within individual layers where grain sizes may locally range up to about 1 mm.

Specific Characteristics and Composition

VEBs throughout Units II and III show remarkably few petrological variations, being largely composed of silt-sized, colorless to slightly brown vitric shards (up to nearly 100 vol%). They are dominated by angular, platy, bubble-wall, subangular pumiceous and elongate fibrous shard shapes that occur in varying proportions in the different units, with the latter two types generally representing the largest shards within individual VEBs. Minerals of igneous origin are present only in trace amounts, with plagioclase laths, often showing multiple twinning, as the most

Table 2. Characteristics of discrete ash layers and ash turbidites in Hole 834.

Core, section, depth	Depth to top (mbsf)	Depth to base (mbsf)	Age (k.y.)	Smear slide	Thickness (cm)	Type of unit	Glass (vol%)	Maximum grain size (μm)	Significant shard morphologies				Igneous minerals present (>1 vol%)
									Tubular	Bubble wall	Angular	Rounded	
135-834A-													
*2H-3	11.13	11.20	500		7	P,H							
2H-4, 45	12.32	12.57	550	X	25	?,G	65		X		X		plag, cpx, opaques
*2H-4	13.17	13.22	600		5	P,H							
5H-5, 76	42.81	42.85	2350	X	4	P,G	100	200	X		X		plag, cpx, opx, biot, amph, opaques
6H-1, 131	46.57	46.95	2600	X	38	E,G	90	200	X	X	X		plag, opaques
6H-2, 37	47.45	47.48	2700	X	3	P,G	98	600	X	X			plag, cpx, amph, opaques
6H-3, 51	48.57	49.11	2700	X	54	E,G	95	300	X	X	X		plag
6H-4, 59	49.88	50.69	2750	X	81	E,G	95	150	X		X		plag, cpx, amph, opaques
6H-7, 35	54.34	55.00	2850	X	66	E,G	85	150	X	X			
7H-1, 24	55.10	55.34	2850	X	24	E,G	90		X	X			
7H-3, 81	55.88	58.94	2900	X	6	E,H	30						
7H-4, 60	60.05	60.29	3050	X	24	E,H	75	100	X	X			
7H-5, 103	62.04	62.15	3100	X	11	P,G	98	150			X		plag, cpx, amph, biot, opaques
7H-5, 148	62.55	62.62	3150	X	7	P,G	98	300	X				plag, cpx, biot, opaques
8H-1, 3	64.60	64.66	3200	X	6	P,H	90	200	X		X		plag, cpx, opx, biot, opaques
*8H-3	67.49	67.64	3300		15	E,G							
8H-4, 37	68.83	69.56	3300	X	73	E,G	45						
*9H-1	75.45	75.48	3450		3	P,H							
*9H-2	76.92	76.95	3500		3	P,H							
9H-3, 105	78.07	78.15	3500	X	8	E,G	90	500	X		X		
*9H-3	78.20	78.22	3500		2	E,G							
*9H-3	78.22	78.24	3500		2	E,G							
*9H-3	78.24	78.41	3500	X	17	E,G	90						
9H-4, 95	78.41	79.61	3500	X	120	E,G	85	200	X		X		
9H-4, 120	79.61	79.84	3600	X	23	E,G	40						
9H-5, 71	80.28	80.84	3600	X	56	E,G	80	500	X		X		
9H-6, 108	80.84	82.69	3600	X	185	E,G	83	250	X		X	X	
*10X-2	85.42	85.60	3650		18	E,G							
*10X-2	86.48	86.58	3700		10	E,G							
10X-3, 86	86.83	87.52	3700	X	69	E,G	80	300	X		X		
10X-3, 117	87.52	88.01	3700	X	49	E,G	85	150	X		X		
*10X-CC	88.10	88.30	3700		20	E,G							
11X-1, 49	93.33	93.77	3750	X	44	E,G	50	400					
11X-2, 50	94.78	95.40	3750	X	62	E	85	300				X	
*11X-3	95.40	96.87	3750		147	E							
12X-1, 65	103.52	103.57	3800	X	5	P,H	80	300					
*12X-1	103.96	103.97	3800		1	P,H							
12X-2, 87	105.08	105.30	3800	X	22	E,G	95	220					
*12X-2	105.30	105.55	3800		25	E,G							
16X-CC, 18	133.30	133.93	3800	X	63	E,G	65	350	X			X	plag, opaques, qtz
135-834B-													
3R-2, 42	79.72	79.73	3600	X	1	P,H	85	250					
*3R-2	80.30	80.43	3600		13	E,G							
3R-3, 30	80.43	81.56	3600	X	113	E,G	90	300	X		X		plag, augite
3R-3, 100	81.56	82.06	3600	X	50	E,G	80	200	X	X	X		
3R-3, 140	82.06	82.30	3600	X	24	E	75		X		X		
*3R-CC	87.30	87.47	3650		17	E							
4R-1, 30	87.40	87.89	3700	X	49	E,G	40	300					
4R-2, 20	88.60	89.11	3700	X	51	E,G	45	250					
4R-2, 133	89.11	90.25	3700	X	114	E,G	85	200	X	X	X		plag, opaques, biot
4R-3, 30	90.25	90.72	3700	X	47	E,G	25	250					

Table 2 (continued).

Core, section, depth	Depth to top (mbsf)	Depth to base (mbsf)	Age (k.y.)	Smear slide	Thickness (cm)	Type of unit	Glass (vol%)	Maximum grain size (µm)	Significant shard morphologies: Tubular	Bubble wall	Angular	Rounded	Igneous minerals present (>1 vol%)
135-834B- (cont.)													
4R-3, 36	90.72	91.10	3700	X	38	E,G	85	200	X	X	X		plag, augite
4R-4, 45	92.35	92.36	3750	X	1	P,H	70	200	X	X	X		plag, augite, opaques
*6R-2	108.72	108.96	3750		24	E							
6R-2, 80	108.96	109.21	3800	X	25	E	70	350					

Notes: Core, section, depth to smear slide sample (cm); * indicates ash layer from which no smear slide was made, only the core and section in which the ash layer occurs are indicated. Type: P = pyroclastic, E = epiclastic, H = homogeneous, and G = graded. Glass (vol%): Glass content normally indicates maximum mode estimated from smear slides; however, glass content may be highly variable in individual units, especially in the graded sequences. Igneous minerals present: Igneous mineral content is noted when more than trace amounts (>1%) are present. Key: plag = plagioclase, cpx = clinopyroxenes, opx = orthopyroxenes, biot = biotite, amph = amphiboles, and qtz = quartz.

Table 3. Refractive indices (n) and SiO_2 concentrations (estimated after Church and Johnson [1980] and Schmincke [1981]) of vitric shards (63–36 µm size fraction) from turbidites in Hole 834A.

Core, section, interval (cm)	Depth (mbsf)	Comments	n	SiO_2 (wt%)
135-834A-				
6H-1, 131	46.91		1.538	62.4
7H-5, 105	62.15		1.513	69.1
8H-4, 37	69.50	An_{85} (n = 1.574)	1.586	51.8
9H-3, 101	78.11	Brown, fibrous, dominant	1.538	62.4
9H-3, 101	78.11	Clear angular, rare	1.522	66.6
9H-4, 96	79.56	Brown, fibrous, dominant	1.534	63.5
9H-4, 96	79.56	Clear angular, rare	1.522	66.6
9H-5, 71	80.66		1.522	66.6
11X-1, 46	83.66	Clear, dominant	1.515	68.6
11X-1, 46	83.66	Brown, rare	1.566	55.9
10X-2, 95	87.55		1.516	68.3
10X-3, 86	88.96		1.534	63.5
11X-1, 49	93.69	Clear, fibrous, dominant	1.514	68.8
11X-1, 49	93.69	Brown, rare	1.550	59.5
11X-2, 120	95.90		1.514	68.8
12X-2, 87	105.10		1.522	66.6

common component. Green clinopyroxenes (augite), hypersthene, opaque oxides, amphiboles, and biotites are only rarely present.

Refractive indices (n) of glass shards in the VEBs range from 1.566 to 1.513 (Table 3 and Fig. 16), corresponding to andesitic and dacitic compositions with SiO_2 contents of 55.9 and 69.1 wt%, respectively. Shards tend to become slightly brown with decreasing silica content.

Seven VEBs (46.91, 62.15, 80.66, 87.46, 88.96, 95.90, and 105.10 mbsf) are each dominated by vitric shards of a constant chemical composition. Two distinct, paired populations of brown andesitic and colorless dacitic shards occur at 78.11 and 79.56 mbsf, respectively (Fig. 17). In both layers, however, the more silicic dacitic shards do not make up more than 10–15 vol% of all shards. Two VEBs at 83.66 and 93.69 mbsf are both dominated by dacitic shards of 69 wt% SiO_2. However, they also contain a bimodal suite of andesitic vitric shards of 56 and 60 wt% SiO_2, respectively, as minor components.

Origin and Source of Ash Turbidites in Lithostratigraphic Units II and III

From the present submarine topography at the margins of the Lau Basin, it seems reasonable to assume that the ash turbidites originated from the slopes of the Lau Ridge. However, because this is separated from the drill site by a small and narrow, discontinuous north-south submarine ridge, the source area was prob-

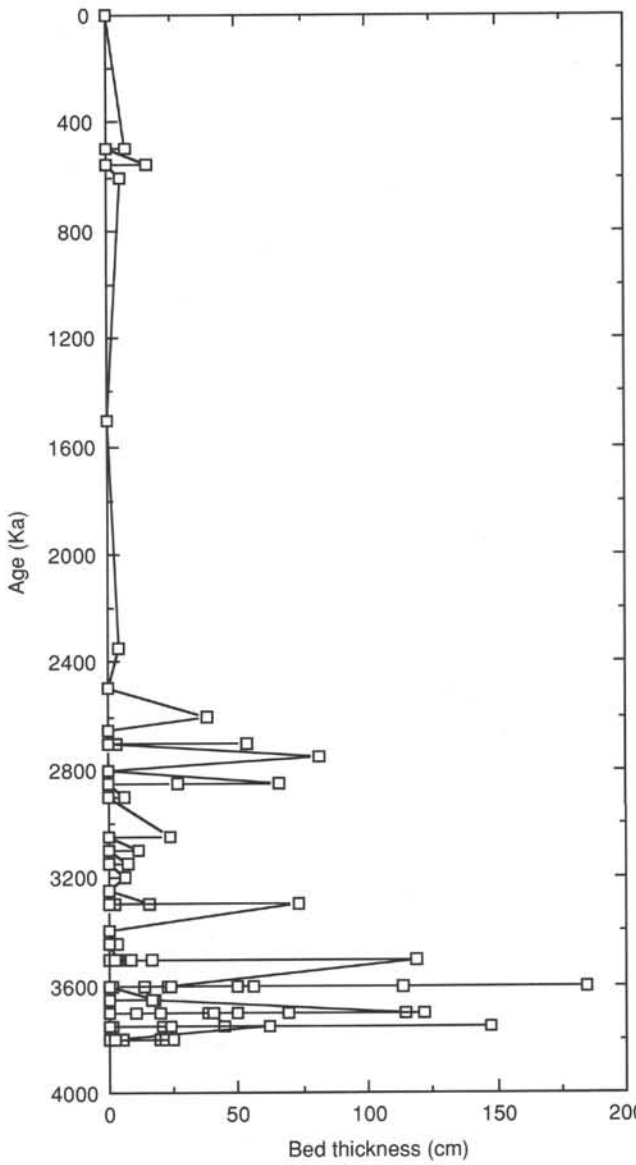

Figure 15. Variation in thickness of turbidites with volcanic-enriched bases (VEBs) in Holes 834A and 834B with time.

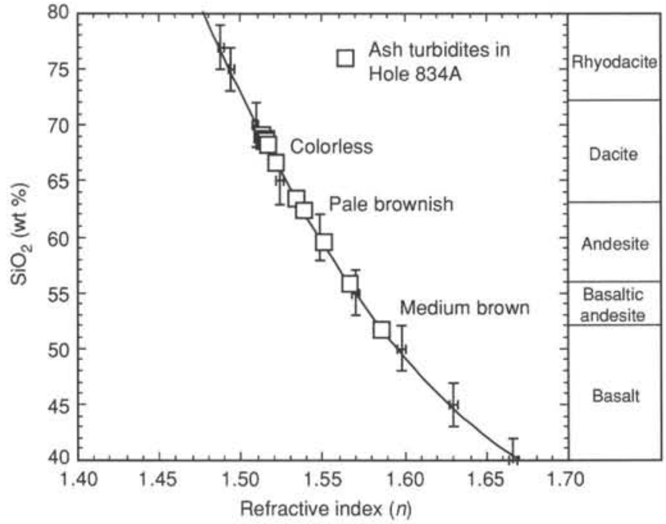

Figure 16. Correlation of refractive indices and SiO_2 concentrations of volcanic glass after Church and Johnson (1980) and Schmincke (1981). The predominant colors of the glass shards, correlated to their chemical composition, are indicated.

ably not located directly to the west, but rather north and/or south of Site 834.

A flowing medium can fractionate and sort clastic detritus according to differences in grain size and density. Most of the turbidites, therefore, probably originally contained a greater amount of clastic material such as rock fragments and igneous mineral grains, as well as volcanic glass shards, but these may have been deposited from the turbidity current more proximally. The VEBs themselves contain evidence for this, as pumice shards are about one ϕ-step larger than dense angular shards in the same unit. According to Fisher (1965), the settling velocity of 3ϕ pumice shards (0.55 m/s) is close to that of vitric shards in the 4ϕ range (0.41 m/s).

Bed BA

The different layers in Bed BA are mainly composed of varying proportions of neritic foraminifers, subangular to subrounded augite and plagioclase grains, and medium brown, mainly fresh vitric shards, although traces of incipient palagonitization occur locally. These shards, which may contribute up to 50% by volume of the sediment, are often highly scoriaceous, containing up to 60% large, round vesicles on a volume basis. Their refractive index of 1.586 is consistent with a basaltic or basaltic andesitic composition. Plagioclase phenocrysts, often with a thin rim of different composition, have an average composition of An_{85}, judging from their refractive index of 1.574. This rather calcic feldspar composition is not uncommon in subduction-related settings (e.g., basaltic andesites from the Troodos ophiolite; Bednarz and Schmincke, in press) and could indicate either a xenocrystic origin or an elevated water content of the host magmas.

Origin of Bed BA

Bed BA differs from most of the ash turbidites in having a different clastic assemblage, maximum grain size, and different bedforms and bed thickness. We interpret the well-developed, small-scale bedding as having originated from a series of small deposition "events" rather than from a single depositional cycle. The mafic nature of glass shards in Bed BA is unique to the whole sedimentary sequence. Their well-preserved scoriaceous to pumiceous morphologies with high vesicle contents are suggestive of a subaerial to shallow submarine (<100–200 m water depth; e.g.,

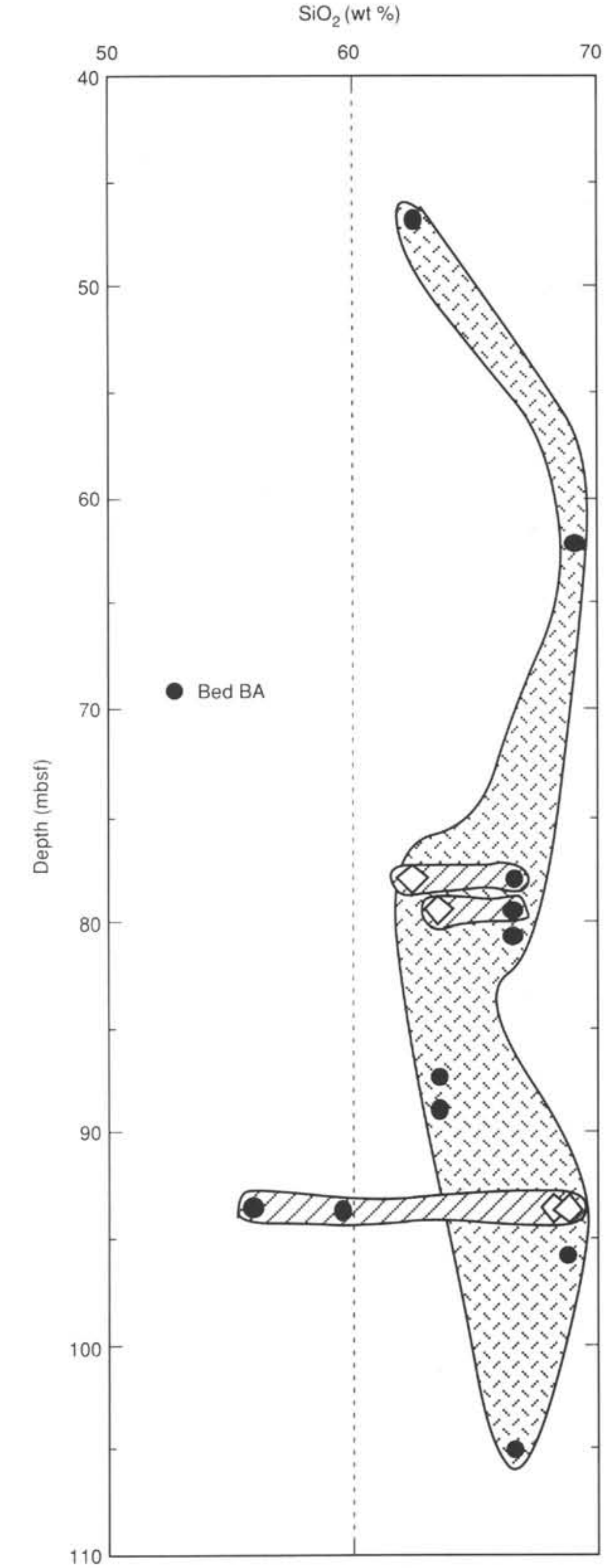

Figure 17. Downhole plot of SiO_2 concentrations in optically clear volcanic glass shards, Hole 834A. Oblique hatched pattern indicates compositional variations within individual samples; discontinuous cross-hatched pattern illustrates the compositional variation of silicic shards. The predominant composition is indicated by diamond symbols, whereas black dots indicate individual samples examined.

Moore and Schilling, 1973) pyroclastic and/or hydroclastic origin of these tephra particles. Further evidence for a different source area from the majority of the turbidites comes from the occurrence of neritic foraminifers within Bed BA. The basalt/basaltic andesitic scoriaceous clasts may be derived from shallow seamounts or flanks of oceanic islands, located on the Lau Ridge or within the Lau Basin. Lavas of basaltic andesitic to dacitic composition have been dredged from the Zephyr shoal, which is located approximately 200 km away from Site 834 (Hawkins, 1976). As the bathymetry around Site 834 is not presently known in detail, more proximal sources cannot be ruled out.

Alteration of Glass Shards

Throughout the core, almost all glass shards appear optically clear (isotropic). Similar optical properties in individual samples indicate that hydration, generally the first alteration process of silicic glasses and well-known in modifying their refractive index (e.g., Ross and Smith, 1955), is only at a very early stage. Low-order birefringence in about 50 vol% of the slightly more mafic pumice shards at 78.11 and 79.56 mbsf shows that glass alteration has reached slightly more advanced stages locally, but that the degree of alteration does not simply correlate to the depth below the seafloor.

Igneous minerals are generally unaltered. One exception is Core 135-834A-16X (a thin intralava sediment), in which the feldspars are clouded throughout. Alteration here may be directly related to hydrothermal circulation driven by the emplacement of the overlying basaltic lava flow. Iron-oxyhydroxide minerals, which are common in the nannofossil oozes, are less common in ash layers but are occasionally found as aggregated lumps.

A likely reason for the preservation of even small glass shards throughout the section is the abundance of clay-sized material in those intervals dominated by sedimentation of nannofossil ooze. This could have locally prevented open-system conditions for exchange of pore- and seawater. We also conclude that the freshness of the volcaniclastics in the turbidite sequences indicates redeposition fairly rapidly after eruption and deposition in a submarine environment.

Summary of Volcanic Chronology

Rapid accumulation of vitric volcanic debris started mainly after the end of extension and magmatism in the basin at Site 834 (3.8 Ma) and continued to the base of Unit I around 2.6 Ma.

The presence of thin sedimentary layers between lava flows shows that the basin is at least about 5.5 m.y. old, but before 3.8 Ma Site 834 provides no record of volcaniclastic sedimentation. Variations in silica content with time in the volcaniclastic record is likely to reflect changes in the composition of arc magmatism. A specific sedimentary sequence containing basaltic to basaltic andesitic scoriaceous shards at about 3.3 Ma (Bed BA) may be related to eruptions of a shallow seamount or on the flanks of an oceanic island.

The sharp decrease in the amount of volcaniclastic input by turbidites after about 2.6 Ma is presumably related to the cessation of volcanism on the Lau Ridge (Woodhall, 1985). To some degree, it may also reflect modification of the drainage and sediment dispersion pattern, for instance, as it resulted from damming or breaching. Seismic reflection data show no evidence for syndepositional subsidence or uplift of basement ridges adjacent to the site.

Five well-preserved, primary dacitic to rhyolitic fallout ashes with distinct phenocryst populations were erupted around 3.1–3.2, 2.7, and 2.4 Ma. They are likely to have had very distal sources on an order of up to several thousand kilometers from the drill site. The basaltic basement did not significantly contribute to the volcanic sediment that overlies it and clearly did not give rise to the silicic shards.

Depositional History

Sedimentation at Site 834 began at least as early as 5.5 Ma, with the oldest sediments recovered represented by the presence of a short section of brown-colored siltstone and brecciated calcareous mudstone (Unit IV) (Core 135-834B-37R). This mixed sediment, containing volcanic glass and quartz, also contains foraminifers and pelagic nannofossils, suggesting that the Lau Basin is at least as old as the upper Miocene (5.5 Ma). This sediment sequence was subsequently covered by lavas, indicating continued proximity to active volcanism.

The principal section (Units I–III) displays a sequence of hemipelagic and pelagic sedimentation. However, the abundance of volcaniclastic material indicates proximity to an eroding volcanic arc for much of the postmagmatic history (3.8–2.3 Ma). Volcaniclastic and later bioclastic material has been redeposited from turbidity currents within the opening backarc basin. Most of the volcaniclastic material is present as turbidites, but some air-fall tuffs are present, particularly in the upper parts of the sequence. Compositionally, the volcanic turbidites are dominated by fresh glass fragments and minor quantities of ferromagnesian minerals and feldspar. The glasses themselves are frequently pumiceous and have chemical compositions in the range from 63% to 68% SiO_2 (and so are derived from andesitic to dacitic magmas). The chemistry of the volcaniclastics, therefore, appears to indicate derivation from an arc source and not the basaltic basement. There is some limited evidence to suggest decreasing silica content of the glasses with time. Paleowater depths must have been shallower than today (2700 m) but were almost certainly at bathyal to abyssal depths for the greater part of the sequence, in view of the almost exclusively pelagic fauna.

Redeposition from the Lau Ridge and possibly the Tofua Arc, the presumed sources of the volcaniclastic turbidites, diminished with time and eventually ended about 2.6 Ma. Around this time erosion of the extinct Lau Ridge was decreasing and the newly active Tofua Arc was also decreasing its contribution to the sedimentation in the western Lau Basin. Although this is likely to have been the underlying reason for the decrease of volcaniclastic turbidites into the basin, their sudden disappearance upsection may have also been the result of changes in the sediment dispersion pattern within the basin. Site 834 was drilled in a small sub-basin, flanked on either side by north-south ridges with several hundred meters relief. These ridges may have acted as effective blocks to sediment flow into the basin.

Since 2.6 Ma, sedimentation has been almost completely hemipelagic to pelagic in character, with occasional minor intercalations of air-fall pyroclastic tuff. Volcaniclastic turbidites are replaced by bioclastic calcareous turbidites that contain minor amounts of glass. These turbidites are probably derived from coral reefs built upon the eroded Lau Ridge. As in pre-2.6 Ma sediments, the nannofossil ooze that accumulated is pale to dark brown in color. The entire sequence of clayey nannofossil oozes that form the background hemipelagic/pelagic sediments are stained by iron and manganese oxyhydroxides, derived from hydrothermal vent systems, suggesting that such activity has been continuous and possibly variable through time. Compared with sedimentation in the period 3.8–2.6 Ma, the sedimentation rates since 2.6 Ma are lower, probably reflecting decreased turbiditic input.

STRUCTURAL GEOLOGY

Sediments

From the core inspection at Site 834, it appears that the small basin in which it is situated has experienced a simple structural history. Evidence for tectonic disturbance is virtually absent in cores from either Holes 834A or 834B. Sedimentary bedding is uniformly horizontal or near-horizontal throughout Hole 834A and shows no systematic change with depth (Fig. 18). The slight variation depicted in Figure 18 is probably principally a result of minor drilling-related disturbances or to scour features at the bases of turbidite flows. From observations of the core alone, it is concluded that no block tilting or other significant tectonic activity has taken place in the vicinity of Site 834, at least since the cessation of volcanism and the onset of regular sedimentation in earliest Pliocene times.

Basement

With the single exception of the minor polishing and striation of joint surfaces at 374 mbsf in Hole 834B, there is no evidence for any fault activity in basement core recovered at the site, either from Holes 834A or 834B. However, with the paucity of recovery at the site and the general difficulty in retrieving faulted rock (see "Structural Geology" section, "Explanatory Notes" chapter), this assertion must be tested by other means. It is addressed further in the "Downhole Measurements" section (this chapter).

Igneous rocks were encountered at 112.5 mbsf in Holes 834A and 834B. Minor interbeds of sediment occur as deep as 311 mbsf in Hole 834B. Predrilling structures are recognizable within this igneous basement. These are planar to irregular cracks and veins that are associated with secondary alteration and must therefore predate the drilling process. The alteration mineralogy is described in more detail in the "Igneous Petrology" section (this chapter). In general, cracks are lined with or stained by yellow-orange-brown iron oxides and hydroxides and may be infilled with calcite, zeolites, and clays. Penetrative brown alteration halos up to a centimeter in width may locally be present in the host lava on either side of veins that are themselves <1 mm thick, suggesting that fluid flux through such veins may have been significant.

As stated above, these cracks and veins display no evidence for any displacement having occurred across them; therefore, the cracks should correctly be termed joints (Hancock, 1985). A set of minor fractures at 374 mbsf, displaying weak down-dip slickensides indicating normal displacement, is the solitary exception. The joints are predominantly steeply dipping (Fig. 19), although it is possible that this distribution may have been modified by the preferential destruction of gently dipping fractures during the drilling process.

Azimuthal data from the joints is presented in Figure 20. These azimuths are derived from individual core measurements and were converted to geographical coordinates using the paleomagnetic declination value at the highest level of magnetic cleaning available on board the ship (15-mT alternating field demagnetization). The natural remanence magnetization (NRM) of most samples is dominated by a low-coercivity component with a characteristic near-vertical inclination that is thought to have been induced during drilling (see "Paleomagnetism" section, "Explanatory Notes" chapter, this volume). This component can typically be removed by alternating-field (AF) demagnetization to leave a stable vector, which can be assumed for the present purposes to be "primary" (e.g., Fig. 21). This analysis is conducted routinely by the onboard paleomagnetists to look for variations in magnetic inclination that will help define a magnetic

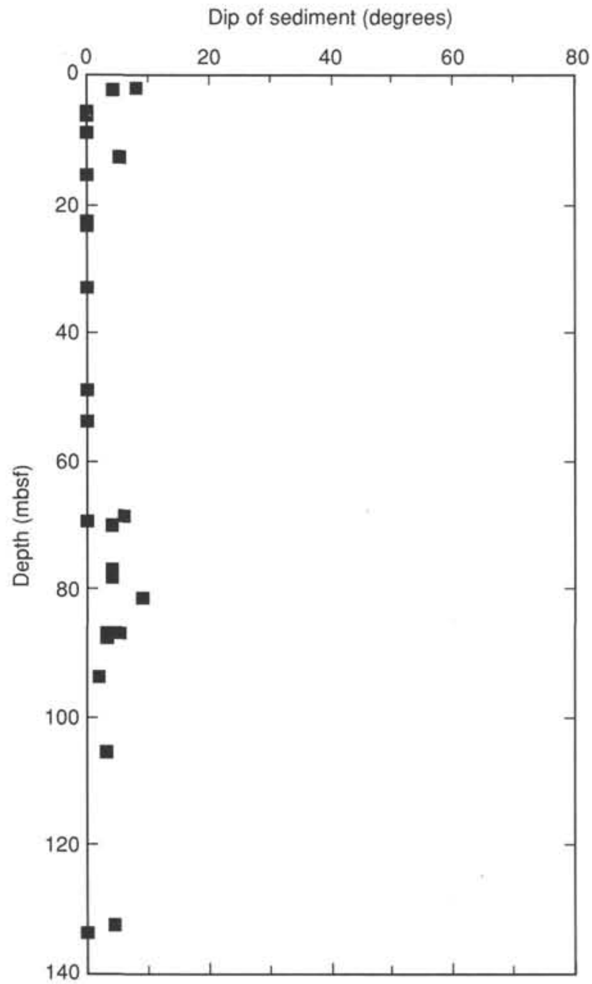

Figure 18. Dip of sediment vs. depth, Hole 834A.

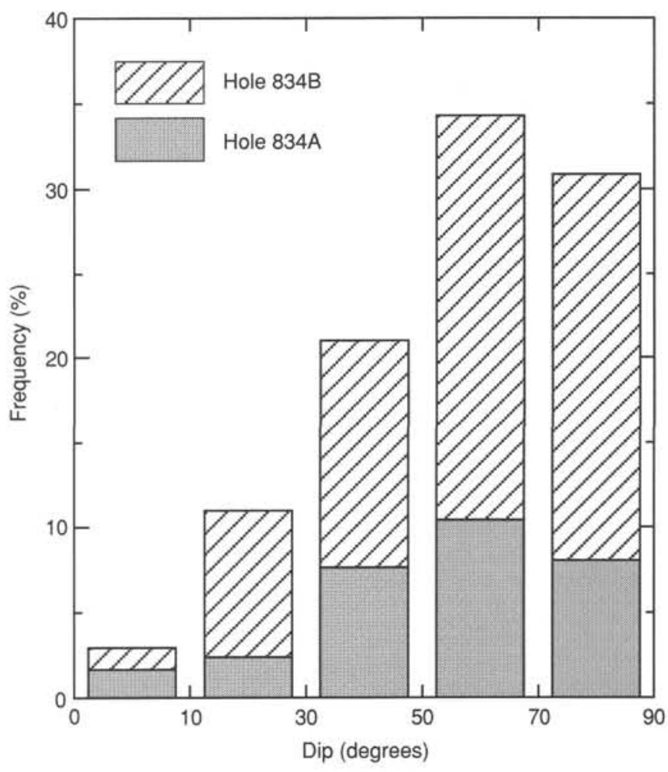

Figure 19. Frequency histogram of the dip of joints relative to the axis of the borehole, Holes 834A and 834B. $N = 135$.

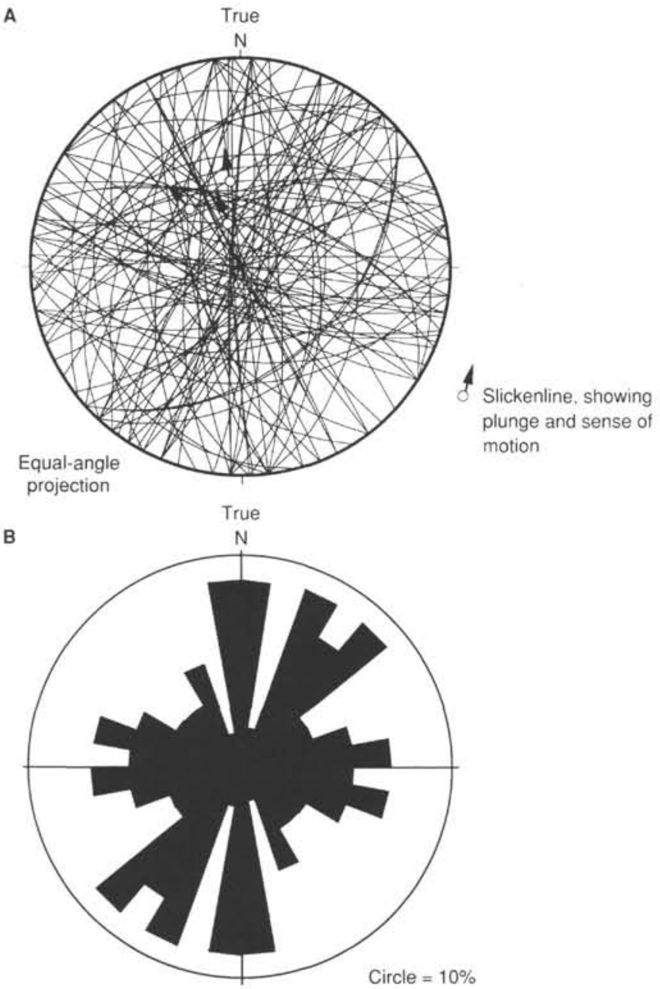

Figure 20. Orientation data for joints from Hole 834B. Azimuths were calculated from paleomagnetic information (see text and Fig. 22) and are given relative to true north (13° W of magnetic north). N = 106. **A.** The equal-angle stereographic projection of joint planes and of the three fault planes are identified, with the slickenside lineation and sense of motion indicated by solid arrows. **B.** Rose diagram of joint azimuths. Note the weak overall maximum between north-south and northeast-southwest.

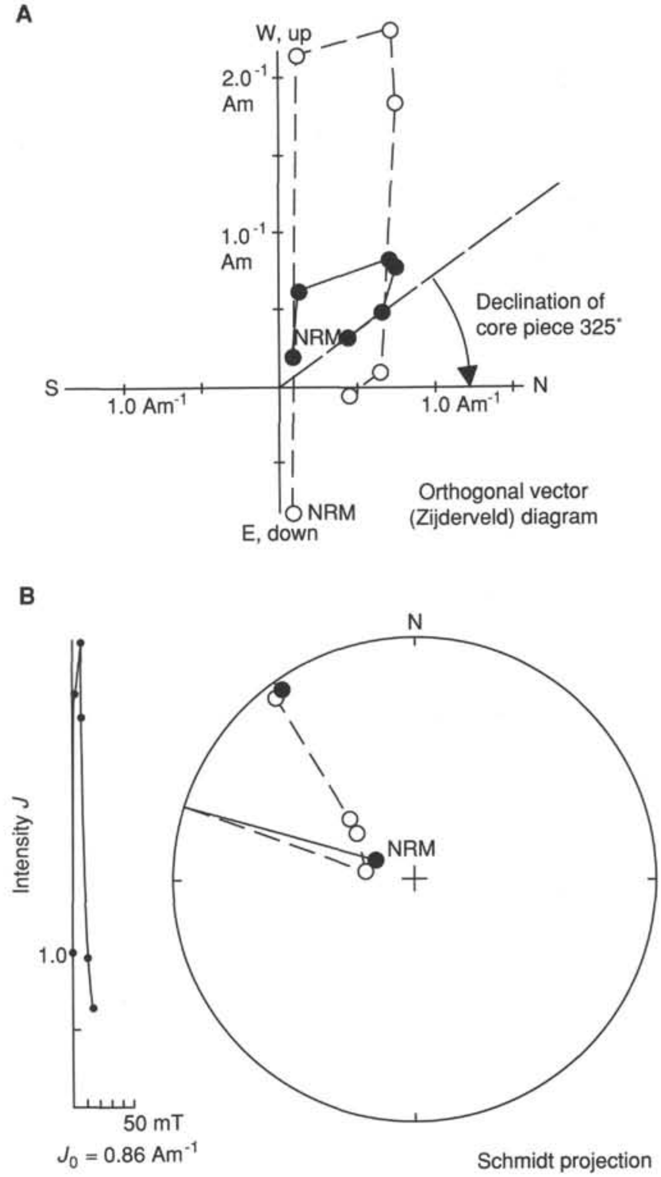

Figure 21. Example of the magnetic properties of a typical basement core sample upon demagnetization to illustrate the method of orienting core pieces. **A.** Orthogonal vector (Zijderveld) diagram showing the variation of the magnetization vector upon progressive alternating field (AF) demagnetization, with the NRM and 2, 5, 6, 10, and 15 mT steps. The axes represent magnetic field intensity, measured in mA/m. Filled circles are in the horizontal plane (declination), and open circles in the vertical plane (inclination). Note the steep initial inclination of the magnetization direction, and its subsequent decrease with increasing levels of demagnetization, upon removal of a supposed drilling-induced component. The declination direction becomes stable and near-constant with an azimuth of approximately 325°, after 10-mT of demagnetization. This declination value is assumed to represent the original north direction of the piece of core (135-834B-8R-1, 110 cm), and structural measurements made on this piece are therefore corrected to geographical coordinates by subtracting 325° from the core declination. **B.** Schmidt equal-area projection of the same sample, together with a plot of the magnetic intensity J (normalized to the NRM value) vs. degree of demagnetization. Filled circles indicate the lower hemisphere of the stereogram, and open circles the upper hemisphere.

stratigraphy (see "Paleomagnetism" section, this chapter); however, with the rotation of the core during drilling, and arbitrary splitting of the core upon recovery, the declination data is of less significance to them. At sites where no significant tectonic rotations are suspected, as at the present site, it is considered justified to use these data to reorient the core by correcting the declination value back to north (south if the inclination is reversed) and applying the same correction to the structural measurements. For Hole 834B it was possible to reorient 106 out of 120 structural measurements in this way. Demagnetization was not performed on all of the basement portions of Hole 834A, and so the 52 structural measurements made have no geographical reference frame and only the dip data are valid.

The dispersion of azimuths in Figure 20 is wide, as is generally to be expected in such a large volume of jointed rock (Hancock, 1985). Note that secular variation can account for changes of up to ±15° in magnetic declination. No systematic variation in either azimuth or dip is apparent with depth (Fig. 22). A weak maximum in joint strike can be discerned in a north-south to northeast-southwest direction with a possible subsidiary east-west maximum (Fig. 21). The north-south to northeast-southwest direction is

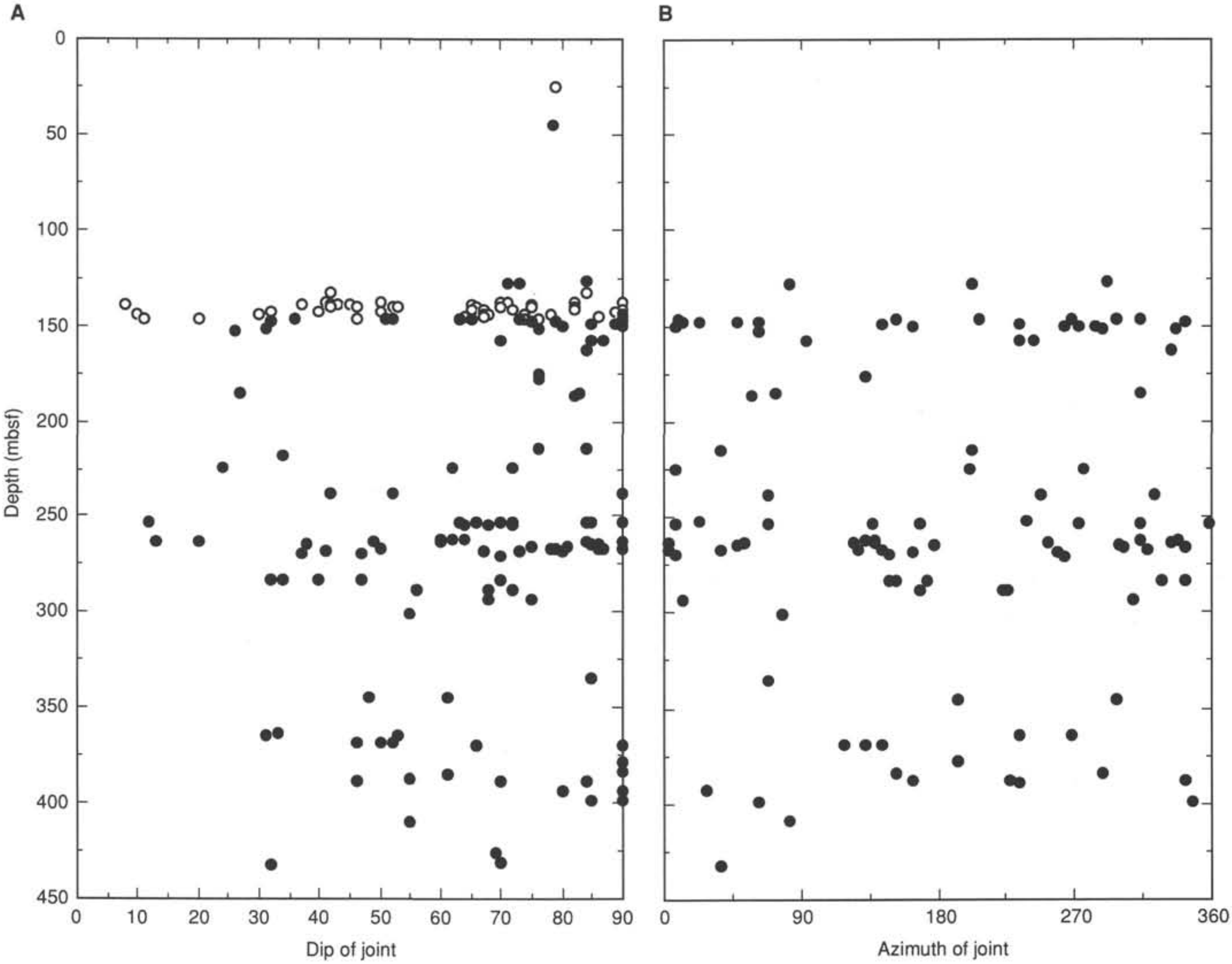

Figure 22. Variations of (**A**) joint dip (Holes 834A and 834B) and (**B**) joint azimuth (Hole 834B) with depth. Open circles = Hole 834A, and filled circles = Hole 834B. N = 135 for Figure 23A and 112 for Figure 23B. Note clustering of data points at depths of about 150 and 250 mbsf, corresponding to the igneous Unit 5 massive flow and the massive portion of igneous Unit 7.

comparable to the north-south or north-northwest–south-southeast strike of the small basin within which Site 834 is situated (see "Background and Objectives," this chapter).

BIOSTRATIGRAPHY

The biostratigraphic results for Holes 834A and 834B are summarized in Figure 23. Figure 24 is a paleontology summary sheet that illustrates the correlation of lithostratigraphic, biostratigraphic, and paleomagnetic data collected at Holes 834A and 834B.

Calcareous Nannofossils

Pleistocene

Sample 135-834A-1H-CC contains a sparse nannofossil flora including *Pseudoemiliania lacunosa* and *Gephyrocapsa oceanica* and is thus placed into Zone CN14.

The section between Samples 135-834A-2H-CC and -3H-CC is assigned to Subzone CN14a. These samples contain abundant floras including *Gephyrocapsa oceanica, G. caribbeanica, Emiliania ovata, Pseudoemiliania lacunosa,* and very abundant small gephyrocapsids. Samples 135-834A-4H-1, 120–124 cm, and 135-834B-1R-CC contain similar floras and are also assigned to CN14a. In addition, Sample 135-834B-1R-CC contains a reworked flora that includes common lower Pliocene taxa and a single specimen of Eocene age.

Pliocene

Two samples examined from Section 135-834A-4H-5 contain floras lacking *Gephyrocapsa oceanica* but containing *Gephyrocapsa caribbeanica, Calcidiscus macintyrei, Helicosphaera sellii,* and abundant small gephyrocapsids. On this basis these samples are placed in Subzone CN13b. Rare overgrown discoasters and sphenoliths in these samples are reworked.

Samples 135-834A-4H-6, 120–124 cm, and 135-834A-4H-CC contain floras including *Discoaster brouweri, D. triradiatus, D. blackstockae, Calcidiscus macintyrei,* and *Ceratolithus rugosus.* These samples are assigned to Subzone CN12d. A single overgrown five-rayed discoaster (*Discoaster pentaradiatus*?) was encountered during the examination of Sample 135-834A-4H-6, 120–124 cm. It is considered reworked.

Samples 135-834A-5H-CC through -7H-CC and Sample 135-834B-2R-CC yielded a flora that was assigned to Subzone CN12a.

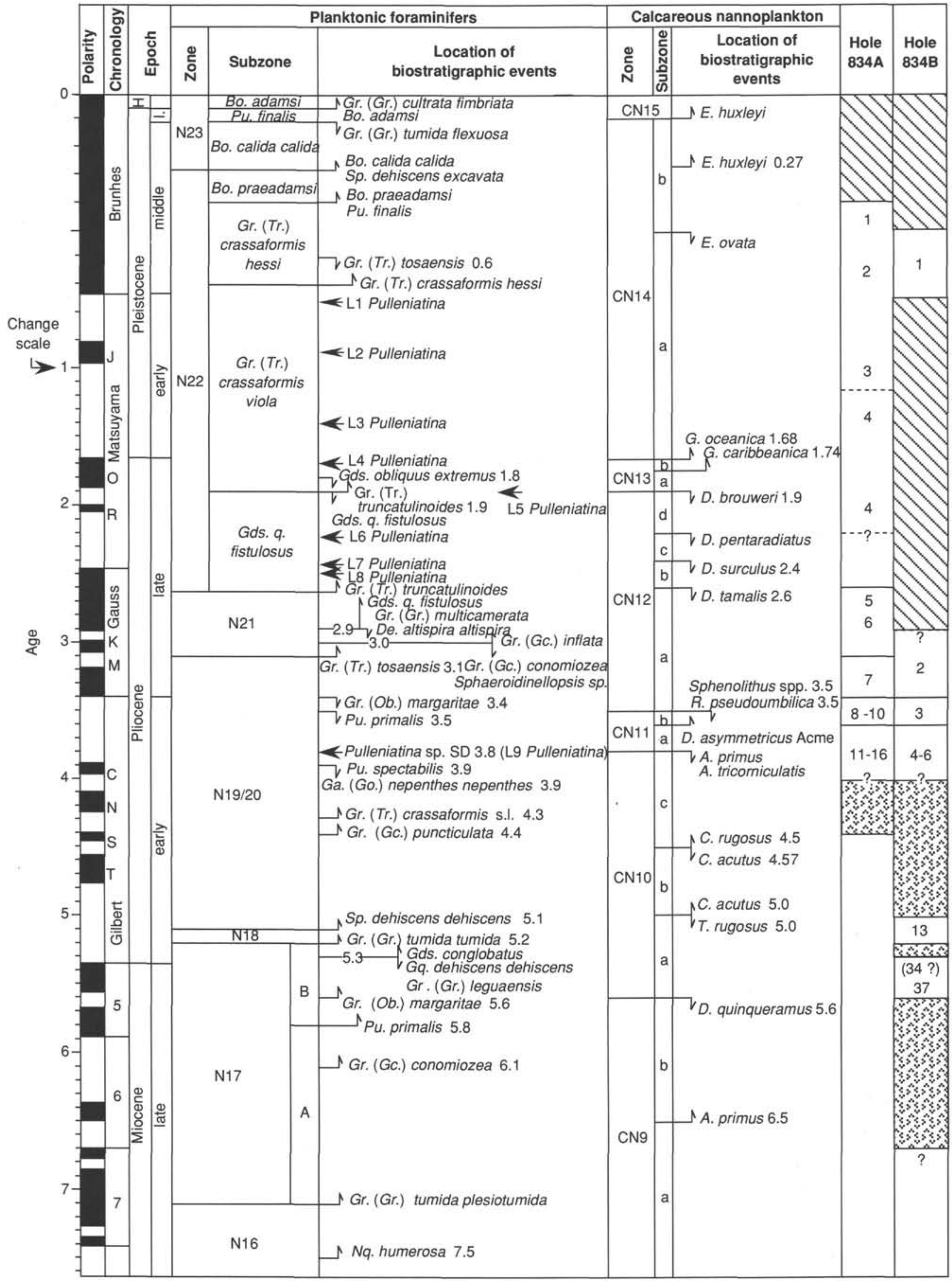

Figure 23. Biostratigraphic results, Site 834. B = barren.

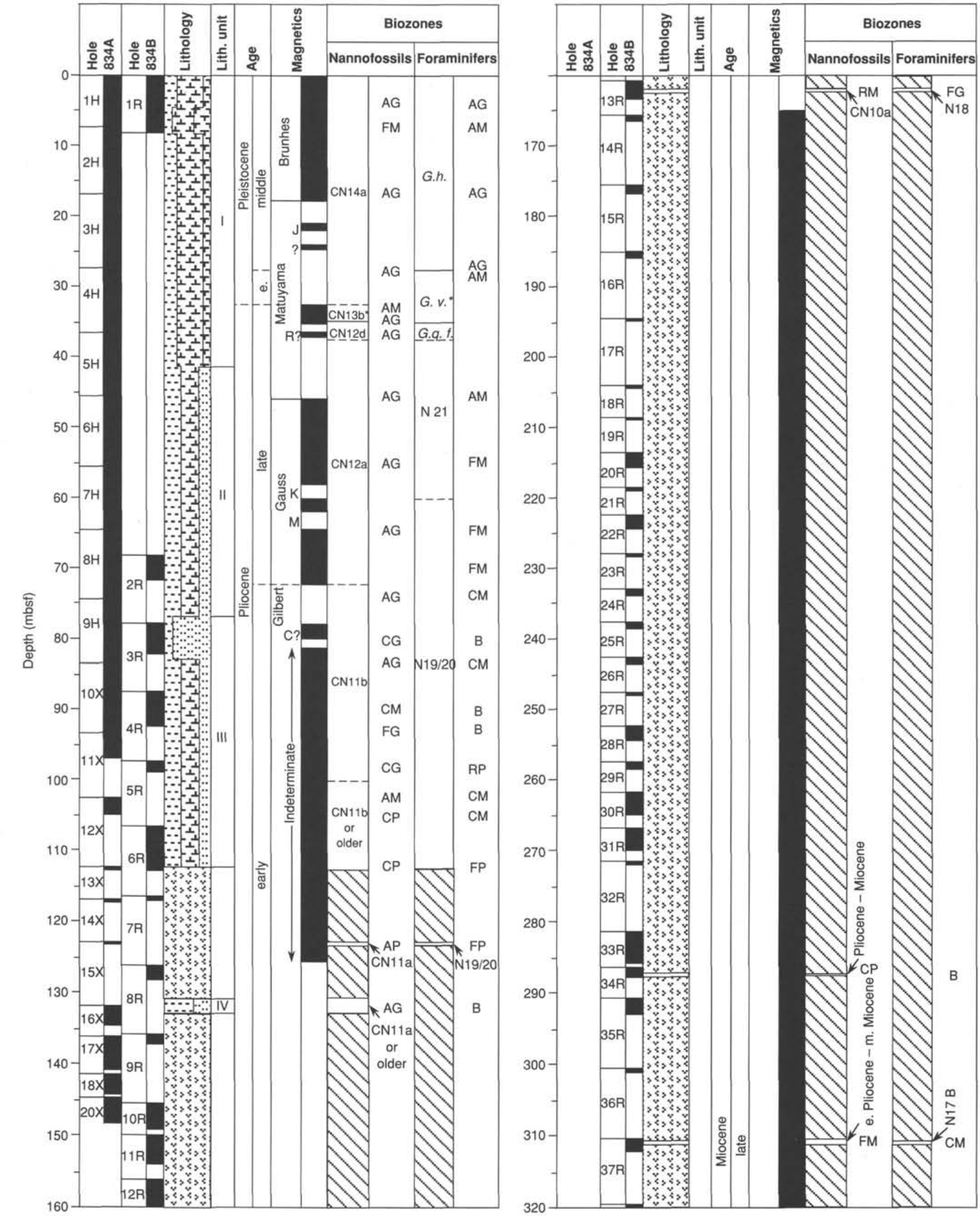

Figure 24. Paleontology summary chart, Site 834. See Figure 1 caption for an explanation of symbols and abbreviations used.

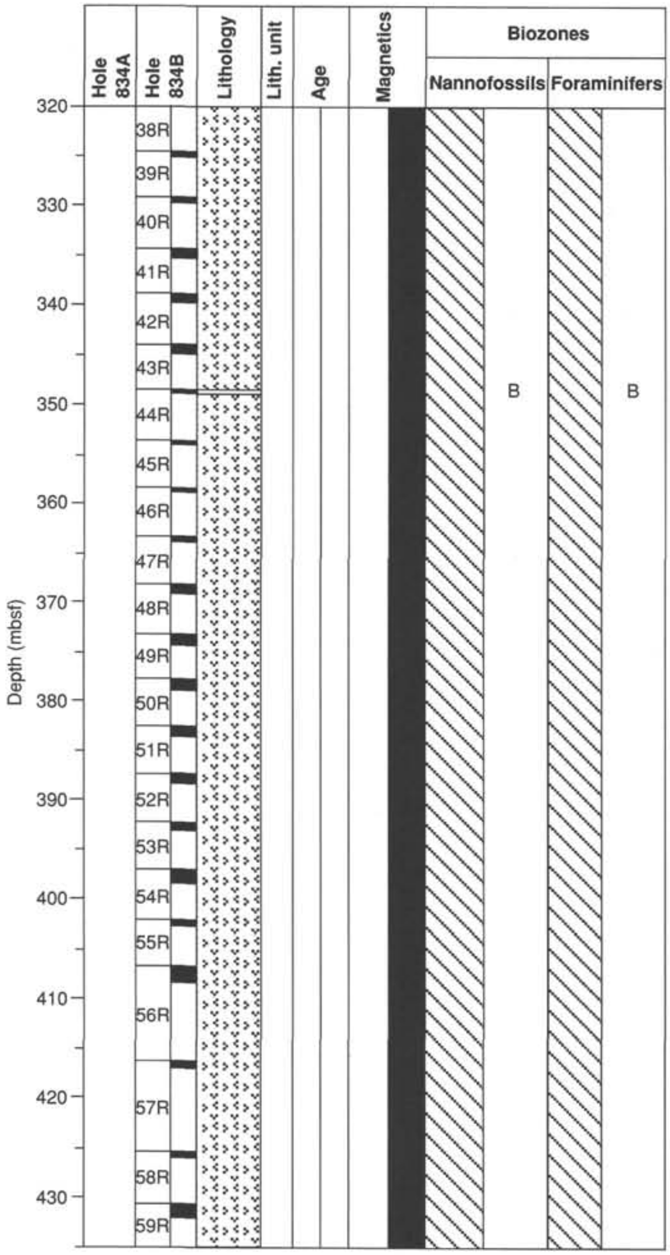

Figure 24 (continued).

This flora includes *Discoaster surculus, D. tamalis, D. pentaradiatus, D. decorus, D. variabilis,* and *D. asymmetricus.*

Sample 135-834A-8H-CC contains flora that include *Discoaster tamalis, D. asymmetricus, D. surculus, D. challengeri, D. variabilis,* and *Sphenolithus neoabies. Reticulofenestra pseudoumbilica* and *Sphenolithus abies* do not occur. The sample can thereby be assigned to either latest Subzone CN11b or earliest Subzone CN12a.

Samples 135-834A-9H-CC and -10H-CC and Samples 135-834B-3R-CC and -4R-CC contain floras that include *Reticulofenestra pseudoumbilica, Sphenolithus neoabies, S. abies,* and *Discoaster asymmetricus.* They are assigned to Subzone CN11b.

Samples 135-834A-11X-CC and -16X-1, 28–29 cm, contain floras including *Reticulofenestra pseudoumbilica* and *Sphenolithus abies* but lacking *Discoaster asymmetricus.* This indicates an age of CN11a or older.

Samples 135-834A-12X-CC and 135-834B-6R yield common but poorly preserved nannofossil floras which contain no diagnostic taxa.

A small section of sediment collected from Sample 135-834B-13R-CC yields a sparse flora including *Ceratolithus acutus, Amaurolithus amplificus,* and *Triquetrorhabdulus rugosus.* This sample is assigned to the boundary between Subzones CN10a and CN10b.

A sediment inclusion in basalt, Sample 135-834B-34R-2, Piece 6, yields a common but poorly preserved Pliocene/Miocene flora that includes only poorly preserved taxa that do not allow assignment to a specific zone. An early Miocene/late Oligocene reworked flora is also present in this sample. It includes *Dictyococcites bisectus*? and *Triquetrorhabdulus carinatus.*

Samples taken from a sandstone and mudstone interval of Core 135-834B-37R contain *Triquetrorhabdulus farnsworthii,* which indicates an age of early Pliocene to mid-Miocene. These samples also include reworked late Oligocene to mid-Miocene floras containing the robust taxa *Dictyococcites bisectus* and *Cyclicargolithus* spp.

Planktonic Foraminifers

The planktonic foraminiferal assemblages of Holes 834A and 834B are typically abundant and well preserved in the Pleistocene and late Pliocene. These assemblages, however, become less diverse and preservation deteriorates in the early Pliocene, ash-dominated sediments, becoming barren near the base of the sequence overlying volcanics. In both holes there is a substantial hiatus between the middle Pleistocene and late Pliocene.

Pleistocene

Samples 135-834A-1H-CC to -3H-CC contain an assemblage typified by *Globorotalia (Truncorotalia) truncatulinoides, Gr. (Gr.) cultrata neoflexuosa, Bolliella calida praecalida,* and *Pulleniatina obliquiloculata; Gr. (Tr.) tosaensis* was restricted to Sample 135-834A-3H-CC. The presence of *Globorotalia (Truncorotalia) truncatulinoides* without *Bolliella calida calida* indicates Zone N22, and the presence of *Gr. (Tr.) tosaensis* indicates the *Gr. (Tr.) crassaformis viola* Subzone within the early Pleistocene in terms of the scheme of Chaproniere (in press). Sample 135-834A-1H-CC contains many shallow-water-derived benthic foraminifers (*Calcarina spengleri, Sorites marginalis*) as well as *Halimeda;* abundant fragmented pteropods are also present.

Dentoglobigerina altispira altispira, Gr. (Gr.) cultrata limbata, Gr. (Gr.) multicamerata, Gr. (Tr.) tosaensis, Globigerinoides quadrilobatus fistulosus, Gds. obliquus extremus, and *Sphaeroidinellopsis seminulina* are present in Samples 135-834B-1R-CC and 135-834A-3H-CC, indicating reworking from either the basal part of Zone N22 or from Zone N21.

Pliocene

Samples 135-834A-4H-CC to -15X-CC appear to represent a continuous sequence from the late Pliocene *Gds. quadrilobatus fistulosus* Subzone (of Zone N22) to the early Pliocene Zone N19/20. Toward the bottom of this sequence, which contains few or no foraminifers, ash beds seem to become finer grained and thicker, resulting in poor biostratigraphic control based on foraminifers, although calcareous nannofossils may be present.

Samples 135-834A-4H-CC and -5H-CC contain *Gr. (Tr.) truncatulinoides, Gr. (Tr.) tosaensis, Gds. quadrilobatus fistulosus, Gds. obliquus extremus, Pulleniatina obliquiloculata,* and *P. praecursor;* the populations of *Pulleniatina* in Sample 135-834A-4H-CC are dominantly sinistrally coiled. This assemblage is typical of the lower part of Zone N22 and the *Gds. quadrilobatus fistulosus* Subzone, which is latest Pliocene. Sample 135-834A-6H-CC contains *Gr. (Tr.) tosaensis, Gr. (Tr.) crassaformis,* and

Gds. obliquus obliquus without *Gr. (Tr.) truncatulinoides* and *Gds. quadrilobatus fistulosus*; this is typical of Zone N21. Samples 135-834A-7H-CC to -9H-CC and Samples 135-834A-11X-CC to -15X-CC lack *Gr. (Tr.) tosaensis* and typically contain *Dentoglobigerina altispira altispira, Gds. obliquus, Sphaeroidinellopsis paenedehiscens,* and *S. seminulina. Gr. (Obandyella) margaritae, Globigerina (Globoturborotalita) nepenthes,* and *Pulleniatina primalis* are present in many of the lower samples; this assemblage is typical of Zone N19/20, possibly the lower part. Sample 135-834A-8H-CC contains *Gr. (Tr.) crassaformis ronda,* which indicates a level within the upper part of this zonal interval. Sample 135-834A-10X-CC was barren of foraminifers, as were all samples below 135-834A-15X-CC.

The latest Pliocene *Gds. quadrilobatus fistulosus* Subzone was not sampled at Hole 834B. Three of the six samples over the interval covered by Cores 135-834B-2R to -12R were from ash beds and were barren of foraminifers, although they contained rare calcareous nannofossils. Those samples with planktonic foraminifers contained the same assemblages as those from Hole 834A and were typical of Zone N19/20. Sample 135-834B-2R-CC contained *Gr. (Tr.) crassaformis crassaformis,* indicating a level within the upper part of Zone N19/20. The lowermost of these samples (135-834A-5R-CC) was from an ash horizon and contained a nondiagnostic fauna of small specimens of *Globigerinita glutinata* and *Turborotalita humilis*. Sample 135-834B-13R-2, 104–106 cm, from an ash unit separating basalt flows, contains a low-diversity fauna with many specimens of *Sphaeroidinellopsis paenedehiscens* together with *Gr. (Gr.) tumida tumida, Gr. (Gr.) tumida plesiotumida, Globoquadrina dehiscens, Globigerina (Globoturborotalita) nepenthes,* and *Pulleniatina primalis;* this fauna and the absence of *Sphaeroidinella dehiscens* indicates Zone N18.

Miocene

Though several cores below Core 135-834B-13R contain sedimentary horizons, most are barren of foraminifers. However, Samples 135-834B-37R-CC and -43R-CC were found to contain foraminifers. Sample 135-834B-37R-CC contained a low-diversity, planktonic-dominated assemblage that included *Globigerina (Globoturborotalita) nepenthes, Globigerinoides obliquus extremus, Gds. obliquus extremus, Sphaeroidinellinopsis seminulina, Globorotalia (Gr.) tumida plesiotumida,* and *Gr. (Obandyella) margaritae,* without *Gr. (Gr.) tumida tumida* and *Pulleniatina primalis*. This fauna is diagnostic of latest Miocene Zone N17B. Sample 135-834B-43R-CC lacked planktonic forms and contained only the benthic form *Bathysiphon*.

SEDIMENT ACCUMULATION RATES

The calcareous planktonic assemblages through the Pleistocene to the late Pliocene Zone N21 are excellent; thereafter, however, they deteriorate within the tuffaceous horizons. Many samples from this interval are barren of foraminifers, but calcareous nannofossil floras are generally of sufficient quality for good age determination. Within the basalt section, two horizons (in Cores 135-834B-13R and -37R) have good planktonic foraminifer faunas that provide excellent time constraints for the dating of the volcanic pile.

Figure 25 is a graphic presentation of depth and age data from Site 834. The ages are based on the bioevents presented in Table 4. In addition, paleomagnetic data have also been superimposed on the biostratigraphic data. Both sources of data overlap for most of the plot, differing only at the bottom part of Hole 834A, where data from both sources are poor.

The very steep part of the graphic display is the earliest depositional period in which the basalts and associated ash were accumulated at rates around 110 mm/k.y. Normal marine sedimentation began at the end of basaltic activity at about 3.5 Ma. Sedimentation rates have remained nearly constant since this time at around 20 mm/k.y.

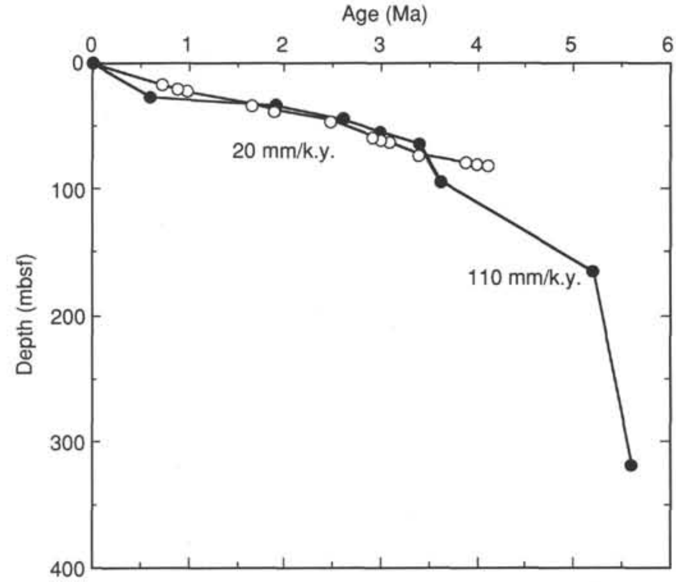

Figure 25. Graphic representation of age vs. depth data illustrating the sedimentation rates at Site 834 by means of the bioevents and depths given in Table 4. A plot of the paleomagnetic data is also included for comparison. Open circles = biostratigraphic data, and filled circles = paleomagnetic data.

Table 4. Depths and ages of bioevents used to plot sediment accumulation rates for Site 834.

Depth (mbsf)	Age (Ma)	Events
26.0	0.6	LAD *G. tosaensis*
34.1	1.9	LAD *G. q. fistulosus*
45.6	2.6	LAD *D. tamalis*
55.1	[a]3.0	FAD *G. q. fistulosus*
64.6	3.4	LAD *G. margaritae*
93.2	3.6	LAD *R. pseudoumbilica*
165.7	5.2	FAD *G. tumida tumida*
319.0	5.6	FAD *G. margaritae*

[a]Ages after Dowsett (1989).

PALEOMAGNETISM

Remanent Magnetism

Most remanent magnetization measurements were made with the pass-through cryogenic magnetometer on archive core halves. Virtually all measurements were made at a spacing of 5 cm. Magnetic cleaning of sediment cores was typically done with alternating field (AF) demagnetization at 5, 10, and 15 mT, whereas 2, 5, 10, and 15 mT AF were used for most basalt cores. A small number of discrete samples were analyzed using the Molspin Minispin spinner magnetometer to investigate magnetic properties in greater detail.

Sediments in advanced piston corer (APC) Cores 135-834A-1H through -9H were measured mainly to determine magnetic polarity stratigraphy. Other cores in Hole 834A were not measured because they suffered moderate to heavy drilling disturbance and were unlikely to produce reliable results in the pass-through magnetometer. Oriented segments of rotary core barrel (RCB) basalt cores from Hole 834B were also measured with the pass-through magnetometer to determine magnetic polarity.

Magnetic Properties

The sediments at Site 834 are strongly magnetic, with natural remanent magnetization (NRM) intensities typically between 1 to 1000 mA. Such strong magnetizations probably result from volcanic material contained in the sediments. Indeed, their color is often dark, reddish brown as a result of abundant iron, mainly contained in ferric oxyhydroxides (see "Lithostratigraphy" section, this chapter). Isothermal remanent magnetization (IRM) acquisition curves (Fig. 26) display rapid saturation with increasing field strength, indicating that the magnetic grains within these sediments behave like magnetite.

Another factor in producing the strong magnetizations is a pervasive upward overprint that gives the sediments NRM inclinations near –90° and completely masks their polarities. The vertical direction of the overprint implies that it results from exposure of the sediments to strong magnetic fields (an IRM) in the core barrel or drill string. The sediments acquired this IRM because some of their magnetic grains have low coercivities, as shown by typically low mean destructive field (MDF) values, 3 mT or less (Fig. 27). Because of this, the sediments easily acquire an overprint. However, because it resides in low coercivity grains, this overprint is readily removed with AF demagnetization (Fig. 28), leaving a more stable, characteristic remanence that holds geologic information.

Typical basalt NRM magnetization intensities ranged from about 1 to 20 A/m. These rocks also displayed a drill-string IRM, but to a lesser extent than the sediments from Hole 834A. The amount of overprint was variable. Some samples had low MDFs (5 mT or less) and low coercivity magnetization components, so they acquired a greater drill-string IRM. Other samples had MDFs greater than 15 mT, so they were less affected (Fig. 29). As with the Hole 834A sediments, AF demagnetization of individual specimens easily removed any drill-string overprint to reveal a stable characteristic remanent magnetization (Fig. 30). However, because AF demagnetization of the core archive halves during Leg 135 was limited to 15 mT, characteristic magnetizations were not always isolated, so the measurements made with the pass-through magnetometer must be regarded as reconnaissance results only.

Magnetic Polarity Stratigraphy

Despite the presence of a strong drill-string IRM in the sediment cores, AF demagnetization revealed a clear magnetic stratigraphy in Cores 135-834A-1H through -8H (Fig. 31). Magnetic reversals were recognized by a change in the sign of the magnetic inclination coincident with a 180° shift in declination. A slight asymmetry in inclinations, with normal polarity inclinations being steeper than reversed polarity values (Fig. 31), implies that not all of the drill-string IRM was removed by AF demagnetization at 15 mT.

Cores 135-834A-1H and -2H show entirely normal polarity and undoubtedly record the Brunhes Chron. In the upper and middle part of Core 135-834A-3H, reversed polarity evidently indicates the end of the Matuyama Chron. Just below the Matuyama/Brunhes boundary, a short normal polarity interval, probably the Jaramillo Subchron, was found. In Cores 135-834A-6H through -8H another long normal polarity period is punctuated by two reversed polarity subchrons (Fig. 31). The relative lengths of these polarity intervals are good matches to published models of the normal polarity Gauss Chron, which contains the reversed polarity Kaena and Mammoth subchrons (Harland et al., 1982; Berggren et al., 1985). Core 135-834A-9H did not display an obvious magnetic polarity stratigraphy. Although it is clearly

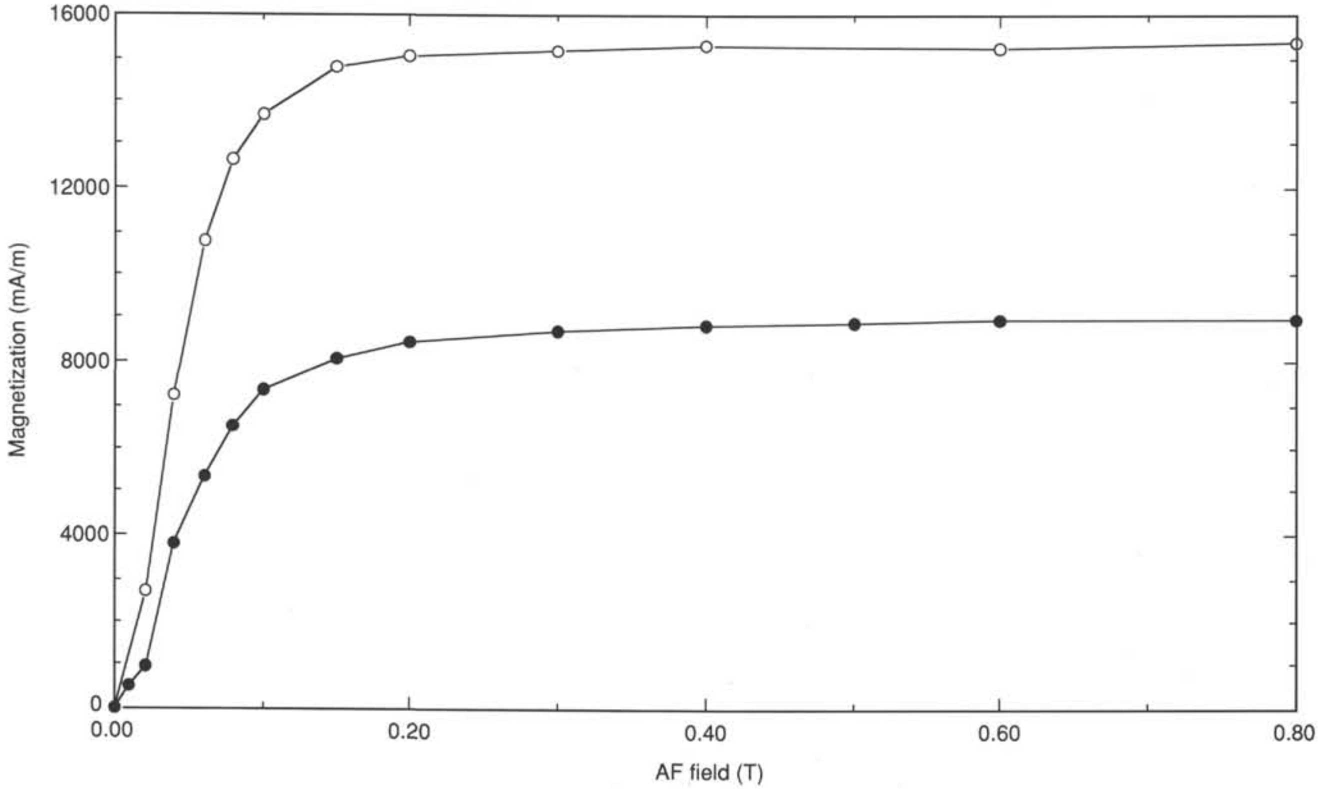

Figure 26. Typical isothermal remanent magnetization (IRM) acquisition curves for Hole 834A sediment samples. Saturation at low applied fields indicates magnetite-type behavior. Filled circle = Sample 135-834A-3H-3, 100–102 cm, and open circle = Sample 135-834A-7H-2, 40–42 cm.

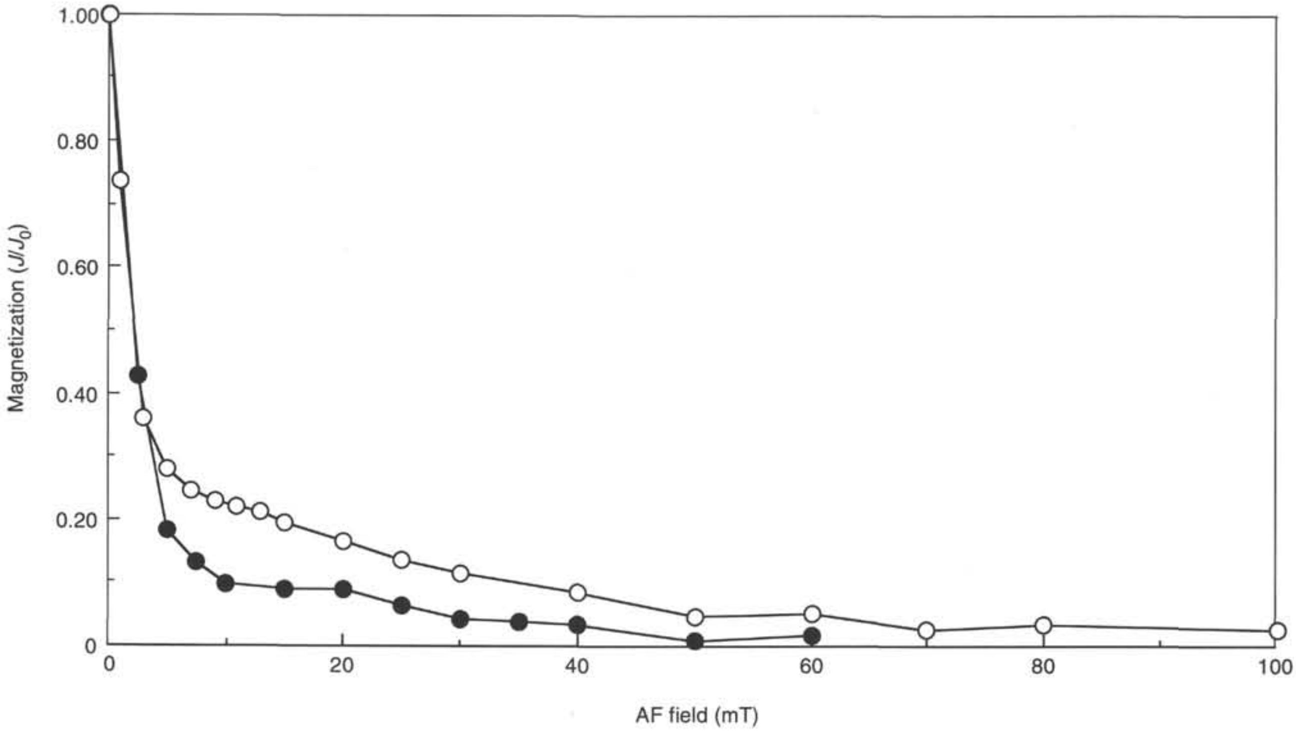

Figure 27. Reduction of magnetization intensity during alternating field (AF) demagnetization of Hole 834A sediment samples. The samples display low coercivities and an IRM acquired from the drill string. This IRM is removed by low AF fields, generally < 3 mT. Filled circle = Sample 135-834A-3H-3, 100–102 cm, with J_0 = 34.8 mA/m; open circle = Sample 135-834A-7H-2, 40–42 cm, with J_0 = 68.1 mA/m.

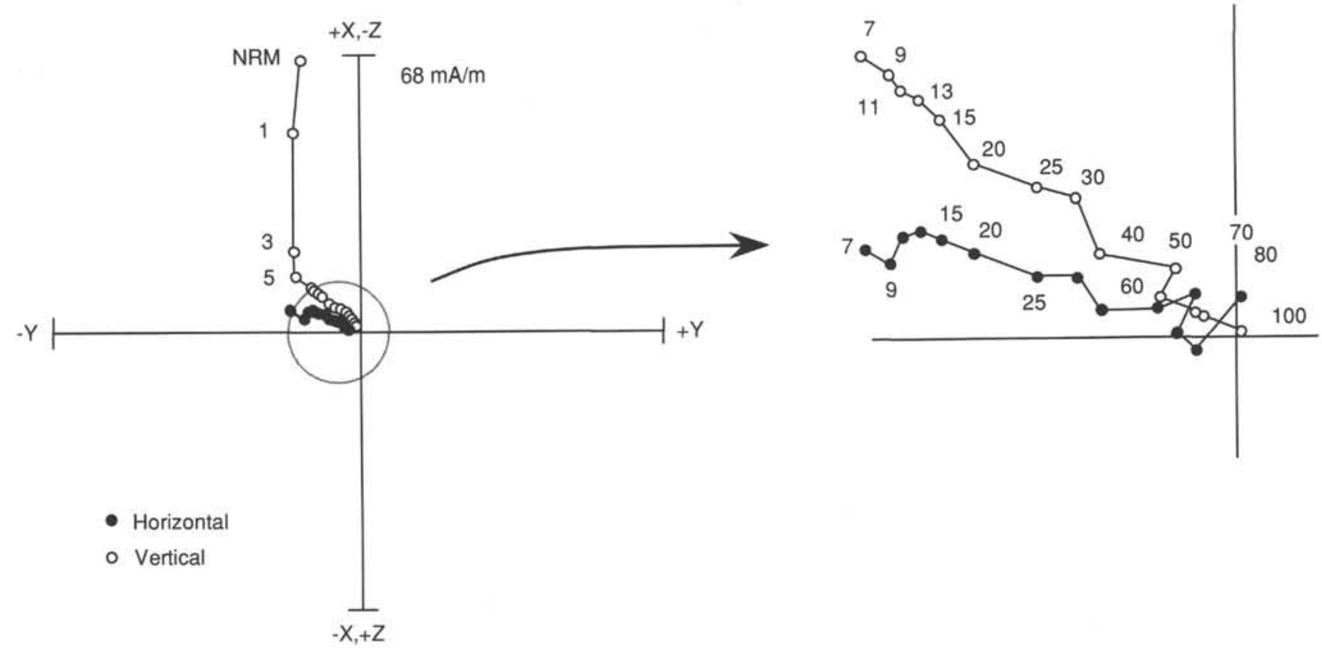

Figure 28. Orthogonal vector plot illustrating the typical behavior of the magnetization directions of a sediment sample from Hole 834A during AF demagnetization. The numbers in the right-hand figure are the AF field strengths in mT. Sample 135-834A-7H-2, 40–42 cm.

reversely polarized at its top, inclinations from most of the core oscillate around zero (Fig. 31). This may be a result of an inability to remove the drill-string IRM with the maximum 15-mT AF demagnetization allowed on archive core halves. A tentative identification of polarities was made by assuming that those parts of the core with inclinations around zero are reversed in polarity whereas those parts with large negative inclinations are normal polarity. Two possible normal polarity intervals were found in this way, and a correlation to the Cochiti and Nunivak subchrons of the Gilbert Chron is suggested. However, these identifications do

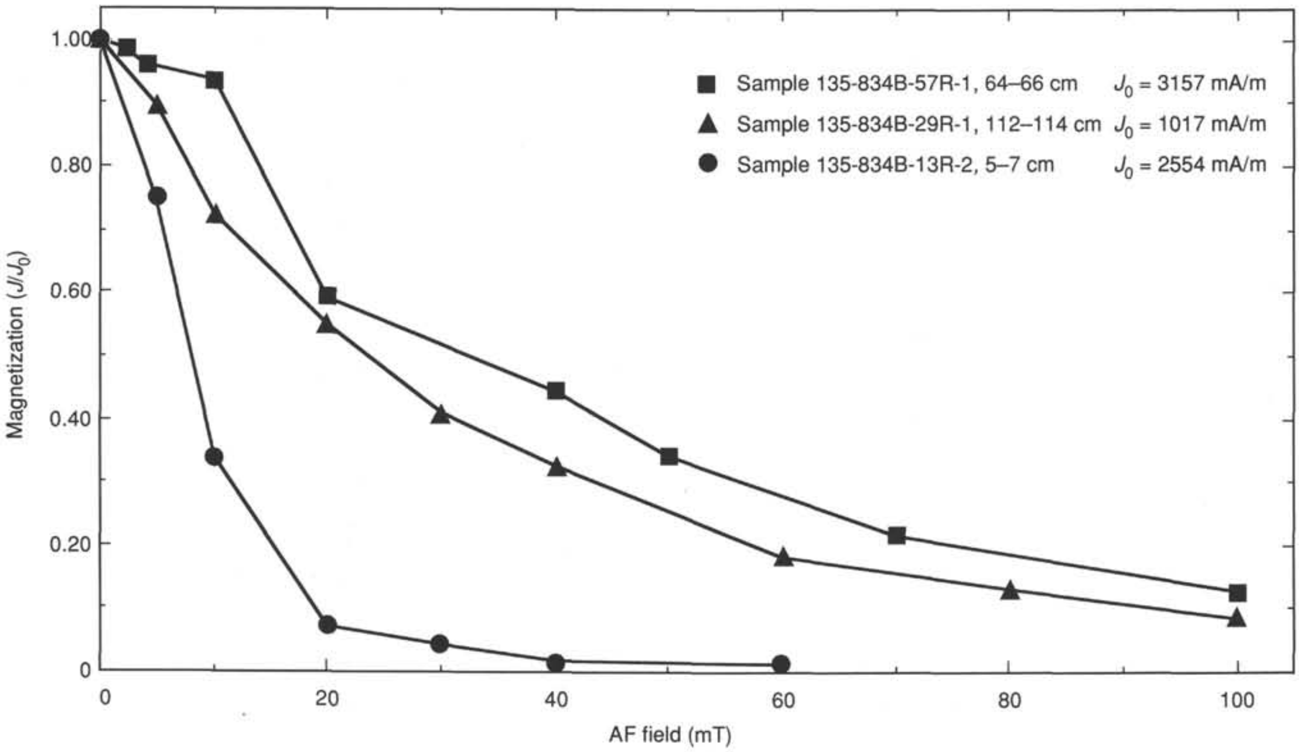

Figure 29. Reduction of magnetization intensity during AF demagnetization of Hole 834B basalt samples. The range in coercivities is wide.

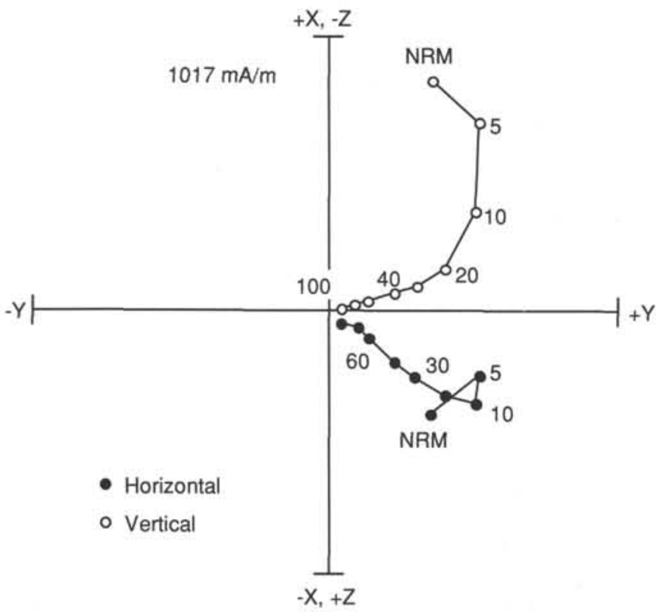

Figure 30. Orthogonal vector plot illustrating the typical behavior of Hole 834A basalt sample magnetization directions during AF demagnetization. The numbers indicate AF field strengths in mT. Sample 135-834B-29R-1, 112–114 cm.

not match the biostratigraphic ages assigned to Core 135-834A-9H (see "Biostratigraphy" section, this chapter) and so they are probably erroneous.

An interesting feature of the magnetic stratigraphy of Core 135-834A-3H is a short normal polarity interval about 2 m below the Jaramillo Subchron. This feature is not included in any geomagnetic polarity reversal time scale, but its stratigraphic location is consistent with the Cobb Mountain Event, which has been measured on land as well as in DSDP and ODP cores at these localities (Mankinen et al., 1978; Clement and Robinson, 1987; Bleil, 1989; Clement et al., 1989). Though the paleomagnetic directions are generally consistent, a few zones show anomalous directions. Some can be related to turbidites or lithologic changes (Fig. 31), but many cannot. Others correlate to core or section boundaries and are probably disturbances caused by core handling and cutting. A few of these variations may represent magnetic field excursions.

Using the magnetic stratigraphy (Fig. 31) and the geomagnetic polarity reversal time scale of Berggren et al. (1985), an age vs. depth curve was constructed for the upper 84 mbsf of Hole 834A (Fig. 32 and Table 5). This curve implies an age of 3.4 Ma for a depth of 71.9 mbsf at the base of the Gauss Chron. Furthermore, it indicates a relatively constant overall sedimentation rate between 16 to 28 mm/k.y. for the upper 80 mbsf of Hole 834A. These rates compare well with those implied by biostratigraphy (see "Sediment Accumulation Rates" section, this chapter).

Magnetic polarity was also determined for the basalt section of Hole 834B using oriented basalt pieces, 7–8 cm in length or longer, from core archive halves. A predominantly reversed polarity was found in Cores 135-834B-8R through -13R (126.3–162.4 mbsf; Fig. 33 and Table 6). The rest of those cores with samples that could be measured showed a predominantly normal polarity. Sporadic reversed samples punctuate the normal polarity cores and vice versa (Fig. 33), probably a result mainly of overturned pillows or basalt rubble whose orientations changed after cooling below the Curie temperature. Only in one instance was an interval of opposing polarity recorded over an interval of as much as 1 m. That occurs in Sections 135-834B-10R-2, 46 cm, through 135-834B-10R-2, 145 cm (Table 6). It is not clear whether this truly represents a normal polarity period within the reversed polarity section, so it is flagged with a question mark in Figure 33.

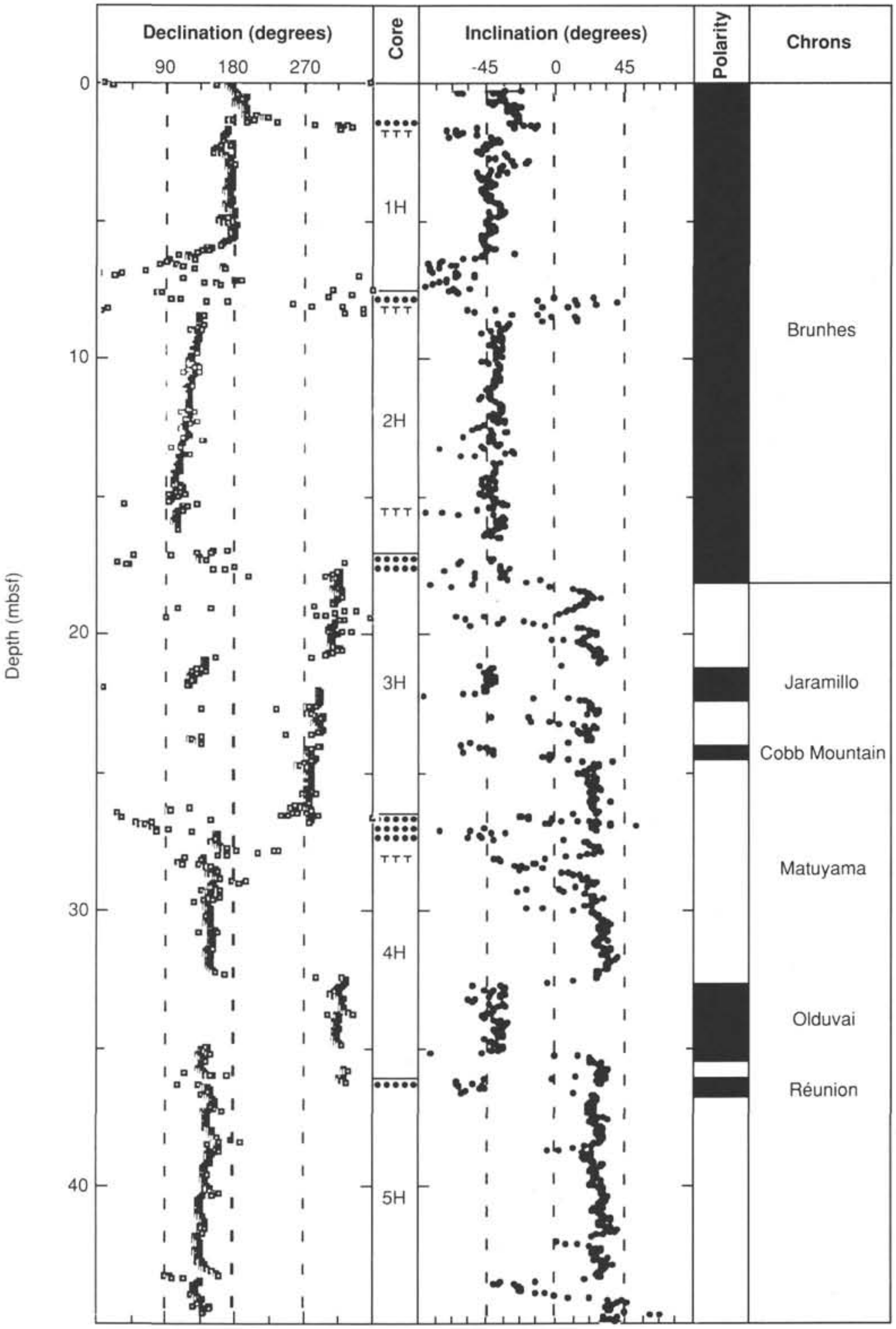

Figure 31. Magnetic polarity stratigraphy of Hole 834A sediments. The declination and inclination of magnetization was measured with the pass-through cryogenic magnetometer and AF demagnetized at 15 mT. The middle column indicates the core boundaries, disturbed core (dots), and turbidites ("T" symbols). The far-right column illustrates the magnetic polarities that have been determined, with their magnetic chron and subchron names (from Harland et al., 1982; Berggren et al., 1985). The black and white bars indicate normal and reversed polarity, respectively. Dark gray and light gray sections indicate intervals of uncertain polarity thought to be normal and reversed, respectively. Hachures denote sections of indeterminate polarity.

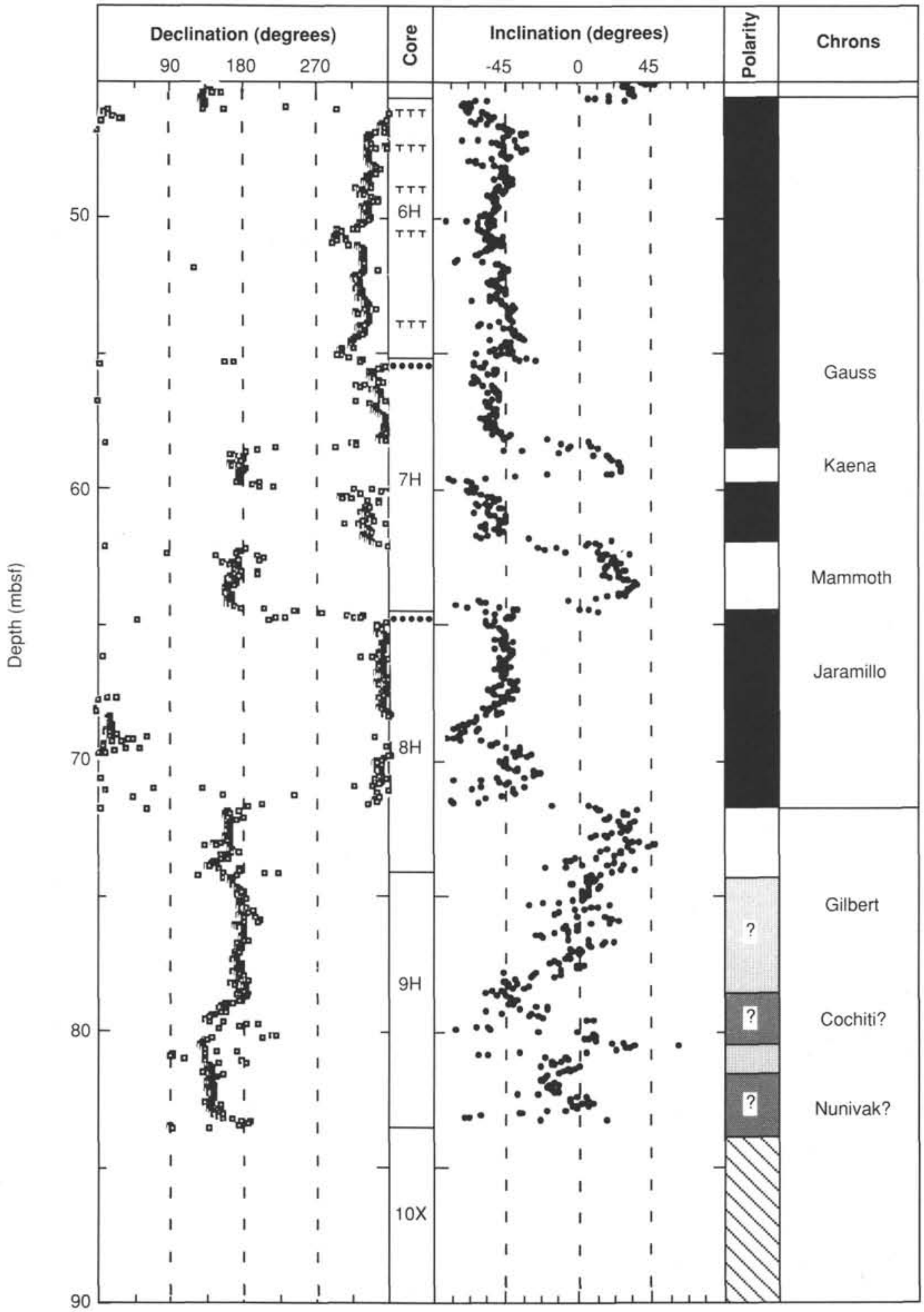

Figure 31 (continued).

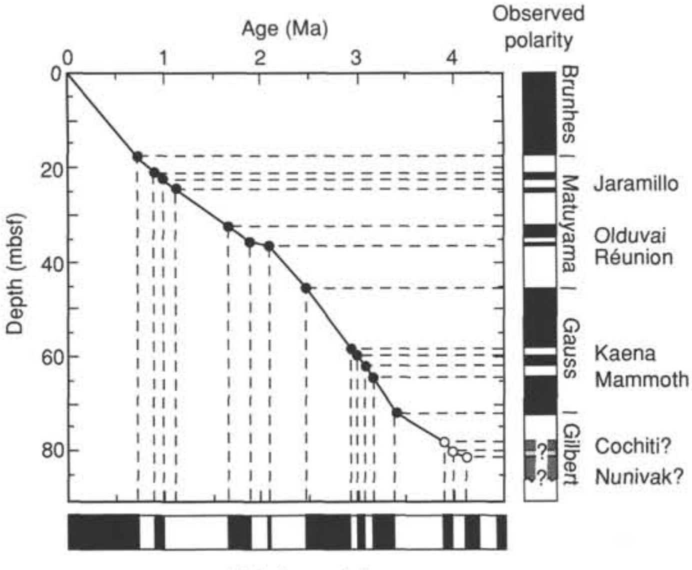

Figure 32. Age vs. depth, Hole 834A, derived from magnetic polarity stratigraphy. Filled circles indicate well-determined polarity transitions, whereas open circles denote poorly constrained transitions. Ages are taken from the magnetic polarity reversal time scale of Berggren et al. (1985), supplemented with subchron dates from Harland et al. (1982) and Clement and Robinson (1987).

Table 5. Magnetic polarity zones, Hole 834A.

Depth (mbsf)	Age (k.y.)	Polarity	Chron/subchron
0.0	0.00		
		N	BRUNHES
18.2	0.73		
		R	MATUYAMA
21.0	0.91		
		N	Jaramillo
22.5	0.98		
		R	
24.1	1.12		
		N	Cobb Mountain
24.5			
		R	
32.6	1.66		
		N	Olduvai
35.3	1.88		
		R	
36.1			
	2.08	N	Réunion
36.6			
		R	
45.5	2.47		
		N	GAUSS
58.2	2.92		
		R	Kaena
59.6	2.99		
		N	
62.0	3.08		
		R	Mammoth
64.2	3.18		
		N	
71.9	3.40		
		R	GILBERT
78.0	3.88		
		N	Cochiti?
80.3	3.97		
		R	
81.2	4.10		
		N	Nunivak?

Magnetic polarity reversal time scale of Berggren et al. (1985), with Réunion Subchron from Harland et al. (1982) and Cobb Mountain Event from Clement and Robinson (1987). Chron names in capital letters, and subchrons in lowercase letters.

Magnetic Susceptibility and Q-ratio

Volume magnetic susceptibility was measured on a routine basis on whole (i.e., unsplit) core sections of both sediments and basalts from both holes at Site 834, whenever the sections appeared to be full.

Sediments

Magnetic susceptibility values in Hole 834A sediments range from about 10×10^{-6} to 1000×10^{-6} cgs and display both long- and short-wavelength variations. The broad-scale variation in susceptibility in Hole 834A sediments (Fig. 34) consists of order of magnitude oscillations over ranges of 5–20 m in depth. Though the cause of these broad peaks is not known, it is likely that they reflect variations in the input of volcanic material, which tends to be strongly magnetic, into the nannofossil oozes, which are typically only weakly magnetic. Three peaks occur within sedimentary Unit I and two more peaks are within Unit II (Fig. 34). The largest of these is that at the bottom of Unit II, where susceptibility values are typically 300×10^{-6} cgs around 70 mbsf. Because these variations do not quite agree with the lithologic units, alternative magnetic units are proposed (Fig. 34). Magnetic Unit I contains the three low-amplitude susceptibility cycles between 0 and 47 mbsf; each oscillation accorded the status of a magnetic subunit. Magnetic Unit II contains the higher susceptibility section of core between 47 and 78 mbsf. Once again, this unit is divided into three subunits. Subunits IIA and IIC correspond to broad susceptibility peaks and Subunit IIB denotes the lower susceptibility region in between (Fig. 34). The deepest sedimentary magnetic unit is Unit III, which is similar to lithologic Unit III. It contains variable susceptibility values that are somewhat lower than those observed at the bottom of Magnetic Unit II. Finally, there also appears to be a difference in susceptibility within the basalt sill section at the bottom of Hole 834A (Fig. 34). Igneous Unit 5 (136.3–149.5 mbsf) displays susceptibilities nearly an order of magnitude higher than those of Units 1–4 above it (106.2–136.3 mbsf), so the basalt section is divided into two magnetic units (Fig. 34).

The most obvious part of the short-wavelength variation appears to be caused by lithologic variations, in particular the occurrence of ash layers. Within the upper two lithologic units, which consist mainly of nannofossil ooze (see "Lithostratigraphy," this chapter), typical susceptibility values are 50×10^{-6} to 100×10^{-6} cgs, with peaks up to 500×10^{-6} cgs. Many, but not all, of these peaks correlate with ash layers. A more detailed analysis is required to ascertain the origin of the peaks in these upper units that are not obviously related to ash layers. In the lowest sedimentary unit, which consists mainly of ash with interspersed nannofossil ooze (see "Lithostratigraphy" section, this chapter), susceptibility values are high, with most values between 100×10^{-6} and 300×10^{-6} cgs in Core 135-834A-8H and the upper part of Core 135-834A-9H. However, in this unit, susceptibility peaks are not well correlated with the observed ash layers. This may be because the unit consists mainly of ash and the susceptibility varies with the iron mineral content of the ash, which may not be obvious to the naked eye.

In addition to the obvious susceptibility spikes caused by ash layers, there are also persistent small-amplitude, short-wavelength cycles of typically 50×10^{-6} cgs amplitude and 0.5-m

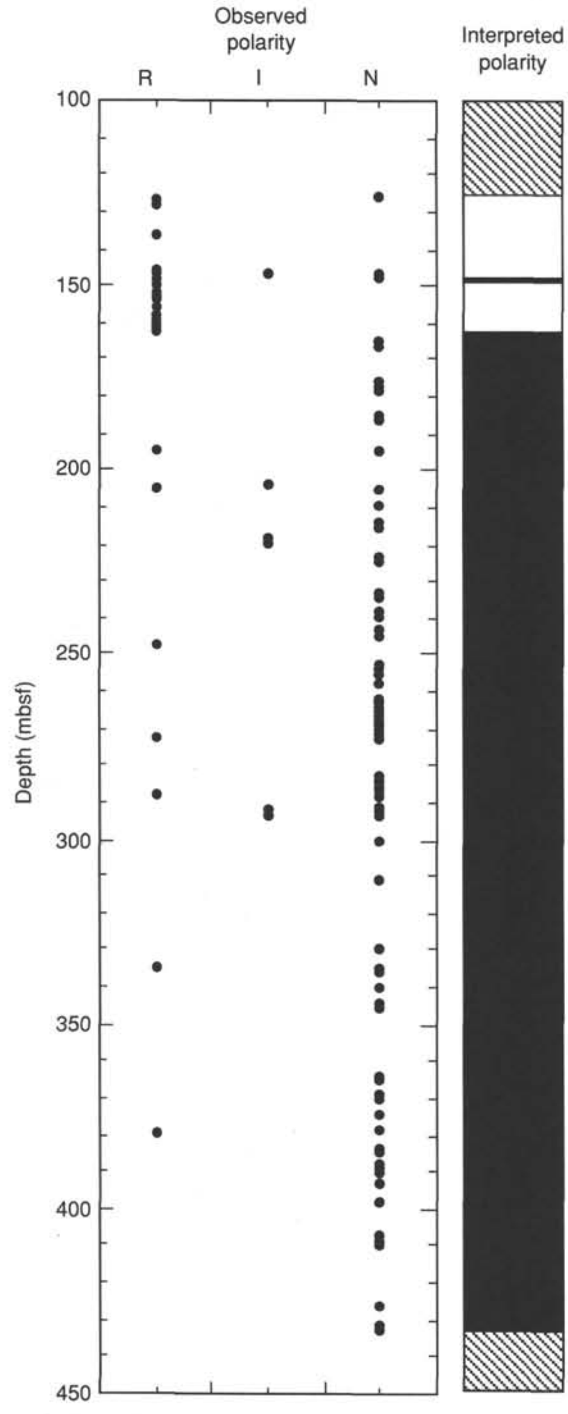

Figure 33. Magnetic polarities of Hole 834B basalt samples vs. depth. Filled circles indicate individual polarity determinations (as listed in Table 6). R = reversed, I = indeterminate, and N = normal.

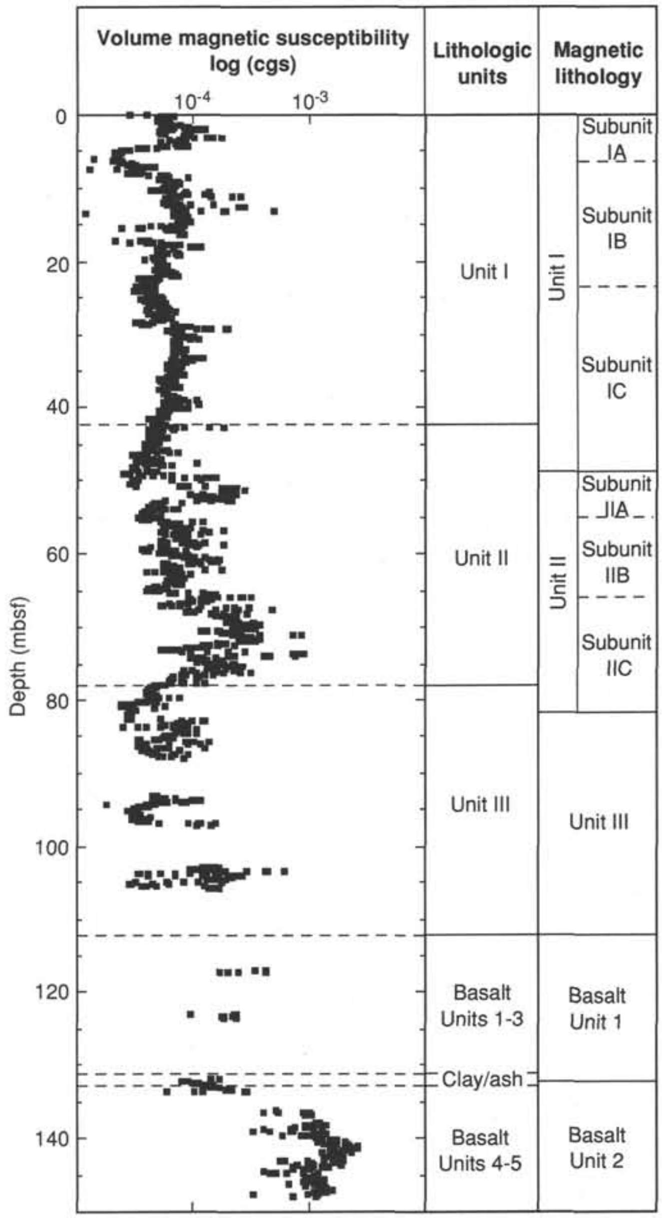

Figure 34. Volume magnetic susceptibility vs. depth, Hole 834A. Susceptibility is plotted on a logarithmic scale to highlight small variations. The sedimentary units illustrated in the right-hand column have been interpreted from susceptibility variations.

wavelength. These variations appear superficially similar to those caused by Milankovitch climate variations in sediments in other oceans (e.g., Wollin et al., 1971). A similar sort of variation was observed in the magnetization intensities measured by the pass-through cryogenic magnetometer, though that record is somewhat obscured by core and section end effects and low-pass filtering caused by the wide sensing region of the magnetometer. These small susceptibility variations are best seen in the upper two lithologic units where there is less interference from ash layers.

To investigate these cyclic variations, a parameter less dependent on material variations than susceptibility and magnetization intensity was sought. Consequently, the modified Q-ratio (Q15 = intensity after 15-mT AF demagnetization/susceptibility) was calculated (Fig. 35 and Table 7). The susceptibility and intensity measurements were made at different spacings (3 and 5 cm, respectively), so it was necessary to interpolate to match the two sets of data. Furthermore, because of the wide sensing region of the pass-through magnetometer, the magnetization intensity readings average a parcel of core 10 cm on either side of the measurement depth, so both data sets were filtered through a 10-cm window.

Counting the number of Q15 cycles in the top 3.4 Ma of Hole 834A (i.e., from the beginning of the Gauss Chron) that contain at least two data points (20 cm width) at maximum and in the

Table 6. Magnetic polarities of Hole 834B basalts.

Core, section, interval (cm)	Depth (mbsf)	N/R
135-834B-		
8R-1,20–30	126.30	N
8R-1,45–55	126.55	R
8R-1,80–86	126.93	R
8R-1,90–106	127.06	R
8R-1,115–121	127.25	R
8R-2,0–45	127.60	R
8R-2,45–87	128.05	R
9R-1,118–28	135.98	R
9R-1,33–57	136.13	R
9R-1,68–78	136.48	R
9R-1,90–100	136.70	R
10R-1,0–70	145.40	R
10R-1,84–98	146.24	R
10R-1,109–117	146.49	?N
10R-1,122–134	146.62	?
10R-2,1–11	146.91	R
10R-2,13–33	147.03	?
10R-2,46–54	147.36	N
10R-2,55–77	147.45	N
10R-2,79–97	147.69	N
10R-2,96–116	147.86	N
10R-2,118–130	148.08	N
10R-2,131–145	148.21	N
10R-3,0–44	148.40	R
10R-3,53–87	148.93	R
10R-3,89–103	149.29	R
10R-3,120–136	149.60	R
10R-3,139–149	149.79	R
11R-1,12–128	150.12	R
11R-2,0–60	151.50	R
11R-2,72–150	152.22	R
11R-3,0–74	153.00	R
11R-3,76–92	153.76	R
11R-3,95–123	153.95	R
12R-1,0–75	156.00	R
12R-2,0–120	156.75	R
12R-3,0–45	157.95	R
12R-3,45–125	158.40	R
12R-4,0–57	159.20	R
12R-4,60–150	159.80	R
12R-5,0–60	160.70	R
13R-1,14–140	161.14	R
13R-2,0–60	162.40	R
14R-1,15–25	165.85	N
14R-1,35–42	166.05	N
15R-1,26–34	175.66	N
15R-1,69–86	176.09	N
15R-1,118–126	176.58	N
15R-1,134–140	176.74	N
15R-2,35–43	177.25	N
15R-2,47–54	177.37	N
15R-2,66–72	177.56	N
16R-1,2–17	185.02	N
16R-2,1–14	186.51	N
17R-1,0–15	194.38	R
17R-1,17–24	194.47	R
17R-1,26–34	194.56	N
18R-1,13–20	204.13	?
18R-1,47–54	204.47	N
18R-1,56–64	204.56	R
19R-1,15–24	208.95	N
19R-1,26–40	209.06	N
20R-1,90–112	214.50	N
20R-2,1–9	215.11	N
20R-2,56–62	215.66	N
21R-1,40–47	218.80	?
21R-1,56–65	218.96	?

Table 6 (continued).

Core, section, interval (cm)	Depth (mbsf)	N/R
135-834B- (cont.)		
22R-1,0–66	223.20	N
22R-1,67–78	223.87	N
22R-1,87–102	224.07	N
22R-1,124–136	224.44	N
22R-1,138–150	224.58	N
22R-2,8–34	224.78	N
24R-1,9–11	232.99	N
24R-1,47–54	233.37	N
24R-1,91–99	233.81	N
25R-1,37–44	238.27	N
25R-1,79–88	238.69	N
26R-1,57–69	243.17	N
26R-1,88–104	243.48	N
26R-1,106–124	243.66	N
26R-1,126–133	243.86	N
27R-1,9–18	247.60	R
28R-1,23–35	252.53	N
28R-1,36–52	252.66	N
28R-1,67–80	252.97	N
28R-1,113–150	253.43	N
28R-2,0–33	253.80	N
28R-2,52–99	254.32	N
28R-2,102–127	254.82	N
29R-1,30–40	257.60	?N
29R-1,67–73	257.97	?N
30R-1,18–27	262.08	N
30R-1,30–43	262.20	N
30R-1,62–72	262.52	N
30R-1,85–142	262.75	N
30R-2,10–20	263.50	N
30R-2,26–38	263.66	N
30R-2,40–58	263.80	N
30R-2,89–97	264.29	N
30R-2,98–148	264.38	N
30R-3,0–117	264.90	N
30R-3,118–133	266.08	N
30R-3,135–145	266.25	N
31R-1,9–35	266.99	N
31R-1,36–68	267.26	N
31R-1,78–106	267.68	N
31R-1,111–138	268.01	N
31R-2,12–27	268.52	N
31R-2,27–43	268.67	N
31R-2,65–117	269.05	N
31R-3,0–13	269.90	N
31R-3,15–78	270.05	N
32R-1,1–9	271.51	N
32R-1,45–53	271.95	R
32R-1,61–70	272.11	R
32R-1,71–81	272.21	N
32R-1,23–55	282.93	N
32R-1,55–80	283.25	N
32R-1,93–116	283.63	N
32R-1,117–142	283.87	N
33R-3,1–50	284.21	N
33R-3,51–95	284.71	N
33R-3,96–145	285.16	N
33R-4,0–55	285.70	N
33R-4,56–139	286.20	N
34R-1,10–20	286.30	N
34R-1,24–33	286.44	N
34R-1,50–99	286.70	N
34R-1,101–129	287.21	N
34R-1,131–141	287.51	N
34R-2,0–35	287.70	?R
34R-2,60–73	288.30	N
35R-1,16–22	290.96	N

Table 6 (continued).

Core, section, interval (cm)	Depth (mbsf)	N/R
135-834B- (cont.)		
35R-1,24–30	291.04	N
35R-1,66–72	291.46	N
35R-1,115–124	291.95	N
35R-2,34–40	292.64	?
35R-2,77–83	293.07	N
35R-2,85–95	293.15	?
35R-2,97–107	293.27	N
36R-1,8–35	300.58	N
37R-2,57–66	310.77	N
40R-1,40–47	329.80	N
41R-1,33–43	334.73	?R
41R-1,64–83	335.04	N
41R-1,95–104	335.35	N
42R-1,40–46	339.50	N
42R-1,48–54	339.58	N
42R-1,99–108	340.09	N
43R-1,8–25	344.18	N
43R-1,45–60	344.55	N
43R-1,90–102	345.00	N
43R-1,104–117	345.14	N
47R-1,17–26	363.67	N
47R-1,27–37	363.77	N
47R-1,38–49	363.88	N
47R-1,70–81	364.20	N
47R-1,82–95	364.32	N
47R-1,96–126	364.46	N
48R-1,32–41	368.52	N
48R-1,59–66	368.79	N
48R-1,102–110	369.22	N
48R-1,131–140	369.51	N
48R-1,141–150	369.61	N
49R-1,88–103	374.08	N
49R-1,133–143	374.53	N
50R-1,38–48	378.28	N
50R-1,137–144	379.27	R
51R-1,60–67	383.50	N
51R-1,103–111	383.93	N
51R-1,114–122	384.04	N
51R-1,130–145	384.20	N
52R-1,58–74	388.08	N
52R-1,100–110	388.50	N
52R-2,10–20	389.10	N
52R-2,38–45	389.38	N
53R-1,30–43	392.80	N
53R-1,46–70	392.96	N
53R-1,75–85	392.25	N
53R-1,88–96	393.38	N
54R-1,85–95	398.05	N
54R-1,123–130	398.43	N
54R-1,133–141	398.53	N
56R-1,62–71	407.52	N
56R-1,2–14	408.40	N
56R-1,33–48	408.73	N
56R-1,55–68	408.85	N
56R-1,70–80	409.10	N
56R-2,92–99	409.32	N
58R-1,1–10	426.01	N
59R-1,60–70	431.60	N
59R-1,70–80	431.70	N
59R-1,108–118	432.08	N
59R-2,1–13	432.51	N
59R-2,15–24	432.65	N
59R-2,106–116	258.36	N

Notes: N = normal polarity and R = reversed polarity.

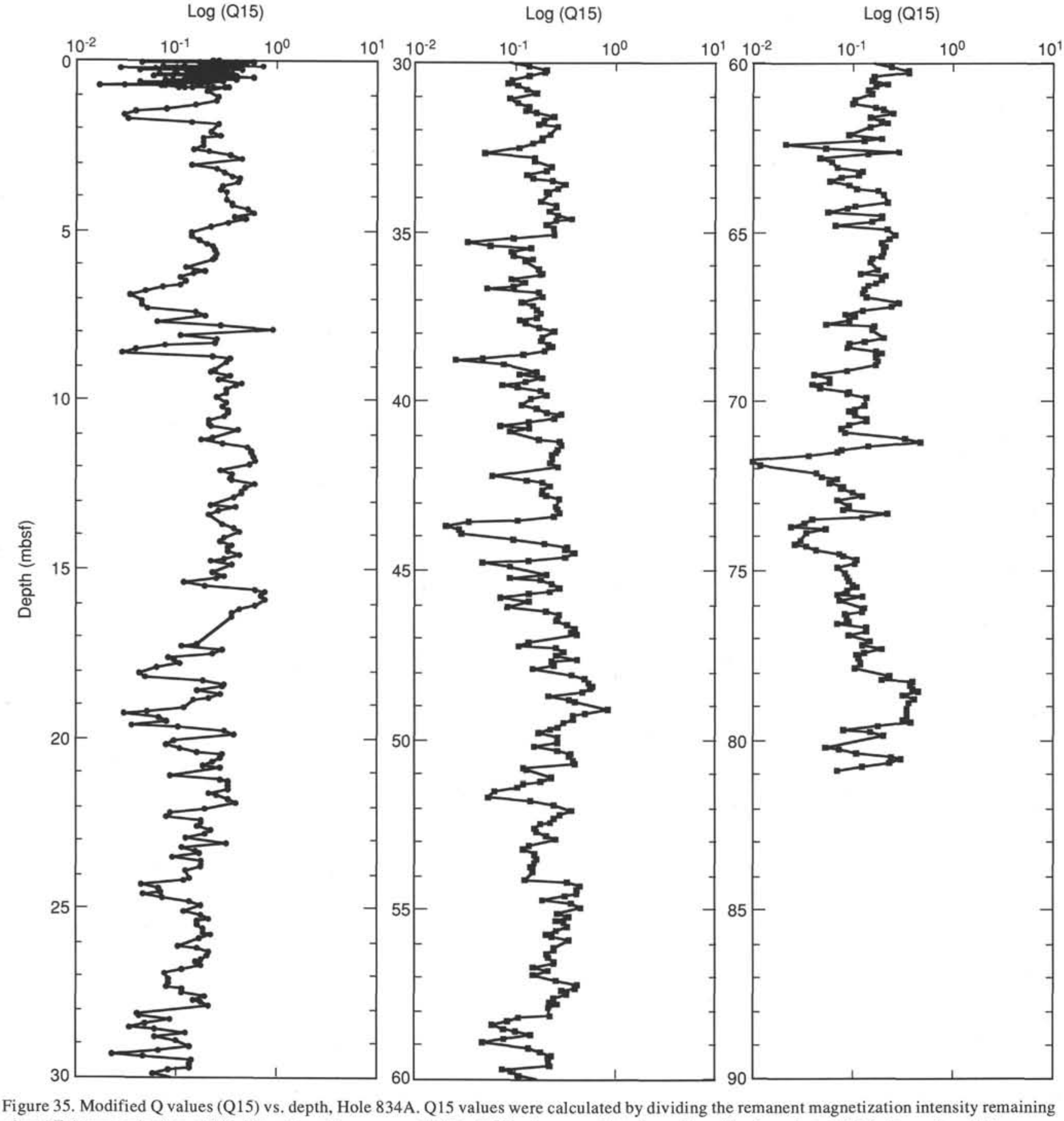

Figure 35. Modified Q values (Q15) vs. depth, Hole 834A. Q15 values were calculated by dividing the remanent magnetization intensity remaining after AF demagnetization at 15 mT by the volume susceptibility. Q15 values are plotted on a logarithmic scale to highlight small variations.

adjacent minimum, 83 cycles were found, yielding an average period of about 41 k.y. per cycle. The period of the Earth's tilt (obliquity) in the Milankovitch cycle theory is 41 k.y. (Berger, 1978; deMenocal et al., 1991), so we conclude that these cycles are likely an indication of the magnetic properties mirroring the climatic changes in the environment.

Basalts

Magnetic susceptibility values in the basalts of Site 834 were extremely variable, ranging from 10×10^{-6} to 5000×10^{-6} cgs (Figs. 34 and 36). This is not surprising as the basalts are expected to have high susceptibilities and most basalt core sections contained voids and fragments of basalts with variable volumes. Voids and volumes less than a full core liner may have produced many of the low basalt susceptibility values. Furthermore, after the basalt cores are split, the pieces are usually separated for curation, so that the core "expands." Thus, it is not usually possible to relate a particular susceptibility reading to a particular piece of basalt in the split core. For these reasons, the whole-core susceptibility measurements must be taken as minimal values and only used for reconnaissance.

Nevertheless, susceptibility displays some interesting trends vs. depth (Fig. 36). High susceptibility readings were recorded from material obtained from the bottom of igneous Unit 2 through Unit 5 (125–162 mbsf), the bottom of Unit 7 (251–290 mbsf), and Unit 12 (361–380 mbsf). Lower susceptibilities were obtained

Table 7. AF-cleaned intensity, susceptibility, and modified Q-ratio.

Depth (mbsf)	Intensity (mA/m)	Susceptibility	Q15 (int/susc)
0.1	6.78	34.0	0.20
0.2	21.08	51.7	0.41
0.3	30.24	66.0	0.46
0.4	23.52	66.0	0.36
0.5	11.23	53.0	0.21
0.6	8.13	49.7	0.16
0.7	8.01	49.8	0.16
0.8	6.99	49.7	0.14
0.9	10.39	51.0	0.20
1.0	14.30	54.5	0.26
1.1	14.82	55.7	0.27
1.2	15.18	61.0	0.25
1.3	9.62	61.5	0.16
1.4	5.35	65.7	0.08
1.5	2.62	65.0	0.04
1.6	1.87	61.0	0.03
1.7	2.25	66.8	0.03
1.8	11.49	82.3	0.14
1.9	27.18	101.0	0.27
2.0	28.16	121.7	0.23
2.1	21.64	96.0	0.23
2.2	16.22	58.5	0.28
2.3	9.40	50.7	0.19
2.4	9.38	50.7	0.19
2.5	9.31	50.7	0.18
2.6	7.87	53.3	0.15
2.7	16.36	75.5	0.22
2.8	30.41	87.3	0.35
2.9	38.13	84.8	0.45
3.0	36.03	91.0	0.40
3.1	20.82	147.0	0.14
3.2	39.55	156.0	0.25

Remainder of Table 7 in backpocket microfiche.
Notes: AF = 15 mT and Q15 = int(15 mT)/susc.

from the other igneous material. Furthermore, Figure 36 shows a downward trend in susceptibility from 162 to 251 mbsf and an upward trend from 361 to 433 mbsf. In part, the higher susceptibilities between 125–162 mbsf and 251–290 mbsf appear to reflect greater recovery in those intervals. However, the susceptibility trends probably also show trends in magnetic mineral content.

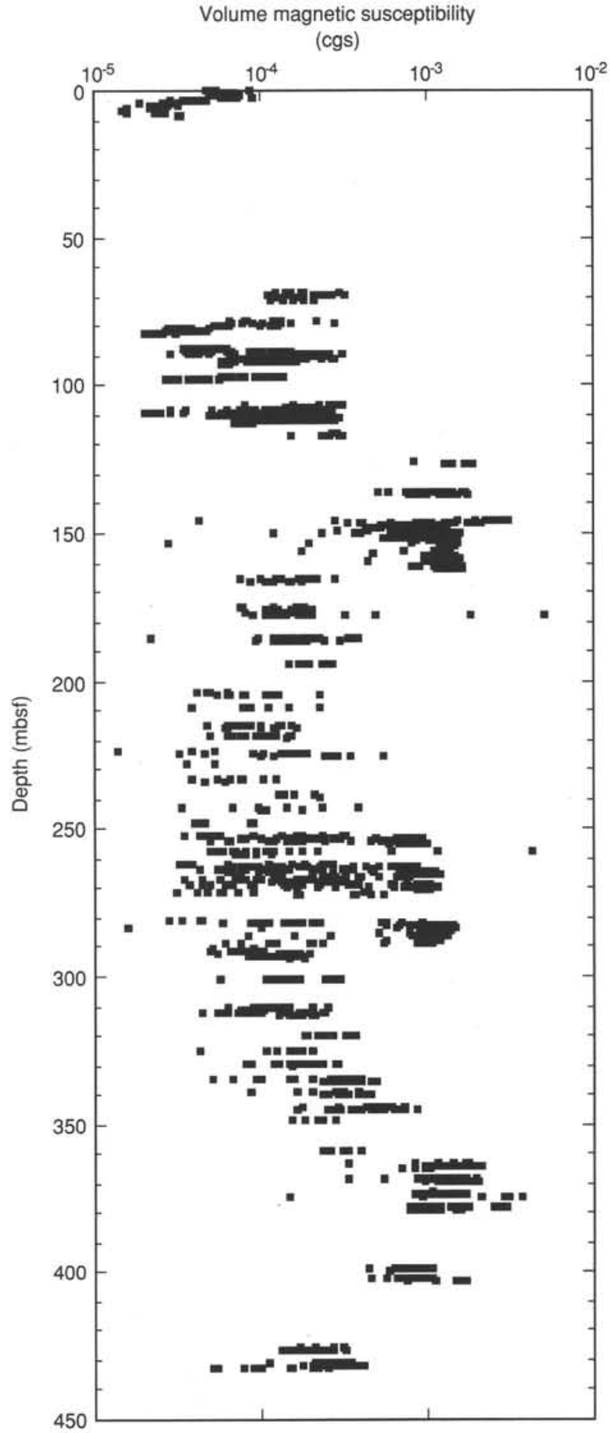

Figure 36. Volume magnetic susceptibility vs. depth, Hole 834B. Susceptibility is plotted on a logarithmic scale to highlight small variations.

Core Orientation

Cores 135-834A-4H through -9H were oriented using the multishot camera (see "Explanatory Notes" chapter, this volume). Usable orientation photographs were obtained for all six cores (Table 8). After plotting the paleomagnetic directions, it became obvious that at least one of the orientation tools was misaligned. Rather than giving declinations near zero, it yielded declinations about 30°–40° west of north (Fig. 31). An examination of the cameras revealed that one of the two compasses, Compass B, was misaligned with the fiducial axis of the APC. Its error was measured at 13° west of north. This still left 20° or more of error unexplained. An examination of the sinker bar assembly found that an alignment bolt had sheared. This allowed an unpredictable error in the orientation data. The bolt was replaced before subsequent sites.

INORGANIC GEOCHEMISTRY

Introduction

In the following text, a brief description is presented of the interstitial water data obtained from Hole 834A. The results are presented in Table 9. Other analyses will be conducted in shore-based laboratories (e.g., trace metals, $^{87}Sr/^{86}Sr$, oxygen and hydrogen isotopes, and also mineralogy and chemistry of the associated sediment samples). The shipboard data are presented in Figure 37.

Major Elements

In Hole 834A, the concentration-depth profiles of the dissolved major constituents (chloride, sodium, calcium, magnesium, potassium, and sulfate) are characterized by fairly uniform values from the mud line to 135 mbsf (Fig. 37).

Table 8. APC core orientations, Hole 834A.

Core no.	Camera no.	Compass	Inclination		Declination
			Direction	Drift	
135-834A-					
4H	3250	B	N200°E	1°	60°
5H	3250	B	220°	1°	110°
6H	3209	A	160°	1°	305°
7H	3209	A	165°	1°	50°
8H	3209	A	225°	1°	250°
9H	3250	B	205°	1.2°	20°

Notes: Inclination is the off-vertical angle of the core. Drift and direction are the dip and dip direction measured clockwise from north of a plane perpendicular to the core axis. Declination is the angle between the double line on the core liner and magnetic north (measured clockwise). Compass B was misaligned; to correct its declination values, add 13°.

Na^+ concentrations were obtained from charge balance calculations. The Na^+/Cl^- ratios in all the interstitial water samples are constant (e.g., 0.857 145 0.005). Therefore, slight deviations in Cl^- and Na^+ concentrations observed along the sedimentary column cannot be related to manipulation artifacts or other noise.

Chloride and sodium concentrations increase from the mud line to 32 mbsf, and each concentration is 3.8% higher than the seawater average (Broecker and Peng, 1982). The increases in Cl^- and Na^+ noted in the upper part of this hole appear to be real and may be associated with minor changes in ocean salinity during Pleistocene time (Manheim and Sayles, 1974). From 32 to 134 mbsf, the Cl^- and Na^+ concentrations show almost constant values with a deviation that can be related to the analytical error in the chloride determination (e.g., 1%).

Ca, Mg, K, and $SO_4$2– concentrations determined in the interstitial water samples are almost equal to the average seawater concentration (Broecker and Peng, 1982). The average concentrations of these species in Hole 834A pore waters are listed in Table 10. The observed deviations from these concentrations do not exceed the analytical uncertainty of the methods of determination (Gieskes and Peretsman, 1986). Unfortunately, we were unable to get a sample of bottom seawater adjacent to the site. Nevertheless, these values are similar to the average concentrations in free seawater (e.g., 28, 10, 53, and 11 mM, respectively; Broecker and Peng, 1982).

The data are consistent with the constant high sediment porosity values and the low downhole temperature gradients (see "Physical Properties" section, this chapter) and suggests that Hole 834A was drilled in the vicinity of a downwelling flow of bottom water recharging a basement aquifer. Therefore, fluid flow patterns cannot be defined from these data. Similar results were obtained on the flank of the Galapagos Spreading Center in a low heat flow area (Maris et al., 1984; Becker and Von Herzen, 1983).

Silica, Strontium, and Manganese

Dissolved silica concentrations range between 200 and 400 mM, which is expected in sediment with little or no biogenic silica (Fig. 37). No interpretation of the absolute concentrations can be made, particularly in view of the temperature of squeezing effect (Gieskes, 1973, 1974). However, relative changes in silica concentration can indicate mineralogical changes. The slight increase in silica with depth, therefore, could be related to the increase of the ash contents in this hole (see "Lithostratigraphy" section, this volume).

Dissolved strontium concentrations increase gradually with depth to reach a maximum value about of 130 mM at 82 mbsf (Fig. 37). Toward the bottom of the hole (above and below the thick igneous Unit 2, which is either a sill or flow), however, a decrease is observed. Increases in Sr^{2+} could be related to carbonate recrystallization processes (Gieskes et al., 1986).

The concentration-depth profile of the dissolved manganese is complex (Fig. 37). For this reason, we discuss the observations over various depth intervals. From the mud line to 40 mbsf, Mn concentrations are fairly uniform. Between 40 and 50 mbsf, the highest Mn concentration was determined. Below 50 mbsf, Mn concentrations decrease and reach values below the limit of the detection of the Flame AA spectrophotometer (e.g., 20 mM). The enhanced Mn concentrations determined in this hole seem to be related to the lithologic unit between 42 and 78 mbsf, which is characterized by the occurrence of interbedded ash layers. However, alterations of the ash and volcanic components in this hole are not suggested by the Ca and Mg profiles (Fig. 37). Hence, more details about the mineralogy and chemistry of the sediment from the shore-based laboratories are necessary to define the chemical reactions affecting the concentrations of dissolved Mn in these interstitial water samples. Furthermore, the low Mn concentrations determined just above and below the thick basalt unit penetrated in this hole (Unit 2) need to be confirmed by additional studies.

It is apparent that interstitial water samples from every third core are inadequate to define the distribution of dissolved manganese in the interstitial water.

Hydrocarbon Gases

Gas chromatograph measurements indicate that the methane concentration dissolved in the interstitial water is lower than the limit of detection of about >5 mM.

Conclusion

The main features revealed by the interstitial water chemistry data of Hole 834A are (1) the lack of a gradient in the concentration-depth profiles of the major elements, and (2) the scatter in the concentrations of the minor elements, which probably results from the interstitial water-mineral interactions. These features

Table 9. Interstitial water chemistry data, Hole 834A.

Core, section, interval (cm)	Depth (mbsf)	pH	Alkalinity (mM)	Salinity	Cl^- (mM)	SO_4^{2-} (mM)	Ca^{2+} (mM)	Mg^{2+} (mM)	K^+ (mM)	Sr^{2+} (µM)	Si^{4+} (µM)	Mn^{2+} (µM)	Na^+ (mM)
135-834A-													
1H-4, 140–150	5.9	7.75	3.04	35.2	558	27.63	9.8	51.7	11.3	115	263	43	478
2H-4, 140–150	13.5	7.35	2.66	35.6	564	28.21	9.7	51.1	11.5	118	317	44	487
3H-4, 140–150	23.0	7.73	2.56	35.2	571	27.89	10.2	53.1	11.1	115	357	42	488
4H-4, 140–150	32.5	7.75	2.54	35.0	571	27.31	10.2	52.6	11.0	128	351	36	488
5H-4, 140–150	42.0	7.71	2.36	35.8	567	27.58	10.5	53.3	11.3	127	337	91	483
6H-4, 140–150	51.0	7.51	2.39	35.0	571	27.89	10.8	54.1	11.4	127	373	97	486
9H-4, 140–150	80.0	7.68	2.37	35.2	569	28.58	11.3	51.7	10.7	130	379	71	489
12X-1, 140–150	104.3	7.67	2.36	35.2	571	27.47	10.9	52.3	11.0	106	407	<20	489
16X-1, 140–150	133.3	8.16	2.44	35.3	565	28.00	10.0	50.9	10.6	81	369	<20	489

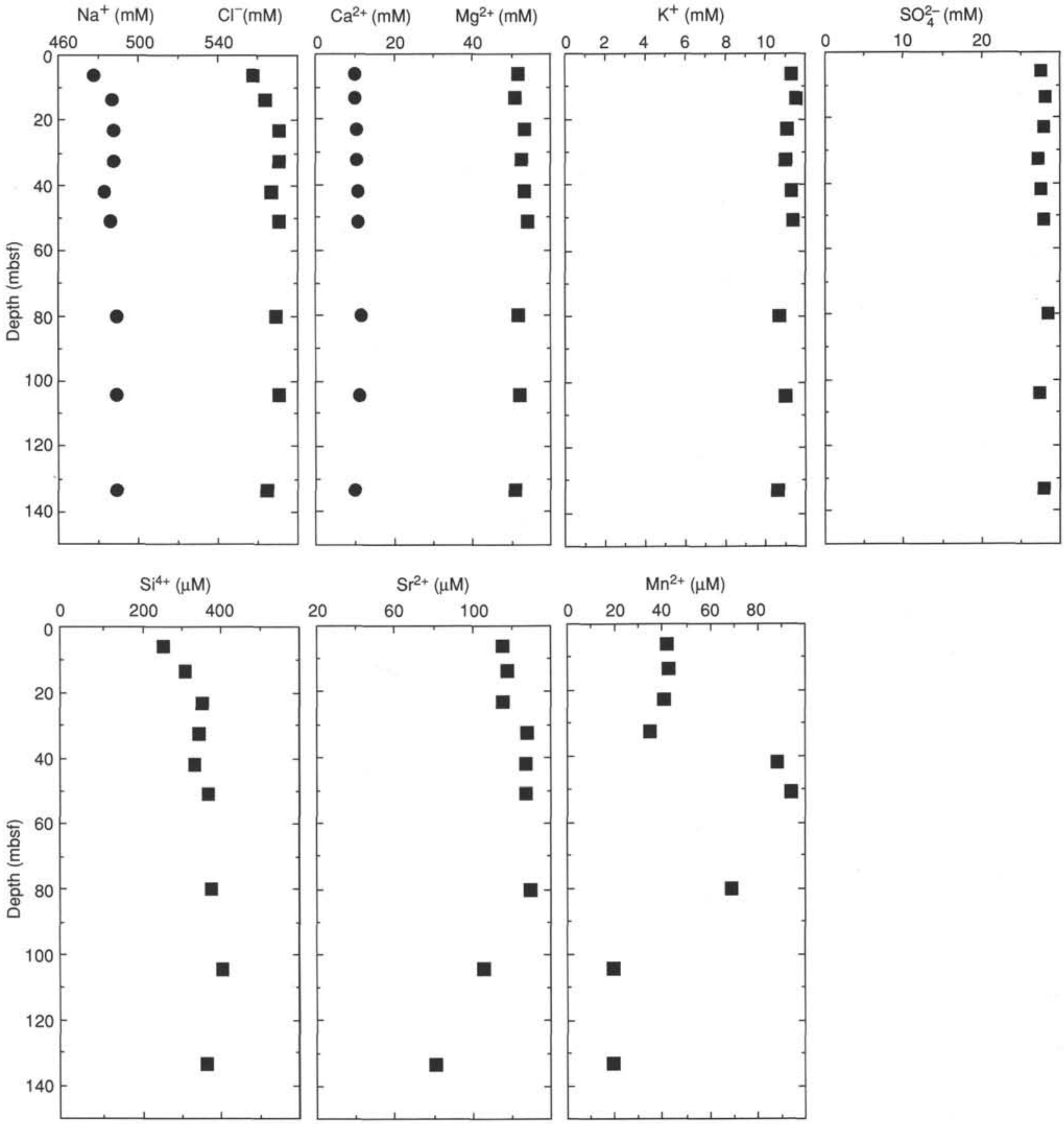

Figure 37. Concentration vs. depth profiles for chloride and sodium, calcium and magnesium, potassium, sulfate, silica, strontium, and manganese, Hole 834A.

Table 10. Average concentration values in pore waters, Hole 834A.

Element	Concentration average (mM)	Standard deviation (±μM)
Sulfate	27.80	0.40
Calcium	10.37	0.54
Magnesium	52.30	1.07
Potassium	11.10	0.31

suggest that, if the sedimentary system is recharged by a downwelling flow of bottom seawater, this flow could be low enough not to affect the scatter of the minor element concentrations.

ORGANIC GEOCHEMISTRY

Shipboard organic geochemical analysis of samples from Hole 834A consisted of 13 determinations of volatile hydrocarbons in sediments using the Carle gas chromatograph; 12 determinations of total nitrogen, carbon, and sulfur using the Carlo Erba NCS analyzer; and 101 determinations of total inorganic carbon using the Coulometrics 5011 coulometer equipped with a System 140 carbonate/carbon analyzer. Details of the analytical procedures used are outlined in the "Organic Geochemistry" section of the "Explanatory Notes" chapter (this volume) and are described in detail by Emeis and Kvenvolden (1986).

The volatile hydrocarbon gases were obtained from the bulk sediment using the head-space sampling technique and were routinely monitored for methane, ethane, and propane. One sample was taken from each of the first 12 cores of Hole 834A, and one was taken from Core 135-834A-16X, in which a sediment interval occurred between igneous rocks. Methane concentrations in the samples were 2–3 ppm, which is very low and at the laboratory background level. Ethane and propane were not detected. The extremely low concentration of methane indicates that methanogenesis is not occurring in these sediments. Sulfate bacteria compete favorably with methanogenic bacteria; consequently, methanogenesis is inhibited in the presence of sulfate (Claypool and Kvenvolden, 1983). Sulfate levels remain at the same level as that of seawater throughout this hole (see "Inorganic Geochemistry" section, this chapter); consequently, at no time were conditions favorable for methanogenesis. Another contributing factor could be that the very low levels of organic carbon (see below) in these sediments were not enough to sustain microbial activity.

Determinations of inorganic carbon (IC) contents were performed on the samples used for physical properties and on additional samples selected by the sedimentologists. Percent $CaCO_3$ is calculated according to the equation:

$$CaCO_3 = IC \cdot 8.334.$$

This equation assumes that all the carbonate is present as calcite. The data from these analyses are presented in Table 11. Carbonate values range from <1% to 93%. Lower carbonate values are associated mostly with samples at sub-bottom depths greater than 60 m, which contain a higher amount of volcaniclastic material. This is discussed in more detail and related to the lithostratigraphic units in the "Lithostratigraphy" section (this chapter).

Also shown in Table 11 are the percentages of total carbon, nitrogen, and sulfur for the 12 samples for which they were measured. Total organic carbon (TOC) is defined here as the difference between the total carbon and the inorganic carbon values. The sediments from Site 834 have organic carbon contents between 0.04% and 0.28% and hence were considered too low for analysis by the Rock-Eval instrument. These values are also so low that any interpretations drawn from them should be regarded as tentative. However, there are some trends in the data which are briefly discussed below.

The six samples analyzed from the top 50 m of Hole 834A all show values above 0.2% TOC, whereas those deeper down the hole have lower values. This could be a reflection of the greater volcaniclastic contribution to the lower sediments. The nitrogen content shows a similar pattern to the organic carbon contents, probably for the same reason. The ratio of organic carbon/nitrogen in these samples is considerably lower (0.1–3.0) than those normally reported for marine sediments (Romankevich, 1984; Rashid, 1985) and shows no systematic variation with depth. This could be partly because total nitrogen is being measured rather than just organic nitrogen. However, the nitrogen content is within the range reported for open-ocean sediments (Romankevich, 1984) and hence the low C/N ratios primarily reflect the low TOC values. Sulfur shows a reverse trend with an increase from below detection limits in the upper samples to about 1% in the deeper samples that were analyzed. The combination of the decrease in organic carbon and the increase in sulfur causes the organic carbon/sulfur ratio to decrease with depth. Hence, it is reasonable to assume that the sulfur is not associated with organic matter but is inorganic (e.g., sulfides) and probably associated with minerals of igneous origin.

IGNEOUS PETROLOGY

Introduction

One of the objectives at Site 834 was to determine the sequence of magmatic events associated with the earliest stages of opening of the Lau Basin. Igneous rocks were recovered from 106.2 to 149.5 mbsf in Hole 834A, and from 112.6 to 435.7 mbsf in Hole 834B, for a total basement penetration of about 323 m. Overall, 13 individual igneous lithologic units have been defined at Site 834. All of the rocks recovered are low-K tholeiitic basalt or basaltic andesite; most are clearly extrusive (e.g., fine grain sizes and the common presence of glassy margins). Unit 5, characterized by coarser grain size and the absence of internal quenched margins, appears to be a single 27-m-thick lava flow or sill. Several sediment intervals (centimeter to meter scale) are interbedded with the lavas; paleontological dating of these intervals indicates that Units 1 to 9 are between lower Pliocene and upper Miocene in age. The presence of additional minor sedimentary intervals are inferred from baked or indurated sediment within fractures or adhering to quenched glassy margins. The igneous units have been defined on the basis of distinctive phenocryst assemblages and texture, especially where further supported by discontinuities such as quenched margins or sedimentary interbeds. Subunits are defined where small intervals of indurated or baked sediment separate apparently identical lithologies. The details of unit boundaries are summarized in Table 12.

In general, there is good agreement in the igneous rock correlations between the two holes, although relatively poor core recovery in the upper 25 m of basement penetration complicates detailed stratigraphic interpretation. The cored intervals, core recovery, and recovered lithology are summarized in the first two columns of Figure 38. Note that in spite of the poor core recovery, the relatively short cores in Hole 834A resolved more lithologic detail than the long cores in Hole 834B. Because equivalent lithologies appeared in both holes, these are given the same unit numbers.

Three igneous units are especially distinctive. Unit 5 is massive, apparently without internal quench margins, in which the "groundmass" is a network of large clinopyroxene oikocrysts that poikilitically enclose small plagioclase crystals. There is abundant interstitial mesostasis. Miarolitic cavities partly replaced or filled with alteration products and secondary minerals, also are common. The clinopyroxene and plagioclase are mostly unaltered, except in the upper 2 m of this unit. These features suggest a thick lava flow or possibly a shallow sill that has been subjected to deuteric alteration. Unit 7 is the only highly phyric unit and, in addition, is the only one lacking significant vesicularity. Unit 8, in contrast, has abundant small vesicles developed in a bluish gray glass enclosing glomerocrysts of plagioclase and clinopyroxene.

Inspection of the core suggested that there might be a relationship between (1) the thickness of flows (or of smaller cooling units, such as pillows, within flows); (2) the size or continuity of pieces within each core; and (3) the total core recovery (Fig. 39). An estimate of flow or cooling unit thickness was made by several different methods, depending on the nature of the core and the amount of recovery. For units made up of many small pieces (the most common case), the number of igneous contacts or chilled margins in each recovered meter of core was counted. Even with low core recovery, the number of such contacts or boundaries per meter of core recovered should be related to the actual number per meter in the unit. The features counted as "contacts" included glass margins, very fine-grained variolitic or microlitic zones, and highly vesicular lithologies adjacent to more massive pieces.

Table 11. Concentrations of inorganic and organic carbon and total nitrogen and sulfur, Hole 834A.

Core, section, interval (cm)	Depth (mbsf)	Total carbon (%)	Inorganic carbon (%)	Organic carbon (%)	$CaCO_3$ (%)	N (%)	S (%)	OrgC/N	OrgC/S
135-834A-									
1H-1, 76–77	0.76		8.89		74.1				
1H-3, 102–103	4.02	7.76	7.50	0.26	62.5	0.12	2.10		
1H-4, 93–94	5.43		10.60		87.9				
1H-5, 89–90	6.89		11.20		93.3				
2H-1, 77–78	8.37		11.00		91.3				
2H-3, 75–76	11.35	8.24	7.96	0.28	66.3	0.14	2.00		
2H-5, 78–80	14.38		7.00		58.3				
3H-2, 60–61	19.20	8.05	7.77	0.28	64.7	0.10	2.80		
3H-2, 88–89	19.48		8.83		73.6				
3H-4, 75–76	22.35		8.87		73.9				
3H-6, 75–76	25.35		8.68		72.3				
4H-2, 0–5	28.10		10.50		87.0				
4H-2, 27–28	28.37		11.00		91.4				
4H-2, 36–37	28.46		10.80		90.2				
4H-2, 39–40	28.49		10.90		90.8				
4H-2, 45–46	28.55		10.90		90.5				
4H-2, 51–52	28.61		10.50		87.4				
4H-2, 100–101	29.10		6.75		56.2				
4H-4, 73–74	31.83	8.67	8.44	0.23	70.3	0.12	1.90		
4H-6, 72–73	34.82		8.59		71.6				
5H-2, 73–74	38.33		7.54		62.8				
5H-4, 73–74	41.33	8.67	8.41	0.26	70.1	0.11	2.30		
5H-6, 73–74	44.33		7.35		61.2				
6H-1, 121–122	46.81		1.38		11.5				
6H-2, 75–76	47.85	5.16	4.89	0.27	40.7	0.09	0.38	3.0	0.71
6H-4, 75–76	50.85		6.97		58.1				
6H-6, 54–55	53.64		9.20		76.6				
6H-6, 75–76	53.85		9.35		77.9				
6H-6, 83–84	53.93		7.49		62.4				
6H-6, 92–93	54.02		10.00		83.4				
6H-6, 102–103	54.12		4.79		39.9				
7H-1, 110–111	56.20		7.41		61.7				
7H-2, 56–57	57.16		7.19		59.9				
7H-2, 80–81	57.40		6.71		55.9				
7H-3, 15–16	58.25		7.51		62.6				
7H-3, 143–144	59.53		5.98		49.8				
7H-4, 81–82	60.41		7.19		59.9				
7H-4, 106–107	60.66		5.31		44.2				
7H-5, 23–24	61.33		5.80		48.3				
7H-5, 105–106	62.15		0.23		1.9				
7H-5, 128–129	62.38		5.84		48.6				
7H-6, 81–82	63.41	6.86	6.79	0.07	56.6	0.08	0.46	0.9	0.15
7H-6, 103–104	63.63		7.11		59.2				
8H-1, 96–97	65.56	4.21	4.05	0.16	33.7	0.08	0.88	2.0	0.18
8H-2, 56–57	66.66		5.57		46.4				
8H-2, 85–86	66.95		5.86		48.8				
8H-3, 66–67	68.26		3.79		31.6				
8H-3, 95–96	68.55		4.41		36.7				
8H-3, 97–98	68.57		4.41		36.7				
8H-4, 7–8	69.17		2.47		20.6				
8H-4, 23–24	69.33		3.03		25.2				
8H-4, 42–43	69.52		6.42		53.5				
8H-4, 66–67	69.76		4.83		40.2				
8H-4, 88–89	69.98		5.48		45.6				
8H-4, 133–134	70.43		5.69		47.4				
8H-5, 109–110	71.69		4.47		37.2				
8H-6, 85–86	72.95		5.91		49.2				
8H-6, 111–112	73.21		2.02		16.8				
8H-7, 27–28	73.87		3.05		25.4				
9H-2, 60–62	76.20		5.95		49.6				
9H-2, 109–111	76.69	5.17	5.16	0.01	43.0	0.08	0.84	0.1	0.01
9H-3, 91–93	78.01		2.03		16.9				
9H-4, 26–28	78.86		0.02		0.2				
9H-4, 56–58	79.16		0.94		7.8				
9H-4, 74–76	79.34		0.92		7.7				
9H-4, 98–100	79.58		0.57		4.7				
9H-4, 111–113	79.71		4.12		34.3				
9H-4, 127–129	79.87		1.77		14.7				
9H-5, 27–29	80.37		1.91		15.9				
9H-5, 71–73	80.81		2.72		22.7				
9H-5, 123–124	81.33		1.05		8.7				
9H-5, 142–144	81.52		0.88		7.3				
9H-6, 50–51	82.10		0.84		7.0				
9H-6, 108–109	82.68		3.43		28.6				
9H-7, 26–27	83.36		4.91		40.9				

Table 11 (continued).

Core, section, interval (cm)	Depth (mbsf)	Total carbon (%)	Inorganic carbon (%)	Organic carbon (%)	$CaCO_3$ (%)	N (%)	S (%)	OrgC/N	OrgC/S
135-834A- (cont.)									
10X-1, 81–82	84.41	7.33	7.25	0.08	60.4	0.07	0.61	1.0	0.13
10X-1, 116–117	84.76		7.24		60.3				
10X-2, 69–70	85.79		6.34		52.8				
10X-2, 95–96	86.05		3.23		26.9				
10X-3, 67–68	87.27		0.76		6.3				
10X-3, 117–118	87.77		0.82		6.8				
11X-1, 18–19	93.38		0.65		5.4				
11X-1, 46–47	93.66		0.75		6.2				
11X-1, 49–50	93.69		0.75		6.2				
11X-1, 77–78	93.97		3.11		25.9				
11X-1, 79–80	93.99	3.52	3.41	0.11	28.4	0.07	0.84	1.6	0.13
11X-1, 140–141	94.60		0.44		3.7				
11X-1, 142–143	94.62		0.45		3.7				
11X-2, 50–51	95.20		0.49		4.1				
11X-2, 51–52	95.21		0.49		4.1				
11X-3, 33–34	96.53		0.37		3.1				
11X-3, 34–35	96.54		0.39		3.2				
11X-3, 96–97	97.16		5.21		43.4				
11X-3, 97–98	97.17		5.75		47.9				
12X-1, 51–52	103.41		5.47		45.6				
12X-1, 52–53	103.42		5.88		49.0				
12X-2, 50–51	104.9		5.21		43.4				
12X-2, 53–54	104.93	4.96	4.92	0.04	41.0	0.07	1.04	0.6	0.04
12X-2, 74–75	105.14		0.63		5.2				
12X-2, 75–76	105.15		1.10		9.2				
16X-2, 42–43	133.82		0.03		0.2				

Many contacts appear on small unoriented pebbles much smaller than core diameter, spread out over several centimeters or more of the core. These could represent fragments of a single contact mixed within the core liner. Therefore, contacts within 15 cm of each other were counted as a single contact unless there were one or more large oriented pieces between them. In the very thick Unit 7, contacts were counted separately for the top, middle, and lower thirds of the unit. Less commonly, where multiple contacts appeared in long, continuous cores, thicknesses between contacts were measured directly. In such long, continuous sections, when no contacts were recovered, the minimum flow thickness was assumed to be the length of recovered core. Units 1, 3, 4, 9, and 11 were too thin and too poorly recovered for meaningful results by any of these methods.

In spite of the obvious limitations of this approach, both the counts of numbers of contacts and the direct measurements of flow thicknesses give the same overall patterns. The results are summarized in Figure 39. Unit 6, the upper third of Unit 7, and Units 8 and 10 appear to be made of many thin flows or small-diameter pillows. Unit 2, the lower part of Unit 7, and Units 12 and 13 are made up of larger pillows or flows, and Unit 5 again appears to be composed of one, or a very few, thick cooling units (Fig. 39A). The same pattern, though noisier, appears when the data are summarized by cores (Fig. 39B). The calculated average flow thickness (Fig. 39C) clearly reflects the data for contacts/meter. Finally, as shown in Figure 39D, core recovery falls off rapidly as contacts per meter increase (i.e., as cooling units become thinner). This is not unexpected, as less coherent rock is more likely to rotate and/or break up during the drilling process. Further discussion of the physical characteristics of these units, and their relation to logging data, are discussed in the "Downhole Measurements" section (this chapter).

Alteration in all units is limited to low-temperature oxidation of crystalline rock, palagonitization of glass, and alteration of mesostasis to clays. Mineralogical effects include conversion of olivine to iddingsite and chrysotile, and of sulfides and oxides to iron-hydroxides. Groundmass clinopyroxene and plagioclase are often turbid and may be partly or completely replaced by clay, chlorite, or zeolites. The formation of zeolite (mainly phillipsite) is widespread throughout the section cored. Where sulfides occur, they appear to be primary magmatic, or late magmatic deuteric, in origin and are tentatively identified as chalcopyrite with some intergrown pyrrhotite(?). Fractures are commonly filled by carbonate, probably derived from interbedded sediment layers.

Lithology and Petrography

Table 12 summarizes the units as they appear in the recovered core, including individual pieces that mark the top and bottom of each unit. Table 13 summarizes their most important petrographic characteristics; all are basaltic. Modal analyses of selected samples are presented in Table 14 and are summarized graphically in Figure 40. The relatively high vesicularity of most of these lavas is notable, the exceptions being Units 1 and 7. These samples also tend to be aphyric to only moderately phyric, but with a tendency for phenocryst content to increase downhole. Below, the general lithologic and petrographic characteristics of each unit are described in detail.

Unit 1

Aphyric to Sparsely Phyric Plagioclase and Olivine Basalt

Unit 1 was recovered only in Section 135-834A-12X-CC and as rubble in Section 135-834A-13X-1; no equivalent was recognized in Hole 834B. It is a sparsely phyric olivine plagioclase basalt. Plagioclase is the major phenocryst, comprising <2% of the rock volume. The plagioclase crystals are euhedral, up to 0.7 mm in length, and are strongly zoned with narrow sodic rims. Olivine phenocrysts are limited to minor occurrences in Sample 135-834A-12X-CC, 1–4 cm. The phenocrysts tend to form glomeroporphyritic clusters and are generally fresh with no signs of incipient alteration.

The groundmass material consists of varying proportions of microcrystalline plagioclase, clinopyroxene, olivine, opaques,

Table 12. Principal lithologic units defined at Site 834.

Unit	Lithology	Hole 834A Top depth (mbsf) Core, section, interval (cm)	Bottom depth (mbsf) Core, section, interval (cm)	Hole 834B Top depth (mbsf) Core, section, interval (cm)	Hole 834B Bottom depth (mbsf) Core, section, interval (cm)	Distinguishing features
1	Aphyric to plagioclase and olivine-bearing basalt	106.17 12X-CC	112.64 13X-1, 20 (Piece 3)	Not recovered		<1% plagioclase phenocrysts; 10%–15% vesicles, minor olivine
2A	Aphyric basalt	112.64 13X-1, 20 (Piece 4)	117.34 14X-1, 44 (Piece 4)	112.55 6R-CC, 0 (Piece 1)	128.58 8R-2, 145 (Piece 10)	Rare plagioclase phenocrysts; microlitic to intergranular groundmass; dark patches of quenched material common; vesicular
2B	Aphyric basalt	117.36 14X-1, 47 (Piece 1)	123.73 16X-1, 0 (Piece 1)	Not defined		Rare plagioclase phenocrysts; microlitic to intergranular groundmass; dark patches of quenched material common; vesicular
3	Moderately plagioclase phyric basalt	131.90 16X-1, 0 (Piece 1)	132.06 16X-1, 17 (Piece 5)	Not recovered		2%–3% plagioclase phenocrysts; highly vesicular
4	Aphyric basalt	134.09 16X-CC, 20	136.30 17X-1, 0 (Piece 1)	Not recovered		30% vesicles, aphyric, no olivine; could be flow top to Unit 5
5	Aphyric basalt	136.30 17X-1, 0 (Piece 1)	149.50 20X-3, 110 (Piece 13)	135.80 9R-1, 0 (Piece 1)	162.41 13R-2, 72 (Piece 2)	Poikilitic clinopyroxenes to 3 mm; 1%–6% vesicles > 1 mm, 10% small vesicles < 1 mm; vesicle fillings are common in upper section
6	Aphyric to sparsely phyric basalt			162.62 13R-2, 105 (Piece 4)	214.04 20R-1, 48 (Piece 7)	Rare plagioclase and olivine phenocrysts; variolitic to microlitic groundmass; highly vesicular (<1 mm); dark patches of quenched lava common
7	Moderately to highly phyric plagioclase basalt			214.04 20R-1, 48 (Piece 8)	287.63 34R-2, 42 (Piece 1B)	10%–15% plagioclase phenocrysts; 1% olivine phenocrysts, rare vesicles
8	Aphyric basalt			287.63 34R-2, 42 (Piece 2)	310.20 37R-1, 0 (Piece 1)	Rare plagioclase and clinopyroxene phenocrysts; 20%–40% small vesicles; minor groundmass olivine; microlitic groundmass
9A	Moderately phyric olivine-plagioclase basalt			310.20 37R-1, 0 (Piece 1)	310.39 37R-1, 25 (Piece 4)	7%–8% plagioclase phenocrysts; 1% olivine phenocrysts; 10%–15% vesicles
9B	Moderately phyric olivine-plagioclase basalt			310.45 37R-1, 34 (Piece 6)	310.59 37R-1, 51 (Piece 8)	3%–5% plagioclase phenocrysts; 20%–30% vesicles
10A	Aphyric basaltic andesite to basalt			311.44 37R-2, 37 (Piece 2)	348.80 44R-1, 0 (Piece 1)	Microlitic to microcrystalline groundmass; >20% small vesicles (<1 mm)
10B	Aphyric basaltic andesite to basalt			348.80 44R-1, 0 (Piece 1)	363.50 47R-1, 0 (Piece 1)	Microlitic to microcrystalline groundmass; >20% small vesicles (<1 mm)
11	Sparsely phyric olivine plagioclase basalt			358.68 46R-1, 37 (Piece 8)	358.71 46R-1, 45 (Piece 9)	1%–2% plagioclase and olivine phenocrysts
12	Aphyric to moderately phyric clinopyroxene-plagioclase basalt and olivine-clino-pyroxene-plagioclase basalt			363.50 47R-1 pc. 1 0 cm	407.90 56R-2, 111 (Piece 12)	Microlitic to microcrystalline groundmass; aphyric in hand specimen; groundmass is weakly seriate micro-crystalline in thin section; 10%–40% vesicles; rare large (>3 mm) clinopyroxene phenocrysts; lower part of unit may have some Unit 13 flows in it
13	Moderately phyric olivine-clinopyroxene-plagioclase basalt			407.90 56R-2, 111 (Piece 13)	435.67 59R-2, 81 (Piece 14)	2%–5% plagioclase, clinopyroxene and olivine phenocrysts; 20%–30% vesicles

Note: Boundaries were extended to the next change in lithology when contacts were not recovered.

and mesostasis. The groundmass phases display elongate quench textures. Microlitic plagioclase laths are up to 0.3 mm in length and randomly oriented. Clinopyroxene occurs as very fine acicular quench crystals that form fanlike bundles. Many of the clinopyroxene crystallites appear to have nucleated on plagioclase microlites and intergrowths of the two phases are common. Olivine (<0.1 mm) is a very minor, yet ubiquitous groundmass phase. The grains are euhedral and always very fresh. Magnetite is the dominant opaque phase (identified in reflected light) and comprises about 2% of the groundmass. The grains are very small (0.002–0.004 mm) and form a fine dusting in the cryptocrystalline groundmass. Cr-spinels (<0.04 mm) are present in trace amounts, either enclosed in or adjacent to large plagioclase phenocrysts. The remainder of the groundmass is interstitial mesostasis, which

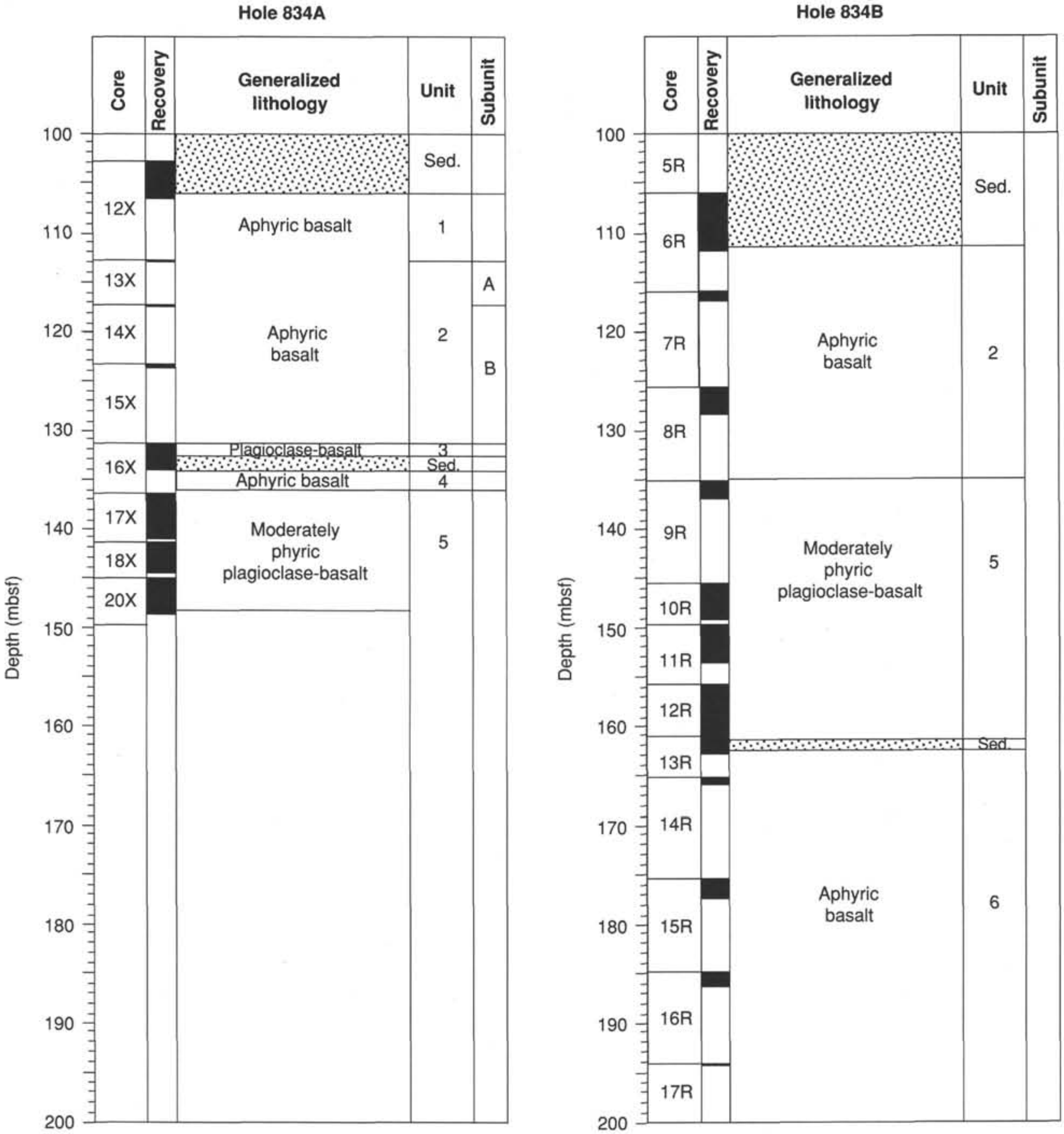

Figure 38. Stratigraphic summary of lower parts of Holes 834A and 834B, showing core recovery, unit boundaries, and sedimentary interbeds (stippled).

has undergone varying amounts of alteration to very fine grained blue-green to brownish clays.

The vesicle content ranges from 10% to 45%, and their size varies from 0.04 to 1.0 mm (less commonly to 4 mm). They tend to form elongate, irregular shapes because of the coalescing of several smaller vesicles. In some portions of the unit, the vesicles are partially filled with brown-green to reddish brown clay minerals.

Alteration of Unit 1 is minimal, with the development of secondary minerals limited to partial replacement of the mesostasis by very fine-grained, greenish brown clays, and partial infilling of the vesicles with a similar material. Locally, iron-oxyhydroxides and radiating crystals of calcite have developed both adjacent to, and within, fractures.

Unit 2

Aphyric Basalt

Unit 2 is an aphyric, intergranular, textured basalt. Subunit 2A is dense, glassy, and nonvesicular along the quenched margins and is associated with clasts of baked calcareous sediment in Hole 834A; in Hole 834B a similar vesicular basalt is interfingered with indurated sediment (Fig. 41). Subunit 2A is relatively fresh; in

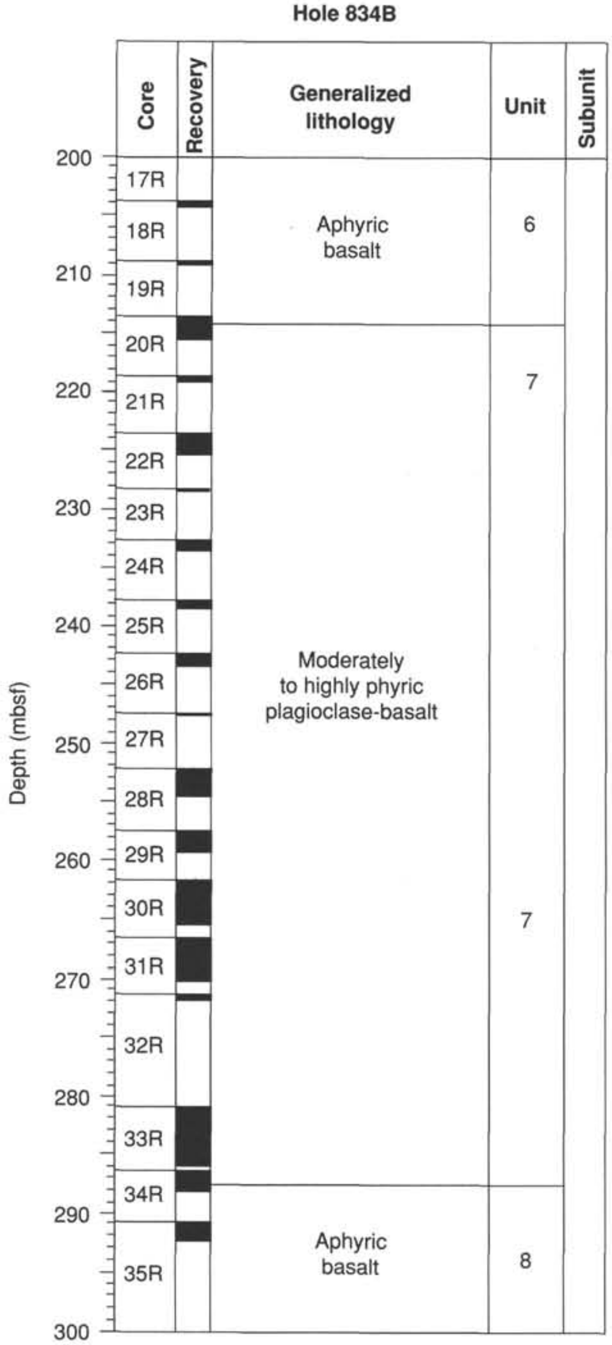

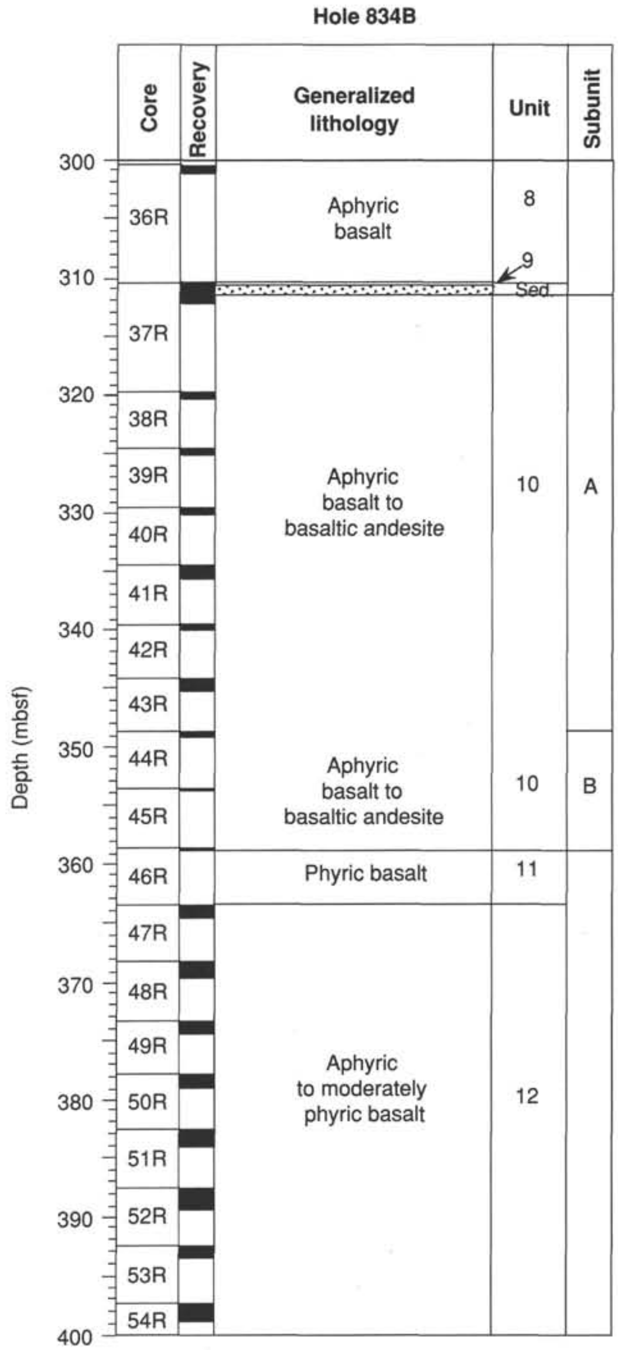

Figure 38 (continued).

Hole 834A it extends from near the top of Core 135-834A-13X to about 44 cm in Core 135-834A-14X, and in Hole 834B from 135-834B-6R-CC to -8R-2, 145 cm. In Hole 834A, a thin sediment interbed separates Subunit 2B from Subunit 2A in Core 135-834A-14X; it is represented in Section 135-834A-15X-1 from 15 to 100 cm. Because of poor core recovery, the actual thicknesses of these units and the core recovery within them cannot be accurately estimated.

Unit 2 contains occasional euhedral plagioclase phenocrysts; these comprise <1% of the rock volume and range in size from 0.2 to 0.8 mm. The larger plagioclase crystals tend to be zoned; narrow, more sodic rims (to about An_{50}) are common. The plagioclase phenocrysts tend to form glomeroporphyritic clusters. The early stages of resorption of the plagioclase phenocrysts are indicated by scalloped edges and resorbed regions in the interiors. Fresh, subhedral clinopyroxene phenocrysts (up to 1.4 mm) are rarely present.

The groundmass includes plagioclase, clinopyroxene, and mesostasis with minor magnetite and olivine. Randomly oriented plagioclase microlites are up to 0.4 mm in length. The plagioclase microlites are often zoned with distinct narrow sodic rims. Groundmass clinopyroxene is subhedral to anhedral and typically equant. Rarely, acicular clusters up to 0.2 mm in length have developed. Fresh, euhedral, isolated olivine grains are a minor, sporadic groundmass component. Magnetite (<0.03 mm) is the only opaque phase. The skeletal to cruciform magnetite crystals

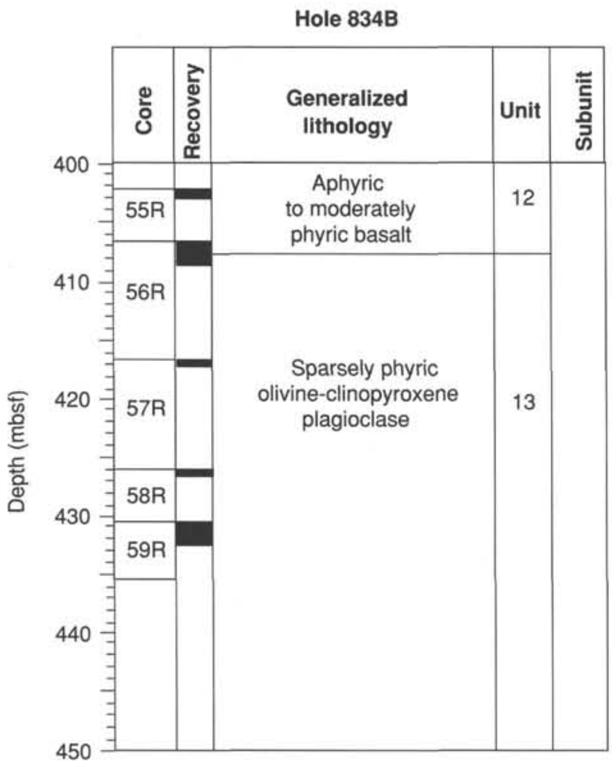

Figure 38 (continued).

form a fine dusting in the cryptocrystalline groundmass. The development of hematite on many of the magnetite rims indicates oxidation of the grains. Interstitial mesostasis comprises 15%–20% of the rock. Much of this brown cryptocrystalline material has broken down into extremely fine-grained green-brown clays.

This unit is partly distinguished by its very high vesicle content (up to 30%). There is a bimodal size distribution of the vesicles (Fig. 42), with large, round vesicles commonly up to 2 mm across, and abundant very small (<0.1 mm) vesicles distributed evenly throughout the groundmass. The large vesicles may be arranged in near-vertical, pipelike zones (Fig. 43). Most of the vesicles are at least partially filled with fine-grained yellow-green clays and/or radiating calcite crystals.

The most coarsely vesicular patches are enclosed by darker gray and very finely vesicular material that contains quench plagioclase and clinopyroxene aggregates (Fig. 44). The contacts with the enclosing host lava are gradational but very narrow. The vesicle content within these quenched lava globular patches is often up to 80%. The origin of these dark globular patches is uncertain, but they may represent squeezing of separate residual lava pockets into previously developed vesicles. Alternatively, they may be incompletely mixed blebs of a separate magma batch within the main body of Unit 2 lava during eruption. They are similar to the segregation vesicles that have been described in deep-sea basalts (Sato, 1978).

Unit 2 shows only very minor alteration. Some plagioclase phenocrysts contain patches of very fine-grained clays. Locally, high proportions of the mesostasis have broken down into fine-grained brownish green clays. Yellow-green, often radiating, clays and zeolites fill or partially fill many of the vesicles. Amorphous iron-oxyhydroxides have developed adjacent to fractures. Narrow calcite veins and calcite-filled vesicles are found in the deeper portions of Unit 2 in Hole 834B and are likely to be related to the thick veins of indurated carbonate sediment that were recovered nearby.

Unit 3

Sparsely to Moderately Phyric Plagioclase Basalt

Unit 3 was recovered only in Section 135-834A-16X-1, 0–20 cm, above a sedimentary interbed; fragments of baked sediment confirm that the recovered material is close to a contact. This is a sparsely to moderately phyric plagioclase basalt; like many of the recovered lavas it is microvesicular with a very porous texture. Plagioclase is the only phenocryst phase, averaging <5% of rock volume. Euhedral phenocrysts range up to 3 mm in diameter and occur both in glomeroporphyritic clusters and as isolated crystals in a microcrystalline groundmass. Narrow sodic rims are common, as are inclusions of dark cryptocrystalline material.

The groundmass consists of roughly equal proportions of plagioclase and clinopyroxene with minor amounts of unaltered mesostasis. Olivine was not identified in the groundmass. The groundmass plagioclase and the larger clinopyroxenes form notably elongate crystals (up to 0.7 mm) with random orientations. Trace amounts of Cr-spinel and minor magnetite occur in the mesostasis.

This highly vesicular unit contains 30%–35% vesicles (up to 3 mm in diameter). The vesicles are generally empty, but a thin lining of cryptocrystalline clays or amorphous silica is present in some. Alteration is minimal except for minor and localized replacement of the mesostasis by pale brownish green, fine-grained clays.

Unit 4

Aphyric Basalt

Unit 4 was recovered as loose fragments in Section 135-834A-16X-CC; no equivalent was found in Hole 834B. No baked sediment occurs with these fragments; thus, the contact with the overlying sediment interbed is interpreted as being depositional. The rock fragments are aphyric basalt and are vesicular on both macroscopic and microscopic scales. They probably represent flow-top breccia intermixed with the sediment. It is possible that this material actually represents the quenched top of Unit 5; this hypothesis is supported by mineralogic and chemical similarities between these units.

This essentially aphyric basalt contains very rare euhedral plagioclase phenocrysts up to 1.3 mm across in a matrix of microcrystalline plagioclase (30%–35%), clinopyroxene (20%–25%), opaques (1%–2%), and mesostasis (10%–15%), much of which has been altered to very fine-grained, green-brown clays. The few phenocrysts that are present show indications of incipient alteration, with scalloping of the margins and resorption of patches within the interiors. The groundmass phases all show elongate quench textures, and complex intergrowths of the plagioclase microlites and acicular clinopyroxene laths are common. Magnetite was the only opaque phase observed. The unit is highly vesicular (35%–40%), and the vesicles are generally unfilled. Alteration is minimal except for minor and localized replacement of the mesostasis by pale brownish green, fine-grained clays.

Unit 5

Aphyric Diabase

Unit 5 appears at the top of Core 135-834A-17X and at the top of Core 135-834B-9R. In Hole 834A, recovery in Cores 135-834A-17X, -18X, and -20X was very high, averaging about 86% for the 13.2 m cored. In both holes, this unit is moderately altered and vesicular on a microscopic to macroscopic scale. Maximum vesicle size varies erratically down through the unit, ranging from 1.5 to 6 mm, although a general downward decrease seems appar-

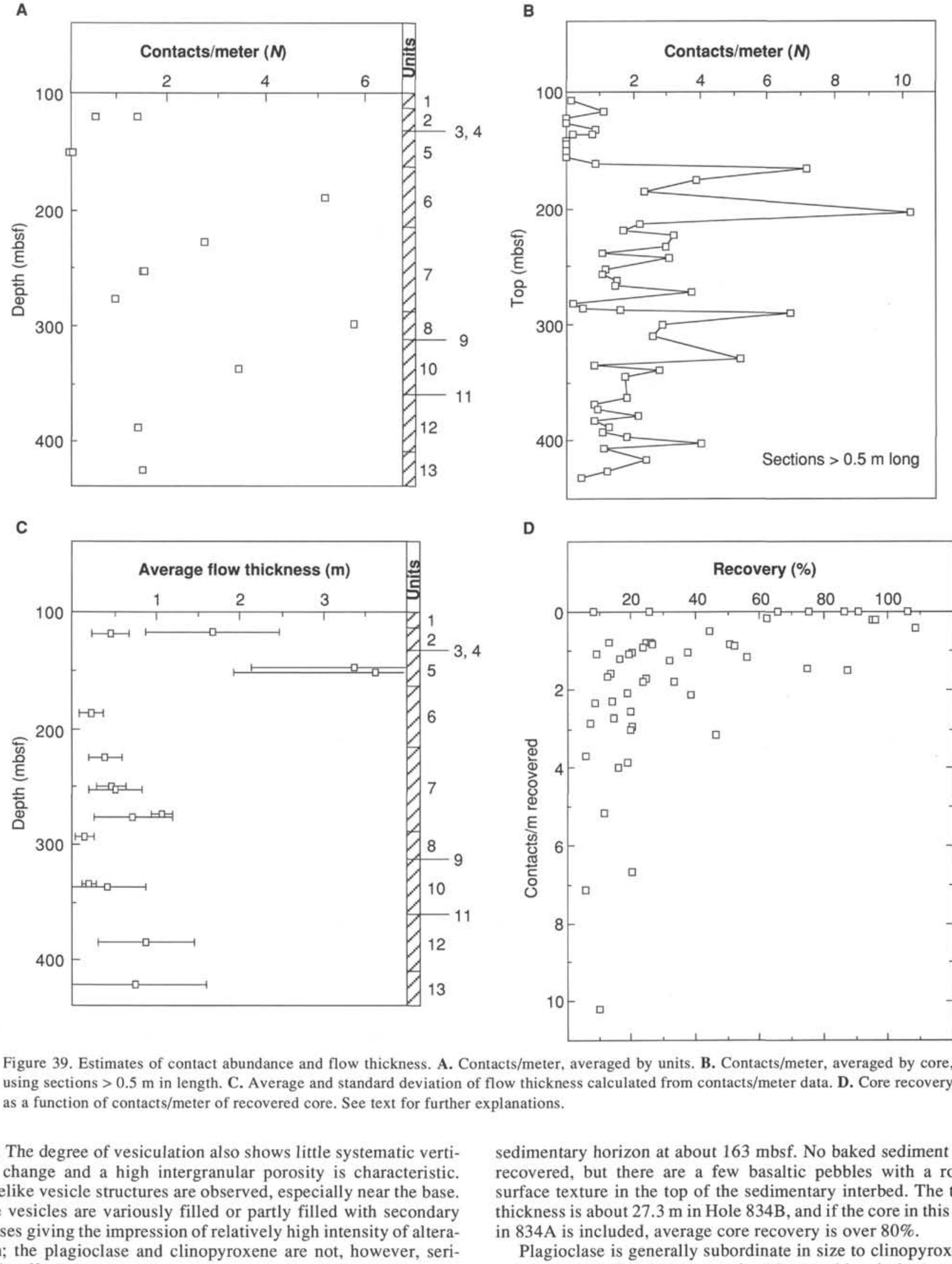

Figure 39. Estimates of contact abundance and flow thickness. **A.** Contacts/meter, averaged by units. **B.** Contacts/meter, averaged by core, using sections > 0.5 m in length. **C.** Average and standard deviation of flow thickness calculated from contacts/meter data. **D.** Core recovery as a function of contacts/meter of recovered core. See text for further explanations.

ent. The degree of vesiculation also shows little systematic vertical change and a high intergranular porosity is characteristic. Pipelike vesicle structures are observed, especially near the base. The vesicles are variously filled or partly filled with secondary phases giving the impression of relatively high intensity of alteration; the plagioclase and clinopyroxene are not, however, seriously affected.

The base of this unit is marked by a transition from massive diabase with prominent pipe vesicles overlying a thin (35 cm) sedimentary horizon at about 163 mbsf. No baked sediment was recovered, but there are a few basaltic pebbles with a ropey surface texture in the top of the sedimentary interbed. The total thickness is about 27.3 m in Hole 834B, and if the core in this unit in 834A is included, average core recovery is over 80%.

Plagioclase is generally subordinate in size to clinopyroxene, but there are a few large enough to be considered phenocrysts. The largest of these are euhedral and up to 2 mm long. They tend to be strongly zoned with sharply defined sodic rims. Many show

Table 13. Generalized petrographic characteristics of rock units defined at Site 834.

Unit and lithology	Phenocryst (%) Phases present	Groundmass (%) Phases present	Vesicles (%) Infilling	Comments
Unit 1 Aphyric to plagioclase bearing basalt	0%–2% plag > ol	55%–95% plag > cpx > ol + mesostasis	10%–45% <1 mm Minor infilling	
Unit 2 Aphyric basalt	Trace plag > cpx	65–80% plag > cpx >> ol + mesostasis	20–35% <2 mm Extensive infilling	Patches of quenched vesicular material fill some vesicles Olivine extremely rare
Unit 3 Moderately phyric plagioclase basalt	3%–5% plag	60% plag = cpx + mesostasis	30%–35% <3 mm Trace infilling	Olivine not present
Unit 4 Aphyric basalt	0%–1% plag	60%–65% plag > cpx + mesostasis	35%–40% <3.5 mm Unfilled	Olivine not present
Unit 5 Aphyric, poikilitic, plagioclase basalt	1%–2% plag	80%–85% plag > cpx + minor mesostasis	10%–20% <6 mm Extensive infilling	Large (up to 4 mm) cpx oikocrysts enclose small (<0.5 mm) plag microlites
Unit 6 Aphyric to sparsely phyric basalt	Trace plag > cpx	50%–70% plag > cpx > ol + mesostasis	30%–50% <1.5 mm Minor infilling	Patches of quenched vesicular material fill some vesicles
Unit 7 Moderately to highly phyric plagioclase basalt	10%–25% plag >> cpx	75%–90% plag > cpx >> ol + mesostasis	Nonvesicular	
Unit 8 Aphyric basalt	Trace plag > cpx	60%–80% plag > cpx + mesostasis	20%–45% <6 mm Minor infilling	Patches of quenched vesicular material fill some vesicles olivine not present
Unit 9 Moderately phyric ol–plag basalt	5%–11% plag > ol	60%–80% plag > cpx >> ol + mesostasis	7%–20% <1 mm Moderate infilling	Patches of quenched vesicular material fill some vesicles
Unit 10 Aphyric basaltic	None	70%–85% plag > cpx > ol + mesostasis	15%–30% <6 mm Minor infilling	Patches of quenched vesicular material fill some vesicles
Unit 12 Aphyric to moderately phyric plagioclase basalt	0%–15% plag > cpx	75%–90% plag > cpx + mesostasis	10% <1 mm Extensive infilling	Patches of quenched vesicular material fill some vesicles Olivine locally present Petrographic variability Rare clinopyroxene phenocrysts
Unit 13 Moderately phyric olivine-clinopyroxene-plagioclase basalt	<5% plag > ol > cpx	50%–60% plag > cpx > ol + mesostasis	30%–35% <2 mm Trace infilling	Patches of quenched vesicular material fill some vesicles

Notes: Abbreviations are as follows: plag = plagioclase, ol = olivine, and cpx = clinopyroxene.

resorption characteristics such as scalloped edges and internal corroded zonal contacts.

The groundmass is dominated by small plagioclase microlites and large clinopyroxene oikocrysts. The plagioclase microlites are generally <0.5 mm in length and often strongly zoned. They form 35%–45% of the rock. Clinopyroxene oikocrysts (Fig. 45) make up 20%–30% of the rock and in some instances are up to 4 mm across. Much of their volume, sometimes up to 50%, is represented by included plagioclase laths. Patchy, irregular optical zoning and sector twins are observed in some of the pyroxenes.

The fine-grained groundmass between the oikocrysts is composed of intergrown bundles of acicular clinopyroxene and plagioclase, with the plagioclase often exceeding pyroxene in abundance. Opaque phases comprise up to 5% of the groundmass. Magnetite is dominant, occurring as large (0.8 mm) cruciform grains. Ilmenite occurs both as lamellae within magnetite and as discrete small bladed crystals (some skeletal). Trace amounts of Cr-spinels and sulfide globules are also present. The remaining 10%–25% of the groundmass is mesostasis.

Unit 5 has a high and variable vesicle content, ranging from 10% to 20%. The largest are up to 6 mm in diameter, usually because of the coalescing of smaller vesicles. The vesicles are all partially to completely filled with very fine-grained clays and zeolites and, in some instances, with radiating aggregates of calcite. A bimodal size distribution of the vesicles is evident, with one population consisting of those <0.4 mm and the other >1 mm; the smaller population is more abundant and imparts a fine-scale pervasive porosity to the rock.

Pervasive alteration is mainly confined to the groundmass. Breakdown of the mesostasis to fine-grained brown-green clays is the most obvious, locally with development of a green to brown phyllosilicate, possibly stilpnomelane. There is some very early stage alteration of plagioclase, and replacement of groundmass pyroxene by clays. Thus, it is sometimes observed that plagioclase

Table 14. Summary of modal analyses from representative thin sections.

Leg	135	135	135	135	135	135	135	135	135	135	135	135
Site	834A	834A	834A	834A	834A	834A	834A	834A	834B	834B	834B	834B
Core, section	12X-CC	13X-1	13X-1	14X-1	15X-1	16X-CC	16X-2	18X-1	10R-1	14R-1	18R-1	20R-1
Interval		0–10	24–29	6–7	26–40	11–13	28–30	113–114	36–37	32–33	33–39	104–108
N	1181	1207,1046	1026	891	1115	1117	1048	1605	1240	1181	1001	972
Unit no.	1	1	2A	2B	2B	3	4	5	5	6	6	7
Phenocrysts:												
Plagioclase	0.8	0.2–0.96	0.3	0.2	<0.1	2.7	0.1	0.7		1.0	0.3	11.1
Olivine	0.2									0.2	0.3	0.3
Clinopyroxene			<0.1							0.3		
Total phenocrysts	1.0	0.6	0.3	0.2	0.0	2.7	0.1	0.7	0.0	1.5	0.6	11.4
Groundmass:												
Plagioclase	16.9		20.7	23.6	34.8	20.2	20.7	41.0	39.8	5.3	6.5	27.0
Clinopyroxene	40.5		29.9	29.0	22.1	27.9	26.1	21.5	21.9	1.5	0.4	38.6
Olivine	3.6		0.3							0.8	0.4	0.2
Opaques	2.3	1–1.2	4.9	2.4	3.1	1.1	1.2	3.4	2.5	0.8	Tr	4.0
Mesostasis	23.8	80.9–82.7	15.5	16.4	17.3	17.9	23.4	19.3	21.4	62.9	67.7	17.7
Total groundmass	87.1	83.0	71.3	71.4	77.3	67.1	71.4	85.2	85.6	71.3	75.0	87.5
Vesicles:												
Infilled vesicles	1.1		2.6	0.4	7.8	7.2		9.7	5.3	0.7		0.6
Open vesicles	10.9	12.0–16.2	25.8	28.1	14.9	23.0	28.6	4.4	9.1	25.8	24.4	0.5
Total vesicles	12.0	14.1	28.4	28.5	22.7	30.2	28.6	14.1	14.4	26.5	24.4	1.1

Leg	135	135	135	135	135	135	135	135	135	135	135	135
Site	834B	834B	834B	834B	834B	834B	834B	834B	834B	834B	834B	834B
Core, section	30R-3	31R-3	35R-2	36R-1	37R-1	37R-1	37R-2	43R-1	47R-1	56R-1	57R-1	59R-2
Interval	105–107	16–19	121–122	20–21	3–5	46–47	61–62	107–110	27–30	7–9	64–65	22–24
N	1019	1062	1000	1026	1169	1000	957	1108	1054	1051	1076	1124
Unit	7	7	8	8	9A	9B	10A	10A	12	12	13	13
Phenocrysts:												
Plagioclase	15.7	10.5	0.5	0.1	7	8.0			5.3	0.7	2.3	2.3
Olivine	0.9	0.3	0.1		0.6	1.8			0.7	0.6	0.9	0.2
Clinopyroxene			0.3	0.3						0.7	1.3	2.1
Total phenocrysts	16.6	10.8	0.9	0.4	7.6	9.8	0.0	0.0	6.0	2.0	4.5	4.6
Groundmass:												
Plagioclase	45.0	39.8	20.2	11.3	19.4	21.0	13.3	14.1	22.4	19.9	15.4	23.6
Clinopyroxene	30.0	29.1	18.3	12.8	35.2	24.1	3.6	4.7	12.7	3.0	5.2	11.7
Olivine	2.3	2.2	0.1		2.1	1.3	0.9		0.1	1.8	1.4	1.5
Opaques	3.2	4.9	0.8	2.1	2.5	2.9	0.8	2.4	2.9	2.0	1.7	2.7
Mesostasis	2.7	13.3	38.0	27.4	19.3	29.5	50.6	51.4	43.6	52.1	46.4	24.1
Total groundmass	83.2	89.3	77.4	53.5	78.5	78.8	69.2	72.7	81.7	78.8	70.1	63.6
Vesicles:												
Infilled vesicles			0.9	13.4	3.1	1.7	4.8	5.5	5.9	0.8	1.2	0.4
Open vesicles	0.2		20.8	32.8	10.9	9.7	26.0	21.8	6.3	17.8	24.2	31.4
Total vesicles	0.2	0.0	21.7	46.1	14.0	11.4	30.8	27.3	12.2	18.6	25.4	31.8

Note: *N* = number of points counted.

microlites enclosed in the clinopyroxene oikocrysts tend to be unaltered compared with those that have not been protected by a poikilitic host. Iron-oxyhydroxides and anhedral to radiating calcite crystals have developed along fractures.

Unit 6

Aphyric to Sparsely Phyric Basalt

Unit 6 begins at about 163.4 mbsf, beneath a thin sedimentary horizon that separates it from Unit 5 in Section 135-834B-13R-2. In hand specimen, most samples are aphyric basalt, although the limited number of thin sections examined range from aphanitic to glomeroporphyritic. This probably is a pillowed flow, as suggested by numerous quenched glass margins. Although these margins are relatively dense, the pillow interiors are microvesicular, giving the surface a spongy texture. Alteration varies from slight to moderate. The base of this unit is 214 mbsf, near the top of Core 135-834B-20R at about 35 cm, for a total thickness of about 50.6 m. Core recovery was relatively poor, averaging a little less than 10%.

Although Unit 6 is generally aphyric, rare euhedral plagioclase phenocrysts (up to 1 mm across), olivine phenocrysts (euhedral to skeletal up to 0.6 mm), and subhedral to euhedral microphenocrysts of clinopyroxene (0.2–0.4 mm across) are present. Locally, well-developed glomerocrysts consist of acicular or

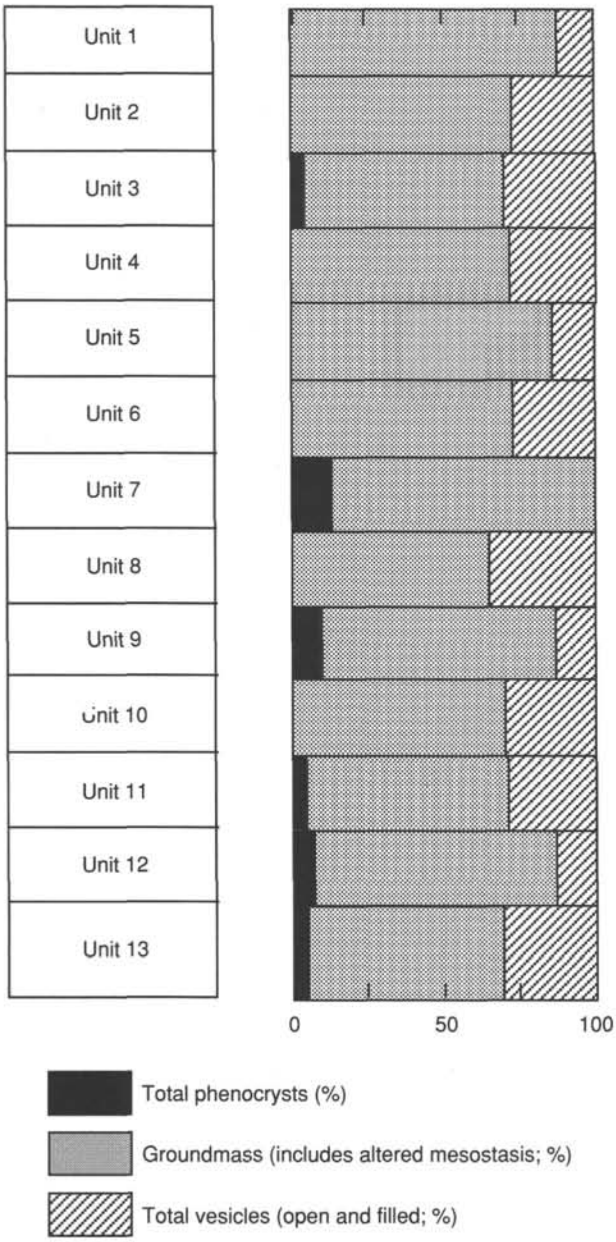

Figure 40. Graphic summary of modal analyses of selected samples. Note that all percentages are based on point counts ($N > 1000$) for at least two thin sections from each unit, except in the case of Unit 11, which was estimated from macroscopic observations.

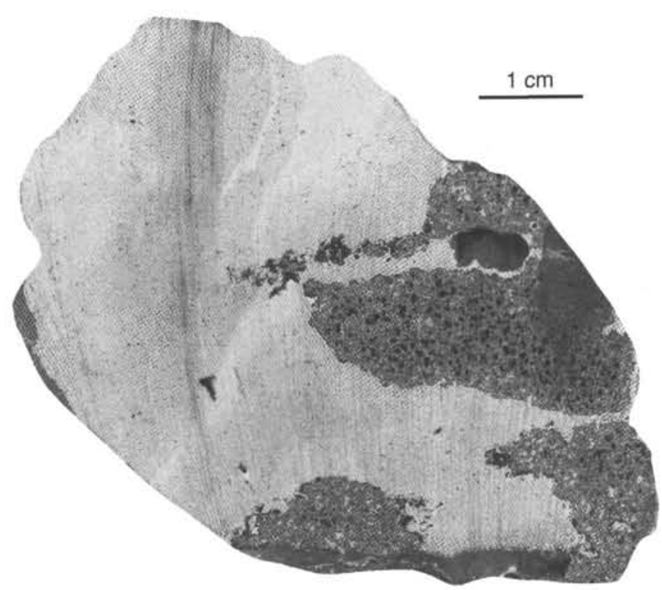

Figure 41. Fine-grained, recrystallized carbonate intermixed with aphyric vesicular basalt; Subunit 2A, Sample 135-834B-7R-1, Piece 13; the carbonate appears to be recrystallized calcareous ooze.

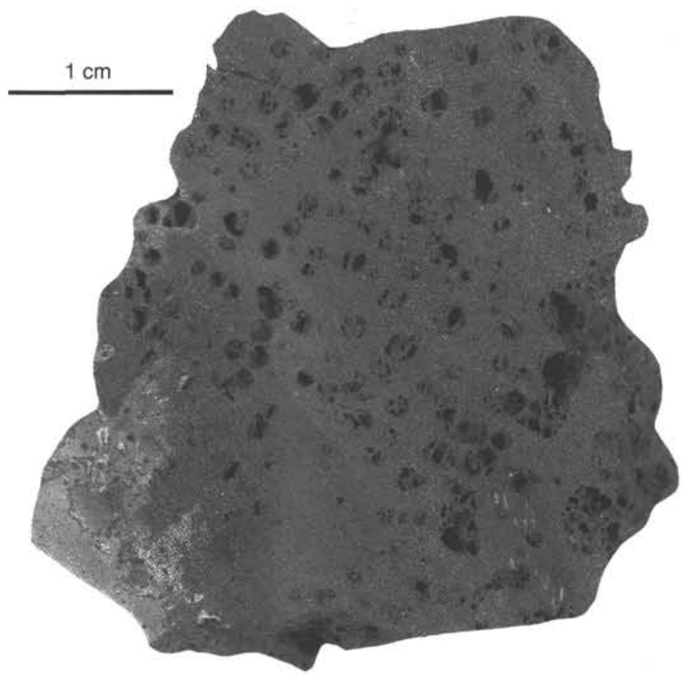

Figure 42. Aphyric basalt with small rim of recrystallized carbonate and a bimodal vesicle population; Subunit 2A, Sample 135-834B-15X-1, Piece 2; note the fine-scale porosity of the groundmass. The sample also exhibits a frothy, quenched filling in many of the larger vesicles.

tabular plagioclase that radiate from central cores of clinopyroxene or cluster randomly with olivine. Much of the clinopyroxene is sector-zoned, and some shows extreme quench growth deformation as revealed by sweeping extinction shadows (Fig. 46). The groundmass is composed of varying proportions of microlitic, acicular, and often skeletal plagioclase (including swallowtail morphology), clinopyroxene, olivine, opaques, and mesostasis showing finely developed quench textures (Fig. 47). These consist of quench crystallites of plagioclase and clinopyroxene complexly intergrown into variolitic and feathery aggregates. Euhedral olivine is a minor (<3%), yet ubiquitous, component of the groundmass. Opaque phases are limited to very small (<0.02 mm) magnetite granules that form a fine dust in the groundmass. The cryptocrystalline mesostasis comprises up to 70% of this unit, but it is typically replaced by extremely fine-grained, greenish brown clays.

The vesicle content is high and variable, ranging from 20% to 50%. The vesicles are generally empty but may have a thin lining of greenish brown clays. They range in size up to 1.5 mm. Distinctly darker, very highly vesicular globular patches (up to 4 mm) have vesicle contents up to 70%. Their groundmass con-

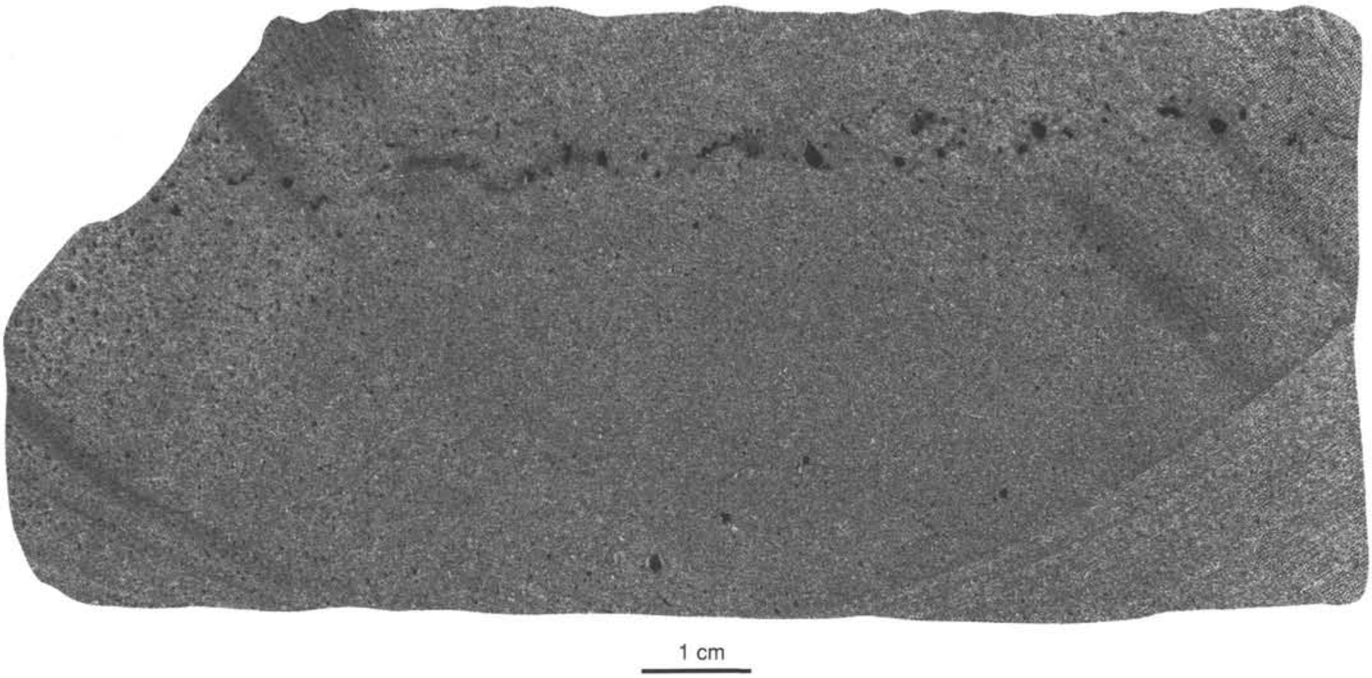

Figure 43. Pipelike distribution of vesicles in aphyric basalt; Subunit 2B, Sample 135-834A-15X-1, Piece 11; similar structures occur at the bottom of Unit 5.

tains quenched plagioclase and olivine grains and large amounts of very fine-grained magnetite. The large amount of very fine-grained magnetite crystals and the high porosity readily distinguish these regions from the host rock. As in Unit 2, they may result from filling of early formed large vesicles by an iron-enriched and volatile-enriched interstitial magma.

Alteration is minimal in Unit 6 except for minor localized replacement of the mesostasis by pale brownish green, fine-grained clays. Iron-oxyhydroxides have developed adjacent to fractures; anhedral and radiating calcite crystals fill occasional veins.

Unit 7

Highly Phyric Plagioclase Basalt

Unit 7 is the thickest of the defined igneous units, extending from 214.3 mbsf in Core 135-834B-20R to about 288 mbsf in Core 135-834B-34R, for a total thickness of about 74 m. Core recovery is variable, reaching 96% in Core 135-834B-33R, but averaging about 33% over the whole interval. It is a moderately to highly phyric plagioclase basalt, and like Unit 6, appears to be made up of pillowed flows. Glassy margins are more abundant in the upper part of the unit, suggesting that it is made up of relatively small pillows. The lower half of Unit 7 is more massive, with fewer quenched margins, although these do appear both at the top and bottom of large cooling units. Unit 7 lacks the spongy microvesicular texture of Unit 6, and also shows more evidence of low-temperature alteration. The base of this unit in Core 135-834B-34R is marked by a few fragments of baked sediment.

This unit is distinct in containing relatively abundant plagioclase phenocrysts, up to 5 mm diameter with prominent melt inclusions aligned parallel to the c-axis. These euhedral crystals are usually glomeroporphyritic and show strong zoning, with distinct rims of more sodic compositions (Fig. 48). Minor euhedral to subhedral olivine phenocrysts are present, ranging in size from 0.5 to 1.8 mm, and also tend to occur as glomerocrysts. The plagioclases show scalloped margins and internal resorbed zonal contacts in their cores; some minor patchy clay development occurs within the grains.

The groundmass consists of randomly oriented plagioclase microlites (up to 1 mm in length), distinctly more sodic than the bulk of the phenocryst compositions, together with elongate to acicular clinopyroxene. The acicular clinopyroxenes often form fanlike radiating aggregates (Fig. 49). Equant grains of olivine up to 0.3 mm are a minor, yet ubiquitous, groundmass phase. Magnetite forms 1%–3% of the groundmass, occurring as equant, anhedral, and cruciform skeletal grains and aggregates, most commonly about 0.1 mm across. Cr-spinel and ilmenite blades are trace minerals. The remainder of the groundmass comprises cryptocrystalline interstitial material that has been largely altered to greenish brown clays.

Vesicles or voids are extremely rare in this unit (<1% of the rock volume), and when present they are usually filled with greenish brown microcrystalline clays.

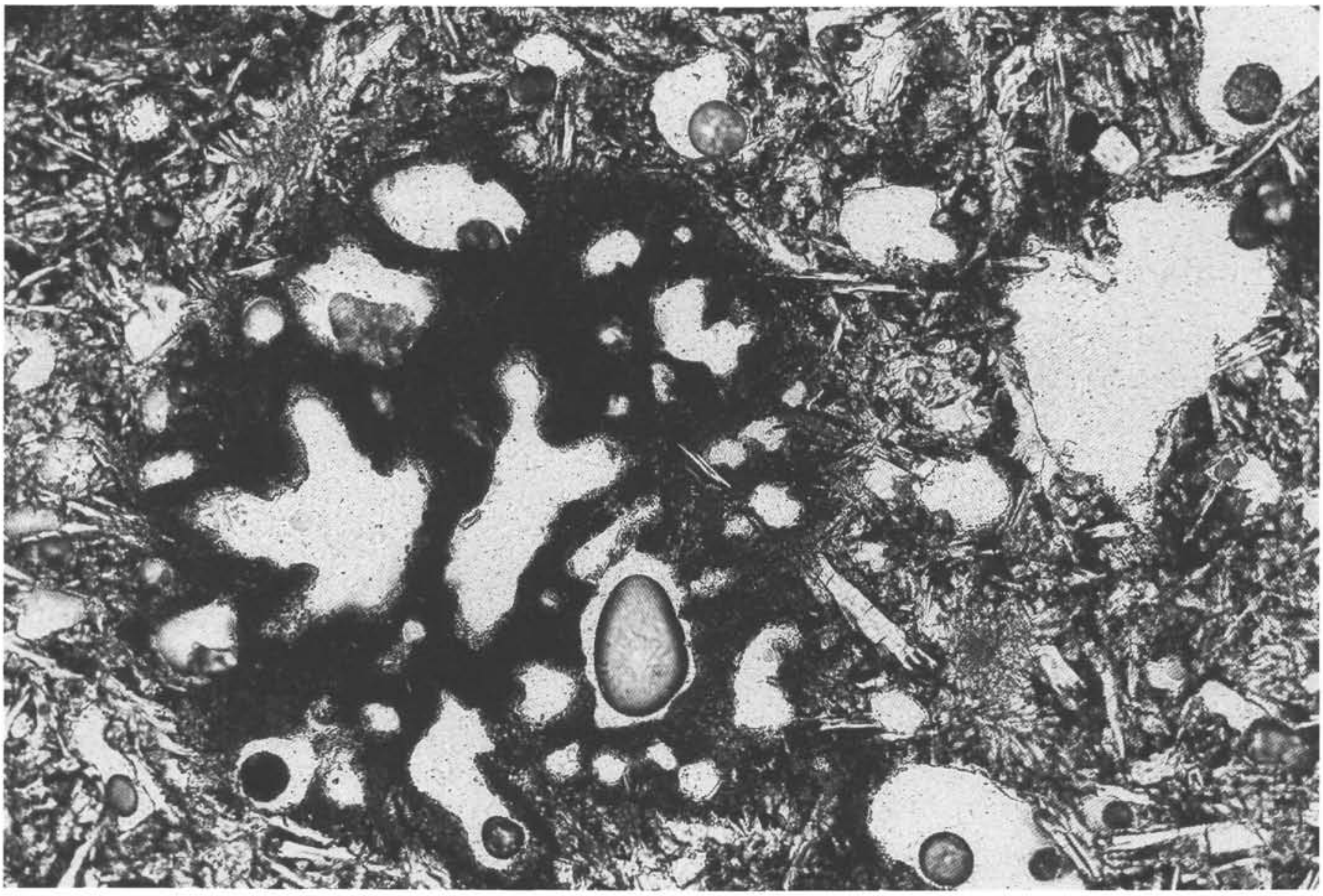

Figure 44. Frothy dark lava filling large vesicles in host lava, which is a common feature in many of the basalts in Holes 834A and 834B; Subunit 2A, Sample 135-834A-14X-1, Piece 1; field of view = 1.5 mm, ordinary light.

Alteration of Unit 7 is minimal and is limited to minor and localized replacement of the mesostasis with fine-grained clays. Breakdown of mineral phases is minor, but some plagioclase is slightly resorbed and contains patches of very fine-grained clays. Iddingsite has formed on rims and in the fractures of the olivine grains. Iron-oxyhydroxides have developed adjacent to fractures, and occasional zeolites fill veins. Alteration halos tend to run parallel to fractures or pillow margins; brownish alteration is common in the variolitic zone beneath glassy rims.

Unit 8

Aphyric Basalt

Unit 8 continues from the baked sediment contact below Unit 7 in Section 135-834B-34R-2 to Section 135-834B-36R-1, at 301.1 mbsf, for a thickness of 13.5 m. Core recovery averaged about 14%. It is aphyric basalt, characterized by small clinopyroxene-plagioclase glomerocrysts and minor olivine microphenocrysts enclosed in a highly microvesicular, almost pumiceous dark gray glass. Numerous glassy margins again suggest that this is a pillowed flow; fractures filled with indurated sediment are common.

This unit contains only sporadic traces of euhedral plagioclase and clinopyroxene phenocrysts. The main part of the lava is composed of microlitic plagioclase, clinopyroxene, and minute magnetite grains. The lathlike to microlitic plagioclase grains are rarely equant and are up to 0.6 mm in length. Clinopyroxene occurs both as equant subhedral to anhedral crystals and as acicular radiating aggregates up to 0.3 mm in length. Minute interstitial magnetite grains (<0.08 mm) vary from equant, to acicular, to skeletal. The abundances of these phases range from 40% to 45% for plagioclase and from 30% to 40% for clinopyroxene; magnetite values reach as high as 2%. The remaining interstitial mesostasis (5%–15% by volume) is cryptocrystalline.

This unit is strongly vesicular, with 20%–45% vesicles as large as 6 mm in diameter. Many vesicles contain a secondary filling of highly vesicular (60%–80%) quenched material, which itself contains quenched plagioclase and clinopyroxene set in a cryptocrystalline groundmass. These are similar in appearance to the quenched globular patches observed in Units 2 and 6.

Alteration is slight and patchy, with development of yellow-green to orange-brown microcrystalline clays locally replacing mesostasis.

Unit 9

Moderately to Highly Phyric Olivine Plagioclase Basalt

Unit 9 consists of two subunits separated by a thin interval of whitish indurated sediment. Subunit 9A is a thin moderately phyric olivine plagioclase basalt flow unit at the top of Core 135-834B-37R. It is petrographically equivalent to Subunit 9B; both are characterized by abundant plagioclase phenocrysts. The total thickness of the Unit 9, based on recovered core, is only

Figure 45. Clinopyroxene oikocryst with plagioclase inclusions; Unit 5, Sample 135-834A-20X-2, 81–82 cm; field of view = 6 mm, crossed polars.

about 35 cm. Unit 9 is noticeably microvesicular, but it is less pumiceous in texture than is Unit 8. Euhedral plagioclase, up to 1.5 mm, and euhedral to subhedral olivine, up to 1 mm, comprise the phenocryst phases. Their abundances range between 5%–10% and 0.6%–2%, respectively. Both tend to occur together in glomeroporphyritic aggregates.

Groundmass phases are plagioclase, clinopyroxene, olivine, magnetite, and mesostasis. The plagioclase forms randomly oriented elongate tabular crystals, up to 0.6 mm in length. These grade into smaller microlitic crystals, their abundance ranging between 20% and 35%. Clinopyroxene occurs as both equant (intergrown with plagioclase) and acicular aggregates up to 0.5 mm in length, constituting 25%–35% by volume. Olivine is relatively minor (1%–3%) and forms discrete equant, euhedral to subhedral crystals up to 0.2 mm diameter. Magnetite (1%–3%) forms very small (<0.05 mm) skeletal grains in the mesostasis. The mesostasis is interstitial, microcrystalline, and is extensively altered to a brown-green material that may be mixed chlorite-clay products.

Samples of this unit are vesicular (7%–20%), with partial infilling and lining of vesicles by brown-green (?) mixed chlorite-clay and iron-oxyhydroxides. These infillings are irregularly developed. As in Units 2, 6, and 8, there are discrete dark, rounded globular patches up to 10 mm diameter. These are highly vesicular (up to 75% of each patch), the remainder consisting of quenched basaltic lava (with quenched-textured plagioclase and clinopyroxene). Their contacts with the enclosing host lava are sharp, but nevertheless there is a zone of size gradation between the infilled material and the host rock.

Alteration in Unit 9 is minimal and is confined to partial and local replacement of the mesostasis by brownish green, fine-grained clays. Iron-oxyhydroxides have developed adjacent to veins.

Unit 10

Aphyric Basalt to Basaltic Andesite

Unit 10 is divided into two subunits. Subunit 10A is represented by 33.9 m of aphyric basaltic andesite to basalt, which begins beneath upper Miocene sediment in Section 135-834B-37R-2 at about 311.4 mbsf. It is separated from another 9.9 m. of petrographically equivalent aphyric basalt (Subunit 10B) by a thin sediment interbed at 345.3 mbsf in Section 135-834B-43R-1. Subunit 10B begins in Section 135-834B-44R-1 at 348.8 mbsf and ends at 358.7 mbsf in Section 135-834B-46R-1. Core recovery in Subunit 10B was very poor, averaging only about 5%.

No phenocrysts were found in this unit. The microcrystalline to microlitic groundmass consists of plagioclase (20%–36%), clinopyroxene (5%–10%), olivine (3%–5%), magnetite (1%–2%), and mesostasis (30%–40%). The plagioclase forms elongate tabular crystals (up to 0.6 mm) grading to a meshwork of smaller microlites. The larger crystals show narrow, more sodic rims. Clinopyroxene forms smaller interstitial anhedral grains, some partially intergrown with plagioclase, and also larger subhedral elongated to acicular crystals (up to 0.3 mm), some developed into radiating aggregates. The larger clinopyroxenes exhibit the shadowy optical extinction patterns and often show the markedly curved crystal and cleavage outlines typical of clinopyroxene

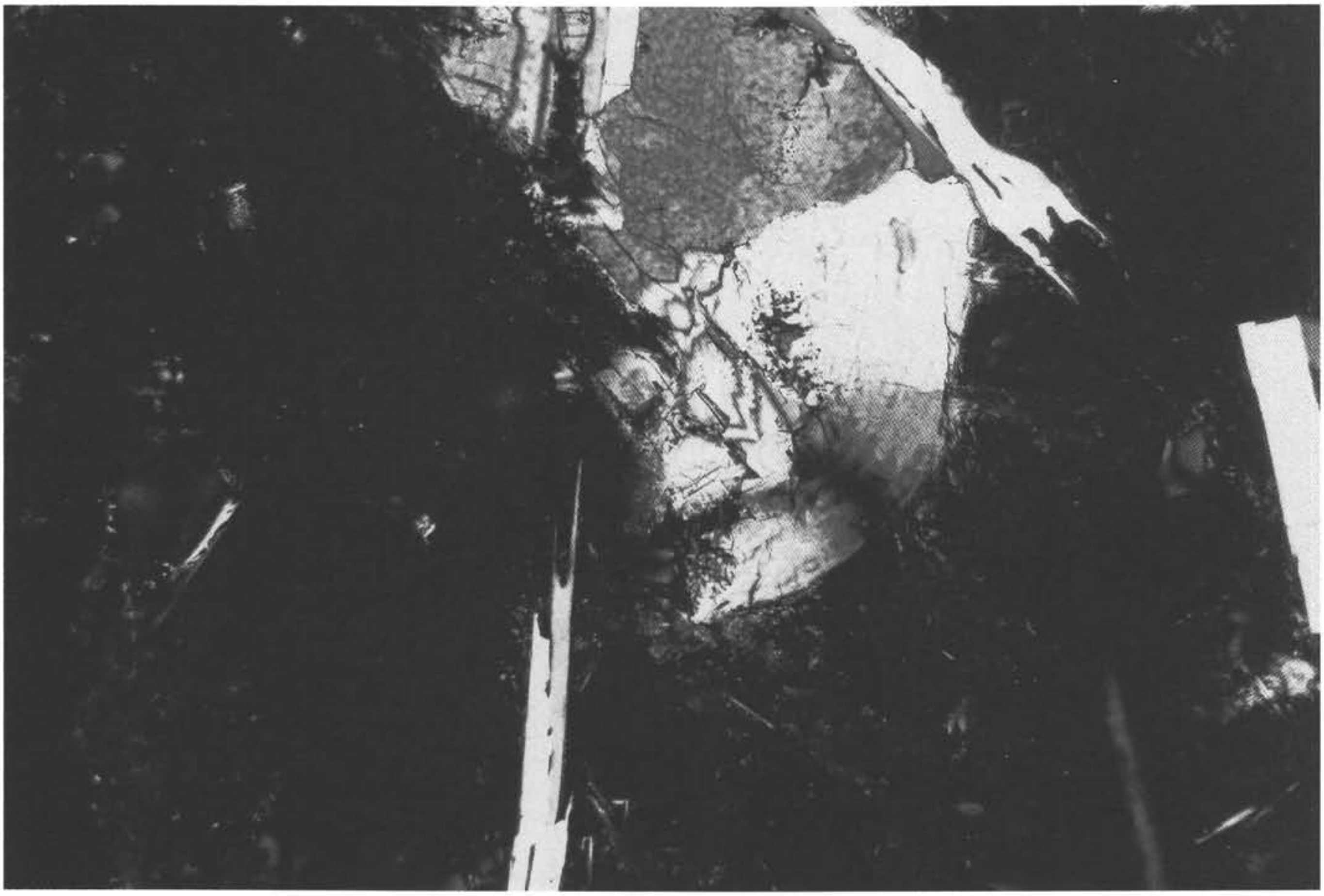

Figure 46. Clinopyroxene microphenocryst illustrating a highly curved growth deformation; Unit 6, Sample 135-834B-14R-1, Piece 7B. This is typical of clinopyroxenes in many of the basalts in Holes 834A and 834B.

growth deformation in water-quenched basalt (Bryan, 1972; Frey et al., 1974). Olivine, up to 0.3 mm, normally forms isolated euhedral to subhedral short prismatic to equant crystals, some of which are hollow. Iddingsite is developed along cracks and grain boundaries in some olivines. Magnetite grains are typically very small (maximum 0.08 mm, more commonly <0.01 mm) and occur within the mesostasis. They display a variety of forms, ranging from euhedral (larger grains) to anhedral, lathlike, and skeletal grain aggregates. The mesostasis is cryptocrystalline (almost vitreous) to microcrystalline. It is dark brown in color when unaltered but is locally replaced by yellow to yellow-brown (?), mixed chlorite-clay phases showing fibrous to microspherulitic textures. These are locally oxidized to reddish brown, nearly isotropic iron-oxyhydroxides.

Samples are highly vesicular, with abundances ranging from 15% to 30%. Their sizes tend to be bimodal, with 0.05–0.3 and 0.5–6.0 mm groupings. Flow banding defined by aligned vesicles is well developed within this unit (Fig. 50). Discrete, darker, rounded globular patches up to 6.0 mm diameter are again present (see also descriptions of Units 2, 6, and 9). These are themselves highly vesicular, with vesicles up to 4.0 mm in some examples (commonly up to 3.0 mm) and which make up greater than 75% of the volume of the globular patches. The remainder consists of quenched basalt showing microcrystalline to cryptocrystalline quenched plagioclase-pyroxene-magnetite aggregates, and an absence of clearly defined and discrete groundmass crystals. The contacts of these patches grade very rapidly into the groundmass of the enclosing host lava.

Unit 11

Sparsely Phyric Olivine-Plagioclase Basalt

This unit begins directly beneath Subunit 10B at 358.7 mbsf. It is represented by only two pieces in Section 135-834B-46R-1, for a recovered thickness of about 4 cm. Because of the small size of the sample recovered, detailed shipboard studies (including thin section petrography) have not been conducted on this unit.

Unit 12

Aphyric to Moderately Phyric Clinopyroxene-Plagioclase Basalt to Olivine-Clinopyroxene-Plagioclase Basalt

Unit 12 starts at the top of Core 135-834B-47R (363.5 mbsf) and ends in Section 135-834B-56R-2 at 407.9 mbsf, giving a total thickness of 44.5 m. There are very sparsely scattered phenocrysts of plagioclase and clinopyroxene; however, this unit has a pronounced seriate texture and the distinction between phenocrysts and the groundmass is indefinite. As a result, hand sample descriptions are aphyric and thin section descriptions are sparsely to moderately phyric. Large vesicles occur in streaks or groups and are locally conspicuous; some pieces are highly microvesicular. The larger vesicles are commonly lined with zeolite. Much of the unit is affected by a pervasive low-temperature alteration that is sometimes manifested in very sharply defined multiple alteration fronts. A "kernel" of unaltered basalt is preserved at the bottom of Section 135-834B- 49R-1 and continues into the top of Section 135-834B-50R-1. Here, sulfides are preserved in vesicles

A

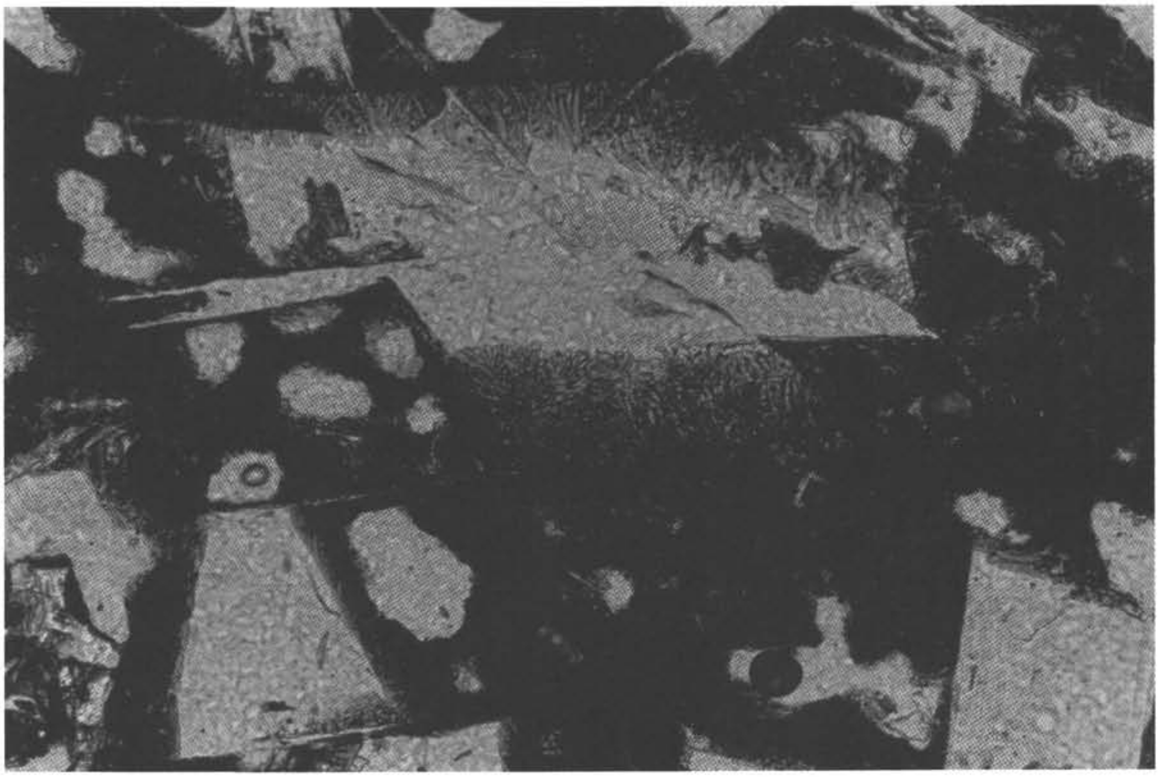

B

Figure 47. **A.** Quench groundmass plagioclase laths showing "swallowtail" and other fine-scale skeletal and acicular overgrowths, set in a dark cryptocrystalline mesostasis; Unit 6, Sample 135-834B-14R-1, Piece 7B; field of view = 1.5 mm, ordinary light. **B.** Feathery quench clinopyroxene nucleated on skeletal plagioclase microlites; Unit 6, Sample 135-834B-18R-1, Piece 10; field of view = 0.3 mm, crossed polars.

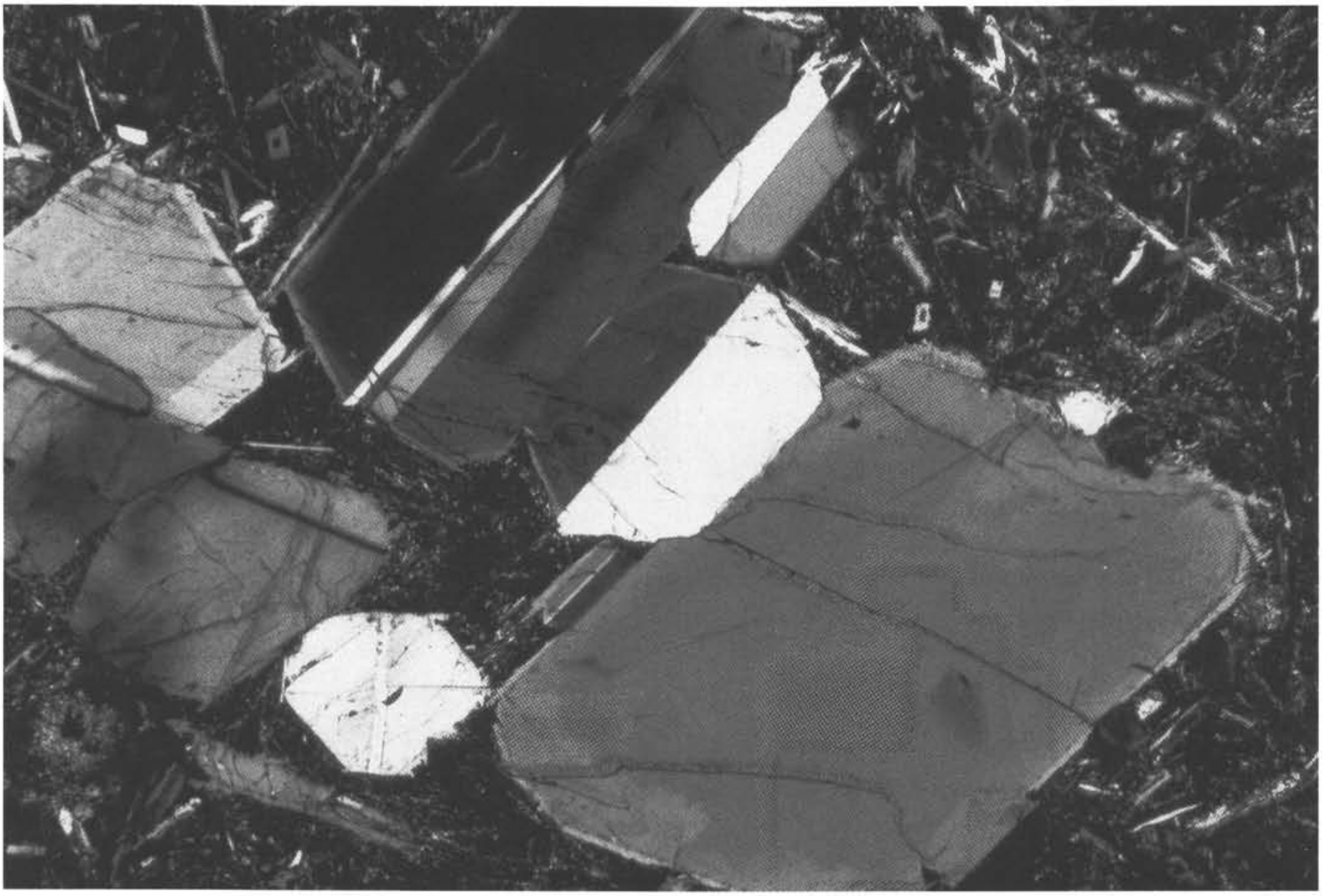

Figure 48. Glomerocryst formed of euhedral plagioclase with narrow, sharp, more sodic rims; Unit 7, Sample 135-834B-30R-3, Piece 16; field of view = 4 mm, crossed polars.

and along fractures, and the basalt has a much darker blue-gray color.

This unit is seriate textured throughout, giving it only a weakly porphyritic appearance. Nevertheless, the larger crystals are classed as phenocrysts. These comprise plagioclase (0.7%–5.0%; 0.7–2.2 mm size range) and clinopyroxene (<1%; 0.2–0.4 mm size range) in the upper part of the unit, but include additional olivine (<1%; 0.2–0.6 mm size range) in the lower part (Table 13). An additional petrographic characteristic is the occurrence and relative abundance of euhedral to subhedral (sometimes skeletal) microphenocrysts of magnetite (0.7%–2.3% to 0.05–0.2 mm size range). These occur as inclusions in plagioclase and clinopyroxene and in the mesostasis. Plagioclase forms normally zoned euhedral tabular crystals, whereas the clinopyroxene is subhedral and equant. Growth deformation of clinopyroxene is unusually well developed, with many of the crystals showing sweeping, shadowy optical extinction and strongly curved cleavage traces.

The plagioclase in the main body of the unit is elongated in euhedral to subhedral laths up to 0.7 mm in length, comprising 20%–35% by volume. Normal zoning is clearly visible in the larger crystals. Clinopyroxene (3%–10%) is subhedral to anhedral, ranging up to 0.2 mm in diameter. It is normally interstitial to plagioclase, especially the smaller grains, and tends locally to develop subophitic form. Groundmass olivine is absent in the upper part of the unit (as is phenocryst olivine), but occurs in the lower part as interstitial subhedral to anhedral grains, <0.2 mm size and <2% by volume. Magnetite, up to 0.02 mm, forms minute skeletal, acicular, trellis structured, and globular grains confined to the mesostasis. The mesostasis is cryptocrystalline to microcrystalline, dark brown when unaltered.

Vesicle abundances are highly variable, from 10% to 40%, with vesicle sizes ranging up to 1 mm diameter (except in the globular inclusions; see below). Partial infilling by fibrous, globular, to microspherulitic green-brown secondary mineral phases (mixed chlorite-clays?) reduces the primary vesicle volume in some samples by 40%–50%. Globular patches of darker quenched basaltic lava, up to 3.5 mm in diameter, are present. As with the previously described examples, these are highly vesicular (vesicles to 2 mm) with the lava composed of skeletal and swallow-tail plagioclase microlites, and microcrystalline feathery and skeletal plagioclase-clinopyroxene-magnetite aggregates and intergrowths. The contacts of these patches, as in the other units, may be sharp or may grade into the matrix of the host lava (Fig. 51).

Much of the mesostasis in Unit 12 is replaced by yellow-brown cryptocrystalline clays. Greenish brown fibrous and radiating alteration products are more pronounced in the upper part of the unit.

Unit 13

Moderately Phyric Olivine Clinopyroxene Plagioclase Basalt

At 407.9 mbsf in Core 135-834B-56R, the aphyric basalt of Unit 12 changes to a moderately phyric clinopyroxene plagioclase basalt, which continues to the base of the hole for a total thickness of 27.8 m. This basalt is seriate textured, with crystal sizes varying continuously from phenocrysts to fine groundmass. Thus, the

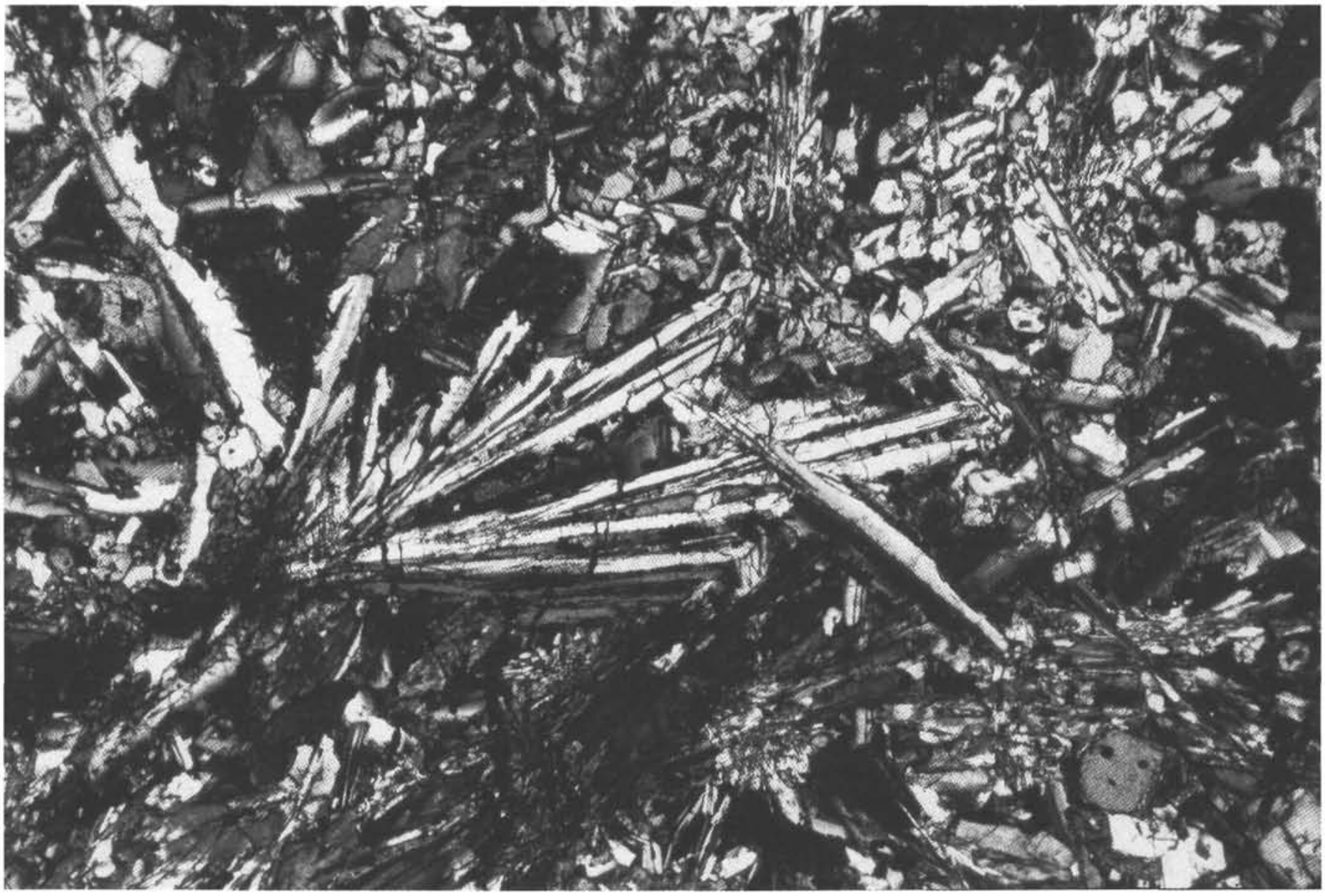

Figure 49. Unit 7, Sample 135-834B-31R-3, Piece 2A; acicular radiating clinopyroxene with intergrown plagioclase forming the bulk of the coarser mesostasis of this sample; field of view = 4 mm, crossed polars.

estimation of modal phenocryst abundances is somewhat arbitrary. Approximate phenocrysts abundances are plagioclase = 2%–3%, olivine < 1%, and clinopyroxene = 1%–2%. Grain sizes are as large as 1.2, 0.6, and 0.6 mm, respectively. The plagioclase occurs as poorly zoned, elongated tabular crystals, euhedral to subhedral, often in glomeroporphyritic aggregates intergrown with subhedral to anhedral clinopyroxene. Olivine is euhedral to subhedral, very rarely with skeletal habit, and occurs both as isolated crystals and (less commonly) in the plagioclase-clinopyroxene glomeroporphyritic aggregates, tending to subophitic. Rarely, there is incipient iddingsitization. One microphenocryst of spinel was found.

Groundmass phases include plagioclase (15%–25%), clinopyroxene (5%–12%), olivine (1%–2%), magnetite (1%–3%), and mesostasis (20%–50%). Plagioclase (up to 0.5 mm) occurs in typical euhedral to subhedral elongate tabular form, grading down to microlite-sized crystals. Clinopyroxene (up to 0.2 mm) is variable in habit, from equant subhedral grains to anhedral interstitial, and less commonly, forms subophitic intergrowths with plagioclase. Very fine-grained interstitial acicular aggregates are also present. Olivine (up to 0.2 mm) is subhedral to anhedral and equant, and commonly occurs as interstitial isolated grains. There are very rare Cr-spinel inclusions in plagioclase. Magnetite (up to 0.05 mm, more usually <0.01 mm) is confined to the mesostasis, forming a variety of complex granular aggregates ranging from equant to rodlike.

The mesostasis in the more rapidly quenched samples from higher in Unit 13 is dark brown, cryptocrystalline to microcrystalline, with patchy development of complex acicular and feathery intergrowths of pyroxene and plagioclase. In lower parts of the unit, the mesostasis is less abundant (less rapid chilling), and shows incipient alteration to yellow-brown mixed clays and iron-oxyhydroxides, evidently controlled by random microfractures. In these lower samples, alteration is again localized and minor. There are occasional vesicle infillings by calcite, yellow-brown or reddish brown mixed clays, and iron-oxyhydroxides, which tend to be localized along microfractures.

Vesicle content is 20%–35% and, as in other units, is strongly bimodal. This unit also has highly vesicular patches of dark lava, representing either frothy fillings of larger vesicles or poorly mixed clots of a different magma.

Petrographic Summary

Initial petrographic examination of the Site 834 samples reveals a number of distinctive and potentially significant features. Although the petrographic characteristics of each unit have been described in detail in the previous section, the following summarizes the general features of the basalts. These are:

1. The lavas are dominantly aphyric to sparsely phyric, with the notable exceptions of Unit 7 (10%–25% phenocrysts) and Unit 9 (5%–11% phenocrysts). Modal analyses using point-count data suggest that the abundance of phenocrysts may increase downhole. Throughout the section, ubiquitous groundmass phases are plagioclase, clinopyroxene, and magnetite.

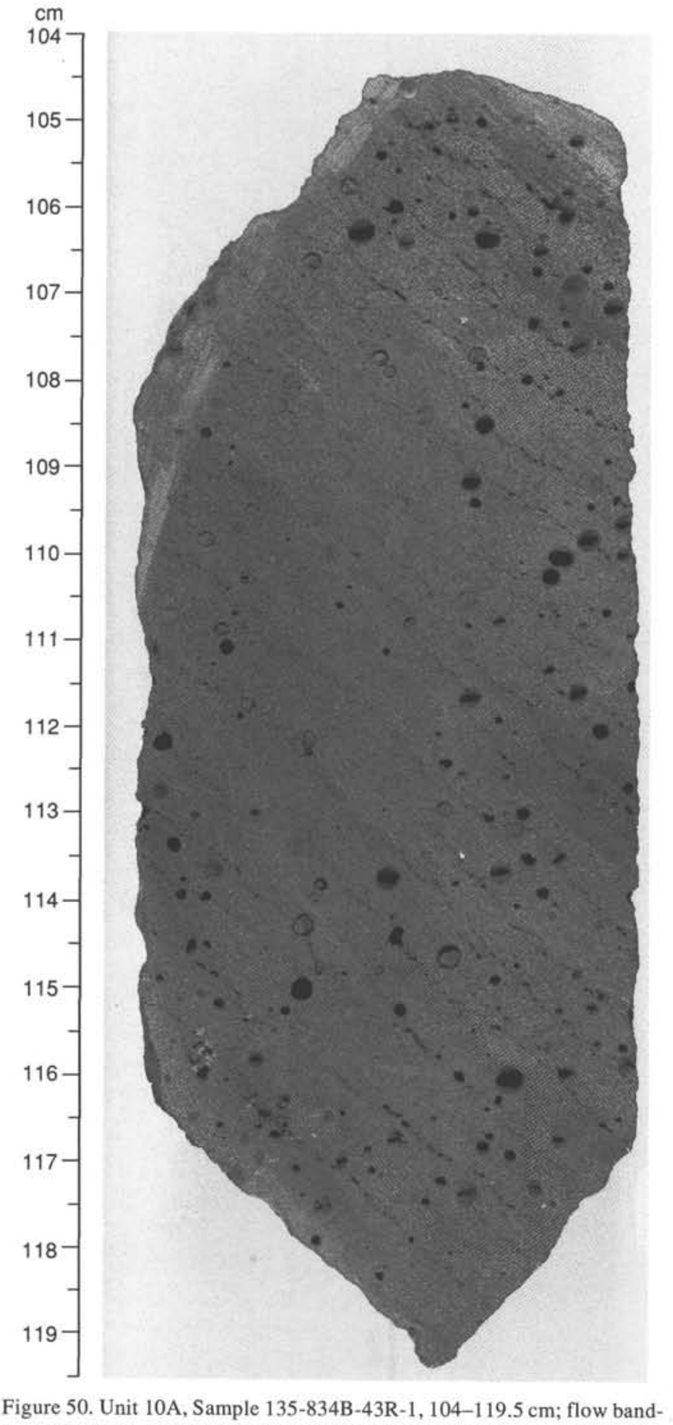

Figure 50. Unit 10A, Sample 135-834B-43R-1, 104–119.5 cm; flow banding defined by aligned trails of vesicles in an aphyric basalt. Note the bimodal distribution of vesicles and the very fine porosity of the groundmass.

2. Calcic plagioclase is the dominant phenocryst phase. Optical properties indicate that its composition is $>An_{70}$, although narrow rims as sodic as An_{50} are common. Clinopyroxene and olivine also occur as phenocrysts, but only rarely do they coexist (e.g., Unit 13 and occasional samples in Units 1 and 6). There is no obvious stratigraphic pattern to the occurrence of the plagioclase + clinopyroxene and the plagioclase + olivine phyric assemblages.

3. Clinopyroxene grains from various units exhibit substantial growth deformation, most apparent as shadowy extinction and curved bent cleavage traces and crystal outlines. These deformed clinopyroxenes are particularly abundant in Units 6 and 12. Although the combination of factors leading to these growth forms are not well understood, they are common in lunar basalts (Dowty et al., 1974) and in water-quenched basalt of appropriate composition (Muir and Tilley, 1966; Bryan, 1972; Frey et al., 1974), and variations in morphology have been reproduced in the laboratory in controlled cooling rate experiments (see Lofgren, 1980, for a review).

4. As noted above, magnetite is present in the groundmass of each unit, but is best developed in Unit 5. Ilmenite is notable by its absence as a primary groundmass phase in nearly all of the units, but rare small-bladed ilmenite grains and sulfide blebs are found in the groundmass of Unit 5. Cr-spinels are observed in Units 1, 3, 5, 7, and 13. These are typically enclosed in or are adjacent to large plagioclase or olivine phenocrysts, but they are occasionally present as isolated grains in the groundmass. Unit 12 is unique in carrying relatively abundant (0.7%–2.3%) clusters of microphenocrystal magnetite.

5. A significant feature of this suite of rocks is the very low degree of alteration of the primary phenocryst and groundmass mineral phases. This is even true for those units in which extensive vesicle infilling and mesostasis replacement has occurred (especially Unit 5). The relatively limited alteration suggests that it was produced by low-temperature (<50°C) waters interacting with the basaltic flows.

6. Samples are remarkably vesicular in all units except Unit 7 (see Fig. 40), with vesicle abundances frequently in excess of 30%. Vesicle sizes range from approximately 0.1 up to 10 mm. Vesicle streams up to 5–6 cm in length have also been noted. In many samples, a bimodal size distribution of the vesicles is apparent, and abundant, very small vesicles produce a significant fine-scale porosity. The larger vesicles are often filled with darker colored, highly vesicular, globular, quenched lava inclusions (discussed below). Vesicles are distributed randomly throughout most of the units. Predictably, flow tops, and in some samples, flow bases, are the most highly vesiculated.

7. A common feature observed in vesicular samples from this hole is the occurrence of dark gray, highly vesicular, globular, quenched lava inclusions, usually ranging in size from 1 to 10 mm. These vary from spherical to amoeboid in cross section, and some are strongly elongated. Maximum vesicle sizes or abundances are usually distinctly higher than in the main body of the host lava, and in all cases examined, these inclusions consist of quenched basaltic lava, usually much finer grained than the host lava groundmass. Their darker color is the result of a much higher abundance of very fine-grained magnetite in the quenched fill material. Contacts with the enclosing host lava groundmass is, as seen microscopically, rapidly gradational, although as in Unit 13, some contacts are quite sharply defined. These globules may be analogous to the segregation vesicles, which seem to have first been described in Australian pillow lavas and which are common in deep-sea basalts (Smith, 1968; Sato, 1978). These highly vesicular fillings can easily be imagined to have occupied preexisting vesicles, driven there by expanding gas. They also might indicate liquid immiscibility, or incomplete mixing of separate magma batches during eruption of the lavas, although the similarity between vesicle fill and adjacent groundmass mesostasis suggests that it is more likely that they are a product of normal cooling and quenching of these highly vesicular lavas.

Alteration Summary

Alteration mineralogy in Holes 834A and 834B is characterized by low-temperature seafloor weathering of extrusive oce-

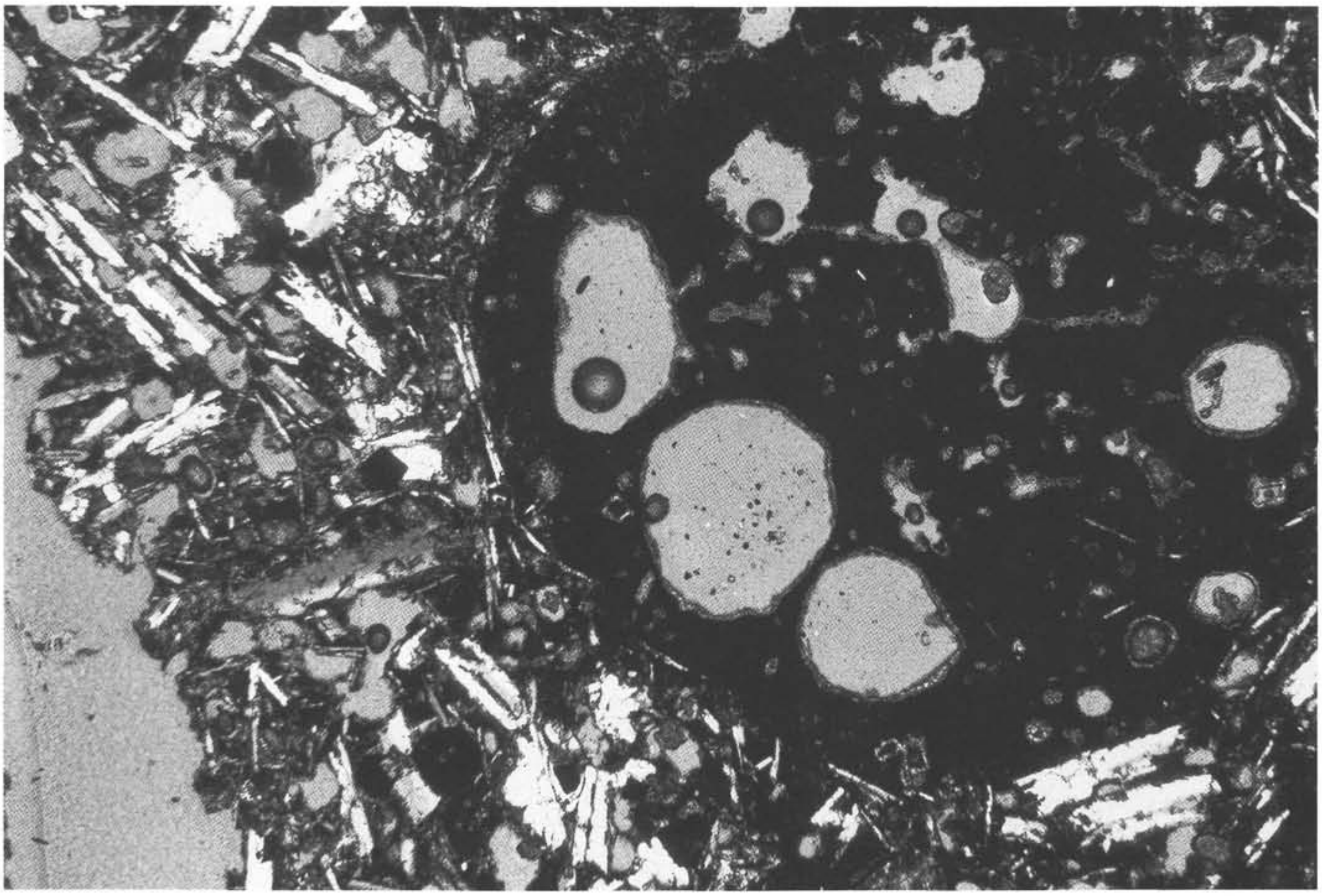

Figure 51. Unit 12, Sample 135-834B-56R-1, Piece 2; example of frothy vesicle filling, in which there are both sharp and gradational contacts with the host lava; note the contrasting vesicle sizes; field of view = 3 mm, ordinary light.

anic rocks. The general features of this alteration are similar to those described for ocean-ridge basalts of similar age (Robinson et al., 1977). Palagonitization of glass and formation of the cubic group of zeolites (mainly phillipsite) is widespread throughout the section cored. In addition, calcite veins up to 3 mm wide occur; these may represent calcium mobilized from interbedded sediment layers. Low-temperature oxidative alteration within the rock pile is also visible because of the presence of iddingsite and chrysotile after olivine, and the occasional turbidity of plagioclase. In addition, celadonitic clay appears as a devitrification product of glass. Iron-hydroxides often line the walls of vesicles and veins. Stilpnomelane has been tentatively identified in a single thin section from Unit 5 (the only occurrence in 42 sections examined). In the lowest part of the section, fibrous zeolites occur that indicate slightly higher temperatures of formation. Exact identification will require shore-based SEM/EDX techniques. The XRD patterns of hand-picked alteration phases indicate the presence of smectite and/or mixed-layer clays, although more specific identification through peak search programs has not been successful.

Geochemistry

Results of XRF analyses of representative samples are presented in Table 15, listed by units and in order of increasing depth. Data, for selected major element oxides, trace elements, and trace element ratios, are shown graphically in Figure 52. The discontinuities in chemical variation with depth in Holes 834A and 834B are consistent with the unit boundaries as defined in the previous section. Units 5 and 7 show the greatest internal homogeneity, as might be expected from their observed petrographic homogeneity and massive character. The suggestion that Unit 4 could be the quenched upper surface of Unit 5 is consistent with the chemical similarities (TiO_2, Na_2O, K_2O, Zr) between these units (Table 15). Differences do exist between Units 4 and 5 (as in MgO and CaO), which may reflect intraflow compositional variations (Fig. 52).

Similarities in major elements are not always matched by the trace element data. For example, the single analysis from Unit 13 is very similar in major element composition to Units 1 and 2 at the top of the volcanic sequence, but is higher in Ni and Cr and lower in V, Ba, and Ce. Overall, Unit 13 most closely corresponds to Unit 8 when both major and trace elements are considered (Table 15). The greatest compositional contrast appears between Units 13 and 12.

In general, there is compositional variation with depth in the cores as indicated by abundances of CaO, MgO, and TiO_2 (Fig. 52A) and by Ba and Zr (Fig. 52B). Only Units 5, 6, and 7 have enough data to permit speculation about intra-unit variation, such as might be caused by crystal settling or by crystal liquid fractionation. Variation is very slight for all components within Unit 5. In Unit 6, the upper three samples are very similar; there may be a slight trend toward a "more evolved" composition at the top of the unit. The lowest sample approaches Unit 7 in composition, which suggests that there was a short transition from Unit 7 to the Unit 6 magma type. In the same way, Units 8 and 9 appear to be

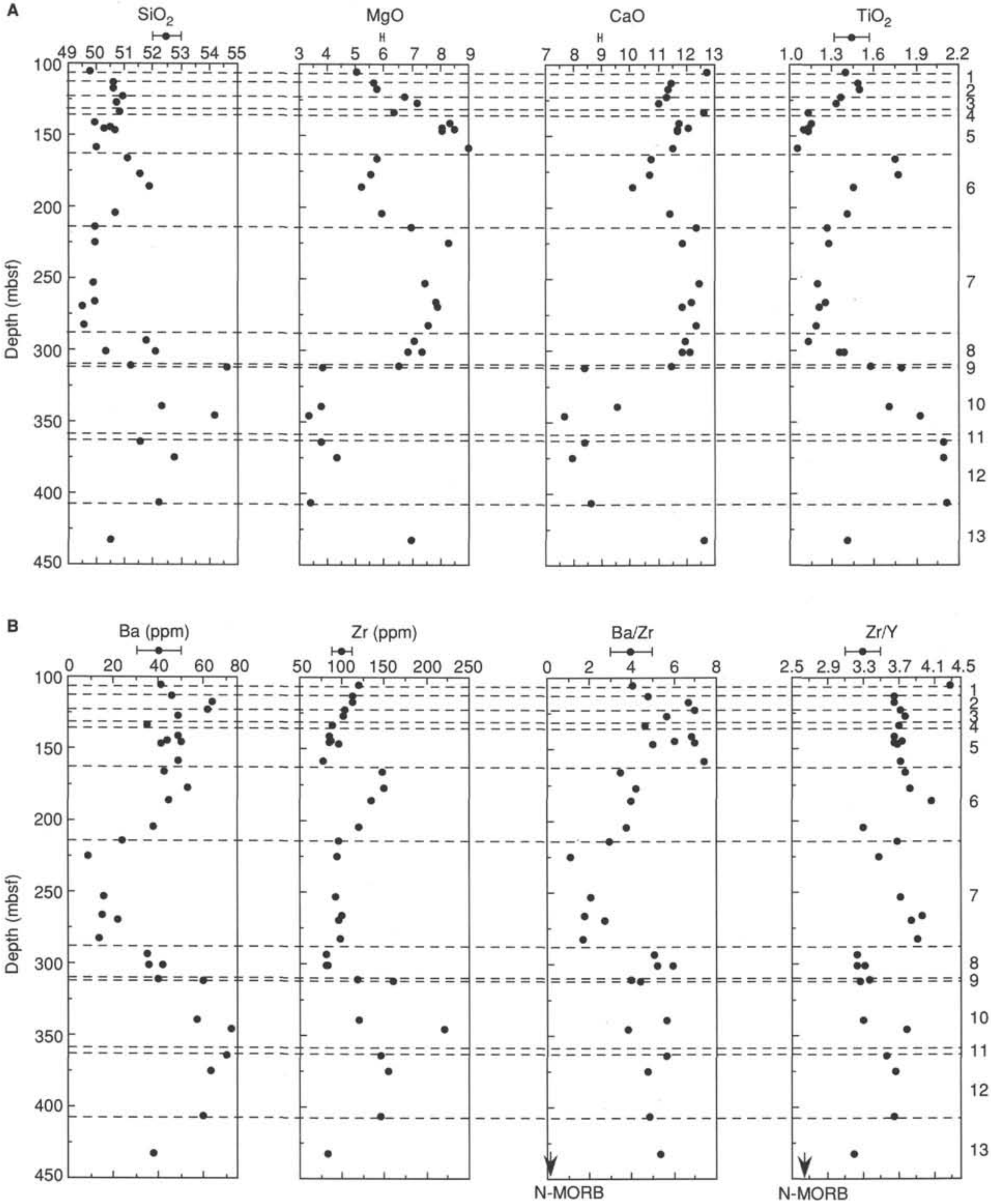

Figure 52. Downhole chemical variation of representative samples. **A.** Selected major element oxides, with values given in weight percent. **B.** Selected trace elements and trace element ratios, with values given in parts per million. Error bars for precision ($\pm 1\sigma$) are based on replicate analyses of reference samples (see "Explanatory Notes" chapter, this volume). Error bars for MgO and CaO are smaller than the symbols.

transitional between Units 7 and 10 in many chemical constituents. The relatively high plagioclase phenocryst content in Unit 7 does not impose a cumulate signature on the chemistry; both the major and trace element concentrations in Unit 7 are very similar to those in Units 5 and 4, which are not highly plagioclase phyric.

The relatively large variation in the ratio of the incompatible elements Ba and Zr probably reflects real magmatic differences because there are sharp breaks at unit boundaries (Fig. 52B). Because Zr is more compatible than Ba, this ratio is not a good indicator of mantle source differences. It can change with varying

Table 15. Major and trace element analyses for representative samples from Site 834.

Unit	1A	2B	2A	2A	2B	4A	5A	5A	5B	5A	5B	6B	6B	6B
Core, section	12X-CC	6R-CC	14X-1	15X-1	8R-1	16X-CC	17X-4	18X-2	10R-1	20X-2	12R-3	14R-1	15R-2	16R-1
Interval (cm)	13–15	19–22	4–6	26–40	105–109	30–33	93–98	114–120	37–43	82–87	66–71	33–40	37–41	113–123
Depth (mbsf)	105.96	112.73	117.04	123.26	127.15	134.13	141.57	144.09	145.77	146.89	158.60	166.03	177.17	186.13
Major elements (wt%):														
SiO_2	49.78	50.58	50.57	50.94	50.70	50.81	49.93	50.49	50.27	50.65	50.00	51.09	51.55	51.86
TiO_2	1.40	1.48	1.49	1.36	1.33	1.13	1.15	1.13	1.10	1.13	1.05	1.75	1.77	1.45
Al_2O_3	17.51	16.50	16.49	16.15	16.24	17.55	17.02	16.89	17.04	16.80	17.20	15.86	15.88	16.71
Fe_2O_3	9.41	10.70	10.82	9.95	10.12	9.04	9.22	8.72	9.22	8.84	8.90	10.36	10.66	10.69
MnO	0.15	0.18	0.18	0.12	0.13	0.13	0.14	0.15	0.15	0.13	0.13	0.17	0.19	0.16
MgO	5.06	5.65	5.77	6.73	7.19	6.34	8.33	8.05	8.50	8.07	8.99	5.73	5.55	5.20
CaO	12.71	11.44	11.36	11.30	11.04	12.59	11.76	12.04	11.66	11.68	11.54	10.74	10.70	10.07
Na_2O	3.08	3.07	3.10	3.08	3.09	2.69	2.54	2.67	2.65	2.64	2.57	3.58	3.51	3.60
K_2O	0.26	0.35	0.36	0.30	0.18	0.11	0.12	0.12	0.12	0.14	0.12	0.33	0.32	0.65
P_2O_5	0.15	0.18	0.18	0.15	0.13	0.11	0.11	0.11	0.10	0.13	0.10	0.20	0.21	0.20
Total	99.48	100.11	100.30	100.08	100.13	100.47	100.31	100.35	100.80	100.19	100.57	99.78	100.33	100.59
LOI	1.01	0.91	0.75	1.78	2.22	0.92	1.71	2.19	1.70	2.30	3.36	1.23	1.67	2.67
Mg#	51.6	51.1	51.4	57.2	58.4	58.1	64.1	64.6	64.6	64.4	66.7	52.3	50.8	49.1
Trace elements (ppm):														
Nb	2	2	2	2	1	2	1	1	1	1	1	2	2	2
Zr	120	113	113	104	102	89	84	86	84	96	78	147	149	134
Y	28	31	31	28	27	24	23	23	23	26	21	39	39	33
Sr	245	211	210	204	187	186	170	176	183	180	170	180	180	197
Rb	5	6	5	3	1	0	1	1	1	1	1	5	5	12
Zn	47	70	68	61	57	37	43	46	42	43	38	73	77	65
Cu	99	55	54	79	74	72	92	82	75	76	82	63	64	54
Ni	53	27	27	54	40	105	81	78	90	80	91	36	37	42
Cr	267	11	6	32	41	234	202	169	148	146	191	87	87	50
Ce	22	16	14	11	13	15	10	6	6	12	7	16	11	14
Ba	41	46	64	62	49	35	49	44	50	41	49	43	53	45

Notes: Mg# represents 100 · (Mg/[Mg + Fe^{2+}]), where Fe^{3+}/Fe^{2+} is assumed to be 0.2. LOI = loss on ignition.

degrees of melting or as a result of fractionation of clinopyroxene. In general, this ratio should decrease as the degree of melting increases and should increase with degree of fractionation. Thus, the high ratio in the otherwise relatively "primitive" Unit 5 is anomalous and may reflect Ba mobilization accompanying secondary alteration of the mesostasis or the deposition of clays and zeolites in vugs in that unit.

As Zr and Y are relatively immobile under low-temperature alteration, the ratio Zr/Y should be a better indicator of source chemistry. It is usually constant for a given magma batch, although these elements may be fractionated at relatively high degrees of crystallization. The variation of Zr/Y within some units (i.e., Units 6 and 7), which could not have experienced much internal fractionation, is therefore also anomalous, as it is as large as the variation between units.

In terms of their major elements and CIPW normative compositions, these basalts are clearly tholeiitic (Fig. 53), as are most arc and backarc rocks recovered from this area (Hawkins and Melchior, 1985; Ewart and Hawkesworth, 1987; Ernewein et al., in press). Also, in many aspects of their geochemistry, and in their projections into the CMAS OL-DI-SI ternary, the Mariana and Lau backarc basin basalt glasses are very similar to MORB (Hawkins and Melchior, 1985). A preliminary comparison of Site 834 trace elements to those of the Holocene dredged lavas indicates that Site 834 volcanic rocks are more similar to those of the Lau Basin backarc than to the modern Tonga island arc, although there is a hint of arc signature in the very low Nb of the Site 834 lavas (Fig. 54). The abundances of the more compatible elements (Ce to Y) are nearly the same in Lau Basin and Site 834 volcanics. The high Rb relative to Ba is also a characteristic of some Lau Basin axial zone glasses as well as some Mariana Trough glasses. However, some primitive glasses from the CLSC have very low Rb, Ba and K, as illustrated in Figure 54.

Geochemical Summary

Chemical analyses of the volcanic rocks from Holes 834A and 834B confirm the distinctions between units defined on petrographic criteria. The narrow transitional zones between some units may indicate limited mixing between successive magma batches passing through a common chamber or conduit system. There is substantial variation downhole from basalt to quartz-normative ferro basalt, approaching basaltic andesite in composition. Variation has not been regular with time but has oscillated between these extremes; the oldest and youngest volcanic compositions sampled are similar. Some units show very subtle internal variations that could reflect minor crystal-melt fractionation during or subsequent to eruption. Compared with modern lavas from this area, incompatible-element enrichment patterns of the Site 834 lavas are more closely related to the Lau Basin backarc setting than to the present-day Tonga Arc.

PHYSICAL PROPERTIES

Introduction

The physical properties measurements made at Site 834 include the standard ODP suite of analyses. Index properties were determined by using a pycnometer and balance, and include bulk density, grain density, porosity, water content, and void ratio. Bulk density was also measured using the continuous gamma-ray attenuation and porosity evaluator (GRAPE) on full APC and XCB cores from Hole 834A. Selected basalt samples from the base of Hole 834A and from throughout Hole 834B were run through the 2-min GRAPE process to determine bulk densities, and some samples were also powdered and the weight and volume of the dried powder determined to give grain density.

Table 15 (continued).

Unit	6B	7B	7B	7B	7B	7B	7B	8B	8B	8B	9B	10B	10B	10B
Core, section	18R-1	20R-1	22R-2	28R-1	30R-3	31R-3	33R-2	35R-2	36R-1	36R-1	37R-1	37R-2	42R-1	43R-1
Interval (cm)	26–35	104–111	29–33	44–50	101–105	19–25	111–115	122–125	21–25	65–68	47–50	62–66	20–23	104–110
Depth (mbsf)	204.26	214.64	224.99	252.74	265.85	269.68	283.15	293.52	300.71	301.15	310.67	312.07	339.30	345.14
Major elements (wt%):														
SiO_2	50.63	49.91	49.95	49.87	49.96	49.51	49.53	51.76	52.09	50.32	51.21	54.59	52.28	54.18
TiO_2	1.41	1.26	1.28	1.20	1.25	1.21	1.19	1.13	1.39	1.35	1.57	1.79	1.70	1.92
Al_2O_3	16.98	17.10	17.12	17.92	17.67	17.57	18.01	16.37	16.75	16.33	16.66	16.31	16.54	16.53
Fe_2O_3	9.56	8.97	9.01	8.44	8.99	8.56	8.58	9.58	9.15	9.16	10.15	10.23	12.04	10.06
MnO	0.16	0.15	0.12	0.12	0.13	0.13	0.12	0.16	0.15	0.14	0.17	0.15	0.18	0.14
MgO	5.91	6.99	8.27	7.46	7.84	7.88	7.58	7.09	6.86	7.33	6.54	3.80	3.76	3.31
CaO	11.40	12.32	11.84	12.44	12.15	11.82	12.33	11.97	12.10	11.83	11.45	8.40	9.51	7.65
Na_2O	3.31	2.71	2.60	2.52	2.59	2.67	2.67	2.54	2.59	2.58	3.01	3.94	3.36	4.67
K_2O	0.31	0.16	0.03	0.02	0.05	0.06	0.04	0.22	0.22	0.19	0.31	0.72	0.69	0.29
P_2O_5	0.21	0.11	0.11	0.11	0.12	0.10	0.11	0.11	0.14	0.12	0.16	0.23	0.19	0.31
Total	99.85	99.66	100.32	100.07	100.74	99.49	100.13	100.92	101.43	99.33	101.21	100.14	100.23	99.05
LOI	0.83	1.36	1.46	0.67	0.79	1.04	1.53	0.41	0.53	1.52	–0.08	1.98	1.94	1.16
Mg#	55.0	60.7	64.5	63.6	63.3	64.6	63.6	59.4	59.7	61.3	56.1	42.4	38.2	39.4
Trace elements (ppm):														
Nb	2	1	1	1	1	2	1	2	1	1	2	2	2	2
Zr	119	96	94	93	99	96	98	81	83	81	118	160	119	220
Y	36	26	27	25	25	25	25	25	25	25	35	49	36	58
Sr	170	164	150	162	168	167	164	159	160	165	142	152	199	182
Rb	5	3	0	1	0	1	0	3	4	3	5	12	12	3
Zn	71	52	49	45	46	44	47	59	58	56	73	94	89	102
Cu	62	72	67	65	67	67	72	66	70	67	64	44	43	38
Ni	70	108	96	100	96	95	89	55	53	52	115	24	24	8
Cr	208	281	254	304	285	313	293	158	137	139	196	17	2	0
Ce	13	7	7	11	8	11	16	9	8	13	16	16	17	22
Ba	38	24	9	16	15	22	14	35	42	36	40	60	57	72

Compressional wave velocities were measured both on whole cores using the continuous P-wave logger and on discrete samples using the Hamilton Frame apparatus. Velocities of unconsolidated sediments were measured in only one direction. Velocities of consolidated sedimentary rocks and basalts were measured in both horizontal and vertical directions.

Vane shear strength was measured on selected undisturbed intervals of the core samples from Hole 834A until the sediment became too stiff (when cracking of the sediment indicated that the assumption of uniform shear by the vane was no longer valid).

Thermal conductivity was measured on undisturbed sediment cores from Hole 834A and on cut cores of lithified sedimentary rocks and basalts from the lower part of Hole 834A and throughout Hole 834B. Details of the physical properties measurement methods are described in the "Explanatory Notes" chapter (this volume).

Two holes were cored at Site 834: Holes 834A (APC and XCB) and 834B (RCB). Hole 834A was drilled to 149.5 mbsf and bottomed in basalt; Hole 834B was washed to about 107 mbsf, just above the basalt, at which point drilling continued with the rotary drill bit. Specific details concerning the coring procedures and depths can be found in the "Operations" section (this chapter). The lithostratigraphic units referenced in this section are those described in the "Lithostratigraphy" section (this chapter). Results from laboratory measurements are listed in Tables 16 and 17 and plotted on Figures 55 through 63.

Index Properties

Hole 834A: Sedimentary Index Properties

Wet-bulk density, grain density, GRAPE continuous bulk density, water content, porosity, and void ratio for sediments and sedimentary rocks from Hole 834A are plotted vs. depth in Figure 55, and values for the gravimetrically determined index properties are listed in Tables 16 and 17. The boundary between sediment and basalt occurred at 112.5 mbsf; data for the basalts are discussed separately. The measured index properties show only moderate changes with depth in the sedimentary section.

Bulk density throughout the hole (Fig. 55) averages 1.53 g/cm^3 on discrete samples and about 1.55 g/cm^3 on the continuous GRAPE data, with only a slight increase in density from the top to the bottom of the hole. Major positive excursions from the average occur throughout the hole; the density variations in the discrete measurements correlate with high density zones in the continuous GRAPE data (Fig. 55) and with high velocity zones in the P-wave logger data (discussed below).

The GRAPE bulk density values have been processed and averaged at 5-cm intervals to remove spurious data points caused by core section ends and voids. The GRAPE data also show little increase with depth, but numerous positive density peaks throughout the GRAPE record reflect the presence of higher-than-average-density sedimentary units; these peaks also commonly are seen on the P-wave logger velocity record (see compressional velocities discussion below). The low-density excursions on the GRAPE record mainly reflect voids or end effects not removed by the routine data processing.

Below about 82 mbsf, the GRAPE densities decrease from about 1.55 g/cm^3 to about 1.50 g/cm^3. Although this decrease is not observed in the discrete bulk-density measurements, the decrease corresponds to a slight decrease in the grain densities of the sediments as measured by gravimetric techniques.

The grain density (Fig. 55) averages 2.71 g/cm^3. A decrease in grain density is present at about 40 mbsf, with values increasing to 80 mbsf. A noticeable decrease in the grain density is present between about 80 mbsf and the top of the basalt at 112.5 mbsf. The top of this zone is near but slightly below the lithologic break between sedimentary Units II and III at 78 mbsf (see "Litho-

Table 15 (continued).

Unit	12B	12B	12B	13B
Core, section	47R-1	49R-1	56R-1	59R-2
Interval (cm)	27–37	131–135	7–15	16–24
Depth (mbsf)	363.77	374.51	406.97	432.59
Major elements (wt%):				
SiO_2	51.51	52.76	52.20	50.51
TiO_2	2.09	2.09	2.11	1.41
Al_2O_3	15.31	15.26	15.71	16.82
Fe_2O_3	13.54	13.50	13.79	9.62
MnO	0.20	0.15	0.20	0.16
MgO	3.78	4.31	3.40	6.97
CaO	8.37	7.91	8.58	12.60
Na_2O	3.84	4.00	3.87	2.62
K_2O	0.53	0.08	0.73	0.24
P_2O_5	0.20	0.20	0.21	0.15
Total	99.33	100.25	100.78	101.08
LOI	1.46	0.71	1.59	1.15
Mg#	35.6	38.7	32.8	58.9
Trace elements (ppm):				
Nb	2	2	1	1
Zr	146	154	146	83
Y	41	42	40	26
Sr	196	189	195	169
Rb	10	0	13	6
Zn	114	105	110	58
Cu	47	46	45	78
Ni	10	5	12	71
Cr	0	0	0	170
Ce	12	12	15	4
Ba	70	63	60	38

stratigraphy" section, this chapter), and density changes may reflect an increasing content of ash within the sediments.

Water content (weight of water/weight of sediment; Fig. 55) ranges between 55% and 134% and averages 107%. Porosity (volume of voids/total volume; Fig. 55) ranges between 61% and 89% and averages 76%. The lowest values of both water content and porosity were measured on samples of sandy nannofossil ooze with foraminifers. The values of water content and porosity ranging above the averages were measured primarily from clay-rich portions of the sedimentary section. Void ratio (volume of voids/ volume of sediment; Fig. 55) mirrors the same trends. The void ratio ranges between 1.6 and 4.3. Again, the lower values are those measured on the carbonate samples and the higher void ratios are typical of clay samples.

The index properties establish a rough physical properties lithology for the sedimentary section. In the plots for water content, porosity, and void ratio, small changes in trend occur at about 40 and 80 mbsf. From 0 to 40 mbsf, all properties are relatively uniform. These properties show a gradual decrease from 40 to 60 mbsf, followed by a gradual, small increase from about 60 to 80 mbsf. Below 80 mbsf, properties are relatively uniform again. These results partly mirror the changes in bulk density and grain density, especially the change at 80 mbsf.

Holes 834A and 834B: Basalt Index Properties

For the basalts from the bottom of Hole 834A (112.5–149.5 mbsf) and from Hole 834B, the index properties determined were bulk density and grain density. The bulk density was obtained using 2-min GRAPE procedures. The grain density was measured by powdering samples of basalt, drying these samples at 110°C for 24 hr, and determining weight and volume with a balance and pycnometer (see "Physical Properties" section, "Explanatory Notes" chapter, this volume). These data are presented in Tables 16 and 17 and plotted vs. depth in Figure 56. Bulk densities for the basalts average 2.67 g/cm^3 and range from 2.20 to 2.99 g/cm^3, whereas grain densities average 2.94 g/cm^3 and range from 2.72 to 3.18 g/cm^3. By comparison, average results for basalts are a bulk density of 2.74 g/cm^3 and a grain density of 3.01 g/cm^3 (Johnson and Olhoeft, 1984).

The data establish three major physical properties lithologic units within the basalt section. Above 186 mbsf (from the middle of Unit 6 to the top of Unit 7), the bulk density averages 2.7 g/cm^3. We have no data between 186 and 215 mbsf. Between 215 and 286 mbsf, the bulk density values are marked higher, averaging 3.0 g/cm^3. Below 300 mbsf, the bulk density decreases to an average of 2.5 g/cm^3. The basalt grain densities (Fig. 56B) show little change, and between 215 and 286 mbsf, the bulk and grain densities are roughly the same. Thus, these changes in bulk density are primarily caused by the changes in vesicularity, and hence porosity, of the basalts. Comparable variations are evident in the compressional velocities from these samples (discussed below). The high-density, high-velocity basalt between 215 and 286 mbsf correlates to Unit 7 of the Lithology column (see "Lithostratigraphy" section, this chapter).

Compressional Wave Velocity

Compressional wave velocity data measured with a Hamilton Frame device and the *P*-wave logger are shown in Figures 57–59 and are listed in Table 16.

In the sediments of Hole 834A, the compressional wave velocity is relatively constant with depth and averages 1480 m/s on the discrete samples and 1510 m/s on the *P*-wave logger data (Figs. 57 and 58). Velocities on the *P*-wave logger data (Fig. 57) show numerous increases that have corresponding increases in density on the continuous GRAPE data (Fig. 58), and correlate with thin turbidite units in the sedimentary section.

Basalt velocities (Fig. 59) show major changes with depth at the same positions as the bulk density changes, and the two data sets outline three distinct lithologic units. At 112.5 mbsf, the transition to basalt is accompanied by an increase in compressional velocity to around 4000 m/s (Fig. 59A). Basalts below 112.5 mbsf in Hole 834A and basalts above 186 mbsf in Hole 834B have an average velocity of 4230 m/s, and range from about 3600 to about 4500 m/s. Velocities between 215 and 286 mbsf average 5040 m/s, with a range from 4500 to 5400 m/s, and with the velocity increasing gradually with depth. Below 300 mbsf, the basalt velocities return to an average of 3920 m/s, slightly slower than in the upper basalt layer, and with a range from 3480 to 4270 m/s.

Velocity measurements of the basalts were made in both horizontal and vertical directions to test for any velocity anisotropy in the basalts caused by flow structure or differential cooling (Fig. 59B). The horizontal velocity measured parallel to the core face (B direction) and the vertical velocity (A direction, along the length of the core) were in good agreement. The horizontal velocity perpendicular to the core face (C direction) differed significantly from velocities in the A and B directions, particularly on samples from between about 200 and 300 mbsf. Because cores are rotated randomly about the vertical axis during coring, the differences in horizontal velocities are unlikely to be real, and more likely reflect experimental error. We think that the most likely source of error is that the samples measured have nonparallel faces in the C direction, as a result of the methods used to cut pieces from the core. Nonparallel faces result in both a poor signal on the Hamilton Frame device, and possibly in a time delay caused by gaps in contact between the sample and the transducer heads of the Hamilton Frame. When we corrected this source of error by insuring that sample faces for the C-direction were parallel (for samples below about 300 mbsf), velocities in the C direction were

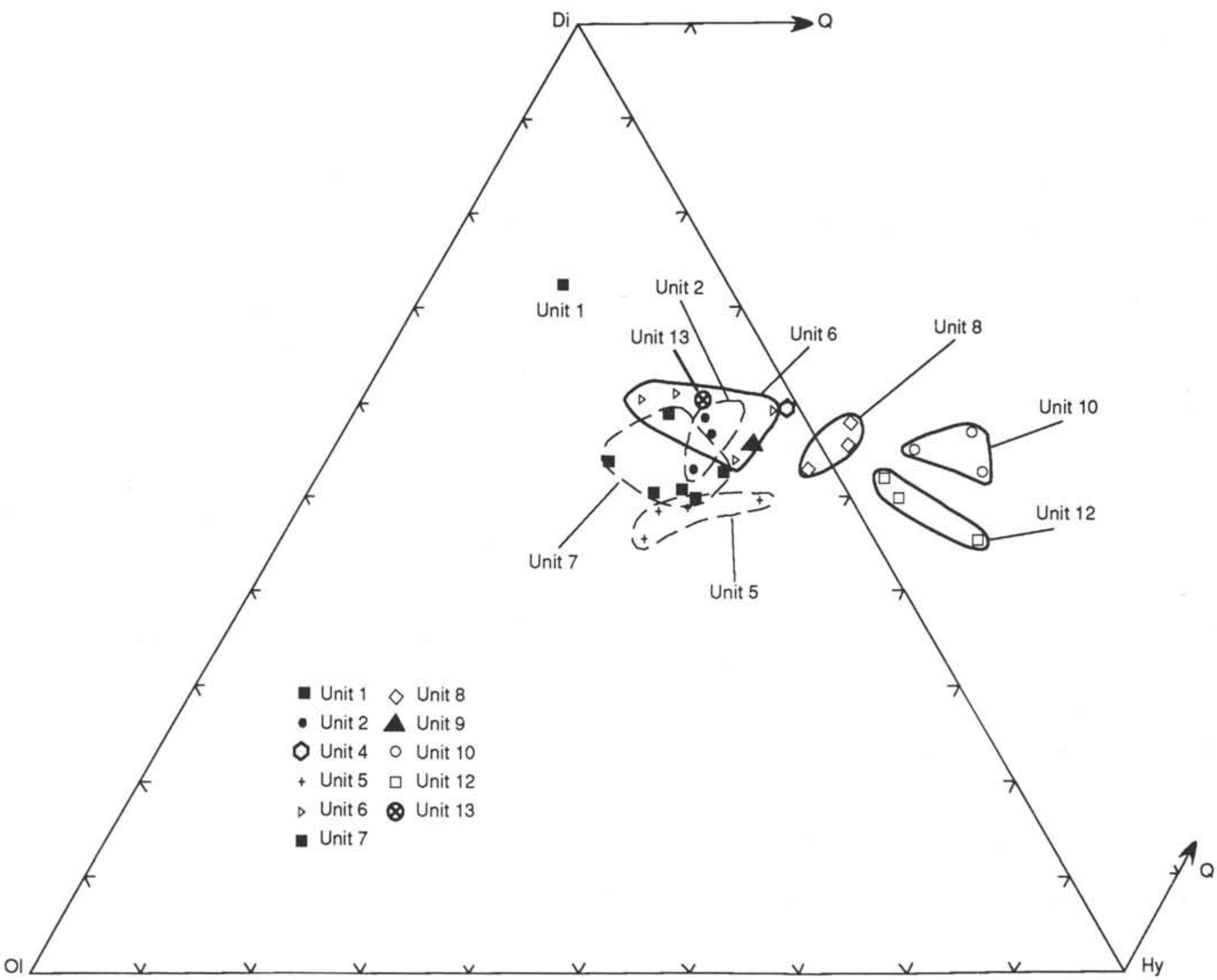

Figure 53. CIPW normative minerals for Site 834, projected onto a ternary diopside-olivine-hypersthene (Di-Ol-Hy) diagram; unit numbers identify various outlined groups or single analyses. Calculations were made using $Fe_2O_3/FeO = 0.2$.

more consistent with the measurements from the other two directions.

Undrained Vane Shear Strength

Values of shear strength in undrained fine-grained sediments were obtained using the standard onboard miniature vane shear apparatus on unconsolidated sediments in Hole 834A; the results are plotted in Figure 60 and reported in Table 16.

The upper 10 m of sediment have very low shear strengths, <10 kPa. At about 25 mbsf, shear strengths increase to about 45 kPa. The low values within the uppermost part of the section were obtained on foraminiferal oozes. The vane shear strength measurement assumes that the sediments tested are undrained fine-grained sediments, rather than coarse-grained sediments with little cohesion. Thus, the measurement was not appropriate in these sediments because they were composed of silt- and sand-size grains. Below 45 mbsf, low shear strengths of about 25 to 40 kPa reflect a change in lithology from the predominantly nannofossil ooze to nannofossil ooze interbedded with ash. Measurements were stopped when the sediment became too stiff for the miniature vane shear apparatus.

Thermal Conductivity

In soft sediment cores, all values were obtained using needle probes inserted through core liners into full core sections. For lithified sedimentary rocks and basalts, the thermal conductivity was measured on the split core face. The thermal conductivity results for both full and split cores are shown in Figure 61 and tabulated in Tables 16 and 17.

Thermal conductivity in the sedimentary section of Hole 834A is fairly uniform although a break is apparent at about 35 mbsf with the conductivity increasing from about 0.9 W/(m · °K) to about 1.1 W/(m · °K). Below about 35 mbsf, low-conductivity values are associated with indurated and fractured sediment. The average thermal conductivity in the sedimentary section is less than 1 W/(m · °K). The rather uniform conductivity mimics the similarly uniform porosity and other index property measurements.

Thermal conductivity in the lithified sediments and basalts averages 1.43 W/(m · °K) and ranges from about 1.12 W/(m · °K) in a sandstone section to 1.97 W/(m · °K) in the basalts. The basalt conductivity generally follows the same lithologic units denoted by the density and velocity data. Conductivity values in the

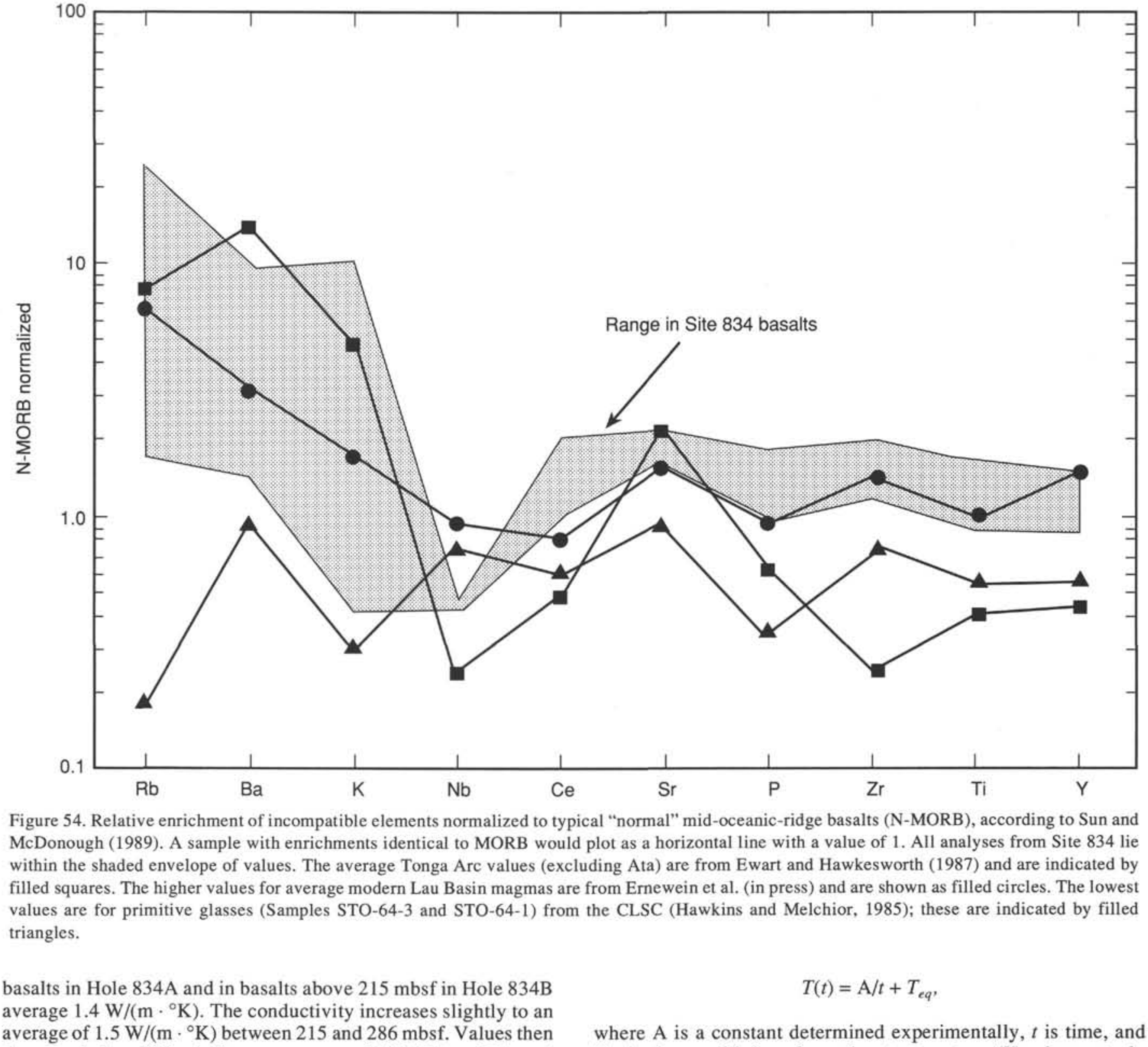

Figure 54. Relative enrichment of incompatible elements normalized to typical "normal" mid-oceanic-ridge basalts (N-MORB), according to Sun and McDonough (1989). A sample with enrichments identical to MORB would plot as a horizontal line with a value of 1. All analyses from Site 834 lie within the shaded envelope of values. The average Tonga Arc values (excluding Ata) are from Ewart and Hawkesworth (1987) and are indicated by filled squares. The higher values for average modern Lau Basin magmas are from Ernewein et al. (in press) and are shown as filled circles. The lowest values are for primitive glasses (Samples STO-64-3 and STO-64-1) from the CLSC (Hawkins and Melchior, 1985); these are indicated by filled triangles.

basalts in Hole 834A and in basalts above 215 mbsf in Hole 834B average 1.4 W/(m · °K). The conductivity increases slightly to an average of 1.5 W/(m · °K) between 215 and 286 mbsf. Values then decrease below 300 mbsf to an average of 1.3 W/(m · °K), and remain low to the base of Hole 834B. A significant affect on the thermal conductivities of the basalts is probably the vesicularity of the basalts. Basalts recovered in Hole 834A and above 215 mbsf and below 300 mbsf in Hole 834B are very vesicular. The basalts in the high thermal conductivity zone, between 215 and 286 mbsf, have low vesicularity as well as higher densities and velocities than the basalt units above and below.

Temperature Measurements

The downhole water sampler temperature probe (WSTP) was used to make temperature measurements at one point in Hole 834A at 45.6 mbsf and at three discrete points in Hole 834B at 30.1, 48.4, and 68.2 mbsf. The results are shown in Figure 62. Of the four runs, the measurement made at 30.1 mbsf in Hole 834B, indicated with the dashed line in Figure 62, appears to be disturbed (Tamaki, Pisciotto, Allan, et al., 1990). The temperature history in the sedimentary section should be such that after 5 min in the sediment, the decay curve should be approximated by:

$$T(t) = A/t + T_{eq},$$

where A is a constant determined experimentally, t is time, and T_{eq} is the equilibrium formation temperature (Hyndman et al., 1987). From Figure 62, the temperature measurement made at 30.1 mbsf in Hole 834B clearly increases rather than decreases linearly, and does so raggedly, indicating that the probe was inserted and moved several times during the measurement period. The temperature gradient defined by the two good points in Hole 834B and the point in Hole 834A is about 5°C/100 m (Fig. 63).

Thermal conductivity measurements (Fig. 61) were used to calculate the heat flow. The slope of the regression line indicates that the heat flow in the region is about 50 mW/m^2.

Discussion

The physical properties data outline general lithologic units for both the sedimentary column and the basalt. Within the sedimentary section, lithologic boundaries are present at about 40 and 80 mbsf, based on grain density and GRAPE continuous bulk density values. These boundaries roughly correspond to changes in the lithology as determined by the sedimentology (see "Lithostratigraphy" section, this chapter). The boundary at about 40 mbsf is near the sedimentological boundary at 42 mbsf, where

Table 16. Physical properties data, Hole 834A.

Core, section, interval (cm)	Depth (mbsf)	Su (kPa)	TC (W/[m · °K])	Bulk density (g/cm^3)	Grain density (g/cm^3)	Porosity (%)	Water content (%)	Void ratio	V_p (m/s)	V_p dir.
135-834A-										
1H-1, 75–76	0.75			1.46	2.68	77	118	3.4	1475	A
1H-1, 87–	0.87	4.5								
1H-2, 60–	2.10		1.0163							
1H-3, 60–	3.60		0.9835							
1H-3, 102–103	4.02	10.2		1.43	2.71	80	134	4.0		
1H-4, 60–	5.10		1.1719							
1H-4, 92–93	5.42	17.9		1.71	2.76	65	64	1.8	1521	A
1H-5, 60–	6.60		1.1605							
1H-5, 89–90	6.89			1.79	2.75	63	57	1.7		
1H-5, 90–	6.90	4.5								
2H-1, 75–76	8.35	3.0		1.78	2.63	62	55	1.6	1800	A
2H-2, 60	9.70		1.0885							
2H-2, 75–76	9.85			1.47	2.02	76	112	3.1		
2H-3, 60	11.20		1.0536							
2H-3, 73	11.33	17.4								
2H-3, 77–80	11.37								1482	C
2H-4, 60	12.70		1.0940							
2H-5, 75–76	14.35	22.9		1.48	2.31	80	123	3.9		
2H-6, 60	15.70		1.0955							
3H-2, 60	61.00	19.2	1.1096	1.48		78	116	3.5		
3H-2, 81	19.41	20.5								
3H-3, 60	20.70		0.9857							
3H-4, 60	22.20		1.0767							
3H-4, 75–76	22.35	31.9		1.55	1.73	74	96	2.9	1529	C
3H-6, 60	25.20		1.0791							
3H-6, 75–76	25.35	42.8		1.48	1.43	79	119	3.7	1506	C
3H-6, 80	25.40	48.0								
4H-2, 35–36	28.45			1.73	2.72	65	62	1.8	1535	A
4H-2, 60	28.70		1.2916							
4H-2, 100–101	29.10			1.48	2.71	80	122	3.9		
4H-2, 100	29.10	53.0								
4H-3, 60	30.20		0.9890							
4H-4, 60	31.70		1.0689							
4H-4, 73–74	31.83	49.7		1.50	2.75	80	120	4.0	1521	C
4H-4, 102–105	32.12								1364	C
4H-6, 60	34.70		1.1220							
4H-6, 73–74	34.83	48.6		1.55	2.71	79	110	3.8	1463	C
5H-2, 60	38.20		1.1182							
5H-2, 73–74	38.33	56.3		1.44	2.69	80	132	4.0	1496	C
5H-3, 60	39.70		1.1125							
5H-4, 60	41.20		1.0422							
5H-4, 73–74	41.33	55.2		1.55	2.69	79	110	3.8	1446	C
5H-6, 60	44.20		1.0603							
5H-6, 73–74	44.33	117.0		1.49	2.60	81	127	4.3	1514	C
6H-2, 60	47.70		1.0796							
6H-2, 73–74	47.83	35.9		1.51	2.61	75	103	3.0	1488	C
6H-3, 60	49.20		1.0146							
6H-4, 60	50.70		1.0336							
6H-4, 73–74	50.83	43.0		1.48	2.74	79	119	3.7	1476	C
6H-6, 60	53.70		1.2205							
6H-6, 73–74	53.83			1.67	2.72	69	73	2.2	1502	C
6H-6, 100–101	54.10	49.1		1.58	2.57	76	96	3.1	1515	C
7H-2, 60	57.20		1.0104							
7H-2, 80–81	57.40	45.2		1.47	2.63	78	120	3.6	1500	C
7H-3, 60	58.70		1.0241							
7H-4, 60	60.20		0.9750							
7H-4, 80–81	60.40	37.5		1.53	2.72	78	108	3.5		
7H-6, 60	63.20		1.0370							
7H-6, 80–81	63.40			1.52	2.78	78	109	3.4	1465	C
8H-2, 60	66.70		0.9991							
8H-2, 84–86	66.94								1402	A
8H-2, 86–87	66.96			1.45	2.72	79	126	3.8	1517	A
8H-3, 60	68.20		0.9020							
8H-4, 25–27	69.35								1672	C
8H-4, 60	69.70		1.1192							
8H-4, 66–67	69.76			1.56	2.87	80	111	4.1	1499	C
8H-4, 88–89	69.98			1.55	2.74	77	103	3.3	1473	A
8H-6, 60	72.70		0.9591							
8H-6, 82–83	72.92			1.53	2.78	81	119	4.3	1473	A
9H-2, 60	76.20		1.0109							
9H-2, 78–81	76.38								1453	A
9H-2, 83–84	76.43			1.53	2.84	80	115	4.0		
9H-3, 60	77.70		0.9809							
9H-4, 60	79.20		0.9568							
9H-4, 63–65	79.23								1508	C

Table 16 (continued).

Core, section, interval (cm)	Depth (mbsf)	Su (kPa)	TC (W/[m · °K])	Bulk density (g/cm^3)	Grain density (g/cm^3)	Porosity (%)	Water content (%)	Void ratio	V_p (m/s)	V_p dir.
135-834A- (cont.)										
9H-4, 73–75	79.33			1.54	2.48	72	92	2.6		
9H-4, 114–116	79.74			1.48	2.62	90	162	8.6		
9H-5, 123–125	81.33			1.54	2.46	74	96	2.8	1460	A
9H-6, 60	82.20		0.9225							
9H-6, 72–73	82.32			1.50	2.44	75	105	3.0	1483	A
10X-1, 61	84.21		0.9945							
10X-1, 78–80	84.38			1.42	2.63	75	119	3.0	1482	A
10X-2, 33	85.43		0.8110							
10X-2, 69–70	85.79			1.45	2.66	79	126	3.8	1446	A
10X-3, 63–65	87.23			1.66	2.61	70	76	2.3	1833	A
10X-3, 87	87.47		0.9555							
11X-1, 50–52	93.70			1.64	2.48	62	62	1.6	1476	C
11X-1, 60	93.80		0.8694							
11X-1, 80–81	94.00			1.42	2.61	80	138	4.1		
11X-2, 38–40	95.08								1540	C
11X-2, 42	95.12		0.9198							
11X-2, 50–51	95.20			1.42	2.39	70	102	2.3		
11X-3, 82	97.02		1.0277							
11X-3, 97–98	97.17			1.49	2.63	80	122	4.1		
12X-1, 50–51	103.40		1.0397	1.48	2.75	79	120	3.7	1481	C
12X-2, 50–51	104.90		1.0806	1.51	2.59	81	120	4.1		
14X-1, 8–10	117.08			2.36					3591	B
14X-1, 8–10	117.08								3791	C
15X-1, 52–54	123.52			2.67					4077	A
15X-1, 52–54	123.52								4259	B
15X-1, 52–54	123.52								3975	C
16X-1, 60–62	132.50			1.53	2.51	74	99	2.9		
16X-2, 40–42	133.80			1.67	2.62	67	70	2.0		
17X-1, 26–28	136.56			2.57	3.00				3104	A
17X-1, 26–28	136.56								3545	B
17X-1, 26–28	136.56								3270	C
17X-2, 65–67	138.45			2.70	2.93				4178	A
17X-2, 65–67	138.45								4304	B
17X-2, 65–67	138.45								3999	C
17X-4, 42–44	141.06			2.80	2.90				4552	A
17X-4, 42–44	141.06								4596	B
17X-4, 42–44	141.06								4239	C
18X-1, 78–80	142.38			2.72					4516	A
18X-1, 78–80	142.38								4445	B
18X-1, 78–80	142.38								4386	C
18X-2, 106–108	144.01			2.70	2.91				4505	A
18X-2, 106–108	144.01								4499	B
18X-2, 106–108	144.01								4213	C
20X-1, 143–145	146.03			2.74	3.02				4564	A
20X-1, 143–145	146.03								4619	B
20X-1, 143–145	146.03								4262	C
20X-2, 139–141	147.46			2.63	2.92				4080	A
20X-2, 139–141	147.46								4333	B
20X-2, 139–141	147.46								4102	C

Notes: Su = undrained vane shear strength, TC = thermal conductivity, V_p = compressional (P-wave) velocity, V_p dir. = velocity direction, where A is the vertical velocity along the core, B is the horizontal velocity parallel to the cut core face, and C is the horizontal velocity perpendicular to the core face.

nannofossil ooze of sedimentary Unit I overlies nannofossil ooze interbedded with ash layers of sedimentary Unit II. The physical properties boundary at 80 mbsf is near the sedimentologically determined boundary between sedimentary Units III and IV at 78 mbsf, with increased vitric ash content below 78 mbsf.

The physical properties boundaries within the basalt correspond to lithologic boundaries determined from the basalts. The increase in velocity and density at 215 mbsf is near the boundary at 214.06–214.31 mbsf between igneous Unit 6, an aphyric basalt, and Unit 7, a moderately to highly phyric plagioclase basalt. Similarly, the lower boundary of the high-velocity, high-density unit at about 286 mbsf corresponds to the boundary between igneous Units 7 and 8 at 287 mbsf. Unit 8 is an aphyric vesicular basalt characterized by lower densities and velocities than in Unit 7. The changes in the physical properties may be related to the high degree of vesicularity within the basalts above and below igneous Unit 7, with the effective porosity of the vesicles leading to decreases in both bulk density and velocity relative to the less vesicular Unit 7.

The heat flow at Site 834, about 50 mW/m^2, is slightly higher than typical values for continental crust. Theoretical heat flow curves for young oceanic crust (less than about 10 Ma) suggest that much higher heat flow values, on the order of perhaps 150–175 mW/m^2 (Anderson et al., 1977) are expected at the 5.5-Ma crust at Site 834. For comparison, heat flow values in the Japan Sea determined in sediments overlying crust of early to middle Miocene age range from about 100 to 150 mW/m^2 (Tamaki, Pisciotto, Allan, et al., 1990). The low heat flow may reflect relatively free circulation of water through both sediments and basalt within the basin. Such circulation is also suggested by chemical data from interstitial water studies (see "Inorganic Geochemistry" section, this chapter), and by the relatively small

Table 17. Physical properties data, Site 834B.

Core, section, interval (cm)	Depth (mbsf)	TC (W/[m · °K])	Bulk density (g/cm^3)	Grain density (g/cm^3)	V_p (m/s)	V_p dir.
135-834B-						
7R-1, 125–127	117.65		2.73	2.92	4207	A
7R-1, 125–127	117.65				4257	B
7R-1, 125–127	117.65				4095	C
8R-1, 3	126.13	1.5917				
8R-1, 95–97	127.05		2.75	2.89	4234	A
8R-1, 95–97	127.05				4115	B
8R-1, 95–97	127.05				4280	C
9R-1, 6	135.86	1.5842				
9R-1, 76–78	136.56		2.62	2.98	4030	A
9R-1, 76–78	136.56				4150	B
9R-1, 76–78	136.56				4011	C
10R-1, 66–68	146.06		2.81	2.85	4558	A
10R-1, 66–68	146.06				4595	B
10R-1, 66–68	146.06				4572	C
10R-3, 73–75	149.05		2.73	2.95	4390	A
10R-3, 73–75	149.05				4457	B
10R-3, 73–75	149.05				4423	C
11R-1, 3	150.03	1.5379				
11R-1, 43–45	150.43		2.79	3.14	4560	A
11R-1, 43–45	150.43				4595	B
11R-1, 43–45	150.43				4547	C
11R-3, 2	152.80	1.9714				
11R-3, 90–92	153.68		2.77	2.86	4250	A
11R-3, 90–92	153.68				4345	B
11R-3, 90–92	153.68				4311	C
12R-3, 33–35	158.27		2.74	2.91	4250	A
12R-3, 33–35	158.27				4335	B
12R-3, 33–35	158.27				4384	C
12R-5, 3	160.74	1.3211				
12R-5, 59–61	161.30		2.70	2.93	4159	A
12R-5, 59–61	161.30				4243	B
12R-5, 59–61	161.30				4128	C
13R-2, 1	162.44	1.4146				
13R-2, 4–6	162.47		2.73	2.96	4361	A
13R-2, 4–6	162.47				4374	B
13R-2, 4–6	162.47				4148	C
14R-1, 60–62	166.30		2.42	2.95	3902	A
14R-1, 60–62	166.30				3989	B
16R-1, 57–59	185.57		2.20		3755	A
16R-1, 60–62	185.60				3737	A
16R-1, 60–62	185.60				3742	B
16R-1, 60–62	185.60				3620	C
16R-1, 112–118	186.12				3422	B
16R-2, 1	186.41	1.3967				
20R-2, 1	215.04	1.5754				
20R-2, 58–60	215.61		2.87	2.89	4947	A
20R-2, 58–60	215.61				5216	B
20R-2, 58–60	215.61				4478	C
21R-1, 4	218.44	1.5974				
22R-2, 2	224.72	1.4769				
22R-2, 11–13	224.81		2.87	2.93	4885	A
22R-2, 11–13	224.81				4916	B
22R-2, 11–13	224.81				4685	C
24R-1, 10	233.00	1.5719				
24R-1, 98–100	233.88		2.89		5103	A
24R-1, 98–100	233.88				5128	B
24R-1, 98–100	233.88				4631	C
26R-1, 9	242.69	1.4073				
26R-1, 101–103	243.61		2.95	2.93	5206	A
26R-1, 101–103	243.61				5153	B
26R-1, 101–103	243.61				4812	C
28R-1, 15	252.45	1.8127				
28R-1, 101–103	253.31		2.96	2.97	5246	A
28R-1, 101–103	253.31				5242	B
28R-1, 101–103	253.31				4886	C
29R-1, 5	257.35	1.4789				
29R-1, 113–115	258.43		2.90		5162	A
29R-1, 113–115	258.43				5241	B
29R-1, 113–115	258.43				4823	C
30R-1, 10	262.00	1.7530				
30R-1, 106–108	262.96		2.97		5279	A
30R-1, 106–108	262.96				5317	B
30R-1, 106–108	262.96				5100	C
31R-2, 69–71	269.00	1.6546				
31R-2, 113–115	269.44		2.99	2.94	5270	A
31R-2, 113–115	269.44				5305	B
31R-2, 113–115	269.44				4746	C
33R-2, 47–49	282.51		2.98	2.93	5285	A
33R-2, 47–49	282.51				4935	B

Table 17 (continued)

Core, section, interval (cm)	Depth (mbsf)	TC (W/[m · °K])	Bulk density (g/cm^3)	Grain density (g/cm^3)	V_p (m/s)	V_p dir.
135-834B- (cont.)						
33R-2, 47–49	282.51				5049	C
33R-2, 60–49	284.20	1.7629				
34R-1, 1	286.20	1.6112				
34R-1, 30–32	286.50		2.96	2.95	5119	A
34R-1, 30–32	286.50				5165	B
34R-1, 30–32	286.50				4890	C
35R-2, 85–91	293.25	1.2474				
36R-1, 12–18	300.62	1.2301				
36R-1, 27–29	300.77		2.58	2.95	4138	A
36R-1, 27–29	300.77				4104	B
36R-1, 27–29	300.77				4313	C
37R-1, 62–72	310.82	1.2634				
37R-2, 74–76	312.19		2.36	2.83	4265	A
37R-2, 74–76	312.19				4228	B
37R-2, 74–76	312.19				4133	C
38R-1, 21–23	320.01		2.46	3.01	4265	A
38R-1, 21–23	320.01				4303	B
38R-1, 21–23	320.01				4048	C
41R-1, 66–76	335.06	1.1253				
41R-1, 81–83	335.21		2.25	3.06	3484	A
41R-1, 81–83	335.21				3458	B
41R-1, 81–83	335.21				3454	C
42R-1, 81–83	339.91		2.58	2.87	3957	A
42R-1, 81–83	339.91				3782	B
42R-1, 100–110	340.10	1.2763				
43R-1, 42–52	344.52	1.1767				
43R-1, 57–59	344.67		2.41	2.82	3945	A
43R-1, 57–59	344.67				3994	B
43R-1, 57–59	344.67				4138	C
47R-1, 69–75	364.19	1.5426				
47R-1, 77–79	364.27		2.51	2.89	4127	A
47R-1, 77–79	364.27				4215	B
47R-1, 77–79	364.27				4215	C
48R-1, 67–76	368.87	1.2165				
48R-1, 71–73	368.91		2.41	3.18	3700	A
48R-1, 71–73	368.91				3773	B
48R-1, 71–73	368.91				3338	C
49R-1, 99–101	374.19		2.59		4031	A
49R-1, 99–101	374.19				3955	B
49R-1, 99–101	374.19				3946	C
50R-1, 5–10	377.95	1.3527				
50R-1, 140–142	379.30			2.91	4258	A
50R-1, 140–142	379.30				4302	B
50R-1, 140–142	379.30				4250	C
51R-1, 76–78	383.66		2.25		3798	A
51R-1, 76–78	383.66				3781	B
51R-1, 76–78	383.66				3771	C
51R-1, 110–110	383.90	1.3888				
52R-2, 38–46	387.88	1.3262				
52R-1, 116–118	388.66		2.58		3979	A
52R-1, 116–118	388.66				4144	B
52R-1, 116–118	388.66				3937	C
53R-1, 57–59	393.07		2.62	2.99	3917	A
53R-1, 57–59	393.07				3996	B
53R-1, 57–59	393.07				3831	C
54R-1, 91–93	398.11		2.39		3425	A
54R-1, 91–93	398.11				3479	B
54R-1, 91–93	398.11				3494	C
54R-2, 12–20	399.57	1.2652				
56R-1, 9–11	406.99		2.37	2.72	3860	A
56R-1, 9–11	406.99				3736	B
56R-1, 9–11	406.99				3915	C
56R-1, 60–70	407.50	1.3784				
56R-1, 69–71	407.59		2.63	2.91	4242	A
56R-1, 69–71	407.59				4235	B
56R-1, 69–71	407.59				4172	C
57R-1, 64–66	416.94		2.35	3.01	3848	A
57R-1, 64–66	416.94				3927	B
57R-1, 64–66	416.94				3869	C
58R-1, 1–10	426.00	1.2240				
59R-1, 60–70	431.60	1.2574				
59R-2, 19–21	432.62		2.42		3933	A
59R-2, 19–21	432.62				3818	B
59R-2, 19–21	432.62				3936	C

Notes: TC = thermal conductivity, V_p = compressional (P-wave) velocity; V_p dir. = velocity direction, where A is the vertical velocity along the core, B is the horizontal velocity parallel to the cut core face, and C is the horizontal velocity perpendicular to the core face.

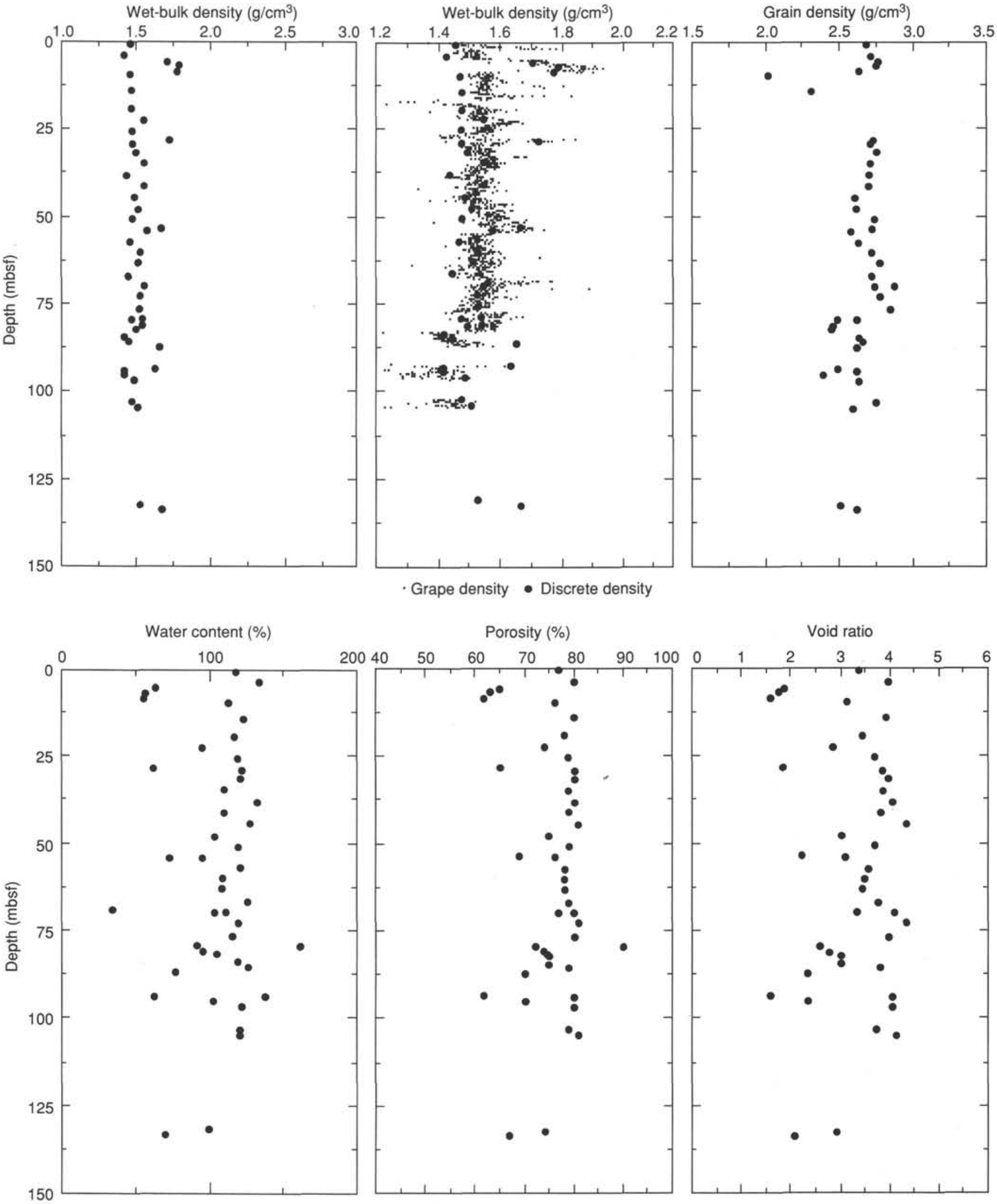

Figure 55. Index properties (bulk density, GRAPE bulk density, grain density, water content, porosity, and void ratio) data vs. depth for the sedimentary section from Hole 834A. GRAPE bulk density is plotted with gravimetrically determined bulk density for comparison.

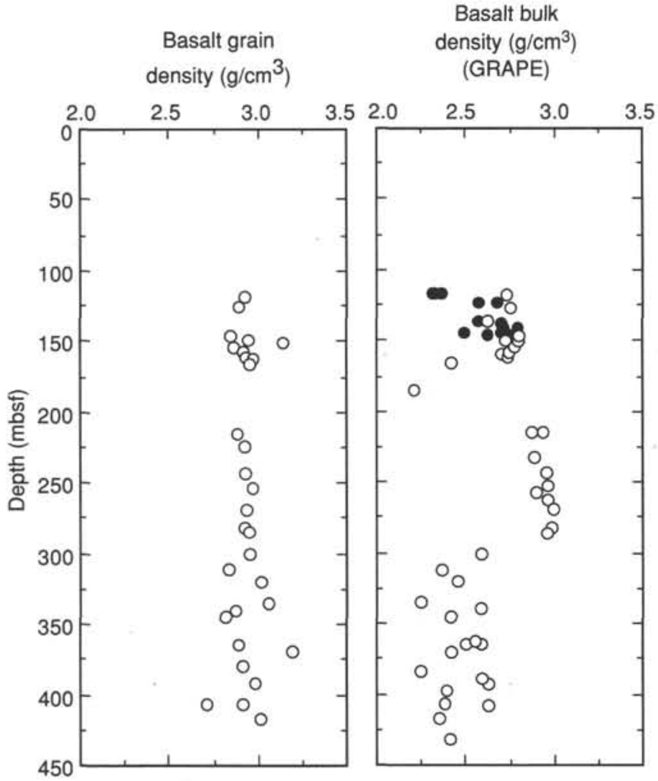

Figure 56. Grain density determinations on discrete basalt samples and corresponding GRAPE 2-min bulk density determinations vs. depth for basalt samples from Holes 834A and 834B. Filled circles = Hole 834A and open circles = Hole 834B.

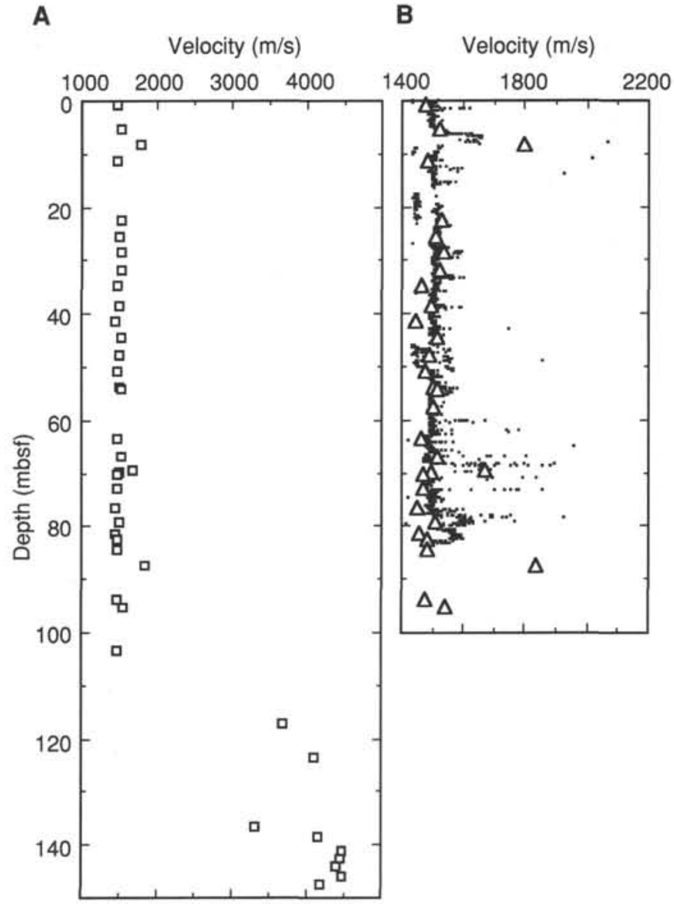

Figure 57. Compressional wave velocity vs. depth, Hole 834A. **A.** Discrete velocity measurements vs. depth. **B.** *P*-wave logger velocities plus discrete velocity measurements vs. depth for part of hole with *P*-wave logger data. Open triangles = discrete velocity data.

changes in physical properties observed within the sedimentary section.

DOWNHOLE MEASUREMENTS

Operations

Logging operations at Hole 834B commenced at 0845 hr UTC on 29 December 1990 and ended at 1600 hr UTC on 30 December. Four logging runs were performed. Three Schlumberger standard tool strings (the quad-tool combination, the geochemical tool, and the formation microscanner [FMS], all mounted with the Lamont temperature logging tool), were run initially, followed by the analog borehole televiewer (BHTV). The quad-tool combination carried a resistivity tool, a sonic tool, a high-temperature litho-density tool, a compensated neutron porosity tool, and a natural gamma-ray tool. The geochemical tool carried a gamma-ray spectrometry tool and an aluminum clay tool, and also a compensated neutron porosity tool and a natural gamma-ray tool, the latter to allow correlation between logging passes. In addition to the FMS sonde itself, the FMS tool string carried a general purpose inclinometry tool and another natural gamma-ray device. Initially, the digital BHTV was set up and lowered down the hole, but problems with the power supply on the surface control panel required us to change to the backup analog BHTV.

The drillers' mud line was at 2699.1 mbrf, and their total hole depth was 435.3 mbsf. At the commencement of the first run, with the quad-tool combination, the bottom of the drill pipe was raised to 74.6 mbsf. Downgoing logs were initially made at a speed of 457 m/hr (1500 ft/hr), but poor hole conditions necessitated a reduction of this to 366 m/hr (1200 ft/hr) at a depth of 183.4 mbsf. The loggers' total hole depth was 437.0 mbsf. Upgoing logging took place at a speed of 306 m/hr (1000 ft/hr). The heave compensator was turned off at a depth of 87.2 mbsf, blocks were raised one stand, and the pipe consequently raised to 47.1 mbsf. A repeat section was logged upward between 33.9 and 138.9 mbsf. The tool was allowed to remain for 3 min at the bottom of the hole and at the mud line (both up and down log) to allow calibration and equilibration of the temperature tool. This was standard procedure on all runs on which the temperature tool was carried.

The second logging run, using the gamma-ray spectrometry tool, started down from the mud line at 610 m/hr (2000 ft/hr). Elapsed time was recorded to calculate a depth curve for the temperature data, as the temperature tool can record time but has no depth recorder. The heave compensator was turned on at 410.0 mbsf and the tool raised to 379.4 mbsf to calibrate the tool; it was then lowered again to 434.2 mbsf at 610 m/hr (2000 ft/hr) to continue the elapsed time curve and allowed to equilibrate. Logging was then completed at a rate of 183 m/hr (600 ft/hr), continuing through the BHA to the mud line, after the blocks were raised one stand. The heave compensator was turned off at 74.6 mbsf and was left switched off during a repeat run from 89.8 to 44.1 mbsf. No evidence was found for spurious gamma-ray counts from earlier irradiation of the formation during the repeat run.

The FMS tool string was used on the third logging run. It was paid out to a depth of 348.9 mbsf at a rate of 1219 m/hr (4000

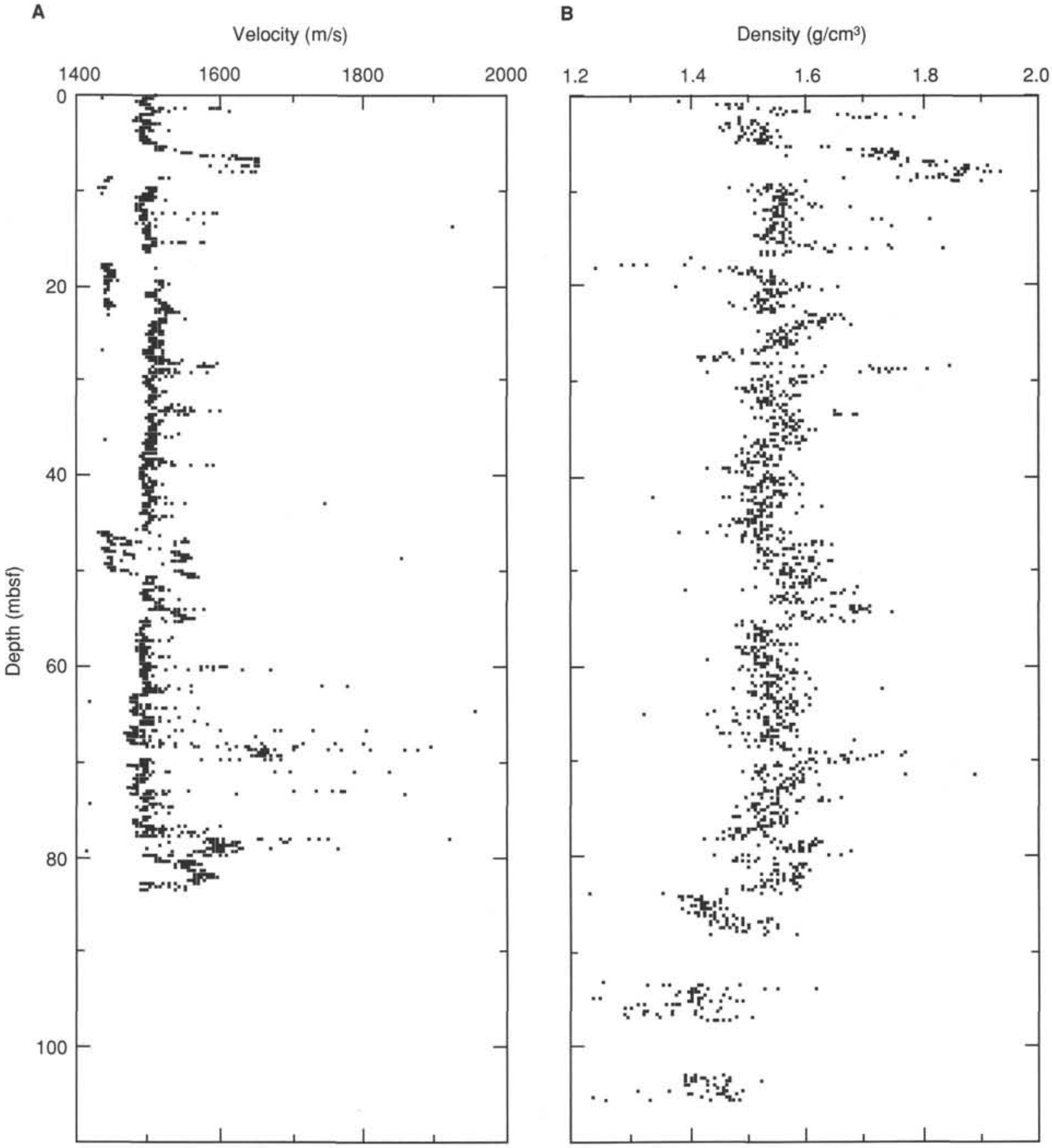

Figure 58. *P*-wave logger (**A**) and GRAPE density (**B**) data presented at the same scale to emphasize the correlation of the thin high-velocity, high-density sedimentary units.

ft/hr) for calculation of the elapsed time curve, and lowered further to a bottom depth of 435.6 mbsf. Logging started at 488 m/hr (1600 ft/hr). At 263.6 mbsf a constriction was encountered and the calipers had to be closed to bridge it. Logging of this pass stopped at 51.7 mbsf. The caliper arms were then closed and the tool returned to the bottom for a repeat run. This second run continued up to 50.0 mbsf.

Following the problems with the digital BHTV described above, the analog BHTV was lowered into the hole for the final logging run. A bridge was encountered at 260.8 mbsf and so logging started at this depth. Above 105.1 mbsf the hole was severely washed out, and the signal was so degraded that the decision was taken to stop the run.

Onboard Processing and Data Quality

Data tapes were corrected for heave compensation by the Schlumberger engineer by subtracting 3.28 m (10 ft), and depths were converted from feet below rig floor to meters below seafloor. Raw sonic logs exhibited extreme cycle-skipping (see below). An algorithm for reprocessing sonic "slowness" from traveltimes was used to get a preliminary estimate of "slowness" (the inverse of velocity). Velocity values below 210 μsec/ft "slowness" (1.45 km/s) and above 40 μsec/ft (7.62 km/s) were discarded. The reprocessed sonic data were then converted to velocity (in km/s). The resistivity curve was edited to remove spurious peaks (>9600 ohm-m).

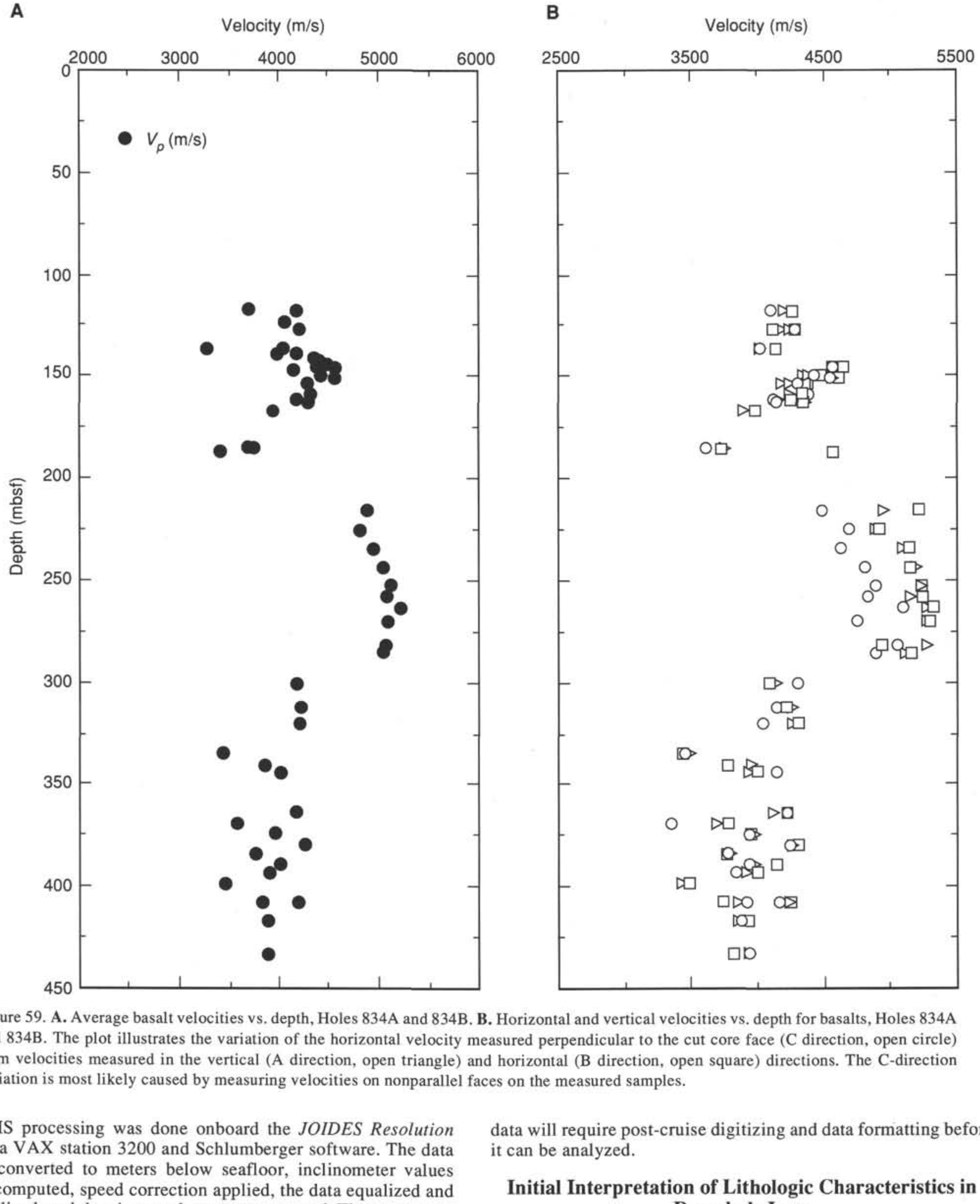

Figure 59. **A.** Average basalt velocities vs. depth, Holes 834A and 834B. **B.** Horizontal and vertical velocities vs. depth for basalts, Holes 834A and 834B. The plot illustrates the variation of the horizontal velocity measured perpendicular to the cut core face (C direction, open circle) from velocities measured in the vertical (A direction, open triangle) and horizontal (B direction, open square) directions. The C-direction variation is most likely caused by measuring velocities on nonparallel faces on the measured samples.

FMS processing was done onboard the *JOIDES Resolution* using a VAX station 3200 and Schlumberger software. The data were converted to meters below seafloor, inclinometer values were computed, speed correction applied, the data equalized and normalized, and then image plots were generated. The two passes of the FMS yielded logs from 53 to mbsf and from 51 to 435 mbsf, respectively. The processed FMS images can be found on microfiche in the back of this volume.

Although software was available for Leg 135 shipboard processing of digital BHTV data, it is not possible to digitize onboard the analog signal collected with the older analog BHTV tool. The data will require post-cruise digitizing and data formatting before it can be analyzed.

Initial Interpretation of Lithologic Characteristics in Downhole Logs

Sediments

Three principal lithologic units were defined by the sedimentologists in their examination of the recovered core (see "Lithostratigraphy" section, this chapter). These are summarized as follows:

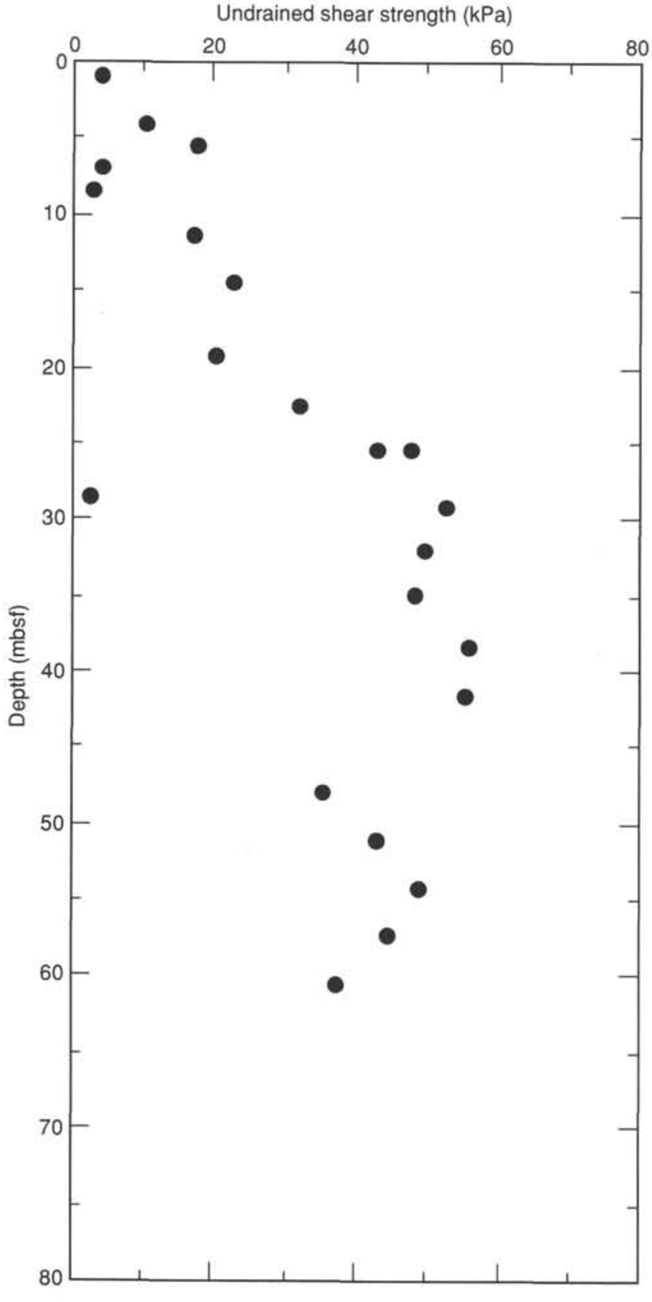

Figure 60. Undrained vane shear strength vs. depth, Hole 834A.

Unit I (0–42 mbsf): clay/nannofossil ooze with rare foraminifers; occasional ash layers.

Unit II (42–78 mbsf): clay/nannofossil ooze with interbedded ash layers.

Unit III (78–113 mbsf): volcaniclastic turbidites with subordinate clay/nannofossil ooze.

The boundary between Units I and II was very close to the bottom of the drill pipe, which was held at about 44 mbsf while logging up hole; therefore, no information could be gathered from the geophysical tools, and those geochemical data that could be collected through the drill pipe were masked by the edge effects when exiting the BHA.

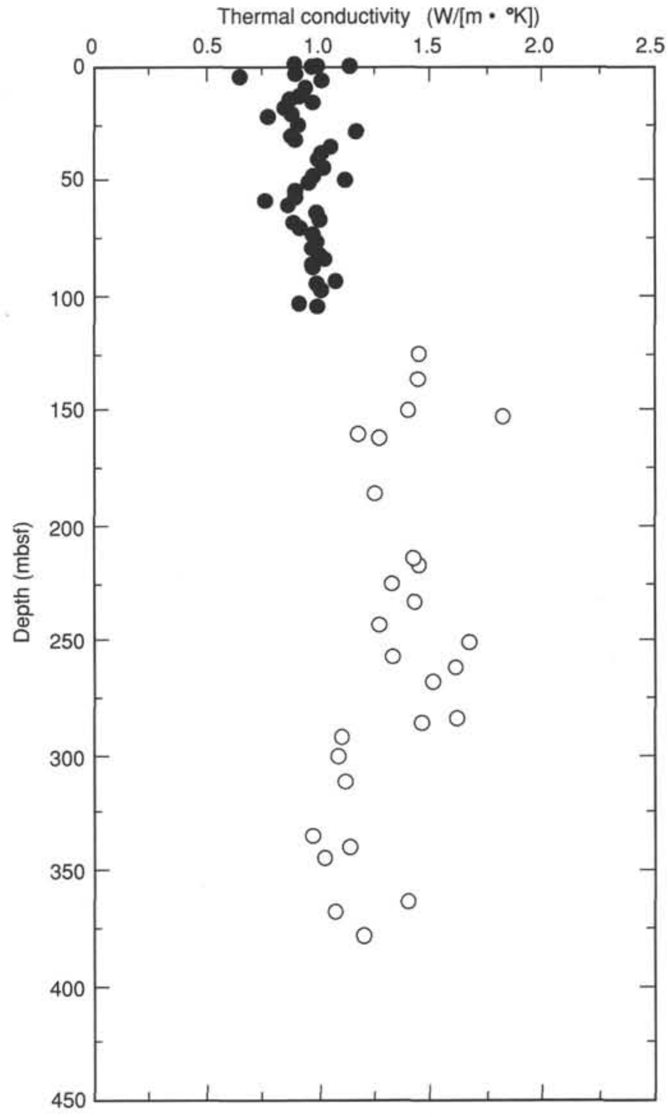

Figure 61. Thermal conductivity vs. depth, Hole 834A. Filled circles = Hole 834A, and open circles = Hole 834B.

The Units II–III contact is defined on sedimentological grounds by a large increase in glass content and a consequent decrease in the proportion of clay and nannofossil debris. On the geochemical logs, this contact is marked by an increase in potassium (from near zero to ≥0.5%) and thorium (from near zero up to 0.5–1 ppm), and a slight increase in the relative content of aluminum and silicon. No significant variations in other elements are obvious at this Unit I/Unit II contact from the initial shipboard interpretation of the geochemical or geophysical logs.

On FMS images, dark tones correspond to weakly resistive lithologies, whereas lighter tones indicate areas of higher resistivity. Throughout the sedimentary section, pale bands or groups of pale bands, indicative of high resistivity, are interlayered (Fig. 64). The pale bands may be up to 2 m in thickness, but bands from a few centimeters to a few tens of centimeters thick are more typical. The bands appear to increase in abundance toward the bottom of the sediment column. We interpret these pale bands as the ash and calcareous turbidite horizons that are interbedded with

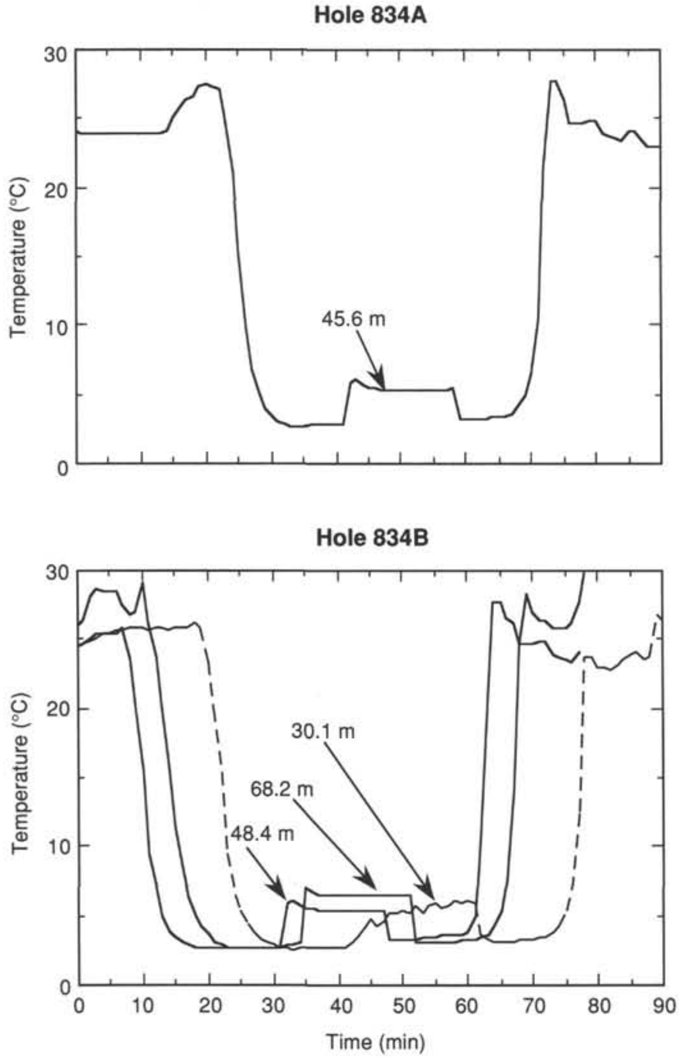

Figure 62. Heat flow measurements, Holes 834A (top) and 834B (bottom), based on WSTP temperature runs.

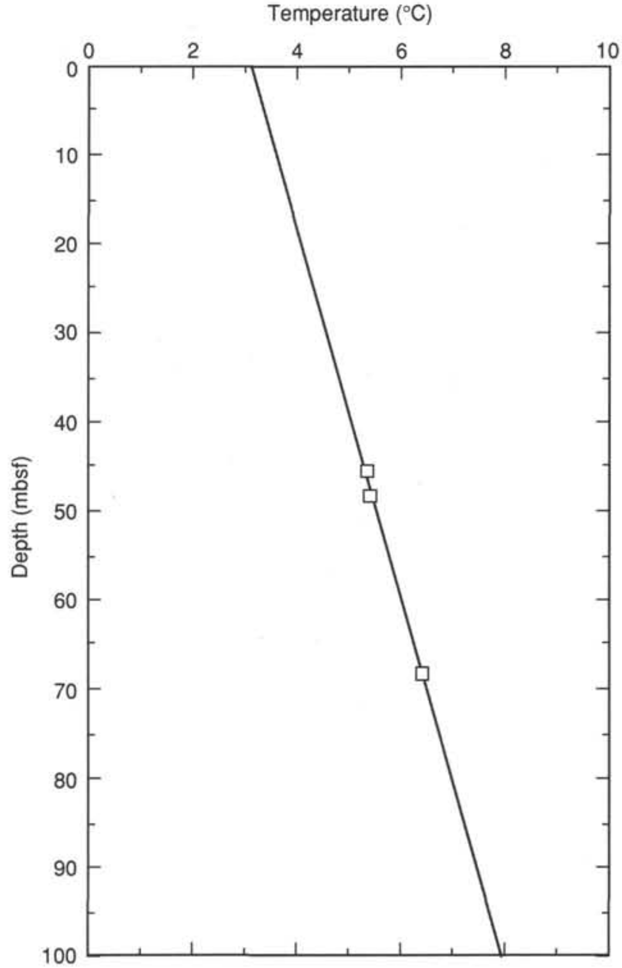

Figure 63. Temperature gradients vs. depth, Holes 834A and 834B. The line through the values indicates the geothermal gradient of 5°C/100 m.

the clays and nannofossil oozes. We suggest that the darker background lithologies on the FMS images correspond to the clays and oozes; such low resistivities are typical of clays (Serra, 1989). Low resistivities might be expected also of the brown oozes, whose color is derived from iron oxide/hydroxide coating of grains. Comparison of the FMS records with the lithostratigraphic data suggests a good first-order correlation. In detail, however, correlations are less straightforward, as the pale (high resistivity) horizons on the FMS images appear to be considerably thicker than the light-colored portions of the core described as ash/calcareous turbidites. The thickness differences are not caused by core recovery problems, as recovery through the sedimentary section was virtually 100%. Instead, we suggest that, in addition to imaging the basal portions of the turbidite flows, the FMS may also be imaging features of the volcaniclastic material higher in each flow that are not recognized by visual observations.

Bedding on the FMS images appears to be subhorizontal throughout, confirming visual observations of the cores themselves (see "Structural Geology" section, this chapter), and no fractures have been identified in those sediments above 114 mbsf. Dipmeter plots, computed from the FMS tool, show sediment dips of no more than 1°–2° toward the west through the entire section (Fig. 65).

Sediment–Igneous Rock Contacts

The most conspicuous changes in a number of the downhole logs are the greatly increased resistivity, seismic velocity, and density, and the decrease in porosity at 112.5 mbsf (Fig. 66). This corresponds to the transition from sediment to igneous rock that was recorded in the core. Low-resistivity/velocity/density and high-porosity conditions reappear at about 130, 137, and 163 mbsf. The change at about 137 mbsf corresponds to a sediment interbed in Hole 834A, separating igneous Units 3 and 4. A comparable incursion at 163 mbsf (i.e., to low velocity, density, and resistivity, and to high porosity) correlates with fragments of sediment recovered from Hole 834B at approximately this depth. This allows more precise separation of igneous Units 5 and 6 (see "Igneous Petrology" section, this chapter) than would have been possible from core observations alone in this area of poor core recovery. A third, but smaller, deviation of the curves occurs at 130 mbsf and corresponds to a change in rock type, from igneous Units 2 to 3. We suggest that the logs provide strong evidence for the existence of a sediment horizon interposed between these two units that was not recovered in the core. A similar decrease in density and resistivity, and an increase in porosity, at about 238 mbsf, may delineate another interlava sediment horizon; however, no change in petrology or geochemistry has been recognized across this contact (which falls within Unit 7), nor can any sediment be recognized on FMS images at this level (see below).

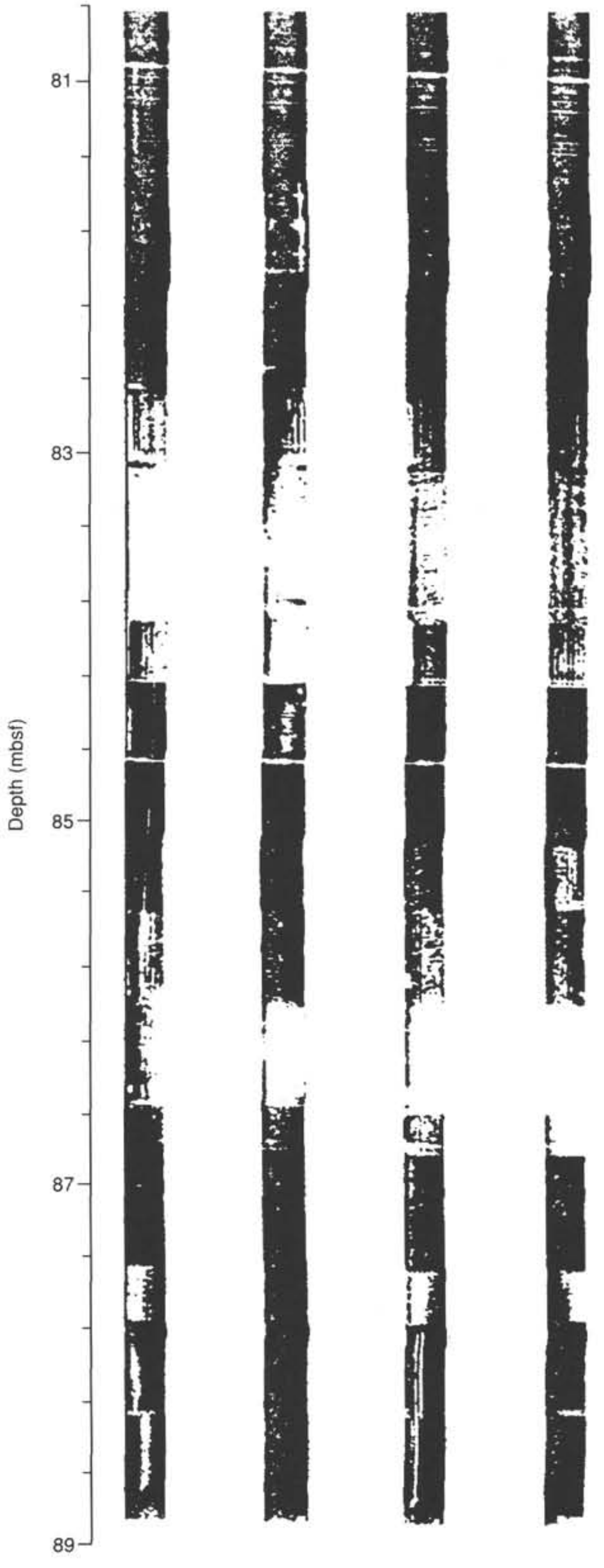

Figure 64. Example of processed formation microscanner data from 81 to 89 mbsf, Hole 834B. The dark areas, which indicate low resistivity, correspond to clay/nannofossil ooze; the light areas, which indicate high resistivity, correspond to ash and/or calcareous turbidite units. Note the sharp bases and gradational tops to the turbiditic horizons. The near-identical levels of the bases of the horizons on each pad demonstrate that the bedding is horizontal (≤1°).

Although the origin of this perturbation of the signal is unknown, it could potentially correspond to a geological feature such as, for example, a fault zone.

FMS logs clearly show the presence of subhorizontal sediment at 126–129 mbsf, corresponding to the boundary between igneous Units 2 and 3. The bedded sediments contrast markedly with the irregular, low-resistivity images, often with clear fracture patterns, that are characteristically obtained from igneous rocks. Further bedded horizons, probably representing sediment, have been identified at approximately 134–135 mbsf, and possibly at 141–143 mbsf. These latter horizons are thought to correlate with the igneous Unit 3/4 or 4/5 boundaries, igneous Unit 4 being a poorly constrained unit inferred from just 14 cm of core. On the FMS records, basalt/sediment contacts are poorly imaged, as the transitions are commonly accompanied by a significant increase in borehole diameter in the sediments. This sometimes causes the calipers of the FMS tool to stick, spin, and/or lose pad contact for a short period after entering or exiting from the igneous basement.

The geochemical logs (Figs. 67 and 68) show that the transition from sediment into igneous basement is accompanied by pronounced increases in Al, Fe, and Si and decreases in S, H, Cl, and K. The gamma-ray signal also decreases in intensity. The interbedded sedimentary horizons discussed in the preceding paragraphs are clearly delineated by gamma-ray intensity, K, and to a lesser extent by U, H, and Cl peaks, and by Al, Si, and Fe minima.

Igneous Basement Characteristics

As described above, and as illustrated in Figure 66, the downhole logs distinguish sediments from igneous rocks very effectively. The principal igneous units toward the top of the succession are bounded by sediment interbeds both above and below, so that the igneous rock boundaries are plainly visible on the logs. Consequently, the logs allow examination of the internal variations in the physical and chemical properties of the igneous units. Two of the thickest units (Units 2 and 5, which appear to be 15 and 25 m thick, respectively) show very rapid changes in velocity, resistivity, density, and porosity at their bases, which suggest sharp and well-defined lower contacts for each unit. At the upper contacts, however, the gradients of the logs are noticeably less steep, such that the upper one-half to one-third of each unit has lower and more variable velocity, resistivity, and density, and higher porosity, than the lower and central parts. These changes could be caused by changes in the hole diameter, as the caliper logs also show a gradually increasing hole width toward the top of the units that could affect the values measured on the other logs. However, we suggest that some real changes in the physical characteristics of the upper portions of Units 2 and 5 cause these changes, including, for example, a higher degree of fracturing, greater vesicularity, a greater number of internal contacts (e.g., pillow or flow margins), and/or more intense alteration of the upper section compared with the lower section. Observations from the cores suggest that the uppermost few meters of Unit 5 are indeed very heavily altered; however, they also reveal only a limited number of internal chilled margins in Unit 2, and none in Unit 5. This suggests that the number of internal contacts is less likely to be a factor here (although see below for discussion of other parts of the borehole), and that both units may represent individual magmatic episodes.

The lack of coherence of the upper parts of these units, when compared with the relative coherence (i.e., very rapid change in log response) of their lower parts, suggests that the units represent lava flows rather than sills. Sills are intruded into preexisting material; hence, the rate transfer of heat at upper and lower contacts is similar, and symmetrical cooling structures normally result, and a similar change in log response should be found at both top and bottom. Submarine flows, however, cool relatively

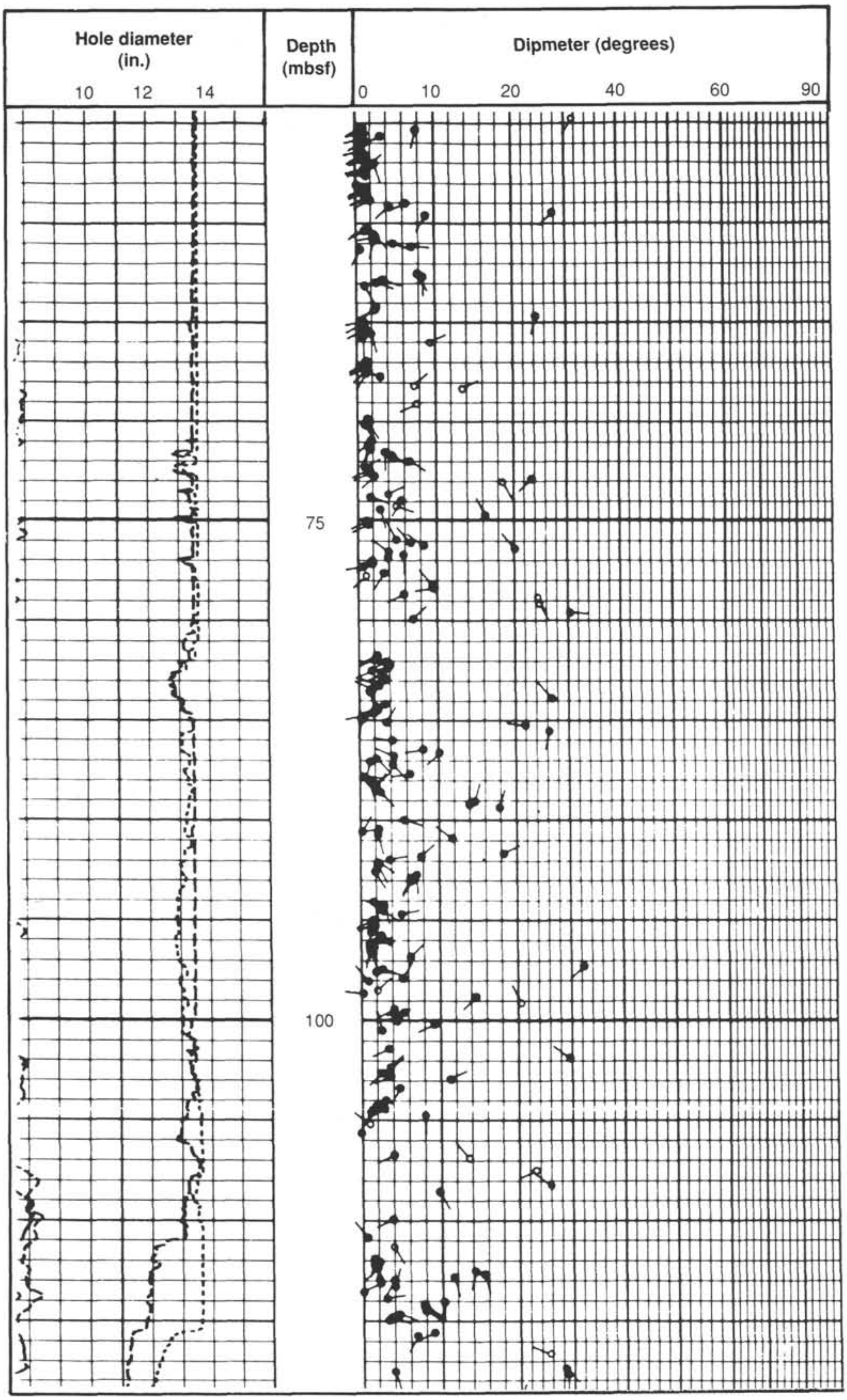

Figure 65. The dipmeter plot processed from formation microscanner (FMS) log on right-hand side; caliper log on left-hand side. Note the clustering of dip symbols between 0° and 2°, indicating the true dip of the succession; the scattered high values are spurious correlations made by the dipmeter calculation program. Filled circles on dip symbols indicate higher quality picks than open circles (see "Downhole Measurements" section, "Explanatory Notes" chapter, this volume).

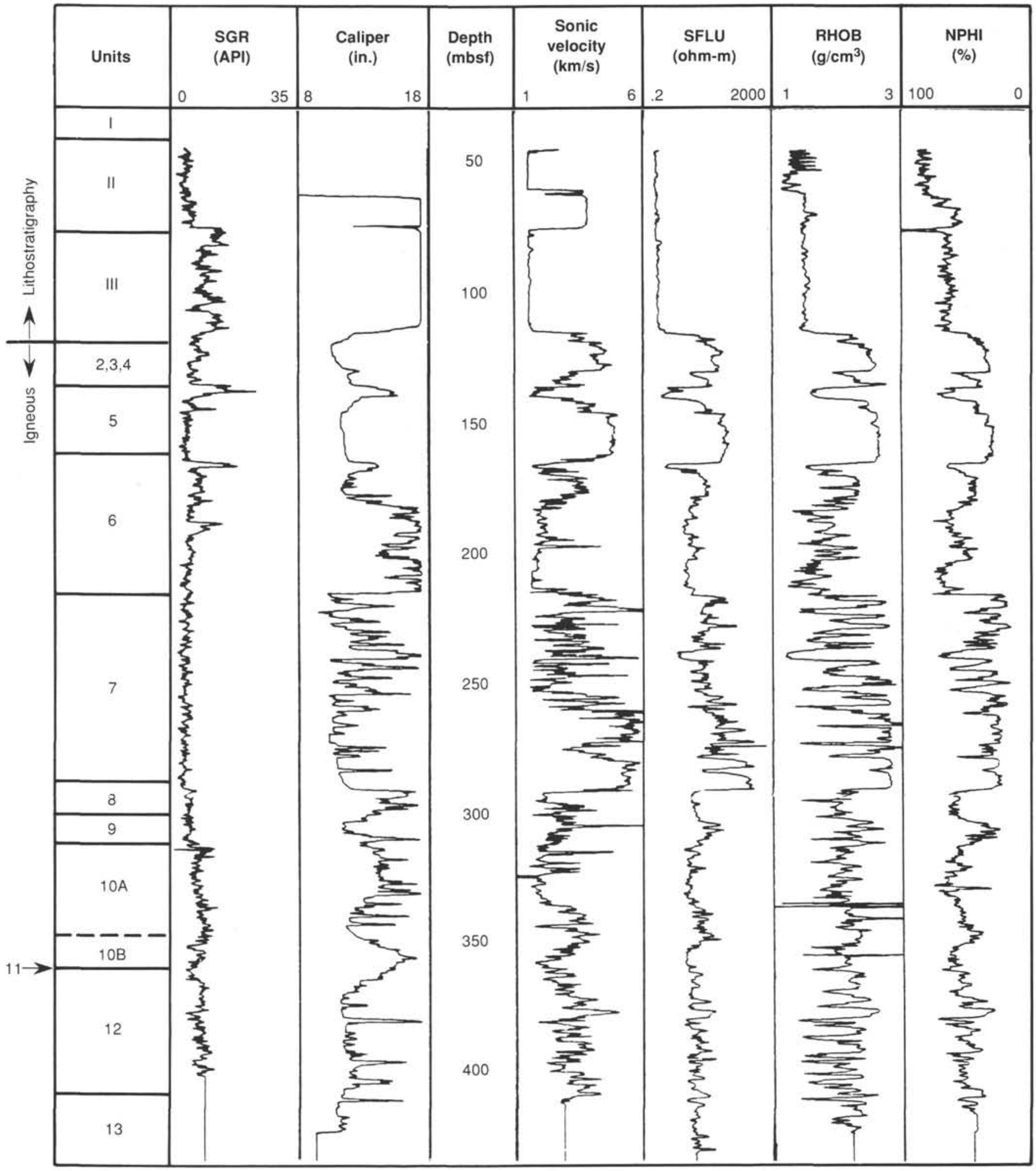

Figure 66. Quad-tool-string logs vs. depth, Site 834. The logs illustrated are as follows: total gamma ray (SGR, in American Petroleum Institute units), caliper hole diameter (in inches), sonic velocity, spherically focused resistivity (SLFU, on logarithmic scale), bulk density (RHOB), and neutron porosity (NPHI). Lithologic and igneous units are illustrated in the left-hand column.

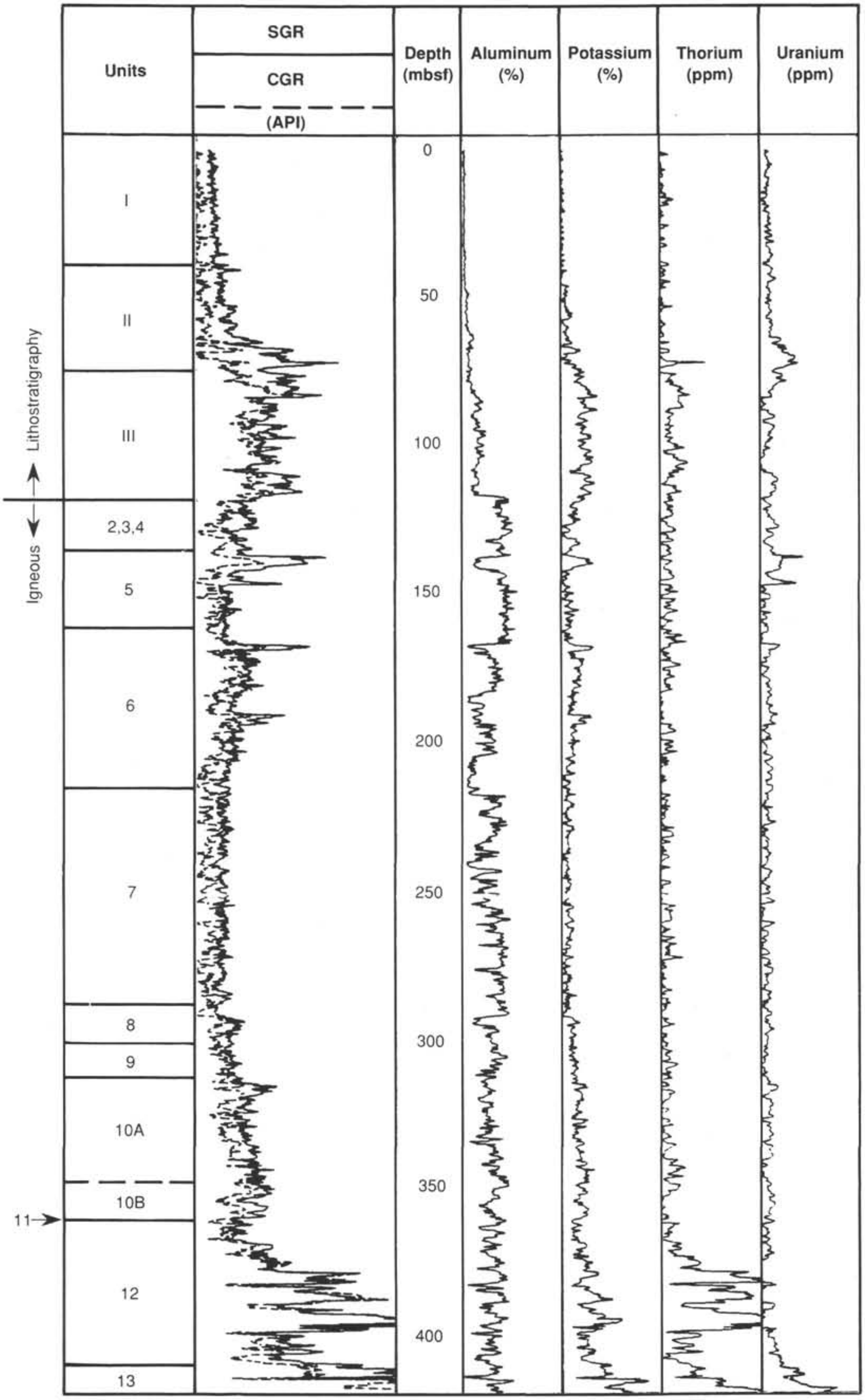

Figure 67. Natural gamma-ray intensity from the geochemical tool string vs. depth, Hole 834A. The logs illustrated are as follows: total gamma ray (SGR), computed gamma ray (CGR), aluminum, potassium, thorium, and uranium. Lithologic and igneous units are illustrated in left-hand column.

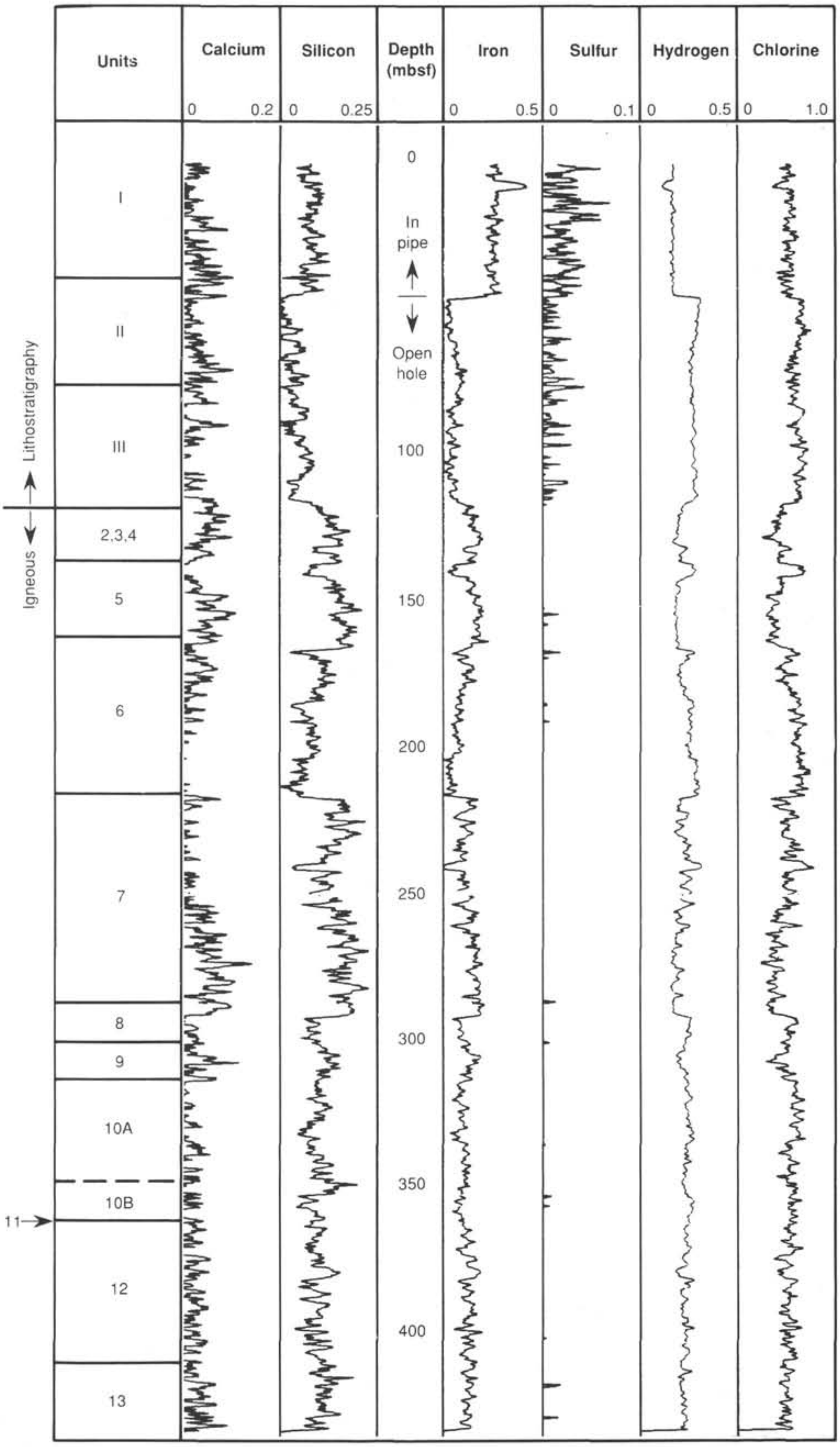

Figure 68. Geochemical yield logs vs. depth, Hole 834A. The logs illustrated are as follows: calcium, silicon, iron, sulfur, hydrogen, and chlorine. Lithologic and igneous units are illustrated in the left-hand column.

slowly at their bases but quickly at their tops, where the lava is chilled by contact with seawater. This imparts a marked asymmetry to their internal structure and a characteristic distinction between a competent and regular zone in the lower two-thirds of the unit and an irregular, highly fractured, rubbly zone in the upper one-third. These characteristics have previously been recognized on downhole records from submarine to subaerial lava flows drilled on the Vøring ringPlateau, northeast Atlantic (ODP Leg 104: Eldholm, Thiede, Taylor, et al., 1987). The conclusion that Units 2 and 5 represent flows rather than sills is supported by preliminary chemical data (see "Igneous Petrology" section, this chapter), which suggests that Units 4 and 5 are chemically similar; Unit 4 is a very thin, highly vesicular unit that very probably represents the eruptive top of Unit 5. The sediments are in depositional contact with this lava, and no alteration that can be related to contact metamorphism (requisite if Unit 5 were a sill) has been preserved in the core.

Examination of the logs (Fig. 66) reveals a far greater variability to most geophysical parameters below about 165 mbsf (i.e., beneath Unit 5). Nevertheless, excursions are visible at or very close to those unit boundaries identified on petrological grounds in lava recovered from the core. Preliminary examination shows that Unit 6 has very low and variable velocity, resistivity and density values, and high porosity for igneous basement and that the calipers were at maximum or near-maximum extent for much of its range. Unit 7 has much higher density and resistivity, higher velocity peaks, and lower porosity than other igneous units. Units 8–13 have values intermediate between those of the above units.

Chemical variations within and between igneous units are implied by the geochemical logs (Figs. 67 and 68). Si and Fe in particular mimic the resistivity, velocity, and density variations, with gentle gradients at the tops and steep gradients at the bases of igneous Units 2 and 5; Units 2, 5, and 7 have the highest values of Si, Fe, and Al. Anomalously high gamma-ray intensity values below 380 mbsf result from previous irradiation of the borehole wall following calibration of the geochemical tool at that depth (see "Operations" section, this chapter). The concluding section will show possible relations of these variations to physical and chemical properties measured in the core.

Variation of Physical Parameters within Lava Flows and the Effect on Downhole Log Characteristics

Petrological studies of the core show that the vesicularity in the igneous units ranges from 0% to 35% (see "Igneous Petrology" section, this chapter). Unit 7 (with an upper margin at 214 mbsf) is a 73-m-thick plagioclase-phyric basalt notable for its very low (<1%) vesicularity. Physical measurements on whole-rock samples from this unit show that it has a systematically higher velocity and bulk density than samples from any other basement unit at Site 834 (see "Physical Properties" section, this chapter). The grain density of crushed rock from this unit is, however, identical within analytical error to those grain densities measured from the other igneous units. From this, one must conclude that the relative variations observed in density, resistivity, velocity, and porosity on downhole logs among the igneous units depend strongly upon the degree of vesicularity of the lava.

Unit 7 is also notable for showing an increase in the number of internal chilled margins from bottom to top, suggesting that it has a relatively massive base and probably a pillowed top (see "Igneous Petrology" section, this chapter). The logs show a decrease in mean velocity, with a concomitant increase in the variability of the signal and a slight decrease in resistivity in the upper part of the unit; however, average and peak values of density and porosity are little changed. These observations suggest that velocity and resistivity may be varying as a function of flow morphology, but that density and porosity may not be significantly affected by it.

Laboratory measurements of velocity and density are relatively consistent for each unit and correspond well with the *maximum* observed value for each unit on the logs. We suggest, for the reasons given below, that the variation recorded on the downhole logs should not be regarded as real. The physical properties of Units 2 and 5, which represent massive or predominantly massive flows, are far more consistent than those of the lower units, most of which have a significant number of internal chilled margins. A weak correlation is apparent between the number of internal chilled zones in a unit and the width and variability of the caliper readings. This suggests that holes may be widened and degraded in thin and/or pillowed flow units. This is confirmed by the marked decrease in core recovery with the increase in number of contacts per meter of core (see "Igneous Petrology" section, this chapter). Much of the short-wavelength, high-amplitude variation of the density and porosity curves on the logs correlates very well with the caliper readings, and is interpreted as an artifact resulting from imperfect contact of the HLDT tool with a highly rugose borehole surface. The recorded signal is probably a combination of both the "real" signal and that of the seawater filling the hole. The poor quality of the sonic curve (which in its raw state exhibits extreme "cycle skipping") is probably also a result of the bad hole conditions.

Poor hole conditions within the basement are probably responsible also for the degraded images seen in some of the FMS data from the lower portions of the borehole. In boreholes with a >16-in. diameter, or those with rugose walls, good pad contact cannot be maintained, and zigzag patterns (indicating spinning of the tool) and vertical striping (indicating sticking and pulling) are common.

Caution should be taken in the interpretation of the chemical variations evident in Figure 68. Unit 7, for example, apparently has the highest Si content of any of the igneous units; however, chemical analysis of samples from this unit by X-ray fluorescence show that Unit 7 has comparable or even lower weight percentages of silica than have the other units. This suggests that, as for the resistivity, density, velocity and porosity tools, the geochemical tool response is significantly affected by borehole rugosity and by petrologic factors such as vesicularity (see discussion above). This appears to apply to all elements measured by the geochemical tool. In addition, there is the added complexity that the Ca, Si, Fe, S, H, and Cl curves have all been normalized to each other. Real chemical variations may be interdependent and therefore their expression will be distorted on the log plots.

DISCUSSION

The primary objectives for Site 834 were successfully achieved in that (1) a sufficient thickness of igneous rock was recovered to confirm that the igneous basement to the site had been penetrated; (2) the age of the oldest sediments recovered determined a minimum age for the basement emplacement; (3) the sedimentary section comprising oozes, sands, and claystones interbedded with vitric ash was used to define the history of the basin fill precisely; and (4) the integration of the biostratigraphic and paleomagnetic data provided the age of rift initiation in this supposedly oldest part of the Lau Basin.

The igneous basement is basalt with LILE and HFSE abundances and ratios that resemble values for N-MORB. In spite of the proximity of the site to the Miocene-Pliocene Lau Ridge volcanic arc, rocks at Site 834 are more like rocks from the modern axial ridges of the Lau Basin than are rocks at other Leg 135 backarc sites even closer to those spreading centers. The uppermost flow/sills are interleaved with sediments of late Miocene age (5–6 Ma), an age that corresponds to previous estimates for the beginning of Lau Basin opening. The occurrence of MORB-like basement at this site, however, and the identification of the restricted areal extent and poorly developed interconnectivity of the sub-basins characterizing the western Lau Basin points to a style of crustal formation different from seafloor spreading but more like brittle extensional rifting. Thus, we speculate that as much as half of the central and southern Lau Basin has formed by crustal extension, with localized magmatism, but without the formation of a mid-oceanic-ridge-type backarc spreading axis.

REFERENCES

Anderson, R. N., Langseth, M. G., and Sclater, J. G., 1977. The mechanisms of heat transfer through the floor of the Indian Ocean. *J. Geophys. Res.*, 82:3391–3409.

Becker, K., and Von Herzen, R. P., 1983. Heat transfer through the sediments of the Mounds Hydrothermal area, Galapagos Spreading Center at 86°W. *J. Geophys. Res.*, 88:995–1008.

Bednarz, U., and Schmincke, H.-U., in press. Petrological and chemical evolution of the northeastern Troodos Extrusive Series (Cyprus, Eastern Mediterranean). *J. Petrol.*

Berger, A. L., 1978. Long-term variations of caloric solar insolation resulting from earth's orbital variations. *Quat. Res.*, 9:139–167.

Berggren, W. A., Kent, D. V., Flynn, J. J., and Van Couvering, J. A., 1985. Cenozoic geochronology. *Geol. Soc. Am. Bull.*, 96:1407–1418.

Bleil, U., 1989. Magnetostratigraphy of Neogene and Quaternary sediment series from the Norwegian Sea: Ocean Drilling Program, Leg 104. *In* Eldholm, O., Thiede, J., Taylor, E., et al., *Proc. ODP, Sci. Results*, 104: College Station, TX (Ocean Drilling Program), 829–901.

Boström, K., and Peterson, M.N.A., 1969. The origin of aluminium-poor ferromanganoan sediments in areas of high heat flow on the East Pacific Rise. *Mar. Geol.*, 7:427.

Bouma, A. H., 1962. *Sedimentology of Some Flysch Deposits:* Amsterdam (Elsevier).

Broecker, W. S., and Peng, T.-H., 1982. *Tracers in the Sea:* Palisades, NY (Eldigio Press).

Bryan, W. B., 1972. Morphology of quench crystals in submarine basalts. *J. Geophys. Res.*, 77:5812–5819.

Shipboard Scientific Party, 1973. Site 203. *In* Burns, R. E., Andrews, J. E., et al., *Init. Repts. DSDP*, 21: Washington (U.S. Govt. Printing Office), 17–32.

Chaproniere, G.C.H., in press. Pleistocene to Holocene planktic foraminiferal biostratigraphy of the Coral Sea, offshore Queensland, Australia. *BMR J. Aust. Geol. Geophys.*

Chase, C. G., 1971. Tectonic history of the Fiji plateau. *Geol. Soc. Am. Bull.*, 82:3087–3110.

Church, B. N., and Johnson, W. M., 1980. Calculation of the refractive index of silicate glasses from chemical composition. *Geol. Soc. Am. Bull.*, 91:619–625.

Claypool, G. E., and Kvenvolden, K. A., 1983. Methane and other hydrocarbon gases in marine sediments. *Annu. Rev. Earth Planet. Sci.*, 11:299–327.

Clement, B. M., Hall, F. J., and Jarrard, R. D., 1989. The magnetostratigraphy of Ocean Drilling Program Leg 105 sediments. *In* Srivastava, S. P., Arthur, M., Clement, B., et al., *Proc. ODP, Sci. Results*, 105: College Station, TX (Ocean Drilling Program), 583–595.

Clement, B. M., and Robinson, F., 1987. The magnetostratigraphy of Leg 94 sediments. *In* Ruddiman, W. F., Kidd, R. B., Thomas, E., et al., *Init Repts. DSDP*, 94, Pt. 2: Washington (U.S. Govt. Printing Office), 635–650.

Cole, J. W., Gill, J. B., and Woodhall, D., 1985. Petrologic history of the Lau Ridge, Fiji. *In* Scholl, D., and Vallier, T. (Eds.), *Geology and Offshore Resources of Pacific Island Arcs—Tonga Region*. Circum-Pac. Counc. Energy Miner. Resour., Earth Sci. Ser., 379–414.

Cole, W. S., 1960. Upper Eocene and Oligocene larger foraminifera from Viti Levu, Fiji. *Geol. Surv. Prof. Pap. U.S.*, No. 374-A.

Colley, H., Hindle, W. H., and Hathaway, B., 1986. Early arc and basinal activity on Viti Levu, Fiji. *In International Volcanological Congress, New Zealand*, 140. (Abstract)

Cronan, D. S., Hodkinson, R. A., Harkness, D. D., Moorby, S. A., and Glasby, G. P., 1986. Accumulation rates of hydrothermal metalliferous sediments in the Lau Basin, S.W. Pacific. *Geo-Mar. Lett.*, 6:51–56.

Cunningham, J. K., and Anscombe, K. J., 1985. Geology of 'Eua and other islands, Kingdom of Tonga. *In* Scholl, D., and Vallier, T. (Eds.), *Geology and Offshore Resources of Pacific Island Arcs—Tonga Region*. Circum-Pac. Counc. Energy Miner. Resour., Earth Sci. Ser., 221–258.

deMenocal, P., Bloemendal, J., and King, J., 1991. A rock-magnetic record of monsoonal dust deposition to the Arabian Sea: evidence for a shift in the mode of deposition at 2.4 Ma. *In* Prell, W. L., Niitsuma, N., et al., *Proc. ODP, Sci. Results*, 117: College Station, TX (Ocean Drilling Program), 389–407.

Dowsett, H. J., 1989. Application of the graphic correlation method to Pliocene marine sequences. *Mar. Micropaleontol.*, 14:3–32.

Dowty, E., Keil, K., and Prinz, M., 1974. Lunar pyroxene-phyric basalts: crystallization under supercooled conditions. *J. Petrol.*, 15:419–453.

Eldholm, O., Thiede, J., Taylor, E., et al., 1987. *Proc. ODP, Init. Repts.*, 104: College Station, TX (Ocean Drilling Program).

Emeis, K.-C., and Kvenvolden, K. A., 1986. Shipboard organic geochemistry on *JOIDES Resolution*. *ODP Tech. Note*, No. 7.

Ernewein, M., Pearce, J. A., Bloomer, S. H., Parson, L. M., Murton, B. J., and Johnson, L. E., in press. Geochemistry of Lau Basin volcanic rocks: influence of ridge segmentation and arc proximity. *Contrib. Mineral. Petrol.*

Ewart, A., and Hawkesworth C. J., 1987. The Pleistocene-Recent Tonga-Kermadec arc lavas: interpretation of new isotope and rare earth data in terms of a depleted mantle source model. *J. Petrol.*, 28:495–530.

Fisher, R. V., 1964. Maximum size, median diameter, and sorting of tephra. *J. Geophys. Res.*, 69:341–355.

______, 1965. Settling velocity of glass shards. *Deep-Sea Res. Oceanogr. Abstr.*, 12:345–353.

Flügel, E., 1982. *Microfacies Analysis of Limestones:* New York (Springer-Verlag).

Frey, F. A., Bryan, W. B., and Thompson, G., 1974. Atlantic Ocean floor: geochemistry and petrology of basalts from Legs 2 and 3 of the Deep Sea Drilling Project. *J. Geophys. Res.*, 79:5507–5527.

Gieskes, J. M., 1973. Interstitial water studies, Leg 15: alkalinity, pH, Mg, Ca, Si, PO_4, and NH_4. *In* Heezen, B. C., MacGregor, I. D., et al., *Init. Repts. DSDP*, 20: Washington (U.S. Govt. Printing Office), 813–829.

______, 1974. Interstitial water studies, Leg 25. *In* Simpson, E.S.W., Schlich, R., et al., *Init. Repts. DSDP*, 25: Washington (U.S. Govt. Printing Office), 361–394.

Gieskes, J. M., Elderfield, H., and Palmer, M. R., 1986. Strontium and its isotopic composition in interstitial waters of marine carbonate sediments. *Earth Planet. Sci. Lett.*, 77:229–235.

Gieskes, J. M., and Peretsman, G., 1986. Water chemistry procedures aboard *JOIDES Resolution*—some comments. *ODP Tech. Note*, No. 5.

Gill, J. B., 1976. Composition and age of Lau basin and ridge volcanic rocks: implications for evolution of an interarc basin and remnant arc. *Geol. Soc. Am. Bull.*, 87:1384–1395.

Hancock, P. L., 1985. Brittle microtectonics: principles and practice. *J. Struct. Geol.*, 7:437–457.

Harland, W. B., Cox, A. V., Llewellyn, P. G., Pickton, C.A.G., Smith, D. G., and Walters, R., 1982. *A Geologic Time Scale:* Cambridge (Cambridge Univ. Press).

Hawkins, J. W., 1974. Geology of the Lau Basin, a marginal sea behind the Tonga Arc. *In* Burk, C., and Drake, C. (Eds.), *Geology of Continental Margins:* Berlin (Springer-Verlag), 505–520.

______, 1976. Petrology and geochemistry of basaltic rocks of the Lau Basin. *Earth Planet. Sci. Lett.*, 28:283–298.

______, 1977. Petrologic and geochemical characteristics of marginal basin basalts. *In* Talwani, M., and Pitman, W. (Eds.), *Island Arcs, Deep Sea Trenches and Back-Arc Basins*, Am. Geophys. Union, Maurice Ewing Ser., 1:355–365.

______, 1988. Cruise Report—PAPATUA Expedition, Leg 04, R/V *Thomas Washington*. SIO Ref. Ser., No. 88-14.

______, 1989. Cruise Report—ROUNDABOUT Expedition, Legs 14, 15, R/V *Thomas Washington*. SIO Ref. Ser., No. 89-13.

Hawkins, J. W., Bloomer, S. H., Evans, C. A., and Melchior, J. T., 1984. Evolution of intra-oceanic arc-trench systems. *Tectonophysics*, 102:174–205.

Hawkins, J. W., and Melchior, J. T., 1985. Petrology of Mariana Trough and Lau Basin basalts. *J. Geophys. Res.*, 90:11431–11468.

Hawkins, J. W., Melchior, J., Florendo, F., and Nilsson, K., 1989. Evolution of backarc basin magmas and their mantle sources—examples from the Lau Basin and Mariana Trough. *Eos*, 70:1389.

Hodkinson, R. A., Cronan, D. S., Glasby, G. P., and Moorby, S. A., 1986. Geochemistry of marine sediments from the Lau Basin, Havre Trough and Tonga-Kermadec Ridge. *N. Z. J. Geol. Geophys.*, 29:335–344.

Hyndman, R. D., Langseth, M. G., and Von Herzen, R. P., 1987. Deep Sea Drilling Project geothermal measurements: a review. *Rev. Geophys.*, 25:1563–1582.

Johnson, G. R., and Olhoeft, G. R., 1984. Density of rocks and minerals. *In* Carmichael, R. S. (Ed.), *CRC Handbook of Physical Properties of Rocks* (Vol. 3): Boca Raton, FL (CRC Press), 1–38.

Karig, D. E., 1970. Ridges and basins of the Tonga-Kermadec island arc system. *J. Geophys. Res.*, 75:239–254.

Lawver, L. A., Hawkins, J. W., and Sclater, J. G., 1976. Magnetic anomalies and crustal dilation in the Lau basin. *Earth Planet. Sci. Lett.*, 33:27–35.

Lofgren, G. E., 1980. Experimental studies on the dynamic crystallization of silicate melts. *In* Hargraves, R. B. (Ed.), *Physics of Magmatic Processes:* Princeton (Princeton Univ. Press), 487–551.

Malahoff, A., Feden, R. H., and Fleming, H. S., 1982. Magnetic anomalies and tectonic fabric of marginal basins north of New Zealand. *J. Geophys. Res.*, 87:4109–4125.

Malahoff, A., Kroenke, L. W., Cherkis, N., and Brozena, J., in press. Magnetic and tectonic fabric of the North Fiji Basin and Lau Basin. *In* Kroenke, L., and Eade, J. V. (Eds.), *Basin Formation, Ridge Crest Processes, and Metallogenesis in the North Fiji Basin.* Circum-Pac. Counc. Energy Miner. Resour., Earth Sci. Ser.

Manheim, F. T., and Sayles, F. L., 1974. Composition and origin of interstitial waters of marine sediments based on deep sea drill cores. *In* Goldberg, E. D. (Ed.), *The Sea* (Vol. 5): New York (Wiley), 527–568.

Mankinen, E. A., Donnelly, J. M., and Grommé, C. S., 1978. Geomagnetic polarity event recorded at 1.1. m.y.r. B.P. on Cobb mountain, Clear Lake volcanic field, California. *Geology*, 6:653–656.

Maris, C.R.P., Bender, M. L., Froelich, P. N., Barnes, R., and Luedtke, N. A., 1984. Chemical evidence for advection of hydrothermal solutions in the sediments of the Galapagos Mounds Hydrothermal Field. *Geochim. Cosmochim. Acta*, 48:2331–2346.

Mazzullo, J. M., Meyer, A., and Kidd, R., 1987. New sediment classification scheme for the Ocean Drilling Program. *In* Mazzullo, J., and Graham, A. G. (Eds.), *Handbook for Shipboard Sedimentologists.* ODP Tech. Note, 8:45–67.

Moore, J. G., and Schilling, J. G., 1973. Vesicles, water, and sulfur in the Reykjanes Ridge basalts. *Contrib. Mineral. Petrol.*, 41:105–118.

Muir, I. D., and Tilley, C. E., 1966. Basalts from the northern part of the Mid-Atlantic Ridge II. The Atlantis collection near 30 degrees N. *J. Petrol.*, 7:193–?

Munsell Soil Color Charts, 1971. Baltimore, MD (Kollmonger Corp.).

Murthy, S.K.M., 1990. Seafloor spreading magnetic lineations in Lau back-arc basin, southwest Pacific. *Inst. Oceanogr. Sci. Deacon Lab. Tech. Rep.*

Nilsson, K., Florendo, F. F., and Hawkins, J. W., 1989. Petrology of a nascent triple junction, northeastern Lau Basin. *Eos*, 70:1389.

Parson, L. M., et al., 1989. RRS *Charles Darwin* Cruise 33/88, 5 May–1 June 1988. Geophysical and geological investigations of the Lau back-arc basin, SW Pacific. *Inst. Oceanogr. Sci. Deacon Lab. Cruise Rep.*, No. 206.

Parson, L. M., Pearce, J. A., Murton, B. J., and RRS *Charles Darwin* Scientific Party, 1990. Role of ridge jumps and ridge propagation in the tectonic evolution of the Lau back-arc basin, southwest Pacific. *Geology*, 18:470–473.

Rashid, M. A. (Ed.), 1985. *Geochemistry of Marine Humic Compounds:* Berlin (Springer-Verlag).

Reich, V., Marchig, V., Sunkel, G., and Weiss, W., 1990. Hydrothermal and volcanic input in sediments of the Lau Back-Arc Basin, S.W. Pacific. *Mar. Mining*, 9:183–203.

Robinson, P. T., Flower, M.F.J., Schmincke, H.-U., and Ohnmacht, W., 1977. Low temperature alteration of oceanic basalts, DSDP Leg 37. *In* Aumento, F., Melson, W. G., et al., *Init. Repts. DSDP*, 37: Washington (U.S. Govt. Printing Office), 775–793.

Romankevich, E. A., 1984. *Geochemistry of Organic Matter in the Ocean:* New York (Springer-Verlag).

Ross, C. S. and Smith, R. L., 1955. Water and other volatiles in volcanic glass. *Am. Mineral.*, 40:1071–1089.

Sato, H., 1979. Segregation vesicles and immiscible liquid droplets in ocean-floor basalt of Hole 396B, DSDP Leg 46. *In* Dmitriev, L., Heirtzler, J., et al, *Init. Repts. DSDP*, 46: Washington (U.S. Govt. Printing Office), 283–291.

Schmincke, H.-U., 1981. Ash from vitric muds in deep sea cores from the Mariana Trough and fore-arc regions (south Philippine Sea) (Sites 453, 454, 455, 458, 459). *In* Hussong, D. M., Uyeda, S., et al., *Init. Repts. DSDP*, 60: Washington (U.S. Govt. Printing Office), 473–481.

Sclater, J. G., 1972. Heat flow and elevation of the marginal basins of the western Pacific. *J. Geophys. Res.*, 77:5685–5696.

Sclater, J. G., Anderson, R. N., and Bell, M. L., 1971. Elevation of ridges and evolution of the central Eastern Pacific. *J. Geophys. Res.*, 76:7888–7915.

Sclater, J. G., Hawkins, J. W., Mammerickx, J., and Chase, C. G., 1972. Crustal extension between the Tonga and Lau Ridges: Petrologic and geophysical evidence. *Geol. Soc. Am. Bull.*, 83:505–518.

Serra, O., 1989. *Formation MicroScanner Image Interpretation:* Houston (Schlumberger Educational Services).

Smith, R. E., 1968. Segregation vesicles in basaltic lava. *Am. J. Sci.*, 265:696–713.

Sun, S.-S., and McDonough, W. F., 1989. Chemical and isotopic systematics of oceanic basalts: implications for mantle composition and processes. *In* Saunders, A. D., and Norry, M. J. (Eds.), *Magmatism in the Ocean Basins.* Geol. Soc. Spec. Publ. London, 42:313–345.

Tamaki, K., Pisciotto, K., Allan, J., et al., 1990. *Proc. ODP, Init. Repts.*, 127: College Station, TX (Ocean Drilling Program).

Thomson, A. F., and Thomasson, M. R., 1969. Shallow to deep water facies development in the Dimple Limestone (Lower Pennsylvanian), Marathon region, Texas. *In* Friedman, G. M. (Ed.), *Depositional Environments in the Carbonate Rocks.* Spec. Publ. Soc. Econ. Paleontol. Mineral., 14:495–516.

von Stackelberg, U., 1990. R.V. *Sonne* Cruise SO 48: summary of results testing a model of mineralisation. *Mar. Mining*, 9:135–144.

von Stackelberg, U., and von Rad, U., 1990. Geological evolution and hydrothermal activity in the northern Lau and North Fiji Basins (Sonne Cruise SO-35—a synthesis. *Jahrb., Reihe D, Mineral., Petrog., Geoch., Lagerstatt.*, 92:629–660.

Walker, G.P.L., 1971. Grain-size characteristics of pyroclastic deposits. *J. Geol.*, 79:696–714.

Weissel, J. K., 1977. Evolution of the Lau Basin by the growth of small plates. *In* Talwani, M., and Pitman, W. C. (Eds.), *Island Arcs, Deep Sea Trenches and Back Arc Basins.* Am. Geophys. Union, Maurice Ewing Ser., 1:429–436.

Whelan, P. M., Gill, J. B., Kollman, E., Duncan, R., and Drake, R. E., 1985. Radiometric dating of magmatic stages in Fiji. *In* Scholl, D., and Vallier, T. (Eds.), *Geology and Offshore Resources of Pacific Island Arcs—Tonga Region.* Circum-Pac. Counc. Energy Miner. Resour., 415–440.

Wollin, G., Ericson, D. B., and Ryan, W.B.F., 1971. Magnetism of the Earth and climate changes. *Earth Planet. Sci. Lett.*, 12:175–183.

Woodhall, D., 1985. Geology of the Lau Ridge. *In* Scholl, D., and Vallier, T. L. (Eds.), *Geology and Offshore Resources of Pacific Island Arc—Tonga Region.* Circum-Pac. Counc. Energy Miner. Resour., Earth Sci. Ser., 2:351–378.

Ms 135A-104

NOTE: All core description forms ("barrel sheets") and core photographs have been printed on coated paper and bound separately as Part 2 of this volume, beginning on page 681.

Formation microscanner images for this site are presented on microfiche in the back of Part 2.

Hole 834B: Resistivity-Sonic-Natural Gamma Ray Log Summary

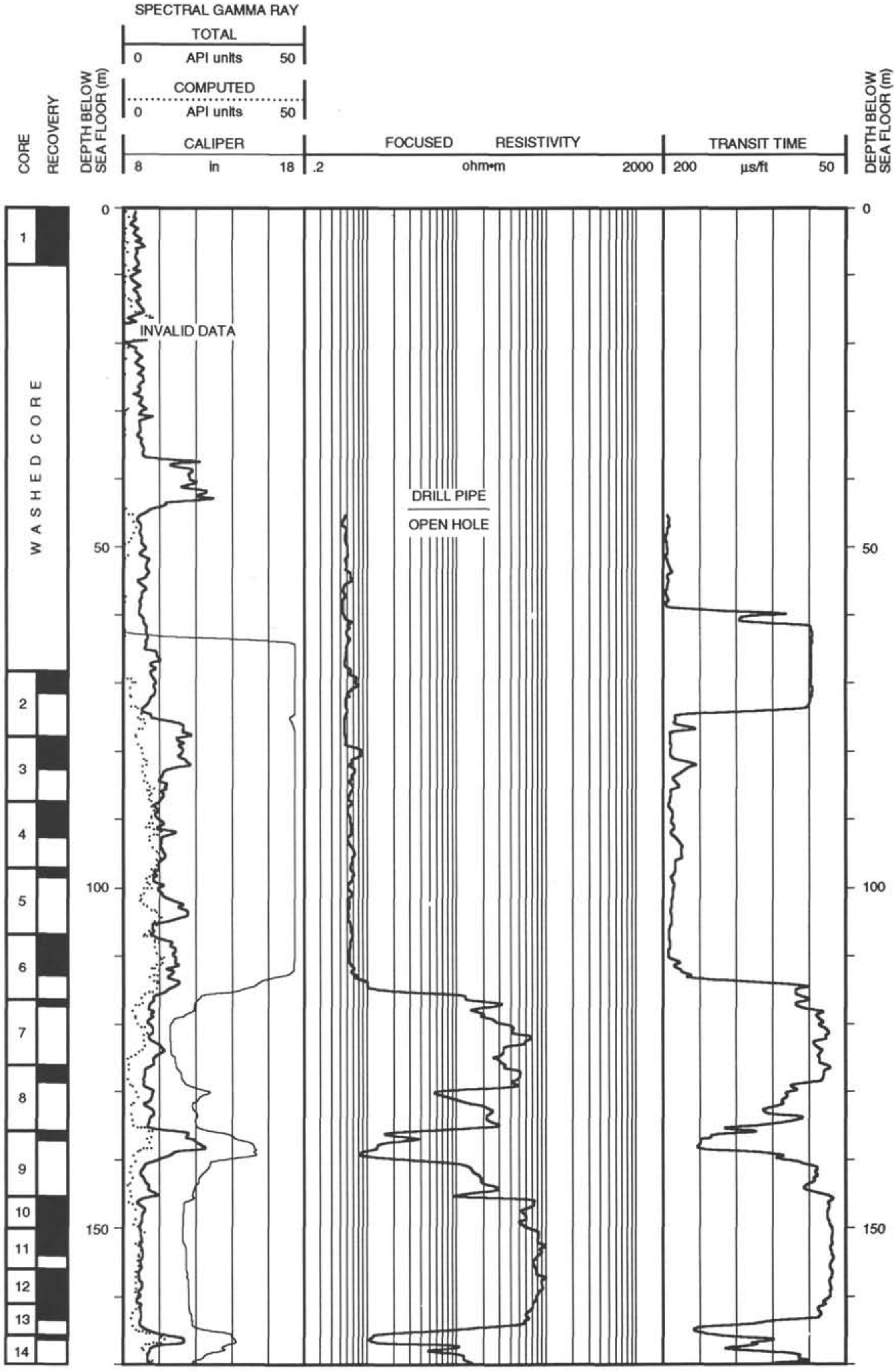

Hole 834B: Resistivity-Sonic-Natural Gamma Ray Log Summary (continued)

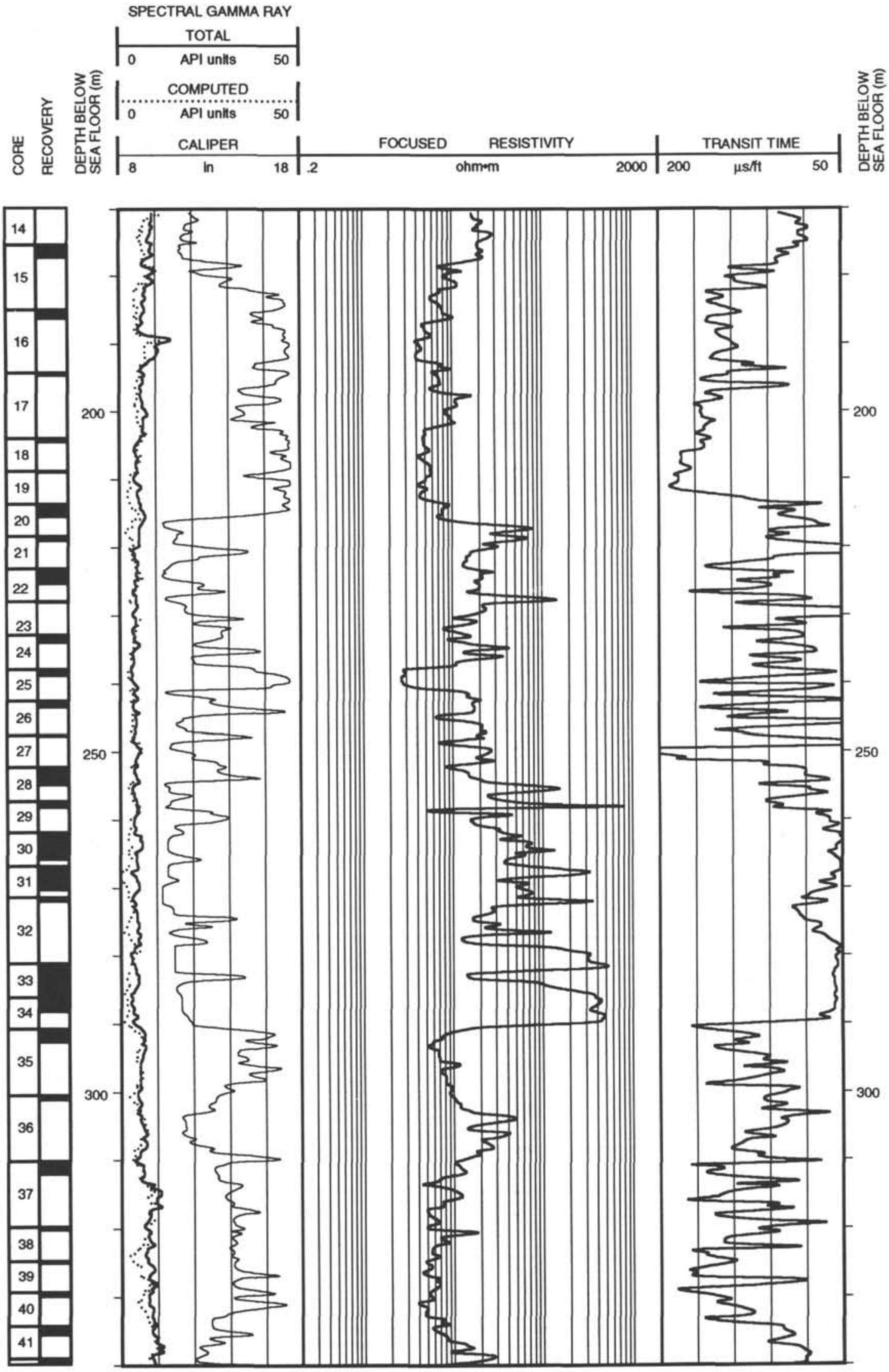

Hole 834B: Resistivity-Sonic-Natural Gamma Ray Log Summary (continued)

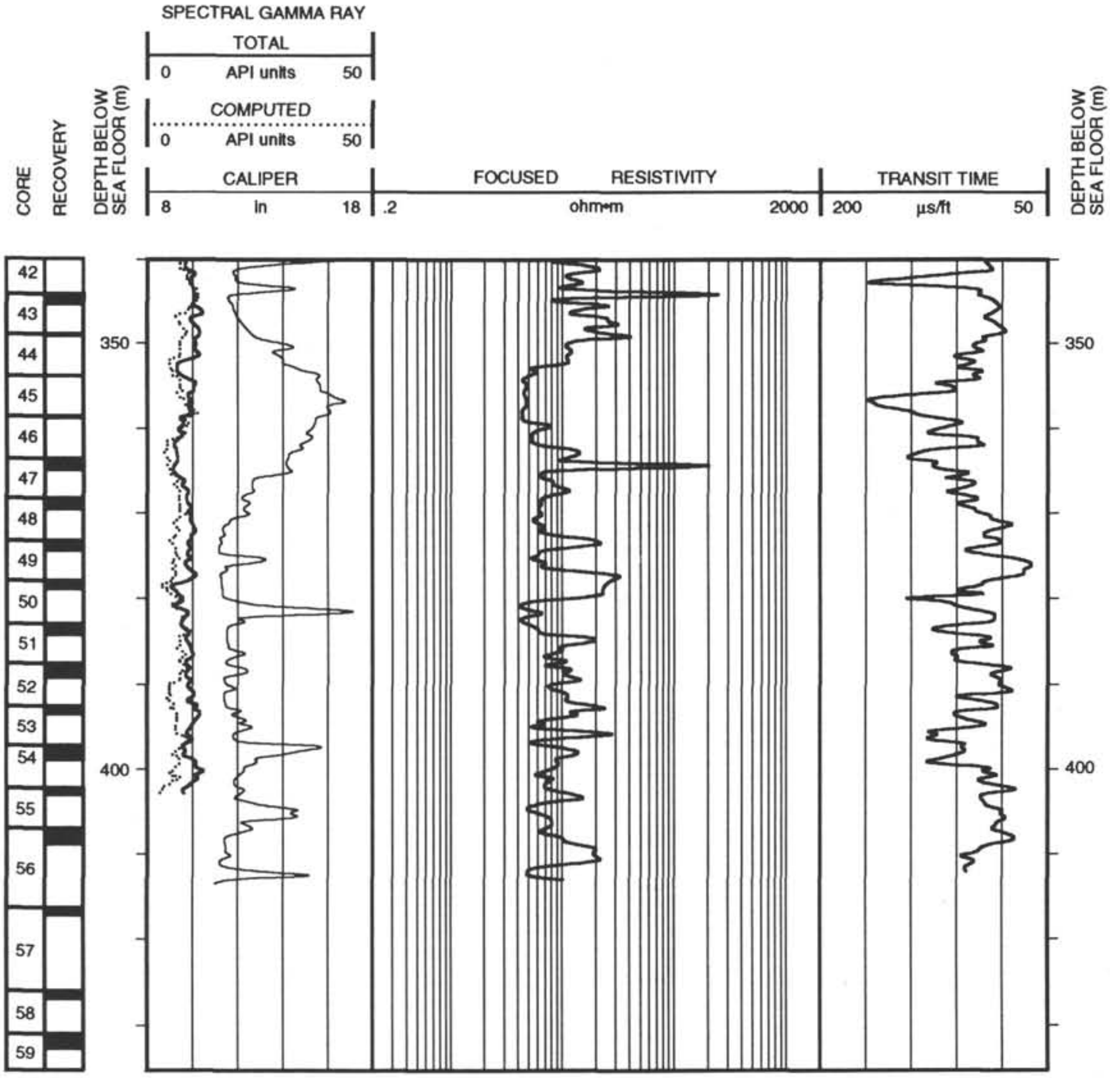

Hole 834B: Density-Natural Gamma Ray Log Summary

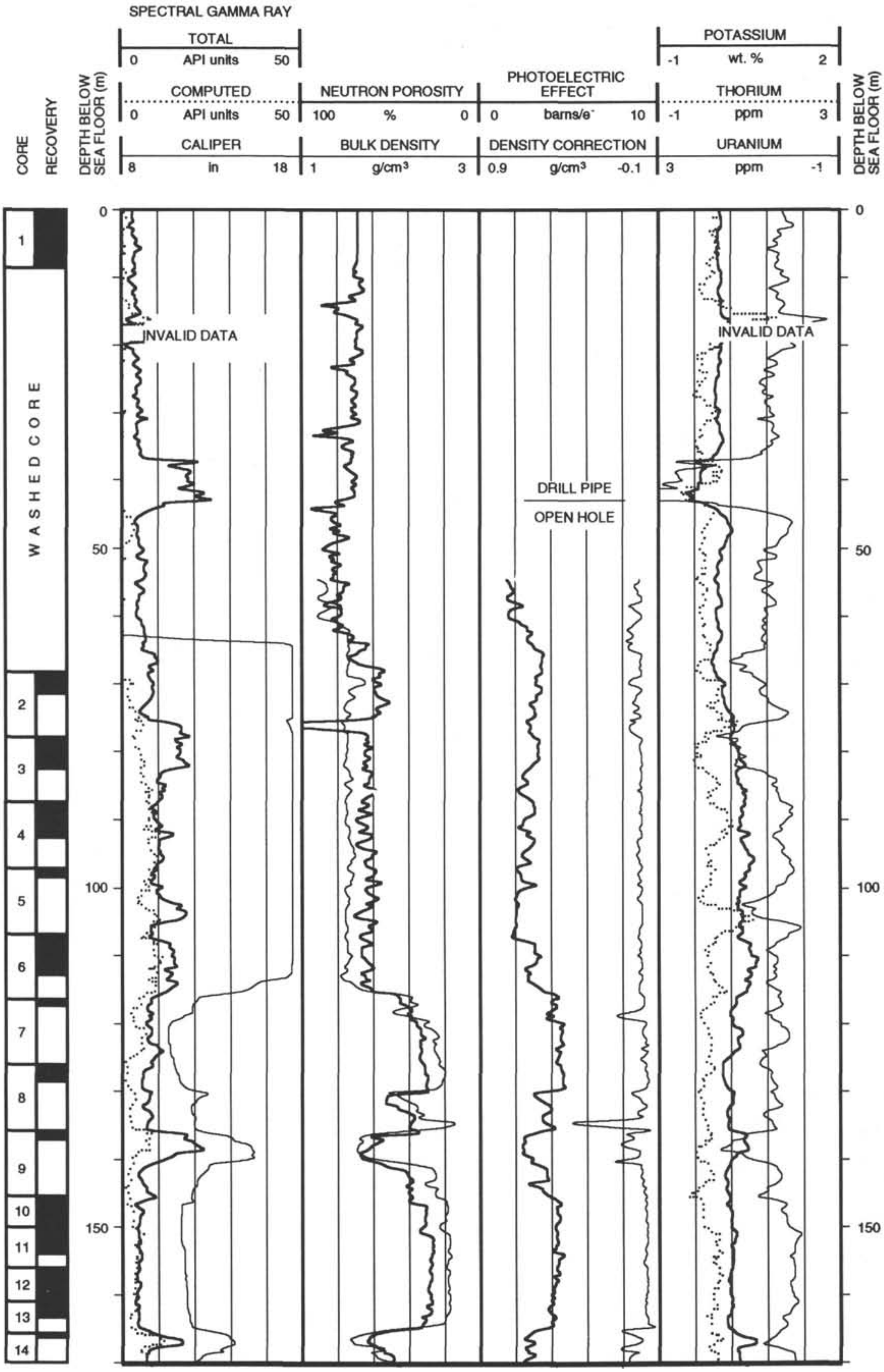

Hole 834B: Density-Natural Gamma Ray Log Summary (continued)

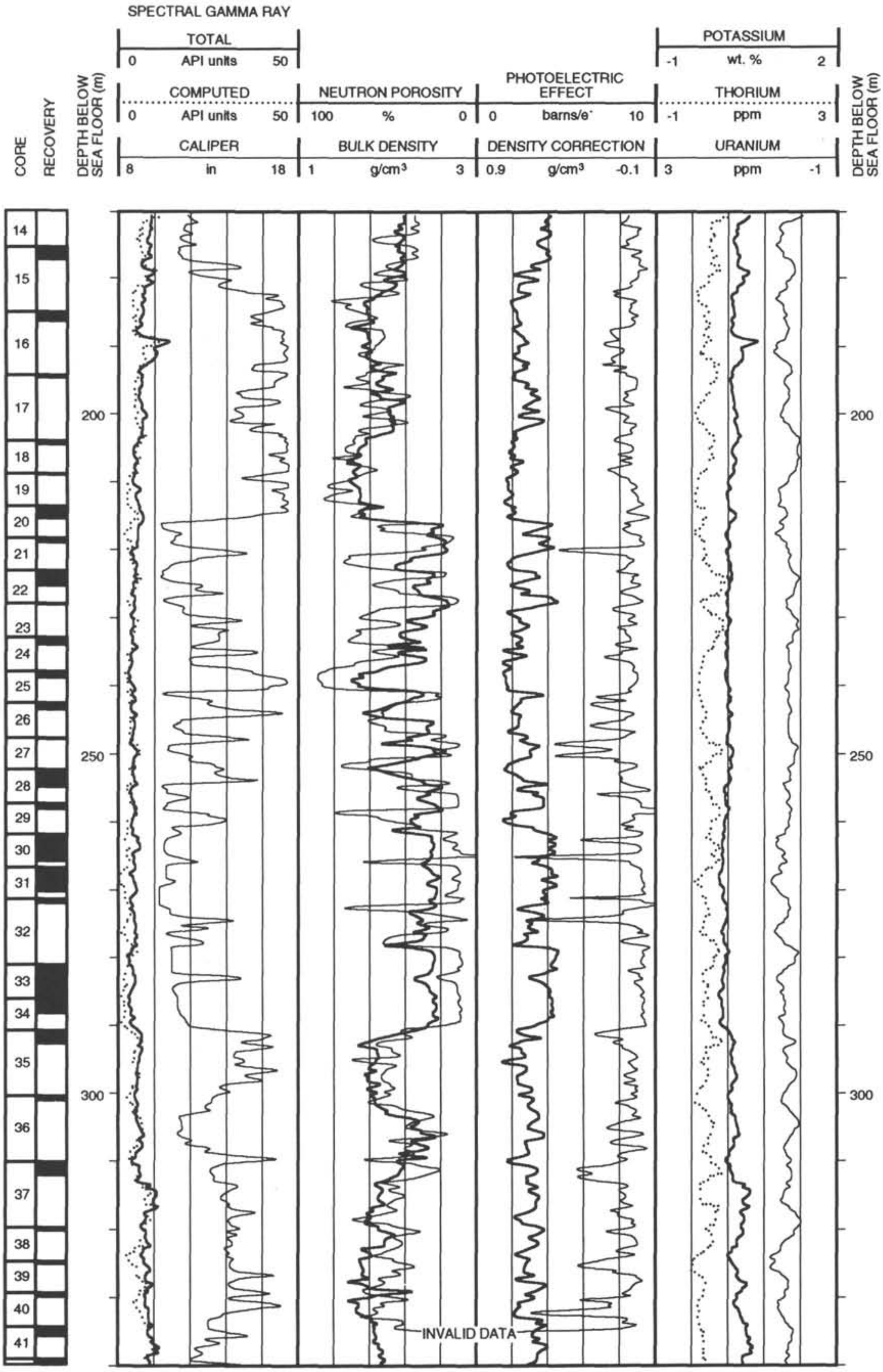

Hole 834B: Density-Natural Gamma Ray Log Summary (continued)

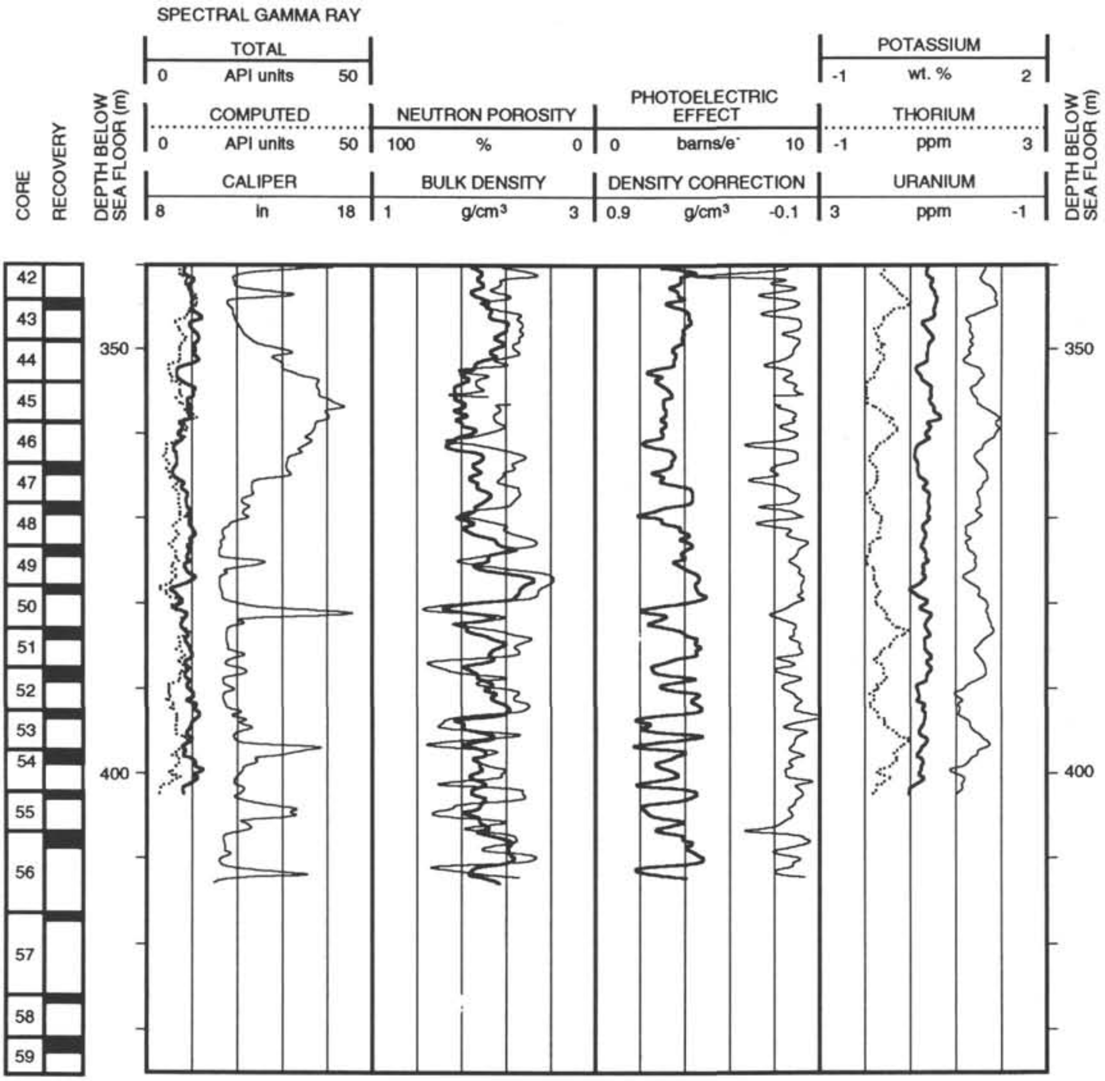

Hole 834B: Geochemical Log Summary

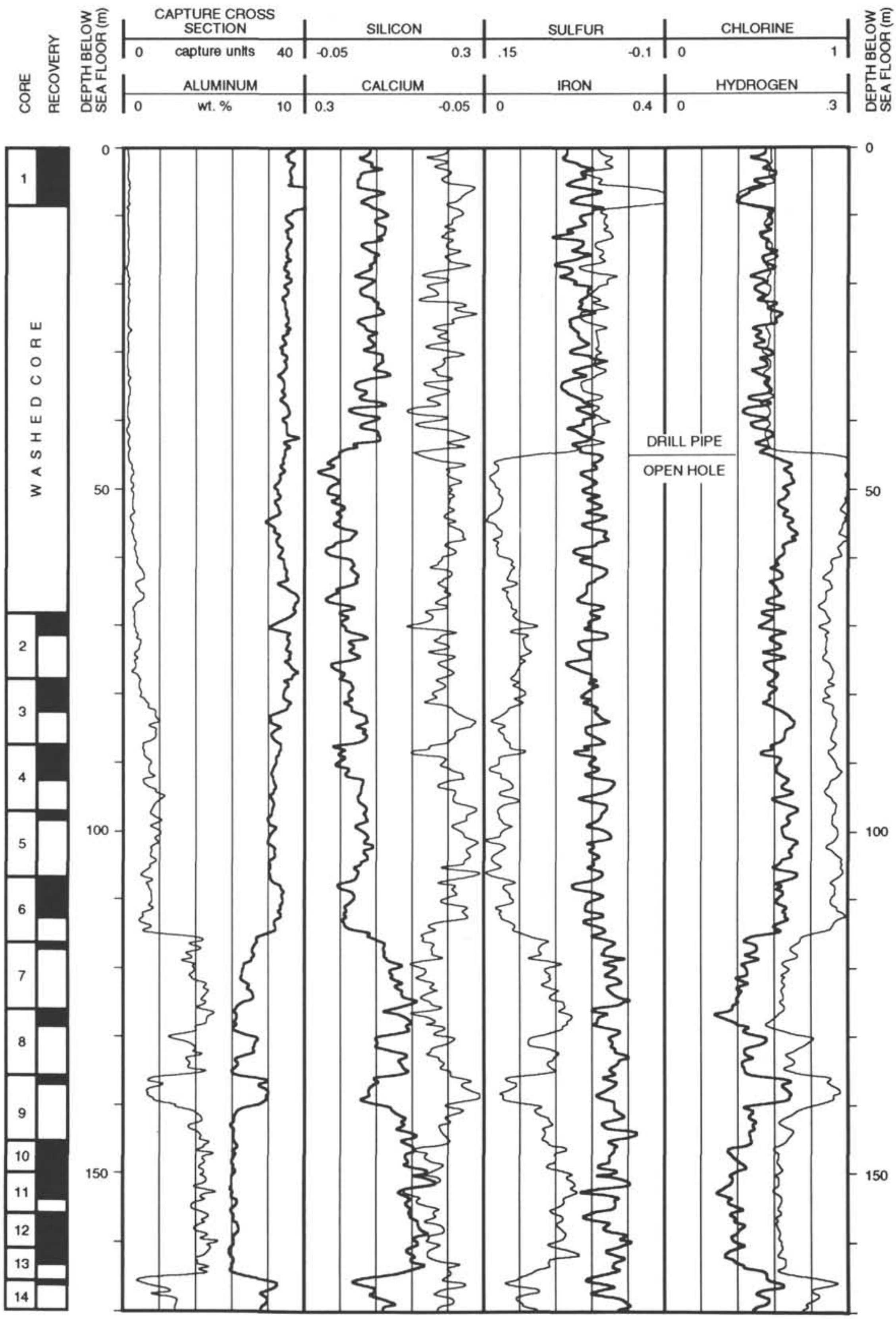

Hole 834B: Geochemical Log Summary (continued)

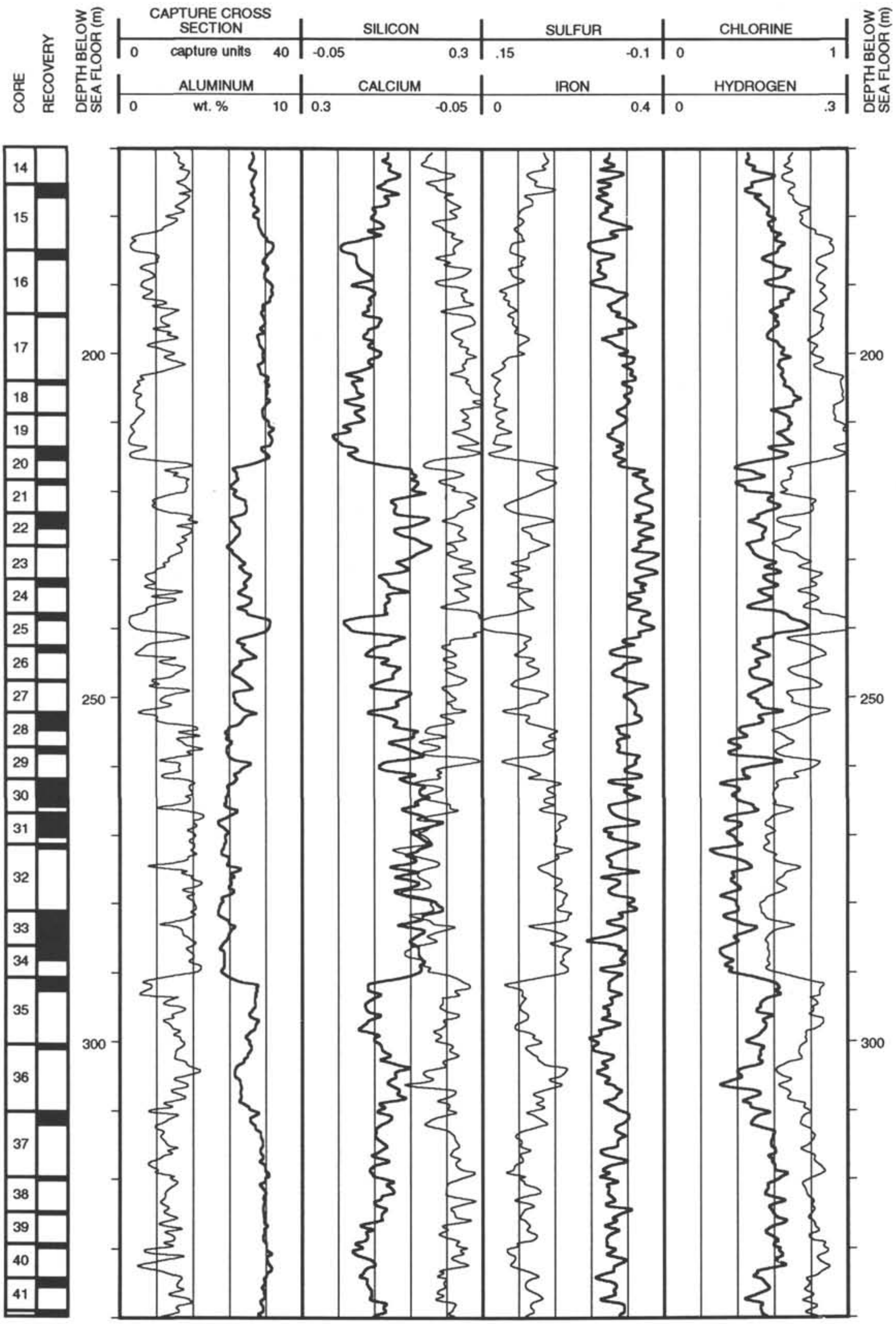

Hole 834B: Geochemical Log Summary (continued)